Anthony Tang

Augmented Dielectric Barrier Discharge Plasma Actuators for Active Flow Control

Anthony Tang

A dissertation submitted in partial fulfillment of the requirements for the degree of

Doctor of Philosophy

University of Washington

2024

Program Authorized to Offer Degree:

Mechanical Engineering

University of Washington

Abstract

Augmented Dielectric Barrier Discharge Plasma Actuators for Active Flow Control

by Anthony Tang

Chair of the Supervisory Committee:

Professor Igor Novosselov

Department of Mechanical Engineering

Electrohydrodynamic (EHD) devices have seen a strong surge in popularity for various applications, including virus inactivation, electrostatic particle collection, and, most interestingly, active flow control. The most promising EHD device for active flow control is a dielectric barrier discharge (DBD) plasma actuator due to its solid-state operation, fast response time, and easy integration. However, DBD actuators have not yet been developed for robust real-world applications. Much of the fundamental physics of DBD actuators remains unclear, and realistic applications of DBD actuators require significantly improved performance. This dissertation aims to improve our understanding of DBD plasma actuators and their complex underlying phenomena and use those insights to optimize them. First, we develop empirical models of critical DBD parameters such as thrust and power usage for standard two-electrode DBD actuators in quiescent, co-flow, and counter-flow wind conditions. Second, this work explores the underlying plasma-fluid mechanisms of a DC-augmented (DCA) DBD actuator with a positively or negatively biased third electrode. With novel DC augmentation insight, this work then explores an AC-augmented DBD for the first time. The AC augmentation illustrates a pathway for continuous DBD acceleration by demonstrating a pull action by a third electrode. Immediately building on the AC augmentation mechanism, this dissertation develops an optimized multi-stage DBD array with key geometric limits. The multi-stage DBD array generates significantly more thrust than previously reported DBD actuators with a thicker wall jet. Finally, the multi-stage DBD array is tested on a Clark Y airfoil in robust co-flow conditions at varying angles of attack. The results suggest an optimized DBD array can control an aerodynamic surface with significantly more control authority at more robust conditions than previously demonstrated.

TABLE OF CONTENTS

LIST OF FIGURES .... **IV**

LIST OF TABLES .... **XI**

CHAPTER 1. INTRODUCTION **1**

1.1 ACTIVE FLOW CONTROL (AFC) 2

CHAPTER 2. PLASMA ACTUATORS **3**

2.1 THEORY OF OPERATION 5
2.2 CHALLENGES 8
2.3 DEVELOPMENTS 10
2.3.1 *Effect of Electrode Geometry and Dielectric Barrier* *10*
2.3.2 *Effect of Electrical Waveform* *12*
2.3.3 *Effect of External Flow and Numerical Modeling* *13*
2.3.4 *DC-Augmented DBD* *15*
2.3.5 *DBD Array* *16*
2.4 RESEARCH OBJECTIVES AND DISSERTATION OUTLINE 17

CHAPTER 3. EXPERIMENTAL FACILITIES AND INSTRUMENTATION **20**

3.1 DBD PLASMA ACTUATOR 20
3.2 THRUST CHARACTERIZATIONS 20
3.3 VELOCITY CHARACTERIZATIONS 24
3.4 ELECTRICAL CHARACTERIZATION 25
3.5 OPTICAL PLASMA CHARACTERIZATION 28
3.6 POWER ELECTRONICS 29

CHAPTER 4. DBD ACTUATOR EMPIRICAL MODEL IN QUIESCENT CONDITION32

4.1 EXPERIMENTAL SET-UP 32
4.2 EFFECT OF VOLTAGE AND FREQUENCY ON THE PLASMA VOLUME 37
4.3 DISCHARGE CURRENT CHARACTERISTICS 39
4.4 VELOCITY CHARACTERISTICS 42
4.5 ENERGY TRANSFER CHARACTERISTICS 45
4.6 RELATIONSHIP BETWEEN DISCHARGE CURRENT AND MOMENTUM 47
4.7 CHAPTER SUMMARY 49

CHAPTER 5. DBD ACTUATOR IN EXTERNAL FLOW **50**

5.1 EXPERIMENTAL SETUP 51

5.2 EFFECT OF EXTERNAL FLOW ON ELECTRICAL POWER CONSUMPTION 55
5.3 OPERATION IN QUIESCENT CONDITION 56
5.4 CO-FLOW EHD MOMENTUM INJECTION 57
5.5 COUNTER-FLOW EHD MOMENTUM INJECTION 60
5.6 MOMENTUM DIFFERENCE 66
5.7 CHAPTER SUMMARY 69

CHAPTER 6. DC-AUGMENTED DBD PLASMA ACTUATOR 71

6.1 EXPERIMENTAL SETUP 73
6.2 VERTICAL AND HORIZONTAL THRUST CHARACTERISTICS OF DCA-DBD 77
6.3 VELOCITY CHARACTERISTICS OF DCA-DBD 78
6.4 MECHANISMS OF DCA-DBD 80
  6.4.1 *Negative DCA 80*
  6.4.2 *Positive DCA 81*
6.5 ELECTRICAL CHARACTERISTICS OF DCA-DBD 82
6.6 SURFACE POTENTIAL 84
6.7 PLASMA EMISSION – OPTICAL CHARACTERIZATION 87
6.8 DISCUSSION 89
6.9 CHAPTER SUMMARY 90

CHAPTER 7. AC-AUGMENTED DBD PLASMA ACTUATORS 91

7.1 EXPERIMENTAL SETUP 93
7.2 PLASMA CHARACTERISTICS 97
  7.2.1 *Time-Integrated Plasma Visualization 97*
  7.2.2 *Phase-Resolved Plasma Characteristics 100*
7.3 ELECTRICAL CHARACTERISTICS 102
7.4 MECHANICAL CHARACTERISTICS 108
  7.4.1 *Thrust Characteristics 108*
  7.4.2 *Wall jet Characteristics 112*
7.5 CHAPTER SUMMARY 116

CHAPTER 8. DBD PLASMA ACTUATOR ARRAYS 118

8.1 EXPERIMENTAL SETUP 120
8.2 PLASMA CHARACTERISTICS 124
8.3 THRUST CHARACTERISTICS 127
8.4 VELOCITY CHARACTERISTICS 130
8.5 ELECTRICAL CHARACTERISTICS 132
8.6 FORCE EFFICIENCY AND TOTAL EFFICIENCY 133
8.7 DISCUSSIONS 136
8.8 CONCLUSION 137

CHAPTER 9. EFFECT OF ACTIVE ELECTRODE SHAPE IN A DBD ARRAY 138

CHAPTER 10. ACTIVE FLOW CONTROL OF A CLARK Y AIRFOIL 140

10.1 EXPERIMENTAL SETUP 141
10.1.1 *Wind Tunnel 141*
10.1.2 *DBD Actuator and Airfoil 144*
10.2 RESULTS 147
10.2.1 *Effect of Embedded DBD Actuator 147*
10.2.2 *Effect of Dual DBD Actuator Array in Co-Flow 147*
10.2.3 *Lift/Drag Ratio Enhancement with Dual DBD 152*
10.3 CHAPTER SUMMARY 154

CHAPTER 11. CONCLUSIONS 155

APPENDIX A. NUMERICAL MODELING OF DBD IN CO- AND COUNTER-FLOW 160

APPENDIX B. DC-AUGMENTED DBD SUPPLEMENTAL INFORMATION 164

APPENDIX C. SURFACE VIRUS INACTIVATION BY IMPINGING FLOW NON-THERMAL PLASMA REACTOR 167

C.1 EXPERIMENTAL SETUP 172
C.1.1 *DBD Flow Reactor 172*
C.1.2 *Reactor Operation: Electrical and Flow Parameters 173*
C.1.3 *Surface Treatment 174*
C.2 RESULTS AND DISCUSSION 176
C.2.1 *Reactor Operation and Ozone Production 176*
C.2.2 *Virus Inactivation 179*
C.3 CHAPTER SUMMARY 181

REFERENCES 183

LIST OF FIGURES

Figure 2.1: A traditional two-electrode DBD Plasma Actuator with an air-exposed active and embedded electrode. The embedded electrode typically is grounded or an out-of-phase AC waveform. 5

Figure 2.3: Traditional DBD Plasma Actuator with transparent quartz dielectric. The high E-field between the active and embedded electrodes creates a non-thermal plasma towards the embedded electrode. The image captures the discharge across several discharge cycles. 6

Figure 2.4: DBD electrical current is commonly divided into a "positive-going" and "negative-going" half cycle, with distinctively different discharge dynamics to create a "push-push" forcing. 7

Figure 2.5: DBD "push-push" forcing mechanism supports a positive force generated in both the positive (voltage rising) and negative (voltage falling) half-cycle. 8

Figure 2.6: A two-electrode DBD (a) has been tested with varying embedded electrode lengths (L_E), active electrode lengths (L_A), and electrode gap lengths (L_G). The width serves as the normalizing dimension. Some works have tested a serrated-edged two-electrode DBD (b) with varying serrated edge length (S_L) and width (S_W). 11

Figure 3.1. The thrust of a three-electrode DBD actuator can be characterized by direct horizontal (a) and vertical thrust (b). The force balance typically comprises an electrically shielded balance with a non-conductive stand to transfer the thrust through the shielding.... 21

Figure 3.2. A DBD actuator thrust is directly measured by holding the flat plate vertically and measuring the reactionary thrust on the flat plate. A thin DBS wire connects a two-stage DBD array (left) and a four-stage DBD array (right). A Faraday shield is commonly placed around the scale. However, the Faraday shield may not be needed in relatively low-voltage conditions (< 20 kV).. 23

Figure 3.3. Proper shielding of the analytical balance in thrust measurements is confirmed with an "off-on-off" test. For example, a DBD actuator with a 3.175 mm quartz dielectric is excited with a 30 kV / 2 kHz sine wave with no thrust measured before and after the HV is applied. 23

Figure 3.4. A pitot tube and pressure transducer characterize the flow field of a two-electrode DBD actuator with a thin Kapton dielectric. The pitot tube is shown an illuminated background (a), and the plasma discharge is visible without background illumination (b)................ 25

Figure 3.5. Traditional DBD Current with a 3.125 mm Quartz dielectric at 40 kV / 2 kHz (left) and the identified capacitive current (right)... 26

Figure 3.6. CCD Camera set up with T1 through T4 quadrant timing for a three-electrode DBD test.. 29

Figure 3.7. "Dual Hot" Custom high-voltage power supply 30

Figure 3.8. The “single hot” custom power supply is built with a power strip, amplifier, power monitor, temperature monitor, voltage monitor, current monitor, utility 12V, and signal input. The temperature monitor typically monitors the custom transformer’s core........... 32

Figure 4.1. Schematic of the dielectric barrier discharge (DBD) plasma actuator. The plasma actuator is mounted on an acrylic glass plate, and the blue region is the dielectric layer separating the electrodes. The velocity is measured using a custom-built glass pitot tube, and the electrical characteristics are measured using a Rogowski coil. 34

Figure 4.2. Plasma discharge region of DBD actuators at 12 kV and 2 kHz. A 98% threshold is outlined in red to calculate the plasma length and volume...................................... 35

Figure 4.3. Experimentally evaluated (a) plasma length and (b) projected plasma volume increase as a function of voltage. Plasma length reaches an asymptotic value with frequency, but the plasma volume continues to increase... 39

Figure 4.4. Discharge current as a function of applied voltage and frequency for the experimental data... 40

Figure 4.5. Discharge current as a function of applied voltage and frequency for the experimental data. The current varies quadratically with applied voltage, and the power-law relationships for positive and negative discharge currents predict the values accurately. 41

Figure 4.6. The current density for total discharge current and the current density remains the same for the two applied frequencies.. 42

Figure 4.7. Wall jet velocity profiles induced by DBD at different locations downstream from the high voltage electrode for different applied conditions (a) 14 kV / 1 kHz, (b) 14 kV / 2 kHz, (c) 18 kV / 1 kHz, and (d) 18 kV / 2 kHz. 44

Figure 4.8. Electromechanical efficiency determined at different voltages for two different frequencies reaches a maximum value of 0.03%... 46

Figure 4.9. Momentum of the wall jet vs. (a) voltage and (b) discharge current. The wall -jet momentum collapses onto a single line for both frequencies and is directly proportional to the discharge current.. 47

Figure 5.1. Schematic of the experimental setup: The DBD actuator is mounted on an acrylic glass plate flushed with the wind tunnel bottom. The blue region is the dielectric layer separating the electrodes. 53

Figure 5.2. DBD power usage at U∞ = 5 m/s and U∞ = 11 m/s external flow in co-flow and counter-flow... 56

Figure 5.3. DBD with no external flow at x = 10 mm (a) and x = 25 mm (b) downstream. The maximum velocity at 19.5 kV is ~ 4.7 m/s at y = 0.5 mm at x = 10 mm downstream.57

Figure 5.4. DBD actuator in co-flow configuration, the first measurement is taken at x=10 mm to avoid plasma region disruption with pitot probe. The plasma region is colored purple. 57

Figure 5.5. DBD actuator in $U_\infty = 5$ m/s co-flow at (a) x = 10 mm and (b) x = 25 mm downstream. The dashed line shows the freestream profile without plasma injection. The DBD voltage varies in the 14 - 19.5 kV range; the AC frequency is set constant at 2 kHz. 59

Figure 5.6. DBD actuator in $U_\infty = 11$ m/s co-flow at x = 10 mm (a) and x = 25 mm (b) downstream. The DBD voltage varies in the 14kV-19.5kV range, and the AC frequency is set constant at 2kHz. 60

Figure 5.7. DBD actuator in counter-flow configuration. The plasma region is colored purple. 61

Figure 5.8. DBD actuator in $U_\infty = 5$m/s counter-flow at x = 10 mm (a) and x = 25 mm (b) downstream. The DBD voltage varies in the 14 - 19.5 kV range, and the AC frequency is set constant at 2 kHz. 62

Figure 5.9. DBD actuator in $U_\infty = 11$ m/s counter-flow at x = 10 mm (a) and x = 25 mm (b) downstream. The DBD voltage varies in the 14 - 19.5 kV range, and the AC frequency is set constant at 2 kHz. 63

Figure 5.10. DBD actuator in $U_\infty = 5$ m/s counter-flow at y = 0.5 mm (a) and y = 1.0 mm (b). The DBD voltage varies in the 14 - 19.5 kV range, and the AC frequency is set constant at 2 kHz. 64

Figure 5.11. X-velocity contour plot for EHD jet in counter-flow for $U_\infty = 5$ m/s for varying voltages. Gridlines correspond to recorded points spaced 0.5 mm apart in the x- and y-direction. 65

Figure 5.12. DBD momentum difference at $U_\infty = 5$ m/s and $U_\infty = 11$ m/s external flow . 67

Figure 6.1.(a) The three-electrode DCA-DBD Plasma actuator has a 3.15 mm thick quartz dielectric barrier. The embedded electrode is covered with thick polyimide tape and silicone rubber. (b) The experimental schematic of the DCA-DBD actuator comprised of (1) an air-exposed electrode, (2) a grounded embedded electrode, (3) an air-exposed third electrode, and (4) a dielectric barrier. The current through the DBD electrode pair and the third electrode is measured with (5) a non-intrusive current monitor and (6) an oscilloscope. The DBD electrodes are powered by (7) a custom power supply with (8) a Trek P6015A HV probe. The third electrode is powered by (9) a Trek 40/15 HV amplifier with a function generator. The custom power supply is controlled with (10) a function generator. The function generator of the custom power supply also controls the trigger outputs to the CCD camera (11) and the UV intensifier (12). 74

Figure 6.2(a) Horizontal and (b) vertical thrust of the DBD-DCA actuator, f=2kHz, AC voltage is varied 25 kV < VAC < 40kV; DCA voltage –24 kV < VDCA < +24 kV. 77

Figure 6.3. X-velocity contour plot at $V_{AC} = 35$ kV with (a) $V_{DCA} = 0$ kV, (b) $V_{DCA} = -24$ kV, and (c) $V_{DCA} = +24$ kV. Grayed-out regions exhibit potential discharge; the data in these regions were not taken. The electrode positions are displayed. 80

Figure 6.4. Trigger frames (dashed lines) superimposed with current on DBD active electrode (blue) and DCA electrode (red), VAC = 35 kV, f = 2kHz; (a) VDCA = 0 kV,(b) VDCA = –24 kV, and (c) VDCA = +24 kV. The t* is the period normalized time.................. 83

Figure 6.5. Surface potential measurements (red) at x = 27 mm superimposed with the surface potential due to the electric field and capacitive potential (dashed lines) and the potential applied to the DBD active electrode (blue). $V_{AC} = 30$ kV, $f = 2$ kHz at (a) $V_{DCA} = 0$ kV, (b) $V_{DCA} = –20$ kV, (c) $V_{DCA} = + 24$ kV... 85

Figure 6.6(a) Mean surface potential at x = 27 mm downstream with varying VDCA potentials. The mean surface potential reflects the dielectric surface's steady accumulation of charged particles. (b) The peak-peak surface potential amplitude at x = 27 mm downstream with varying VDCA potentials. The surface potential increases with positive DCA relative to the peak-peak surface potential due to only the electrical field and capacitive potential (dashed lines)... 86

Figure 6.7. Phase-resolved plasma discharge images with DCA electrode; VAC = 35 kV, f = 2 kHz (a) VDCA = 0, (b) VDCA = –24 kV, (c) VDCA = +24 kV. T1 and T2 are positive-going cycles, showing a high concentration of positive ions; T3 and T4 are negative-going cycles, with low optical emission at the edge of the active electrode. The leading edge (–), embedded electrode edge (– –), and third electrode edge (–.–) are shown in the T1 phase of (a).87

Figure 7.1 The ACA-DBD Experimental setup. The active and third electrodes are flush-mounted onto quartz dielectric. The embedded electrode is mounted on the back side of the dielectric layer and encapsulated with polyimide and silicone rubber layers. The active and embedded electrodes are connected to a custom power supply, while a Trek 40/15 HV amplifier powers the third electrode. The current is measured with a Pearson 2877 probe and a Tektronix DPO 7254C oscilloscope 94

Figure 7.2. T1 - T4 quadrants of phase-resolved CCD imaging defined relative to VDBD. The VACA (blue) is phase-shifted by Φ from VDBD (black). The T1 and T2 quadrants capture discharges on the voltage-rising cycle associated with streamer discharge, while the T3 and T4 quadrants capture discharges on the voltage-falling cycle associated with glow discharge. 95

Figure 7.3. Time-integrated plasma emissions at varying ACA phase shift Φ, at VDBD = 30 kV (a), 35 kV (b), and 40 kV (c). The third electrode gap is 10 mm, and $V_{ACA} = 28$ kV. The active DBD electrode is located at the bottom of each image; the primary EHD flow is directed upwards. The third electrode is located on the top of each image; the third electrode discharge is directed downwards... 99

Figure 7.4. Phase-resolved plasma extension with a L = 10 mm gap at $V_{DBD} = 40$ kV without a V_{ACA} (a), with $V_{ACA} = 28$ kV / Φ = 0° (b), and $V_{ACA} = 28$ kV / Φ = 180° (c)........ 101

Figure 7.5. Instantaneous voltage and current of the primary DBD with gap distance L = 10 mm; smooth magenta line - primary DBD voltage, $V_{DBD} = 40$ kV; Smooth green line - ACA voltage, $V_{ACA} = 32$ kV. The thin purple line is the current on the primary, and the thin green

line is the current through the ACA electrode. The dashed lines are provided for reference of the phase shift. (a, b) Φ = 0°; (c, d) Φ = 180°. 103

Figure 7.6. Third electrode positive and negative discharge current at varying phase shift and V_{ACA} with L = 10 mm spacing (a) V_{DBD} = 25 kV and (b) V_{DBD} = 40 kV. The positive and negative discharge current is determined similarly to previous works [12]. The standard deviation is determined across at least 10 voltage cycles. Two standard deviation error bars are plotted. 105

Figure 7.7. Instantaneous voltage and current of the primary DBD with gap distance L = 25 mm; magenta line = primary DBD voltage, V_{DBD} = 40 kV; green line = ACA voltage, V_{ACA} = 32 kV. The thin purple line is the current on the primary, and the thin green line is the current through the ACA electrode. The dashed line is provided for reference of the phase shift. (a, b) Φ = 0°; (c, d) Φ = 180°. 106

Figure 7.8. Third electrode positive and negative discharge current at varying phase shift and V_{ACA} with L = 25 mm spacing at V_{DBD} = 25 kV (a) and V_{DBD} = 40 kV (b). The standard deviation is determined across at least 10 voltage cycles. Two standard deviation error bars are plotted. 107

Figure 7.9. Horizontal Thrust at V_{ACA} = 20 – 32 kV at 2 kHz with varying Φ with V_{DBD} = 25 kV (a), 30 kV (b), 35 kV (c), and 40 kV (d) at 2 kHz. The distance from the embedded electrode to the third electrode is L = 10 mm. The DBD baseline thrust without a third electrode is a dashed line. 109

Figure 7.10. Thrust at V_{ACA} = 20 – 32 kV at 2 kHz with varying phase shift. V_{DBD} = 25 kV (a), 30 kV (b), 35 kV (c), and 40 kV (d). The third electrode gap L = 25 mm. The DBD baseline thrust without a third electrode is a dashed line. 110

Figure 7.11. X-velocity profiles: V_{DBD} = 40 kV, L = 25 mm; V_{ACA} = 0 kV, (a) and (b). V_{ACA} = 32 kV Φ = 0° (c) and Φ = 180° (d). The profiles are compared at X = 15 mm and X = 55 mm (e), y = 1 mm and y = 2 mm (f). 114

Figure 7.12. X-velocity profiles at VDBD = 40 kV in-phase with VThird = 20 kV (a) and VDBD = 40 kV out-of-phase with VThird = 28 kV (b) with a L = 10 mm third electrode gap. 115

Figure 8.1. The experimental schematic of the alternating electrode DBD array (top) and “resistive” alternating electrode DBD array (bottom) with N = 4 stages. L_A represents the length of an air-exposed electrode, L_E represents the length of an embedded electrode, and L represents the spacing between each DBD actuator stage from the embedded electrode to the following air-exposed electrode. L_A and L_E are fixed at L_A = 10 mm and L_E = 20 mm. L varies from 10 mm to 20 mm depending on geometry. The electrodes are powered by a custom power supply with two out-of-phase high-voltage outputs similar to Thomas *et al.* [98]. The electrodes connected to the first air-exposed electrode (blue) are connected to one of the high-voltage outputs. In contrast, the alternating electrodes attached to the first embedded electrode (red) are connected to the second high-voltage output. In the resistive

DBD array configuration, an additional electrode is placed before each air-exposed electrode and is connected by a 1MΩ resistor. 121
Figure 8.2. Plasma emissions of a four-stage DBDL=10 array (a) with in-phase active HV electrodes (b) and alternating-phase active HV electrodes (b). Both DBD arrays are powered at 40 kV / 2 kHz with a 10 ms exposure time to capture the plasma emission of 20 discharge cycles. 125
Figure 8.3. Plasma emissions of an $\text{RDBD}_{L=10}$ array (a) with air-exposed HV electrodes in series (b) and air-exposed HV electrodes alternating (b). Both DBD arrays are powered at 40 kV / 2 kHz with a 10 ms exposure time to capture the plasma emission of 20 discharge cycles. 126
Figure 8.4. $\text{DBD}_{L=20}$ array thrust at varying voltages (a) and DBD stages (b), $\text{RDBD}_{L=20}$ array thrust at varying voltages (c) and DBD stages (d), and $\text{RDBD}_{L=10}$ thrust at varying voltages (e) and DBD stages (f). The $\text{DBD}_{L=20}$ array experienced filamentary streamers above 40 kV, while the $\text{RDBD}_{L=20}$ array and the $\text{RDBD}_{L=10}$ array withstood 45 kV before any filamentary streamers or arcing. The standard deviation of the time-averaged thrust across the three sampling periods for each data point is approximately 3%. 128
Figure 8.5. X-velocity profile of the $\text{RDBD}_{L=20}$ array at 40 kV at varying heights above the dielectric surface at a fixed x-position (a) and varying downstream distances at a fixed y-height (b). The starting x = 0 mm position corresponds to the edge of the first active electrode and the chosen x-positions for control volume analysis correspond to 15 mm after each active electrode. Two standard deviation error bars are plotted. 130
Figure 8.6. X-velocity profile of the $\text{DBD}_{L=20}$ array at 40 kV at varying heights above the dielectric surface at a fixed x-position (a). The starting x = 0 mm position corresponds to the edge of the first active electrode and the chosen x-positions correspond to 15 mm after each active electrode. The velocity-derived thrust using eq.(17) is compared to the directly measured thrust after each DBD stage (b). Two standard deviation error bars across the >20 s sampling period are plotted. 131
Figure 8.7. DBD Array power usage scaling with a simple $\text{DBD}_{L=20}$ array (left) and $\text{RDBD}_{L=20}$ array (right) with a fixed L = 20 mm gap. Two standard deviation error bars across a minimum of 10 voltage cycles are plotted. The simple DBD array was tested at 45 kV; however, filamentary streamers began to form at the highest voltage. 132
Figure 8.8. Total thrust scaling with power usage of $\text{DBD}_{L=20}$ array and $\text{RDBD}_{L=20}$. Two standard deviation error bars in power (horizontal) and thrust (vertical) are plotted. 134
Figure 8.9. Total Efficiency of $\text{DBD}_{L=20}$ and $\text{RDBD}_{L=20}$ at 40 kV / 2 kHz. 135
Figure 9.1. Schematic of dual serrated-edged DBD array (a) and the original dual straight-edge DBD array (b) 139
Figure 9.2. Serrated-Edged DBD Array 139
Figure 9.3. Serrated-Edged DBD Array 140
Figure 10.1. The University of Washington Sam Wilson 0.7 m x 0.383 m Wind Tunnel.142

Figure 10.2. Experimental schematic for lift, drag, and pitching moment measurements with angle attack control. The bottom and top plates sit flush with the wind tunnel wall, and the airfoil assembly rests on an air bearing. Electrically grounded metal walls surround the load cells to prevent electrical interference. 144
Figure 10.3. Diagram for Clark Y airfoil with dual DBD configuration. 146
Figure 10.4. C_L and C_D versus angle of attack for a Clark Y airfoil at 5 m/s. 148
Figure 10.5. C_L and C_D versus angle of attack for a Clark Y airfoil at 10 m/s. 148
Figure 10.6. C_L and C_D versus angle of attack for a Clark Y airfoil at 15 m/s. 149
Figure 10.7. C_L and C_D versus angle of attack for a Clark Y airfoil at 20 m/s. 149
Figure 10.8. C_L and C_D versus angle of attack for a Clark Y airfoil at 25 m/s. 150
Figure 10.9: CL / CD versus angle of attack for a Clark Y airfoil at U∞ = 10 m/s. DBD actuator voltage is varied, VDBD = 25 - 35 kV. 152
Figure 10.10: CL / CD versus angle of attack for a Clark Y airfoil at U∞ = 15 m/s. DBD actuator voltage is varied, VDBD = 25 - 40 kV. 153
Figure 10.11: CL / CD versus angle of attack for a Clark Y airfoil at U∞ = 20 m/s. DBD actuator voltage is varied, VDBD = 25 - 40 kV. 153
Figure 10.12. CL / CD versus angle of attack for a Clark Y airfoil at U∞ = 25 m/s. DBD actuator voltage is varied, VDBD = 25 - 35 kV. 154

LIST OF TABLES

Table 1. Summary of EHD Device Mechanisms with typical geometry and applied electrical waveform. 2

Table 2. Comparison between traditional and novel active flow control devices. ★ = Worst, ★★★★ = Best 3

Table 3: Summary of empirical expressions for different properties of DBD actuator.... 48

Table 4. Conditions of separation due to a DBD Jet in counter-flow 68

Table 5. DBD and ACA electrode power usage at L = 10 mm and L = 25 mm. 108

Table 6. Total thrust at V_{DBD} = 40 kV at L = 10 mm and L = 25 mm. 111

Table 7. Velocity-derived momentum, power, and efficiency of the three-electrode DBD system compared to the baseline two-electrode DBD. The momentum can be compared to the directly measured thrust. 116

Table 8. Summary of force and total efficiency. * Shows the range of efficiencies between 1 and 4 DBD stages. 136

ACKNOWLEDGEMENTS

This research represents not only my efforts but also the guidance, encouragement, and collaboration of many exceptional people who stood by me throughout my life, and it is with gratitude that I acknowledge those who have been instrumental in bringing this work to fruition. First and foremost, I want to sincerely thank my Ph.D. advisor, Professor Igor Novosselov, for supporting me and my research of electrohydrodynamics. Professor Igor warmly welcomed my high-energy personality from the first day I joined his lab in my junior year of undergrad. I will forever admire Professor Igor’s work ethic and pursuit of academic knowledge. Without his guidance, I would not be the researcher and engineer I am now.

I would like to thank Professor Alexander Mamishev and Professor Alberto Aliseda for serving as strong mentors and academic resources during my Ph.D. I want to thank Professor Alexander Mamishev for welcoming me into his lab when I first inquired about EHD control of an aircraft and for allowing me to conduct research in his space at the Bowman building. I will cherish our conversations stemming from his unique perspective on all aspects of life that often extend far past the realms of academia. I want to thank Professor Alberto Aliseda for being my go-to fluids expert for experimental and analytical techniques. Professor Alberto also exemplifies what I believe academia should embody, and I am grateful to have learned more about hot-wire anemometry, PIV, and turbulence through our conversations. I would also like to thank Dr. Alan Duong for his immense support in my academic research and development as a technical leader and communicator. I will cherish our time working together and tackling problems that we never expected to overcome.

During my undergraduate and graduate school journey, I have significantly benefitted from fellow students and engineers who have laid the groundwork for my research, directly aided in my success, and will continue my studies. These individuals include Ravi Vaddi, Yifei Guan, Patrick Fillingman, Jiaxing Fu, Darren Liu, Nicholas Kirschbaum, Joshua Fan, Byron Ockerman, Benjamin Price, Landon Norris, and Karsten Fetter. These individuals have made my Ph.D. journey plausible and enjoyable, and I am grateful for their support. My thesis continues Ravi's work, and I am indebted to him for introducing me to EHD.

Next, I want to acknowledge my amazing groups of friends who have come from different communities to support my life during my undergraduate research and Ph.D. journey. While I met

them before college, I know I always have had the support of my high school friends, including Kalle, Evan, Dylan, Delmar, Isaac, and Jun. Another Hawaii group of friends that always brings me excitement and joy includes Ryan, Jason, Chao, Kallen, and Jimmy. During college, I have been fortunate to meet other great friends, including Shelbi, Dayni, Nick, Kevin, Judi, and the enormous welcoming communities of the Chinese Student Association, Hawaii Club, and the Campus Tour Guides. In particular, I'd like to acknowledge Judi, for without her, I would not be as happy or as mature as the individual that I am today.

I am grateful for all the academic support from the University of Washington's Mechanical Engineering Department, the College of Engineering, and the fantastic teachers throughout my years. While some classes were more enjoyable than others, UW provided me with all the necessary resources for my Ph.D. I would also like to thank the irreplaceable UW staff, including Bill Kuykendall and Eamon McQuaide, who have supported my research and personal projects. While many of these individuals supported my academic journey, I will also cherish our playful conversations supporting my copious and sometimes crazy personal projects.

Finally, I would like to acknowledge the personal support from my family that has followed me from well before college. First, I want to thank my older sister, Tiffany, for being a monumental role model and pushing me to be a better person every day. I want to thank my parents for the love and support they gave me in my early years, and they have been a constant source of encouragement and support throughout my life. Next, I want to thank Aunty Barbara, Uncle Matt, and Aunty Lisa for caring for my sister and me after we were thrust into their lives. They all have unconditionally loved my sister and me through my highs and lows, and I will forever be in their debt. Aunty Barbara, Uncle Matt, and Aunty Lisa have supported me in all my life's efforts as if I were their child, and they inspired me to follow my passions. I am fortunate to have a large and supporting family, and I, unfortunately, do not have the space to name them all. Still, I could not have matured into the person I am without the help of Aunty Shannon, Aunty Sandy, Uncle Patrick, and Uncle Sylvester. My family has been my bedrock, and I am lucky to have them all.

DEDICATION

I dedicate this thesis to my parents, who could not witness my journey in person but continue to motivate me daily, and my Aunty Barbara, Uncle Matt, and Aunty Lisa, who have supported me unconditionally.

Chapter 1. Introduction

Over the past several decades, researchers and engineers have exhausted significant efforts exploring electrohydrodynamics, or EHD. EHD can be broadly described as the joint research of electrodynamics and fluid dynamics or the study of ion-driven fluid flows. EHD overlaps several other fields, including electromagnetism, plasma dynamics, power electronics, and chemistry. EHD research has wildly grown in popularity due to its wide range of applications, including virus inactivation [1-3], ozone generation [4, 5], satellite propulsion [6, 7], and active flow control [8, 9]. This dissertation focuses on active flow control using EHD actuators, a more novel application of EHD. However, research on different applications of EHD continues to aid in developing and understanding EHD actuators for flow control. Active flow control has experienced extreme interest over the past two decades because of the ever-growing demand for improved methods to control the fluid dynamics of an aerodynamic surface.

Unlike electromagnetic devices that employ electric and magnetic fields, EHD devices rely solely (or primarily) on electric fields. As a result, the applied electrical waveform, geometry, and working fluid are typically the distinguishing factors between different EHD devices. This dissertation focuses on EHD flows in atmospheric air. The most commonly used atmospheric EHD devices are driven by corona discharge or dielectric barrier discharge (DBD). Other discharge mechanisms include Townsend discharge, glow discharge, and arc discharge [10]. However, these are typically only seen with easily ionized gasses (Helium or Argon) or at low pressures. A summary of EHD devices and their unique electrical and geometric conditions is shown in Table 1.1 and is discussed in Irhanshahi *et al.* [11]. As discussed later, corona discharge and particle charging use a steady high voltage (HV) direct current (DC) waveform, while dielectric barrier discharge uses an HV alternating current (AC) or pulsed waveform.

Table 1.1. Summary of EHD Device Mechanisms with typical geometry and applied electrical waveform.

EHD Device Mechanism	Corona Discharge	Particle Charging & Ion Diffusion	Volumetric Dielectric Barrier Discharge	Surface Dielectric Barrier Discharge
Geometry	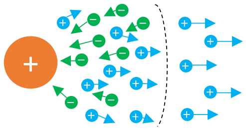	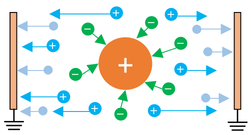	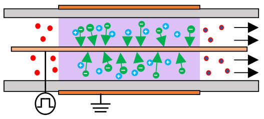	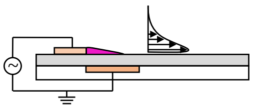
Waveform	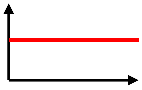	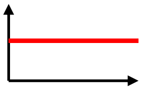	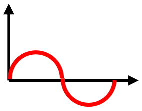	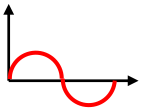

1.1 Active Flow Control (AFC)

Active flow control (AFC) refers to the control of an aerodynamic surface or body through actuation. Unlike passive flow control, such as dimples on a golf ball, active flow control requires energy to move objects or impart a force. Currently used active flow control technologies include mechanical flaps and deflectors on aircraft wings to change wing lift and drag characteristics. While these technologies are well-tested, flaps' bulky and mechanical nature is often a source of failure. Many novel techniques aim to replace traditional technologies while remaining lightweight, instantaneous, and without moving parts. The emerging novel active flow technologies include synthetic blowing jets, microfabricated electro-mechanical systems (MEMS) / piezoelectric pumps, and plasma actuators. Among these emerging technologies, plasma actuators have received the most interest because they are the only solid-state technology without mechanical parts. Plasma actuators are also physically the simplest of the novel flow control technologies and, thus, easy to retrofit into a preexisting system if the electrical requirements are met. A summary of the existing and emerging novel flow control technologies is outlined in Table 1.2. Despite many recent publications on plasma actuators and other similar electrohydrodynamic

(EHD) devices, significant uncertainties about plasma actuators remain regarding variables that influence thrust, unsteady plasma-fluid momentum transfer, electrical plasma discharges, and other complex phenomena. Some publications aim to optimize plasma actuators through unique electrical and mechanical changes; however, the same fundamental questions remain. This dissertation explores the design, integration, mechanisms, and optimization of plasma actuators for active flow control by developing empirical models of plasma actuators in various flow conditions, optimizing plasma actuators, and exploring the mechanisms of these enhanced plasma actuator systems. This work is based on the author's publications [1, 12-16].

Table 1.2. Comparison between traditional and novel active flow control devices. ★ = Worst, ★★★★ = Best

	Flaps or Slots	Synthetic Jets	MEMS / Piezoelectric Pumps	Plasma Actuators
Response	★	★★★★	★★★★	★★★★
Maintainance	★	★★	★★	★★
Intrusiveness	★	★	★★	★★★★
Noise Level	★	★	★★★	★★★
Forcing	★★★★	★★	★	★★
Requirements	N/A	Compressed Air	N/A	High-Voltage

Chapter 2. Plasma Actuators

Non-thermal plasma devices for active flow control have seen great scientific and engineering interest over the past two decades [9, 17-22]. As previously mentioned, plasma actuators have the potential to instantaneously change a fluid system by exerting an electrostatic force while staying silent and compact [23-25]. Categorized by corona discharge or dielectric barrier discharge (DBD), a plasma actuator generates an EHD force by first ionizing the fluid around the actuator with an electric field that exceeds the working fluid's dielectric strength. In corona discharge, the ionization occurs between two high voltage (HV) direct current (DC) electrodes [26, 27], while DBD actuators use pulsed or alternating current (AC) [28, 29]. The free electrons and ions create a quasi-neutral plasma and are then accelerated in the electric field. Through collisions with the neutral air molecules, the EHD force is generated. Within active flow control [30], several works have proposed plasma actuators for mixing enhancement [31, 32], aerodynamic drag reduction [33, 34], lift augmentation [25, 35], separation control [36, 37], and electric propulsion [38-41]. Despite their lower electromechanical efficiencies than corona actuators, DBD actuators are more effective at providing a stronger, consistent EHD force [4, 9]. As a result, many developments in plasma actuators have focused on DBD plasma actuators. This dissertation focuses on DBD plasma actuators. However, studies on corona-driven flows can offer supporting insight into DBD-driven flows. The research of this dissertation builds upon the works of previous researchers, including Vaddi [42-44], Guan [26, 45-49], and Fillingham [50-52].

While plasma actuators for active flow control are a relatively new concept, the field of electrohydrodynamics has existed for decades. Briefly, plasmas, in general, were studied as early as the 1920s by Langmuir [53]. However, very few works have studied plasma-driven fluid flows before 2000 due to the lack of robust power electronics to generate plasma in atmospheric air, and one of the first scientific papers on plasma-fluid interaction was Velkoff and Ketchman [54] in 1968. In the 1990s, a few groups began to explore air flow generated by corona discharge, and by the early 2000s, groups began to propose flow control with corona discharge and DBD. The early works that demonstrated DBD and corona actuators for flow control include Roth *et al.* [55], Corke *et al.* [23], Enloe *et al.* [56], Pons *et al.* [57], and Touchard [58]. Since then, significant developments in power electronics, fluid measuring techniques (particle imagining velocimetry, laser-doppler anemometry, etc), and material science have allowed for further studies of DBD and more robust DBD applications. Moreau *et al*. [31] and Corke *et al*. [13] further summarize the early history of plasma actuators for active flow control.

2.1 Theory of Operation

In its simplest form, a traditional DBD actuator comprises two electrodes separated by a dielectric barrier. One electrode, known as the active electrode, is air-exposed, and the other electrode is embedded into the aerodynamic surface or tightly mounted onto a flat surface for encapsulation. The embedded electrode is typically grounded or powered by an AC waveform opposite the active electrode. Encapsulation is necessary to ensure that plasma discharge is only experienced on the desired aerodynamic surface, not the dielectric's backside. The effect of encapsulation of a DBD actuator encapsulation is studied in Laurentie *et al.* [59]. Figure 2.1 depicts a traditional two-electrode DBD plasma actuator mounted to a flat plate for encapsulation.

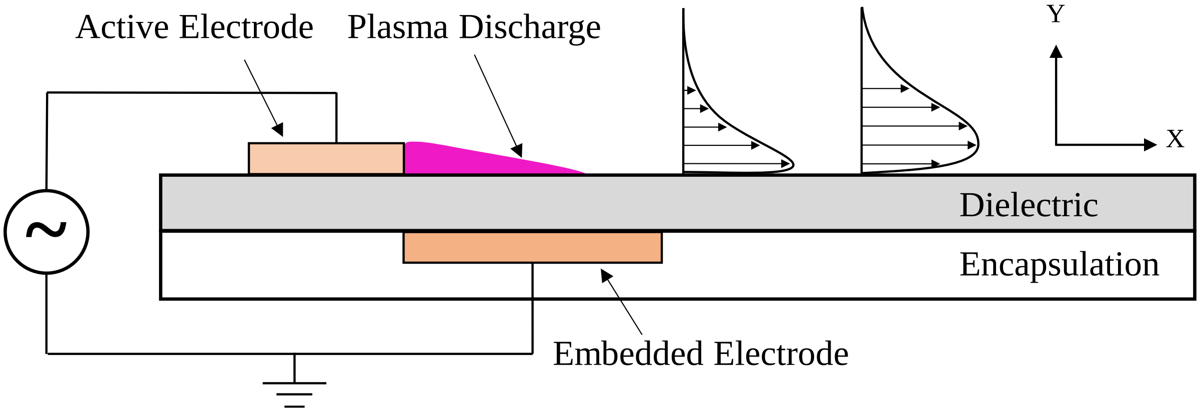

Figure 2.1: A traditional two-electrode DBD Plasma Actuator with an air-exposed active and embedded electrode. The embedded electrode typically is grounded or an out-of-phase AC waveform.

When high voltage is applied to the active electrode, the electric field is strongest at the edge of the active electrode (ignoring the embedded electrode edge), resulting in plasma generation towards the embedded electrode. As the ions attempt to enter the downstream embedded electrode, the ions collide with neutral air molecules, forming a wall jet. The plasma discharge of a two-electrode DBD actuator separated by a transparent quartz dielectric is shown in Figure 2.2.

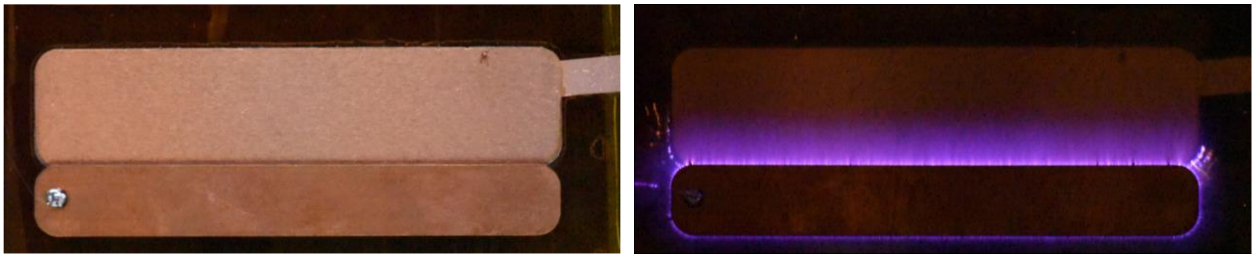

Figure 2.2: Traditional DBD Plasma Actuator with transparent quartz dielectric. The high E-field between the active and embedded electrodes creates a non-thermal plasma towards the embedded electrode. The image captures the discharge across several discharge cycles.

Since DBD is powered by a high-frequency (typically > 1 kHz) AC waveform, Figure 2.2 illustrates the total plasma emissions over several discharge cycles. The color of the discharge is characteristic of the ionized gas (atmospheric air in Figure 2.2) and the resulting reactive species generated during the discharge. Since HV AC powers DBD, there is a constant generation of positive and negative charge species that differ across both cycles. Through primary and secondary ionization, the reactive species of DBD in atmospheric air include O_3, O, H_2N_2, NO, NO_2, HNO_3, NO_3, and several other reactive oxygen and nitrogen species [60].

The momentum injection by two-electrode DBD actuators has been characterized by several investigators, e.g., [12, 61, 62]. However, the time-dependent multiphysics interactions responsible for energy transfer in electromechanical systems such as DBD are poorly understood due to the complex coupling between electric field, surface and space charging, species recombination, and charge–flow interaction. The plasma–flow interaction is commonly divided into positive- and negative-going voltage half-cycles. One of the most accepted forcing mechanisms is the 'push-push' mechanism: positive ions are repelled from the active electrode in the positive-going voltage half-cycle, and negative species are repelled from the active electrode in the negative-going voltage half-cycle [20]. Time-resolved current measurements support that negative electrons are stripped during the positive-going voltage half-cycle, resulting in positive ions and the opposite in the negative-going voltage half-cycle [20]. The development of time-resolve particle imaging velocimetry (PIV) has aided the experimental study of the unsteady EHD forcing. The push-push mechanism to show forcing during each half-cycle has been supported in experimental works such as Debien *et al.* [63]. The electrical voltage and current of a typical two-electrode DBD actuator with a positive and negative voltage half cycle are depicted in Figure 2.3. The push-push mechanism of a two-electrode DBD is depicted in Figure 2.4.

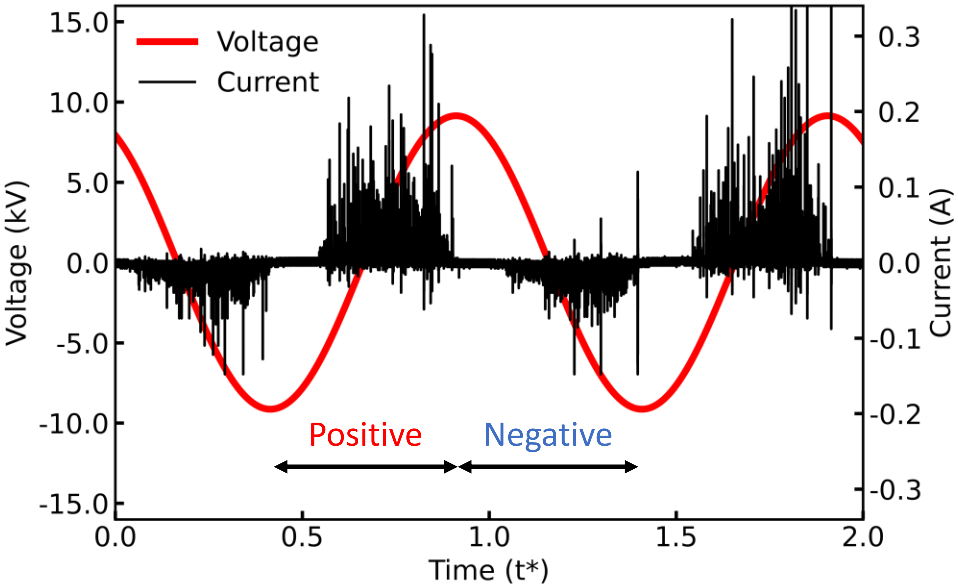

Figure 2.3: DBD electrical current is commonly divided into a "positive-going" and "negative-going" half cycle, with distinctively different discharge dynamics to create a "push-push" forcing.

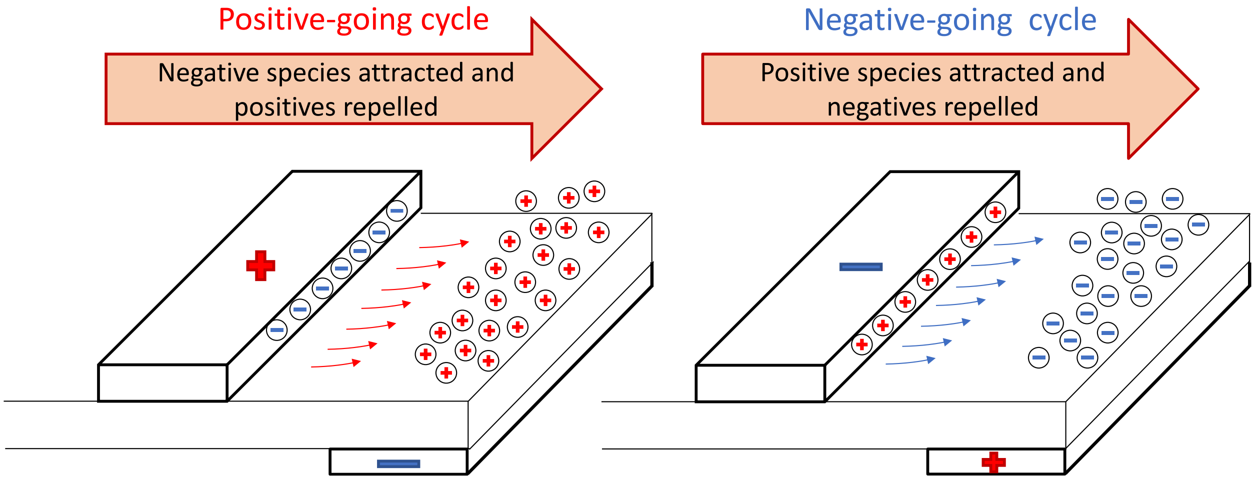

Figure 2.4: DBD "push-push" forcing mechanism supports a positive force generated in both the positive (voltage rising) and negative (voltage falling) half-cycle.

In actuality, the interactions are more complicated. Electric current measurements and high-speed plasma visualizations show that the positive half-cycle leads to positively charged streamer discharge, and the negative half-cycle produces smaller and more frequent discharges associated with glow discharge [64, 65]. Though the discharge current is higher in the positive half-cycle [12], some reports suggest that the forcing terms can be as strong in the negative half-cycle due to the high mobility of electrons and the stability of the negative ions [61, 66]. Some studies have supported a "push-pull" mechanism; however, most fluid analyses have supported that the "pull" is simply due to the significantly more push in one cycle compared to the other [20].

2.2 Challenges

While many fundamental concepts and mechanisms are shared between DBD and corona discharge, there are unique scientific challenges for DBD plasma actuators. The primary scientific challenge is understanding the unsteady plasma-fluid interactions due to complex phenomena, including ion recombination, surface and space charge propagation, and streamer and glow discharge dynamics in traditional and enhanced DBD systems. Enhanced DBD systems include DBD actuators with additional electrodes to provide an additional downstream "pull" [15]. This uncertainty is partly due to the significant time-scale difference between high-frequency forcing, chemical reaction rates in plasma, and flow time. EHD forcing from the corona discharge can provide insights into the charge species/ flow interaction. In positive corona discharge, the positive ions are accelerated in the E-field, producing EHD force acting on the volume fluid, and the steady-state forcing term can be derived analytically [26, 67]. The interaction between the plasma discharge and the flow is more complicated in the negative corona discharge. The glow discharge primarily consists of electron emission, which can interact with the neutral molecules, triggering an electron (bombardment or impact) ionization mechanism. The E-field accelerates the negatively charged ions, which augments the EHD forcing [68]. Recent work on unsteady corona discharge addressed the optimization of EHD forcing. Sohbatzadeh *et al.* [69] demonstrated that unsteady corona discharge produced 4-2 times greater force than steady DC corona for the same voltage range due to increased ion collision frequency. Since DBD actuation uses positive and negative ion acceleration, ion recombination and space and surface charge are influenced by both species. The resulting unsteady interactions of the charged species, dielectric, and electrodes play a significant role in the resulting steady-state EHD force.

The engineering challenges of plasma actuators are related to their demand for high-voltage power electronics and relatively low total force. High-voltage power electronics (amplifiers, transformers, batteries, etc.) can be several kilograms, and with a total force typically under 1 N, plasma actuators have a low force-to-weight ratio when the weight of current commercial HV equipment is factored. As a result, current DBD applications are limited to flow control at low-speed conditions [70, 71]. While capable laboratory-grade custom power electronics are developed for this dissertation, developing these key components is not the primary focus. However, this development will be necessary for future DBD applications. Examples of recent developments in miniature power electronics for DBD include Sato *et al.* [72] and Truong *et al.* [73].

2.3 Developments

While many underlying mechanisms in DBD actuation are still debated, several publications have identified vital variables influencing a DBD actuator's performance. Early characterization and optimization work are well covered in Corke *et al*. [4], Thomas *et al.* [20], and Benard *et al*. [21]. Based on early characterizations, some works have proposed enhanced DBD systems; however, the underlying mechanisms of these improved systems are largely unknown.

2.3.1 Effect of Electrode Geometry and Dielectric Barrier

Early DBD research has identified the electrodes' geometry and the dielectric barrier as critical influences for an actuator's performance [74-78]. The key electrode variables include the active and embedded electrode length, shape, and the gap between the active and embedded electrodes. In the simplest case, a DBD actuator with a straight-edged active and embedded electrode with a spanwise uniform electric field produces a two-dimensional forcing on the fluid, resulting in a 2D planar jet. The electrode spanwise width serves as the nominal dimension. Other electrode shapes have been considered, including serrated electrodes that typically demonstrate more force per spanwise width than a straight-edge actuator and produce a three-dimensional flow field [79-81]. Serrated DBD actuators are summarized and tested on a NACA 0012 airfoil in Vaddi [42]. Since the flow field and plasma dynamics of a serrated-edged DBD actuator are more complex, most works exploring the plasma dynamics of DBD consider the planar 2D DBD actuator with a straight-edge active electrode. A traditional two-electrode DBD with a straight-edge and serrated-edged active electrode is illustrated in Figure 2.5.

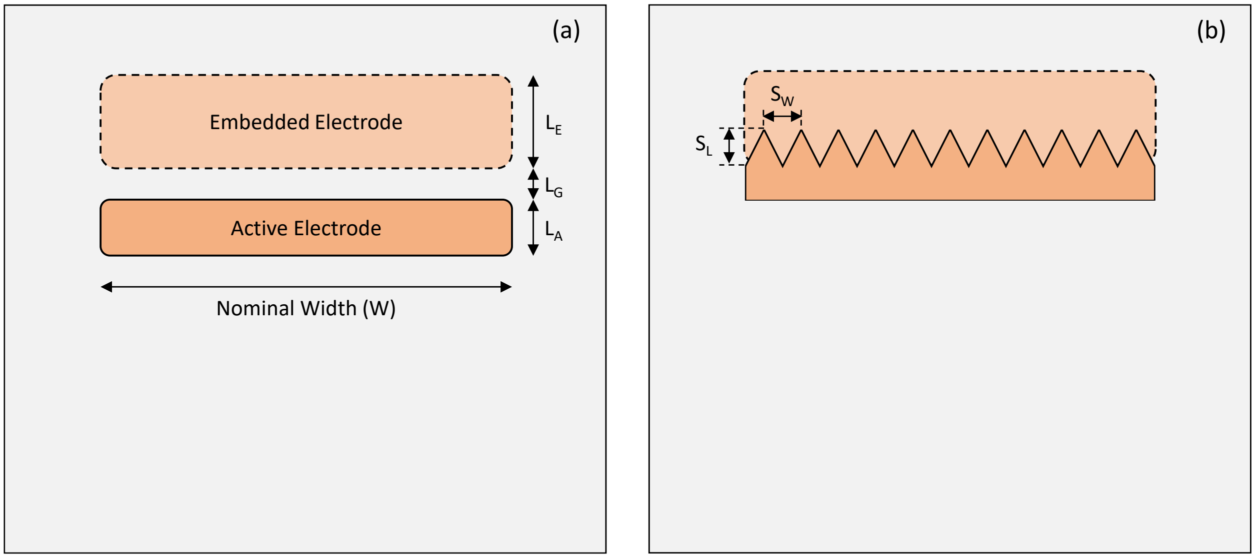

Figure 2.5: A two-electrode DBD (a) has been tested with varying embedded electrode lengths (L_E), active electrode lengths (L_A), and electrode gap lengths (L_G). The width serves as the normalizing dimension. Some works have tested a serrated-edged two-electrode DBD (b) with varying serrated edge length (S_L) and width (S_W).

The dielectric barrier between the electrodes significantly influences the electromechanical properties of the DBD, as the dielectric barrier is the primary source of electrical capacitance. Thomas *et al.* [20] increased the maximum thrust of a two-electrode DBD actuator by using thicker dielectrics (> 5mm) to increase the maximum possible voltage before the formation of large filamentary streamers. Large filamentary streamer formation reflects a saturation limit when further increases in applied voltage do not result in significant increases in thrust. The mechanisms and factors that determine when filamentary streamers form are still unclear. Previous works have highlighted that thrust scales approximately to the second-order polynomial with applied voltage before streamer formation. However, studies have incorporated vital parameters such as dielectric thickness and constant for different scaling relations [22, 23]. The temporal behavior of the discharge within a DBD cycle is outlined in Hoskinson *et al.* [24], and several efforts, such as Debien *et al.* [25], have aimed to inhibit streamer formation from increasing the mechanical performance of a DBD actuator.

The cold capacitance of a DBD actuator can be approximated similarly to a parallel plate and expressed as $C = \frac{\varepsilon_0 \varepsilon_r A}{d}$ where ε_r is the dielectric constant of the dielectric barrier, ε_0 is the dielectric constant of free space, A is the effective area of the two electrodes, and d is the distance between the electrodes. Thus, thicker dielectrics have a lower capacitance, less energy is transiently stored in the dielectric barrier, and the overall DBD is more efficient. A tradeoff of a more efficient and thicker dielectric barrier is the need for higher applied voltages to generate the same electric field to ionize the working fluid. Some, including Enloe *et al.* [56] and Kuknhenn *et al.* [82], have modeled the overall electrical capacitance of a two-electrode DBD actuator. However, the mechanisms affecting the cold capacitance of the dielectric barrier and the "hot" capacitance of the unsteady plasma discharge over the dielectric are unclear.

2.3.2 Effect of Electrical Waveform

Other characterization and optimization work has focused on a single DBD actuator with varying electrical configurations. Since the applied HV AC can influence the rate and timing of charged species production, previous works have explored electrical parameters such as different waveforms and frequencies for DBD actuators [26]. Using a standard two-electrode DBD, Benard *et al.* [27] found that overall, symmetric waveforms (square and sine waves) produced the greatest average thrust for the standard DBD geometry and that a sine waveform was more efficient than a square waveform. The variation in performance due to the different waveforms is tied to the spatiotemporal plasma morphology between the two cycles, which has a strong frequency dependency. Several optimization works have highlighted an optimal frequency for DBD, approximately between 1.5 kHz and 4 kHz [21]. Higher frequencies are generally believed to allow for additional discharge and ion production; however, the electromechanical efficiency diminishes with frequency due to shorter periods and more ion recombination, in addition to an earlier saturation limit [22]. More recently, new insights into the space and surface charge effects in DBD actuation have led researchers to explore custom waveforms with a combination of HV AC and HV pulses [83-85]. These works have highlighted that more significant EHD forcing is associated with greater streamer and charge extension over the dielectric surface.

2.3.3 Effect of External Flow and Numerical Modeling

Until recently, few works have explored the performance of DBD actuators in external flow; however, the characterization of DBD actuators in external flow is critical for numerical modeling as it serves as a realistic boundary condition [86-88]. Modeling DBD discharge from first principles is cost-prohibitive due to the significant separation of timescales, so studies of corona-driven ionic flows can be relevant to gain insight into the flow-ion interactions [89, 90]. Early numerical efforts led to the development of simplified DBD ion injection models, including the Suzen & Huang [91], Orlov [92], and Shyy [93] models that were able to predict quiescent EHD flow through a simplified ion–flow interaction scheme [88]. More recent work extended the models to explore the performance of DBDs, such as the evolution of the velocity field in the DBD-driven jet [87, 94]. Other strategies have been proposed for more robust, computationally lean momentum injection models for EHD-driven jets [95, 96]. These models were developed and validated in quiescent conditions and are yet to be tested in an external flow condition and explore inertial and viscous flow interactions.

The two traditional external flow conditions include co-flow, when the jet direction is the same as the external flow, and counter-flow, when the momentum injection is opposite to the external flow. Pereira *et al.* [97] reported direct force measurements in co- and counter-flow DBD injection. They found that the total EHD thrust (or the difference between EHD thrust and shear stress at the surface) was identical for both co-flow and counter-flow using load cell measurements

[97]. However, the range of freestream velocities (10 – 60 m/s) in increments of 10 m/s did not address the regime where the EHD velocity equals the external flow (0 – 10 m/s), and the study does not present any velocity results to explore the behavior of the DBD in co-flow or counter-flow [97]. Probing the underlying fluid dynamics requires measuring the velocity profiles near the momentum injection location. Benard *et al.* [61] reported on the velocity profiles of a DBD actuator in co-flow at a single electrical condition and found that the effect of the DBD injection diminished at higher external velocities; however, the authors did not investigate counter-flow conditions of the DBD, the impact of varying electrical conditions, or the fluid momentum displacement of the DBD at the varying conditions [61]The literature does not previously report any experimental characterization of velocity profiles in the counter-flow injection by DBD.

The numerous demonstrations of DBD-actuated aerodynamic surfaces drive the need to characterize DBD actuators in external flow. Over the past decade, several studies have been conducted on DBD actuators mounted to various airfoils [98-101], multi-element airfoils [102], flaps [103, 104], and full-scale or near full-scale aircraft [38, 70]. In most studies, the DBD actuator is mounted in co-flow and demonstrated an ability to change aerodynamic performance by increasing airfoil lift, decreasing drag, or changing pitching moment. However, many studies do not provide insight into the fluid flow field and the underlying physics responsible for the lift or drag changes [105, 106]. Recently, Gu *et al.* [107] employed a momentum injection numerical model to explore the effects of a DBD actuator Gurney flap at external flows up to 20 m/s by modeling a pair of DBD actuators: one actuator in co-flow on the pressure side and one actuator in counter-flow on the suction side of the trailing edge of an airfoil. As shown in this study, the counter-flow momentum injection can readily be coupled with the traditional co-flow injection to potentially manipulate the flow field more efficiently to increase or decrease drag and lift and change the pitching moment of the airfoil. Numerical studies note a lack of experimental velocity data to validate the numerically predicted recirculation vortex on the trailing edge [107, 108].

2.3.4 DC-Augmented DBD

With a two-electrode DBD actuator well characterized by several authors and other works demonstrating flight capability with two-electrode EHD actuators, recent works have proposed novel DBD geometries to overcome some of the shortcomings of EHD actuators. These new geometries give more insight and support to early optimization studies speculating on the plasma-fluid momentum transfer mechanisms. One of the first novel enhanced DBD systems proposed was a three-electrode DBD system with an additional HV DC electrode. Known as DC-augmented (DCA-DBD), works such as Debien *et al.* [109] and Moreau *et al.* [110] have tested a three-electrode DBD configuration with a downstream positively biased HV DC third electrode with improvements in thrust (up to ~50%) compared to a two-electrode DBD [109-112]. In this arrangement, the DBD electrode pair ionizes the gas, and the biased third electrode accelerates negative species, promoting their interaction with neutral molecules. Since negative species are accelerated outwards during the glow discharge cycle, Moreau *et al.* [110] suggest that the increase in force due to a positive third electrode is generated by a net acceleration of negative species despite the repulsion of the positive species during the streamer discharge cycle. When the third electrode is biased negatively, the DBD jet can become deflected from the surface depending on the magnitude of the third electrode, decreasing the horizontal thrust and introducing a wall-normal force [112, 113]. While the mechanical characteristics of three-electrode DBDs have been characterized using velocity measurements [110], the underlying plasma-fluid interactions of the DCA-DBD are poorly understood [114].

2.3.5 DBD Array

While the three-electrode DBD systems can improve the performance of a two-electrode DBD, some have pointed to a need to develop a scalable DBD array for substantially more robust applications [9]. Early efforts tested DBD arrays constructed of DBD actuators in series to demonstrate an increase in the total thrust. However, a counter-wind (sometimes called a cross-talk phenomenon) is produced on the back side of a downstream active electrode when the electrodes are spaced closely, thus creating a slight backward-facing discharge and limiting the overall system's efficiency [99, 115]. These works, including Forte *et al.* [115], Thomas *et al.* [99], and Berendt *et al.* [116] have tested DBD arrays with different electrode geometries, waveforms, and spacings. Due to cross-talk between DBD stages, it was previously stated that DBD array thrust does not increase linearly with the number of actuator stages [99]. Subsequential DBD array investigations have attempted to reduce the effect of cross-talk in DBD arrays by modifying the DBD actuator geometry. Benard *et al.* [117] proposed a DBD array comprised of a three-electrode DBD actuator with two dielectric layers and two embedded electrodes per actuator stage. In this study, the modified geometry reduced backward flow due to cross-talk by up to 65%; however, some cross-talk persists, and the additional embedded electrode significantly increases manufacturing complexity while requiring higher than typical voltages.

More recently, optimizing work has expanded on DBD systems with multiple DBDs in series with varying geometric and electrical conditions. With the goal of a continuously accelerated EHD force, some works demonstrated that DBD arrays with alternating air-exposed HV electrodes and grounded electrodes experienced minimal cross-talk. This was first presented by Debien *et al.* when it was shown that the EHD jet was accelerated up to ~10.5 ms^{-1} with a four-actuator DBD system [64]. This approach used wire-to-planar electrodes and is more straightforward, with better results than the multi-electrode system proposed by Benard *et al.* [117]. Recent promising results of successively accelerated DBD actuation were presented by Sato *et al.* [118], demonstrating linearly scaling DBD array thrust for the first time using custom power electronics. This study used a DBD configuration similar to Debien et al. [63]. However, the electrodes were planar-to-planar, and the HV waveform was a nanosecond pulsed DC voltage. Sato *et al.* [118] also suggested introducing a resistor to the downstream air-exposed electrode to limit and prevent arc discharge from each downstream electrode. While these studies offer promising approaches to continuously accelerate an EHD jet and maximize thrust, most of the presented results are limited to low-power operations and include solely the velocity or thrust measurements in small parameters. There is a lack of understanding of the influence of various key DBD array actuator parameters and their resulting electromechanical characteristics in these multi-electrode systems. It is of great interest to the active flow control community to understand the mechanisms of multi-DBD systems with more conventional electrical parameters (i.e. sinusoidal waveform) and their mechanical limits.

2.4 Research Objectives and Dissertation Outline

Plasma actuators lie at an intersection of several fields, including plasma science, power electronics, chemistry, and fluid dynamics, and they have several other promising applications. This dissertation aims to contribute to our understanding of DBD plasma actuator fundamentals and to optimize DBD systems for more robust applications of DBD actuators. Thus, the main research objectives are to explore these categories: 1) theory, 2) mechanisms, 3) optimization, and 4) aerodynamic applications.

Theory: This dissertation first improves our understanding of DBD plasma actuators in quiescent and external flow conditions. Previously, experimental models did not explain fundamental DBD characteristics such as discharge current, thrust, and plasma volume. An empirical model is developed based on the AC inputs to calculate the discharge current, momentum injection, and plasma volume. The model can readily be applied to determining more realistic boundary conditions in numerical simulations. The early characterization work lays a foundation for crucial DBD parameters such as discharge current and power. The work is expanded by exploring similar characteristics in an external flow. Using a benchtop wind tunnel, the DBD electrically is found to behave independently of an external co- or counter-flow. However, the mechanical forcing and fluid effects of the DBD in co-flow and counter-flow are much more profound, and a new nondimensional term relating to external flow momentum and DBD injection momentum is proposed to predict DBD performance in an external flow.

Mechanisms: While previous works have tested enhanced DBD systems with various electrical and geometric conditions, there is a lack of understanding of DBD and EHD forcing mechanisms in three-electrode DBD actuators. An enhanced three-electrode DBD with an HV DC and AC third electrode is probed with time-resolved current and plasma images to optimize more effectively. Correlating the resulting EHD force to the unsteady plasma dynamics, the forcing mechanisms of DC-augmented and AC-augmented systems are discovered. The results give insight into the favorable and adverse surface and space charge dynamics critical to optimizing plasma-fluid momentum transfer in more robust DBD systems.

Optimization: With a new understanding of DBD forcing mechanisms and electromechanical performance, new DBD systems are proposed and explored. This dissertation's optimization work focuses on AC-augmented systems and DBD arrays. This work explores the first three-electrode AC-augmented system, and an optimized DBD array is built upon the fundamentals of the three-electrode AC-augmented DBD. In both cases, a DBD system that is significantly more robust than previous literature is demonstrated. The DBD array is revealed to scale well for larger applications, a feat not yet documented.

Aerodynamic Applications: After benchtop optimization, the novel DBD array is tested on a high-lift Clark Y airfoil to demonstrate greater active flow control. The 2D airfoil is manufactured and tested in-house with a dedicated wind tunnel and custom power electronics. The plasma actuator performance is characterized in a moderate-speed wind tunnel (up to ~35 m/s), at Reynolds numbers higher than most previous literature. The lift, drag, and moment coefficients are determined, and the overall effectiveness of this enhanced DBD system is evaluated based on the high-lift airfoil. While the full development of a commercial DBD actuator is out of the scope of this dissertation, this work highlights the necessary developments for eventual large-scale control of aerodynamic surfaces using DBD plasma actuators.

Specific contributions of this dissertation to the academic and research community include:

- Development of an empirical model for two-electrode DBD plasma actuators relating plasma length, plasma height, plasma volume, discharge current, and momentum injection
- Analysis of DBD plasma actuators in external co- and counter-flow and the introduction of a non-dimensional relation between a DBD actuator and an external flow to predict separation in a counter-flow injection
- Exploration of unsteady plasma dynamics and momentum transfer mechanisms in a three-electrode DC-augmented DBD actuator (DCA-DBD)
- Demonstration of the first AC-augmented DBD (ACA-DBD). EHD augmentation mechanisms were discovered through time-resolved electro-optical, velocity, and direct thrust measurements.

- Optimization and demonstration of a scalable high-powered DBD array suitable for active flow control with significantly more thrust than previously demonstrated.
- Active flow control of a Clark Y airfoil with an optimized dual DBD array at external flow speeds up to 25 m/s

Chapter 3. Experimental Facilities and Instrumentation

3.1 DBD Plasma Actuator

The traditional straight-edged two-electrode DBD actuator shown in Figure 2.1 is a baseline and default configuration for all work presented in this dissertation. However, several critical physical variables, such as dielectric material, dielectric thickness, electrode width, and number of electrodes vary between subsequential studies. In the early experimental characterization work, electrical parameters are explored: voltage, frequency, and waveform. Later efforts include additional straight-edged electrodes in a three-electrode or DBD array configuration. Each section corresponding to a unique study will define its tested DBD actuator.

3.2 Thrust Characterizations

Direct horizontal and vertical thrust measurements characterized the mechanical thrust performance of the DBD actuator systems. Like many works [99], direct thrust is often measured vertically or horizontally by holding the plasma actuator system on a sensitive force balance.

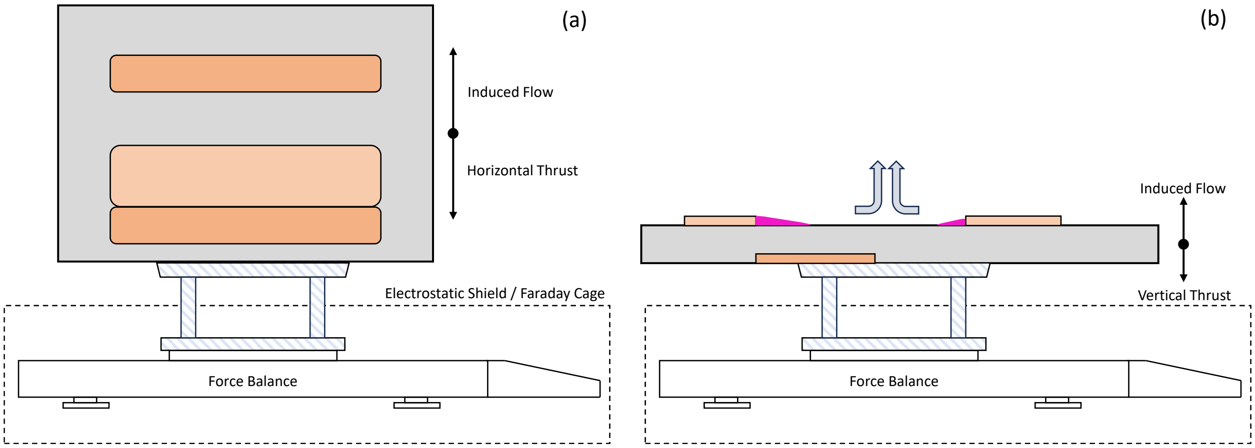

Figure 3.1. The thrust of a three-electrode DBD actuator can be characterized by direct horizontal (a) and vertical thrust (b). The force balance typically comprises an electrically shielded balance with a non-conductive stand to transfer the thrust through the shielding.

In the directly measured thrust setup, plasma-induced flow is directed away from the balance, and the reactive downward thrust on the flat plate dielectric is measured by the balance. Depending on the size of the DBD system, the direct forces were measured with an Ohaus SPX223 analytical balance (0 – 220 g range resolution with 1 mg resolution) or an Ohaus SPX622 analytical balance (0 – 620 g range resolution with 10 mg resolution). It is essential to ensure no electromagnetic (EMI) interference to the scale and its wiring, tension from the HV wiring, or electrostatic forcing from the wiring to the scale to create reliable and repeatable thrust measurements.

To prevent EMI and electrostatic forcing to the scale, a metal shield/faraday cage was placed around the scale, and the DBD plate was mounted to a non-conductive four-column acrylic or Polylactic acid (PLA) stand that rests ~ 50 mm above the scale and transferred the forcing from the actuator to the balance. To ensure no tension force from the wires is exerted onto the scale, extremely thin conductive DBS (Drawn Brazed Strand) wire (0.1 mm OD) is used for all wire connections to the electrodes. The DBD thrust assembly rests within an enclosure, and properly shielded HV cables connect the power supply to the DBS wire through through-wall connections mounted to the walls of the enclosure. The independence of wire movement and tension on the thrust measurements can be confirmed by lightly tapping the wire to induce movement. If the scale does record a force when the wire is moving, then there is no tension in the wires. Placement of the electrodes on the dielectric or mounted surface is considered to minimize thrust losses due to the dielectric/flat plate. The effects of DBD actuator plate length on its recorded thrust measurements are assessed in Durscher and Roy [119].

Proper electrical shielding can be verified by introducing another non-conductive platform stand between the balance and the mounted DBD assembly. With this additional platform, the plasma actuator assembly rests ~10 mm above the balance, and the mechanical forcing should not be transferred to the scale when voltage is applied to the system. If no force is read when the plasma is generated, there are no electrostatic or EMI effects from the wires or the plasma discharge onto the nearby scale. Thrust data from the scale is transferred to a computer through a shielded USB cable with galvanic isolation to prevent the scale from being grounded. However, tests without the data isolation yielded nearly identical results as the Faraday cage typically provides enough protection. In lower voltage cases, the thrust tests without a Faraday cage also yielded the same results as those with the Faraday cage. Thrust data points are usually averaged over three intervals of 10 seconds. A vertical force is recorded when an additional electrode creates a reverse discharge or deflected jet. In this case, the plate was plated parallel to the surface. The vertical and horizontal thrust measurement configurations are shown in Figure 3.1. An example of a thrust setup with and without a Faraday shield is shown in Figure 3.2. In an adequately shielded thrust measurement, the thrust will read zero before the HV is applied to the DBD actuator, non-zero when the HV is applied to the DBD actuator, and zero again immediately after the DBD actuator is turned off. Previous time-resolved studies have demonstrated that the DBD jet reaches steady-state thrust nearly instantly [20]. Before any study, these “off-on-off” are conducted to ensure proper setup, and an example thrust result from an “off-on-off” test with a two-electrode DBD actuator is presented below in Figure 3.3.

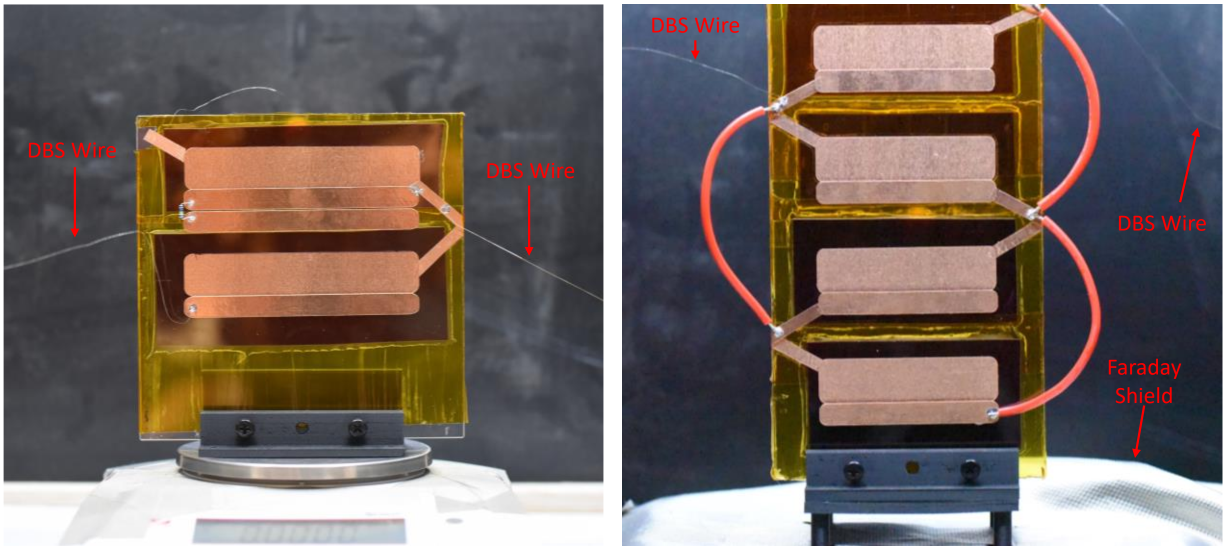

Figure 3.2. A DBD actuator thrust is directly measured by holding the flat plate vertically and measuring the reactionary thrust on the flat plate. A thin DBS wire connects a two-stage DBD array (left) and a four-stage DBD array (right). A Faraday shield is commonly placed around the scale. However, the Faraday shield may be unnecessary in relatively low-voltage conditions (< 20 kV).

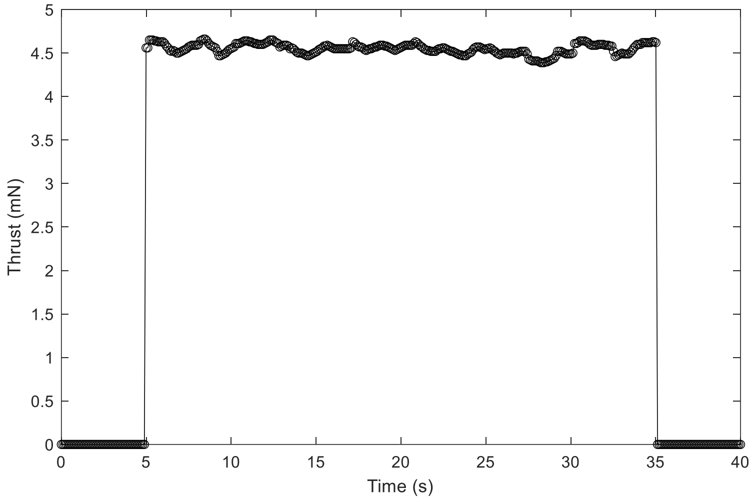

Figure 3.3. Proper shielding of the analytical balance in thrust measurements is confirmed with an “off-on-off” test. For example, a DBD actuator with a 3.175 mm quartz dielectric is excited with a 30 kV / 2 kHz sine wave with no thrust measured before and after the HV is applied.

3.3 Velocity Characterizations

Velocity profiles at different locations around the DBD actuator are recorded to support the direct thrust measurements and to gain insight into the fluid dynamics of the DBD plasma actuators. To measure and characterize the flow field over a large field of view, we employ a custom-made glass pitot tube with as small an inner (ID) and outer (OD) diameter as possible, typically ID = 0.4 mm and OD = 0.6 mm. Over time, glass pitot tubes are replaced, and the physical dimensions of each pitot tube are unique. However, the OD is kept under 0.8 mm. All glass pitot tubes are fabricated at the University of Washington Physics Glass Shop. Compared to traditional stainless steel pitot tubes, the glass tube minimizes interference with the plasma. This method has been extensively used to accurately characterize plasma actuators' performance without the need for tracer particles that risk being influenced by the strong electric field [20, 58, 64]. The pitot tube is mounted on an optical table and is controlled in the x and y - axis by linear stages while connected to a differential pressure gauge. In all studies, the pressure transducer outputs a 4 – 20 mA current, linear in its pressure range, and it was placed in series with a 1.5 kΩ resistor. The pressure within the pitot tube equilibrates nearly instantly after changing the flow condition or position. The voltage across the resistor is recorded for at least 20 seconds with a Hydra Data Logger II. The Hydra Data Logger II records/samples data at approximately 1 Hz, and the 0.005% accuracy is suitable for accurately recording a steady-state signal. With the time-averaged pressure (P), a time-averaged wind velocity (v) is calculated using Bernoulli's equation with a calibration correction factor (C) that is characteristic for each custom pitot tube expressed as

$$\Delta P = C\rho v^2, \tag{1}$$

where ρ is the fluid density. The pitot tubes are calibrated every few weeks or after any significant physical change to the system to ensure the best accuracy and accommodate any drift. Since each pitot tube is unique, they require constant calibration. Our experiments' typical velocity measurements had a standard deviation < 0.03 ms^{-1} over the sampling period. The positions and vastness of velocity profiles are unique to each study, and these conditions are defined in each section. The pitot tube is typically angled downwards or constructed with a step to ensure that the tip of the pitot tube can touch the dielectric surface without interference. All calibrations are completed with the pitot tube in place with the linear stage by introducing a laminar internal pipe flow and characterizing the parabolic velocity profile. The stepped pitot tube with a two-electrode thin Kapton DBD actuator is illustrated in Figure 3.4.

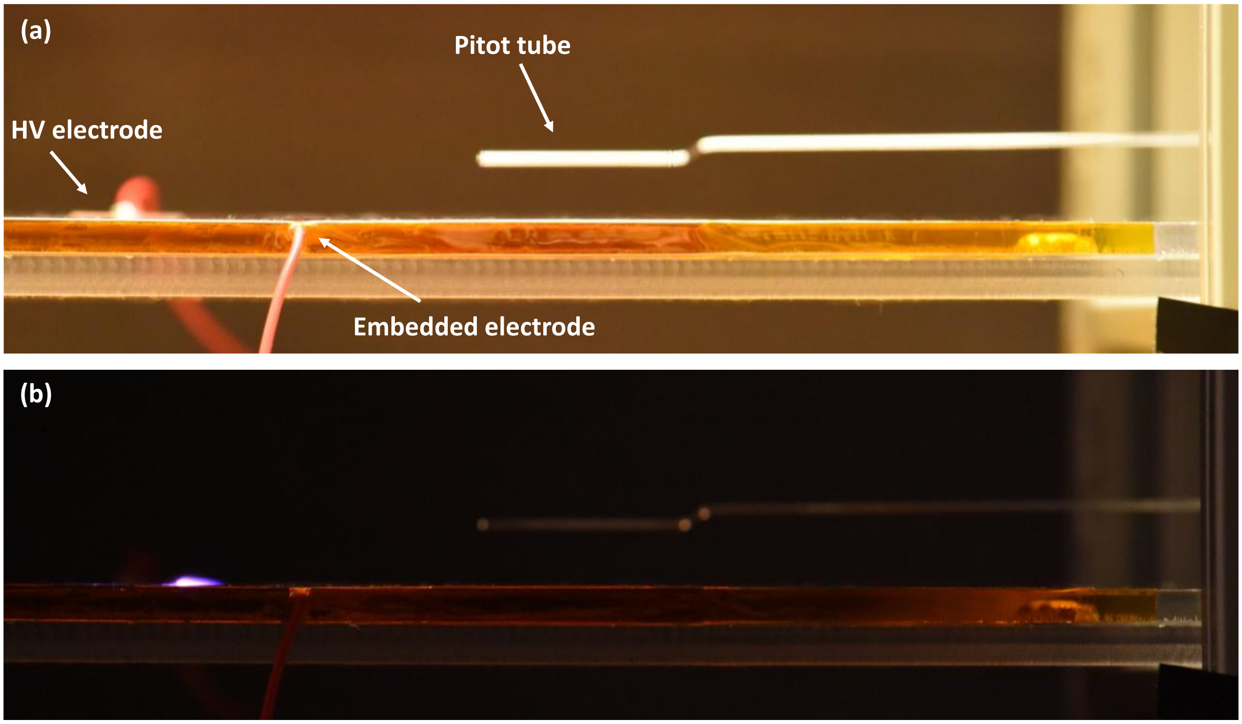

Figure 3.4. A pitot tube and pressure transducer characterize the flow field of a two-electrode DBD actuator with a thin Kapton dielectric. The pitot tube is shown an illuminated background (a), and the plasma discharge is visible without background illumination (b).

3.4 Electrical Characterization

A DBD actuator is typically electrically characterized by its electrical current, discharge current, and total power usage. The electric current in the DBD circuit is a superposition of a capacitive current and a discharge current. A key parameter in numerical modeling, the discharge current, is associated with the total number of ions generated at each electrode during plasma microdischarges, and they appear as a series of fast current pulses [64], as shown in Figure 3.5 below.

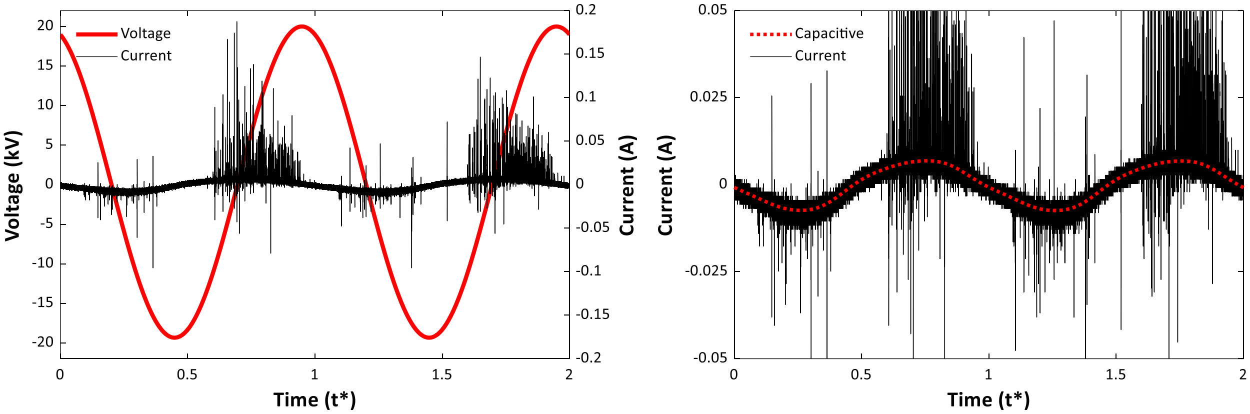

Figure 3.5. Traditional DBD Current with a 3.125 mm Quartz dielectric at 40 kV / 2 kHz (left) and the identified capacitive current (right)

The current through the DBD electrodes is most commonly measured using a 200 MHz bandwidth non-intrusive Pearson 2877 current monitor with a rise time of 2 ns. The current monitors are connected and recorded alongside their respective voltage with a high bandwidth oscilloscope, such as a Tektronix DPO 7054 oscilloscope (500 MHz bandwidth) with a sampling rate of 1 GS/s to resolve 500 MHz. These conditions are essential for accurately capturing individual discharges that occur over a ~30 ns duration on average [59]. The high bandwidth and the sampling rate minimize the noise during the current measurements and can be used to compute the time-averaged electrical power [52]. To determine the currents associated with the plasma micro-discharges, determining the capacitive current through analytical methods has been explored [92, 120]; removing the capacitive current through signal processing methods, including low-pass filters or Fast-Fourier Transform (FFT) has also been attempted [59, 64, 121]. Fourier transform analysis typically identifies the capacitive current to include the nodes of frequencies up to approximately

5 times the voltage frequency [12]. Typically, the FFT analysis identifies the capacitive current as roughly the first 20 nodes to match the expected capacitive current. However, the number of nodes can differ significantly with geometry and applied voltage.

With the electrical current non-intrusively measured, we compute the time-averaged electrical power consumed by the actuator or any electrode as

$$W_{elec} = f_{AC} \int_{t^*=0}^{t^*=1} \varphi(t) \times i(t)\, dt, \tag{2}$$

where f_{AC} is the frequency of the applied voltage in Hz, and φ(t) and i(t) are the voltage and current at each moment. The normalized time (t^*) represents a single voltage cycle; therefore the integral in eq. (2) represents the power in a single voltage cycle. When using the electrical current to derive power and eq.(2), the resulting total power is typically averaged from at least ten separate voltage periods to reduce the noise impact and any possible deviation. The electrical current can also be measured intrusively by introducing a shunt resistor (i.e., a 1 Ω resistor) between the embedded electrode and the electrical ground. In this case, the voltage across the resistor is measured with a high-bandwidth probe; however, this approach risks adverse interference.

Another approach to calculating the total electrical power consumption of a DBD actuator is through a Lissajous curve that requires introducing a capacitor between the embedded electrode and the power supply [20]. Since total power consumption is primarily driven by capacitance, other works, such as Kriegseis *et al.* [122], have used Lissajous curves to approximate the effective DBD capacitance with and without discharge present. Some authors, including this work, have found that while both methods yield similar total power measurements, the overall current and discharge current are more consistently measured through the high-bandwidth non-intrusive current monitors than the high-bandwidth voltage probes used for Lissajous curves.

3.5 Optical Plasma Characterization

Time-integrated and phase-resolved optical images visualize the physical plasma discharge characteristics corresponding to the discharge current. This work typically takes time-integrated optical images with a 24 MP Nikon D750 DSLR camera and a 200mm macro lens. Each image is usually captured with ~ a 20 ms exposure time. Each photo captures several voltage cycles since the DBD voltage cycle period is typically less than one ms.

A high-speed monochromatic CCD camera (Vision Research Phantom V12.1) coupled with a 200 – 550 nm UV intensifier lens (Specialised Imaging SIL3) is used to resolve the time-dependent plasma characteristics in each voltage cycle. Based on spectroscopy of DBD in atmospheric air, all (visible and UV) light emissions are assumed to be associated with reactive nitrogen and oxygen species with wavelengths approximately between 300 nm and 450 nm [123, 124]. All time-resolved plasma images are conducted in later studies with a fixed frequency of 2 kHz. Synced with the 2 kHz voltage cycle, a signal generator sends triggers to the CCD and intensifier at 8,000 Hz. The CCD typically employs a 120 μs shutter time, and the intensifier typically employs a 105 μs shutter to resolve the voltage cycle into four equal quadrants, similar to previous works [64]. These quadrants, denoted as T1 through T4 represent the two halves of the voltage-rising cycle and two halves of the voltage-falling cycle and are depicted below in Figure 3.6**.** The signal generator is synchronized with the waveform generator of the custom power supply that controls the DBD actuator. For each test, the DBD is typically powered on first, and the CCD camera and intensifier are triggered to begin capturing exactly 3 seconds after the start of the maximum voltage amplitude.

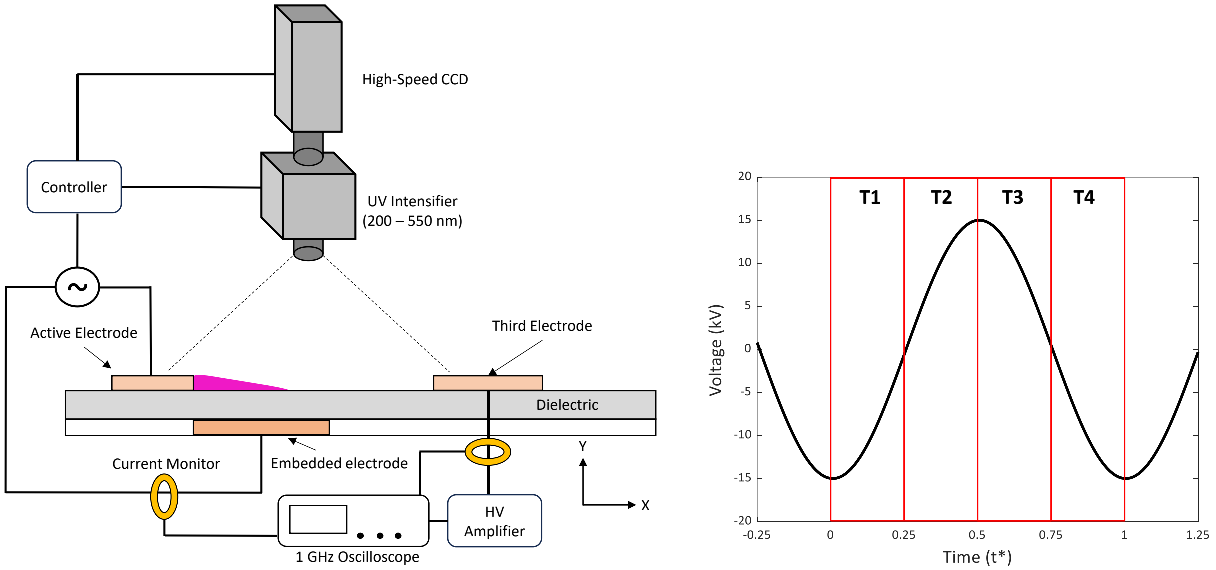

Figure 3.6. CCD Camera set up with T1 through T4 quadrant timing for a three-electrode DBD test

3.6 Power Electronics

High-voltage power supplies are necessary for all high-voltage research, and this dissertation uses a combination of commercial and custom power electronics. In the early electromechanical characterization work, a Trek 615-10 High Voltage AC-DC generation (0 – 20 kV p-p) and a Trek 40/15 high voltage amplifier (0 – 80 kV p-p) supply a single excited high voltage wire, and an electrical ground connects to the embedded electrode. Both commercial high-voltage power supplies are robust and can safely generate various waveforms, frequencies, and voltages. However, a limiting factor of these power supplies is the total current that can be supplied (e.g. the Trek 40/15 has a maximum output current of ±0.015 A_{rms}). During this dissertation, we develop two custom high-voltage power supplies to accommodate larger DBD actuators requiring more power and current: a "dual-hot" custom power supply and a "single-hot" power supply.

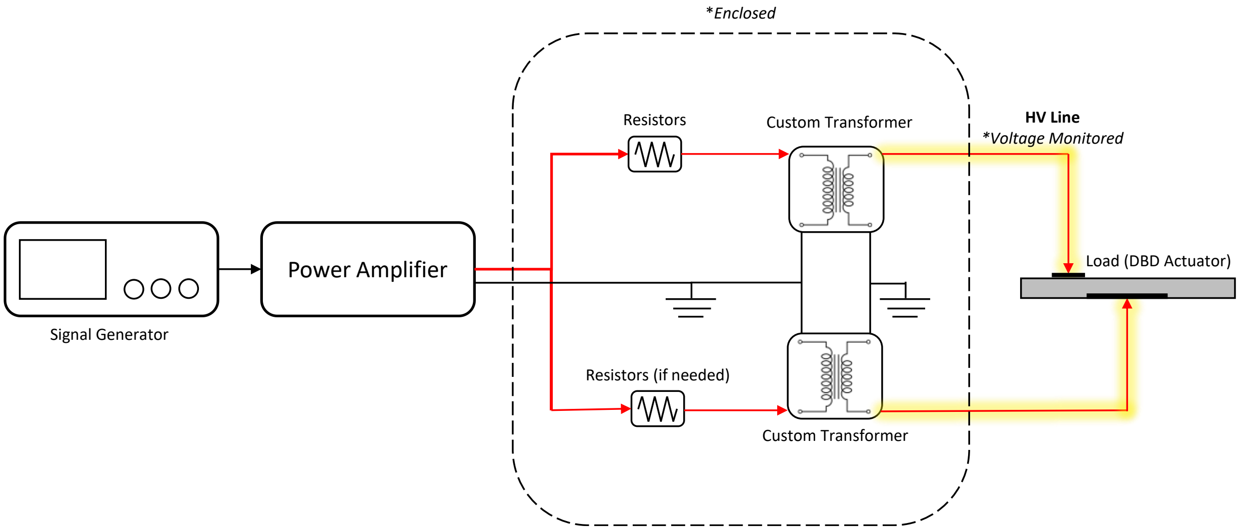

Figure 3.7. "Dual Hot" Custom high-voltage power supply

The high-level electrical schematic of the "dual hot" custom power supply is shown in Figure 3.7. It primarily comprises a signal generator, a power amplifier, and two custom high-voltage transformers (Corona Magnetics) rated up to 35 kV peak-to-peak each at 2 – 20 kHz. The secondaries of both transformers can be used out-of-phase for up to 70 kV peak-to-peak between the two electrodes effectively, or only one of the transformers can be used with the other electrode connected to an electrical ground. When both transformers are out-of-phase, the active and embedded electrodes experience the maximum possible electric field strength; however, the embedded electrode is not grounded. Based on several different experiments, we have not seen any difference in time-integrated results when the DBD is generated by a single transformer (e.g. 30 kV / 2 kHz sine) with an embedded grounded electrode (0 kV) versus when the DBD is generated with two out-of-phase transformers (15 kV / 2 kHz sine each). Using two out-of-phase powered electrodes is analogous to a floating ground appropriate for a battery-powered DBD actuator. Additionally, the dual-hot power supply requires less electrical insulation for the HV wires. For the dual hot power supply, the HV output wires are rated to 40 kV. The output voltage of one of the excited wires is monitored directly by a Tektronix P6015A high-voltage probe.

In the “single hot” power supply, the electrical connections are similar to the dual hot power supply; however, only a single transformer is installed. When using the single hot power supply with a two-electrode DBD, the DBD’s embedded electrode is connected to an electrical ground. The single hot power supply transformer is another custom transformer (Corona Magnetics) rated up to 70 kV at 0.2 A_{rms} at a frequency of ~ 900 Hz – 5 kHz. Since the transformer of the single hot power supply operates at a lower frequency, the transformer experiences more capacitive energy in the transformer core, and more robust cooling is necessary. The front operational panel of the custom power supply is shown in Figure 3.8. Both custom power supplies take the physical form of a portable rack case for ease of installation, transportation, and modifications. The custom power supplies are equipped with removable HV connectors mounted to the back of the power supply (TE Connectivity LGH High Voltage Connectors). Auxiliary circuits and components in each power supply typically include a 12V line (for fans, lights, etc.), a temperature monitor on the transformer core, a voltage monitor, a total power monitor, and a current monitor through a 1 Ω shunt resistor before the transformers.

Figure 3.8. The "single hot" custom power supply is built with a power strip, amplifier, power monitor, temperature monitor, voltage monitor, current monitor, utility 12V, and signal input. The temperature monitor typically monitors the custom transformer's core.

Chapter 4. DBD Actuator Empirical Model in Quiescent Condition

This section presents the first significant research effort exploring the theory and empirical modeling of DBD actuators in quiescent conditions. The discharge characterization work in this section serves as a powerful design tool, lays the foundation for electrical, mechanical, and optical analysis for later studies, and sheds insight into the essential fundamental mechanisms of DBD. The work on the DBD actuator empirical model was published in the Journal of Physics D: Applied Physics [12].

4.1 Experimental Set-Up

This section outlines the experimental setup to characterize the electromechanical performance of a traditional two-electrode DBD actuator constructed of thin copper electrodes separated by a thin dielectric layer. The layout of the two-electrode DBD is shown in Figure 4.1. Both electrodes have straight edges, producing a uniform spanwise discharge and, thus, a 2D velocity profile. The dielectric material used is polyimide, known as Kapton (7700 VPM @ 25 °C). Each actuator has one layer of Kapton-FN (FEP layered Kapton) and four layers of Kapton-HN with a total thickness of ~330 μm (including the adhesive). The DBD actuator is installed on the 6″ by 8″ acrylic plastic sheet. The ground electrode (copper, 50 μm thick, 25 mm long, 110 mm wide) is flush-mounted on the acrylic plate. The upper electrode (copper, 50 μm thick, 15 mm long, 110 mm wide) is glued onto the top of the Kapton dielectric layer. The high-voltage (HV) electrode is exposed to atmospheric pressure air. The air-exposed HV electrode is connected to a Trek PM04014 power supply that provides up to 20 kV AC high voltage. The voltage and frequency were varied from 12 kV – 19.5 kV and 0.5 kHz – 2 kHz. There is no overlap between the electrodes in the x-direction.

The traditional two-electrode DBD with a thin Kapton dielectric is characterized by its plasma volume, electrical, and velocity characteristics. The mechanical thrust is derived from a control volume analysis. The motivation of this work is to derive necessary numerical modeling parameters such as charge density while discovering scaling relationships for a commonly used flexible dielectric. The charge density is used in simplified plasma models that include the Orlov model [45], Shyy model [20], and Suzen & Huang model [46, 47]. In these models, the effects of the plasma actuator are modeled by introducing the EHD body force term into Navier-Stokes equations. This term is expressed as

$$\vec{f}_{EHD} = \rho_c \vec{E}, \tag{3}$$

where ρ_c is the charge density and $\vec{E}$ is the electric field. The charge density is approximated by measuring the electrical discharge current using the Ragowsky coil placed around the HV wire connected to the active electrode and characterizing the plasma discharge volume through time-integrated plasma images. The experimental setup is shown in Figure 4.1.

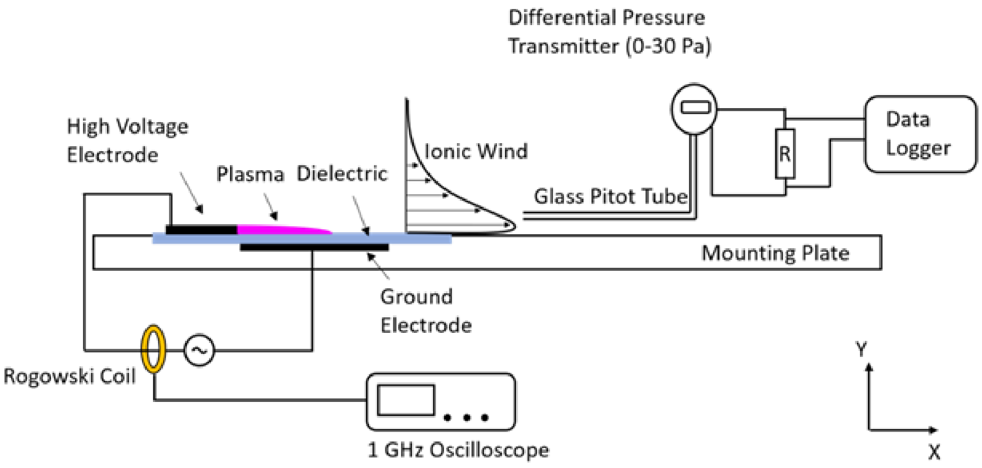

Figure 4.1. Schematic of the dielectric barrier discharge (DBD) plasma actuator. The plasma actuator is mounted on an acrylic glass plate, and the blue region is the dielectric layer separating the electrodes. The velocity is measured using a custom-built glass pitot tube, and the electrical characteristics are measured using a Rogowski coil.

To measure the two-dimensional plasma discharge region, a Nikon D750 DSLR Camera with a Nikon AF-S NIKKOR 70 to 200 mm f/4G ED VR Zoom Lens is mounted horizontally 0.5 m from the side of the plasma actuator. The field of view has a resolution of 0.022 mm per pixel. We first binarized the image with a 256-bit histogram to identify the discharge's volume. Then, we use a 98% Otsu threshold to identify an effective plasma volume region. A 98% threshold matches previously determined one-dimensional plasma lengths, which have been experimentally and numerically validated [64, 92, 125, 126]. Typical lengths of plasma streamers range between 3 mm and 8 mm. However, previous studies have shown that streamers can reach lengths up to 20 mm when thicker dielectrics are used [92, 127]. Figure 4.2 illustrates the plasma volume projection onto the x-y plane during the typical operation of the actuator. The threshold for this analysis is chosen to be 98% spectral intensity. Other 95-99% range values were evaluated, and the results were not affected significantly. The resulting identified plasma images are used to calculate the discharge region's length, height, and projected volume. Note that the projected plasma volume has a sloped bottom boundary consistent in PIV measurements of EHD force distribution [128]. This is believed to be due to the effect of surface charge on the dielectric surface.

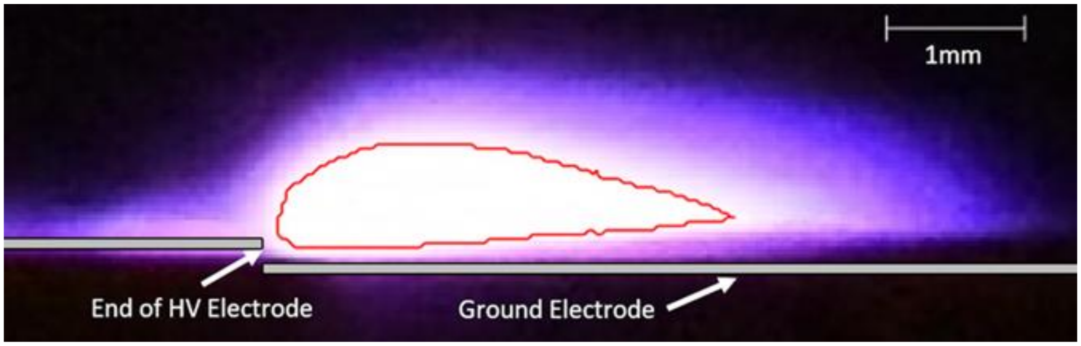

Figure 4.2. Plasma discharge region of DBD actuators at 12 kV and 2 kHz. A 98% threshold is outlined in red to calculate the plasma length and volume.

The velocity profiles are conducted using the previously mentioned pitot tube setup with a custom glass pitot tube with ID = 0.4 mm and OD = 0.5 mm. In this experiment, only x-velocity measurements are taken at varying x positions (10 mm, 15 mm, 40 mm, and 75 mm) downstream on the active electrode edge. At each x position, the y-velocity profile is obtained from the surface to 6 mm above the plate at increments of 0.25 mm or 0.5 mm (at a higher location). Due to the pitot tube's geometry, we cannot capture velocity at heights < 0.25 mm. As a result, we assume the velocity is linear between the no-slip condition at y = 0 mm and the velocity at y = 0.25 mm.

From a vertical velocity profile, the DBD actuator’s total mass flow rate per meter spanwise, Q, can be computed by

$$Q = \rho \int_{y=0}^{y=\infty} U(y) dy, \tag{4}$$

where $U(y)$ is the measured velocity at varying heights at a constant x location. Similarly, the DBD actuator’s total momentum per meter spanwise can be found by multiplying the mass flow rate at each vertical position with its respective velocity such that

$$M = \rho \int_{y=0}^{y=\infty} U^2(y)dy. \tag{5}$$

The momentum should theoretically be conserved in all velocity profiles with no freestream flow and no external force. However, this is not true in all profiles due to viscous forces and spatial charge effects. The mechanical power of a given DBD plasma actuator corresponding to the kinetic energy (W_{mech}) in the actuator can be computed by

$$W_{mech} = \frac{1}{2}\rho L \int_{y=0}^{y=\infty} U^3(y)dy. \tag{6}$$

With both the electrical power, as in Eq.(2), and the mechanical power of a given actuator, the overall electromechanical efficiency of the plasma actuator can be calculated as

$$\eta = \frac{W_{mech}}{W_{elec}}. \tag{7}$$

The asymmetric electrode configuration has a similar structure to a corona discharge, though the transient behavior and the alternating field add significant complexity to the problem. For model development, an empirical relationship similar to Townsend's quadratic relationship can be used as a starting point to model discharge current [62, 63]. We can use the modified corona discharge energy consumption (W) equation to determine the discharge current of the actuator as

$$W \sim f_{AC} C_0 (\varphi - \varphi_0)^2, \tag{8}$$

where C_0 is the capacitance of the electric circuit, f_{AC} is the applied AC frequency, φ and φ_0 are the applied and initiation voltage. We have assumed a power-law relation with frequency for the discharge current, as shown in Eq. (8)

$$I_{dis} \sim {f_{AC}}^{\alpha} C_0 (\varphi - \varphi_0)^2, \tag{9}$$

where α is the AC frequency effect on the discharge current. The capacitance of the DBD actuator with charges temporally on the surface is hard to determine, so Eq. (9) is rewritten as

$$I_{dis} = {f_{AC}}^{\alpha} K(\varphi - \varphi_0)^2 \tag{10}$$

where K is the empirical constant similar to C_1 in Townsend's current relationship $I_{dis} = C_1\varphi(\varphi - \varphi_0)$. The empirical relation in Eq. (10) can be used to determine the expressions for total discharge current, PD, and ND currents, and we can evaluate the microdischarge properties in both cycles. The value of φ_0 is determined from modified Peek's law [64] as shown in Eq. ((11)

$$\begin{gathered}\varphi_0 = m_v g_v \left(\frac{t_e}{2}\right) ln \left(\frac{2t_d + \frac{t_e}{2}}{\frac{t_e}{2}}\right), \\ m_v = 1, g_v = 31 \left(1 + \frac{0.308}{\sqrt{\frac{t_e}{2}}}\right),\end{gathered} \tag{11}$$

where t_e and t_d are the thickness of the electrode and dielectric layer, respectively. The value of φ_0 is calculated to be 4.75 kV and it is used for developing different power-law relationships for the discharge current, the plasma volume, and the momentum induced by the wall jet.

4.2 Effect of voltage and frequency on the plasma volume

The impacts of voltage and frequency on the effective plasma region generated by a two-electrode DBD with a thin Kapton dielectric are discussed. Figure 4.3(a) presents the plasma length, measured from the edge of the plasma actuator to the furthest point downstream, as a function of voltage (12 kV – 19.5 kV) at varying frequencies (0.5 kHz – 2 kHz). The results support previously reported experimental and numerical results that plasma length increases linearly with applied voltage [54, 58]. However, increases in frequency appear to increase plasma lengths until 2 kHz asymptotically. This asymptotic limit may correspond to the asymptotic limit between the max velocity and frequency at similar voltages where max velocities did not increase after frequencies larger than approximately 2 kHz [27]. However, Orlov reported that plasma length asymptotically approaches a limit of roughly 6 kHz while at 5 kV [58]; thus, there may be different asymptotic limits with varying dielectrics and electrode configurations. At our maximum conditions of 19.5 kV and 2 kHz, the dielectric layer breakdown occurred after 60 min of operation, which was not often sufficient to take the entire set of the velocity data; thus, we did not explore higher frequency conditions. It was possible to operate the actuator at lower voltages and higher frequencies and then develop universal power-law equations. However, as we attempted to maximize the momentum injection, this exploration is out of the paper's scope, and further experimentation at a broader range of frequencies is necessary.

While physical mechanisms such as ion recombination may play a role in limiting the plasma length, the thickness of the dielectric material has been previously noted to play a large role in plasma extension length. These results support previously reported lengths between 3 mm and 8 mm when the dielectric is less than 1 mm [5, 54, 56]. Thicker dielectrics have seen plasma lengths up to 20 mm. Thus, the asymptotic nature of Figure 4.3(a) may be due to the limiting length or thickness of the dielectric or the underlying ground electrode [5].

Figure 4(b) presents the plasma volume from the summation of pixels in the total effective plasma region as a function of voltage (12 kV – 19.5 kV) at varying frequencies (0.5 kHz – 2 kHz). Our results suggest that the volume varies quadratically with the applied voltage. Interestingly, the plasma volume continues to grow with a frequency up to 2 kHz. In contrast, the plasma length approaches a limit at 2 kHz at these operating conditions due to continued growth in plasma height. The results suggest that the assumption of a half-Gaussian space charge distribution in the length and height holds for voltages and frequencies, which may not be accurate at higher values. A change in plasma height would not be proportional to plasma length and will likely change the distribution of charges and the resulting force and velocity profile.

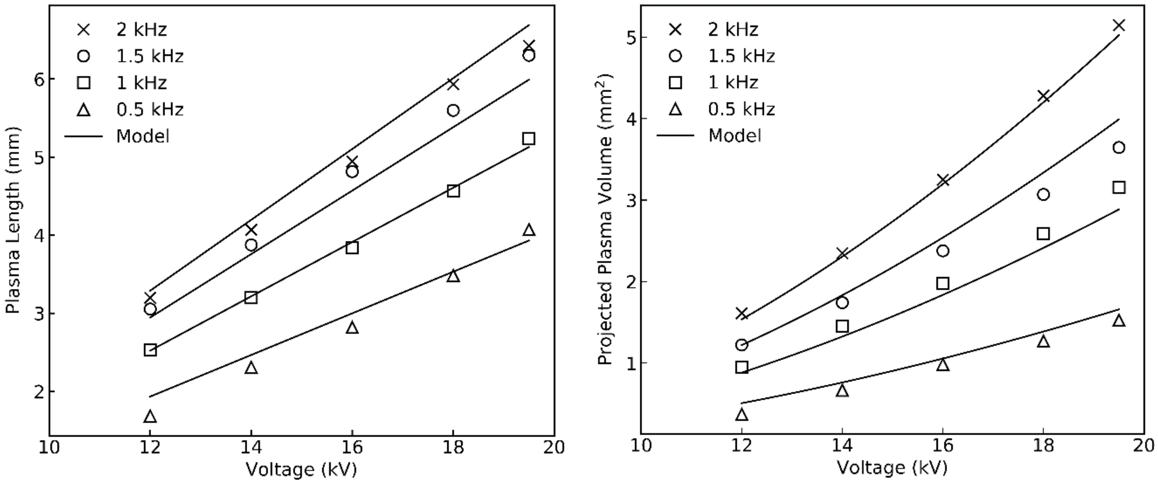

(a) (b)

Figure 4.3. Experimentally evaluated (a) plasma length and (b) projected plasma volume increase as a function of voltage. Plasma length reaches an asymptotic value with frequency, but the plasma volume continues to increase.

The empirical expressions for the plasma length and height can be determined through curve fitting. In this voltage range, plasma length (L_P) is found to vary linearly with voltage and by power-law with frequency as expressed in Eq. (12) and plasma volume (V_P) is found to exhibit a power-law relationship with both voltage and frequency as expressed in Eq. (13)

$$L_P = K_1 {f_{AC}}^{\alpha_1}(\varphi - \varphi_0), \tag{12}$$

$$V_P = K_2 {f_{AC}}^{\alpha}(\varphi - \varphi_0)^{\gamma}. \tag{13}$$

In numerical modeling for a source term, one needs to define the volume of charge injection. A Gaussian ion-concentration distribution can then be applied to the empirical plasma length and height, and this relationship eliminates the dependency on a guessed Debye length. Subsequent coupling of Eq. (3) and the Navier-Stokes equation allows for modeling the EHD force term.

4.3 Discharge current characteristics

Temporally resolved current measurements allow for characterizing the micro-discharges for both the positive and negative cycles. During the microdischarge, the charged species are transported toward the electrodes, thus generating an electrical signal in the form of a pulse superimposed on a slow-moving capacitive current. The latter can be subtracted, and the current associated with microdischarges can be analyzed. In the positive discharge (PD) portion of the cycle, the electrons move toward the exposed electrode, and in the negative discharge (ND), the electrons move towards the ground. We calculate the charge transported in each microdischarge and the total transported charge by adding up the contribution of each current microdischarge; the total discharge current is shown in Figure 3(b). The discharge current is normalized by a unit of time. Previous work showed that a net charge of 40 nC is transported in a positive discharge cycle at 8.5 kV [39] and 10 nC is transported in a negative discharge cycle. As a comparison, we have observed a charge transport of 45 nC in PD and 15.3 nC in ND at 12 kV, 500 Hz. The discharge current is calculated for PD and ND, and the net discharge current is calculated by adding both cycles. The experimental data is shown in Figure 4.4.

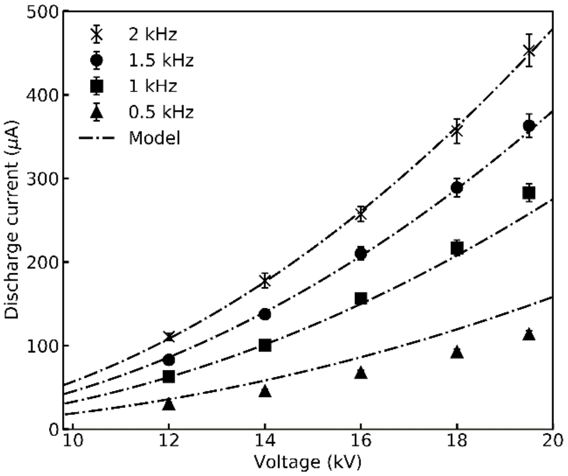

Figure 4.4. Discharge current as a function of applied voltage and frequency for the experimental data.

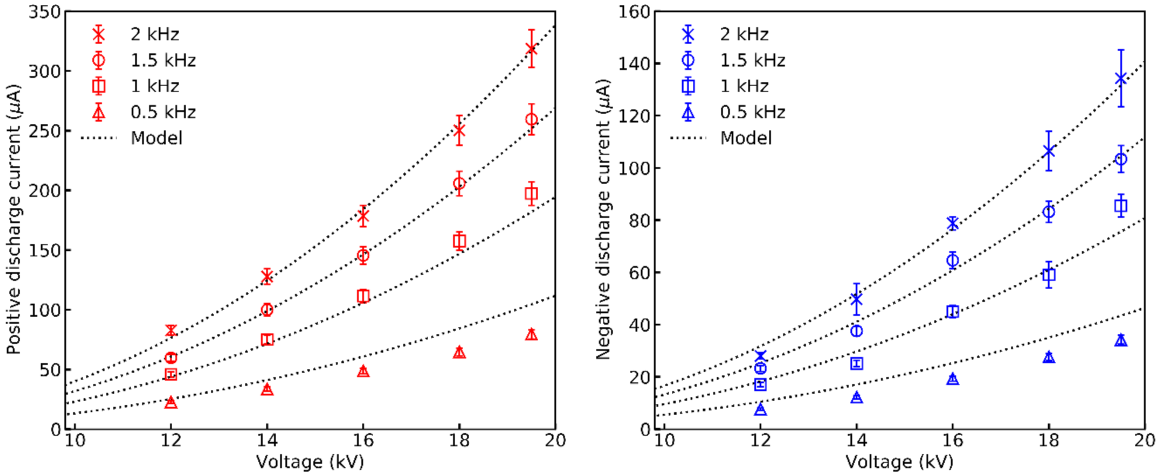

Figure 4.5. Discharge current as a function of applied voltage and frequency for the experimental data. The current varies quadratically with applied voltage, and the power-law relationships for positive and negative discharge currents predict the values accurately.

The relationships for the discharge currents are obtained by comparing the experimental results and using the expression in Eq. (10). The I_{dis} versus φ trends are similar to previously reported quadratic trends in the literature [17, 66, 67]. As expected, the discharge current increases when the frequency increases since the number of cycles increases with the increase in frequency. However, the discharge current cannot continuously increase with the increase in frequency because the build-up of charges on the dielectric surface tends to dampen the charge transport. The model agrees with the experimental results at all voltages and frequencies within ~10% error. The large asymmetry is due to the number of current pulses in each cycle and the different mean charges transported by a single discharge [39]. The positive and negative discharge current models as shown in Eq. (14) and Eq. (15) are used to compare the empirical model and experimental data

$$I_{dis\_PD} = K_3 {f_{AC}}^{\alpha} (\varphi - \varphi_0)^2, \tag{14}$$

$$I_{dis\_ND} = K_4 {f_{AC}}^{\alpha} (\varphi - \varphi_0)^2, \tag{15}$$

where I_{dis_PD} and I_{dis_ND} are the discharge currents associated with positive and negative discharge, K_3 and K_4 are the empirical constants. In our experiments, the ratio of the K_3 and K_4 is

2.5, such as the positive discharge current is 2.5 times greater than the negative discharge current, as shown in Figure 6.

We calculate the current density from the discharge current and plasma volume. In Figure 7, the charge densities are plotted for 1 kHz and 2 kHz at varying voltages from 12 kV – 19.5 kV. The current density increases linearly with voltage in our experimental range. However, the current density is independent of frequency. The empirical relationships developed in the present study can be used to determine the charge density. In previous work, the simulation's charge density input is "tuned" to match the velocity profiles measured experimentally using an iterative approach [68]. The discharge current and discharge volume computed in this manuscript can be used as input parameters for a numerical model. The expressions in Eq. (14) and Eq. (15) can be used to gain insight into the momentum transfer process in positive and negative cycles.

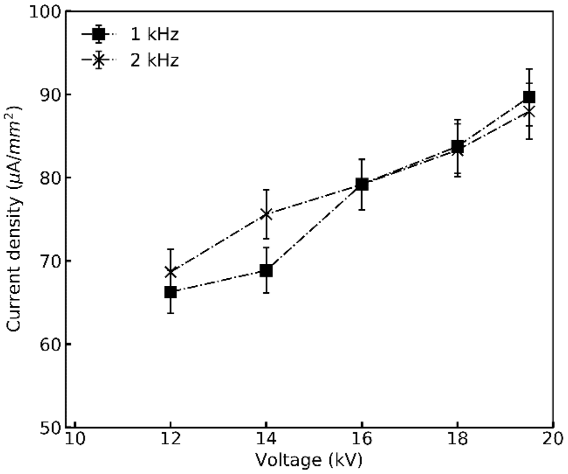

Figure 4.6. The current density for total discharge current and the current density remains the same for the two applied frequencies

4.4 Velocity characteristics

The velocity profiles of the DBD wall jet are used to determine the momentum injection. Figure 8 shows the velocity profiles at different x locations for 14 kV and 18 kV at 1 kHz and 2 kHz. In all cases, the profile nearest to the active electrode shows the highest maximum velocity,

U_{max} and the greatest velocity gradient, i.e., shear stress. The flow is accelerated in the plasma discharge region [69], and as the wall jet propagates downstream, the velocity profile flattens due to viscous losses, momentum displacement [42], and specific to the EHD scenario, due to space charge effects. This jet-like expansion from the active electrode has been shown in similar pitot-tube experiments and the PIV experiments, and some have modeled DBD actuators using wall-jet similarity [26, 42, 43]. The plasma lengths are less than 10 mm in all cases, so we estimate that at 15mm, the EHD forcing is significantly reduced, and the velocity profiles are influenced mostly by viscosity and boundary layer momentum displacement. This is analogous to the analysis of EHD-driven flow by Guan *et al*. [25] where the ratio of Coulombic force and an inertial term in the Navier-Stokes equation is presented as a nondimensional parameter X. In the region of $X > 1$, the flow is dominated by the Coulombic force, i.e., accelerating, and for $X \ll 1$, the EHD force can be neglected. For the cases presented in Figure 8 (d) 18 kV at 2 kHz, the max velocity is 4.30 m s^{-1} at y = 0.5 mm and x = 10 mm. The location and magnitude of maximum velocity agree with other experimental studies [1, 27, 70]. Some previous work report U_{max} ~ 5.0 m s^{-1} at similar electrical input conditions, however, differences associated with electrode configuration and measurement methods can influence the U_{max} measurements [27]. Also, PIV measurements show steep velocity gradients in the wall jet; thus, a slight difference in the probe position or finite dimension of the pitot tube (ID = 0.4 mm) may also cause lower U_{max} values [26, 71]. Charging the pitot tube could also adversely affect the electric field, thus decreasing the maximum velocity at the pitot tube tip. In the case of PIV measurements behavior of the highly charged particles in a strong electrical field [72] may influence velocity measurements. Given the ambiguity in U_{max} measurement, we do offer an empirical expression.

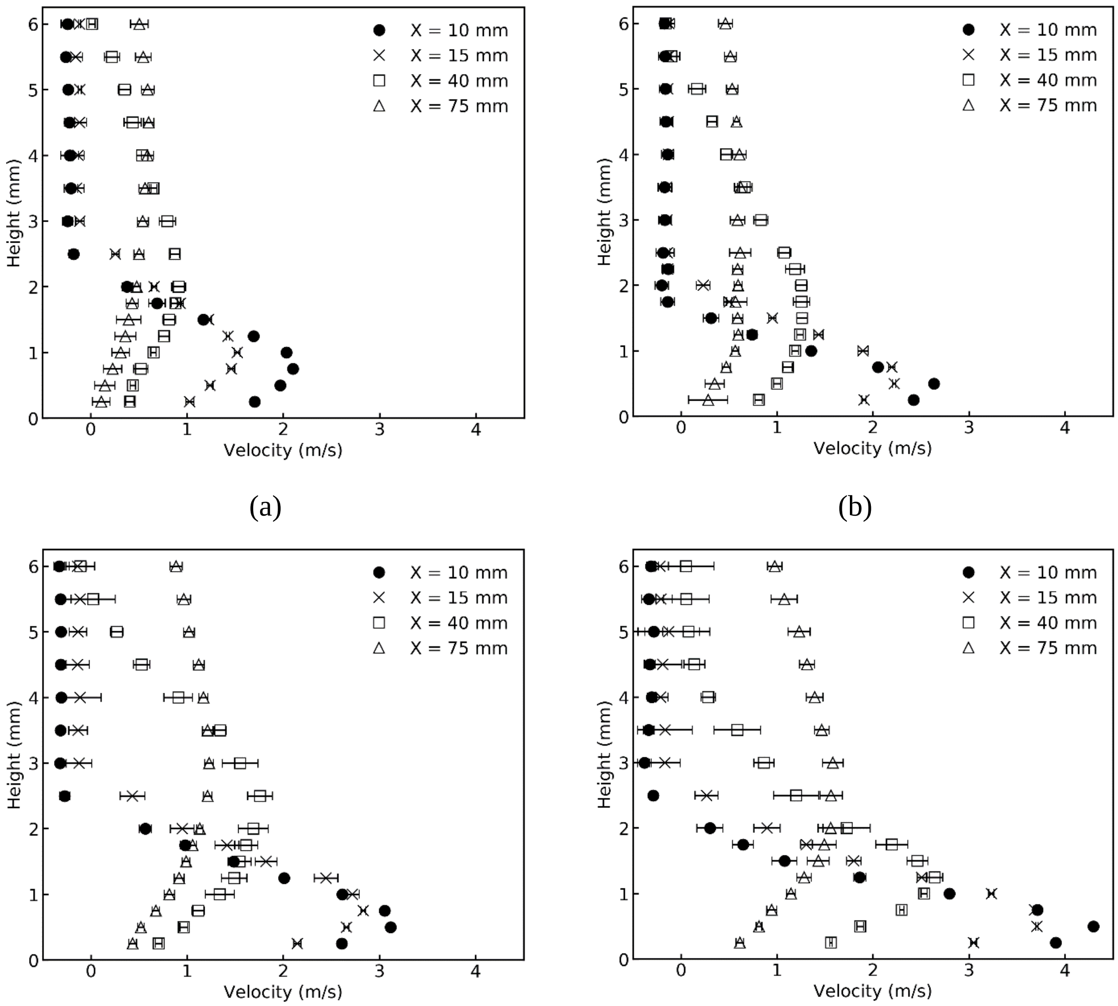

(a) (b)

(c) (d)

Figure 4.7. Wall jet velocity profiles induced by DBD at different locations downstream from the high voltage electrode for different applied conditions (a) 14 kV / 1 kHz, (b) 14 kV / 2 kHz, (c) 18 kV / 1 kHz, and (d) 18 kV / 2 kHz.

An interesting phenomenon with pitot tubes is seen consistently in the velocity profiles. Negative velocities are observed above the wall jet region (y > 3.0 mm) at downstream locations of x = 10 mm and x = 15 mm, at downstream locations of x = 40 mm and x = 75 mm the x velocities are always positive, see Figure 8. The magnitude of the negative velocity is larger at x = 10 mm than at x = 15mm. One possible explanation is that the fluid entrainment by the wall jet creates an adverse pressure gradient near the virtual origin that entrains the fluid from all directions, including from the downstream region. This trend was observed in PIV measurements by Debien [59];

however, it has not been reported in pitot tube measurements, such as Benard [5]. At this time, we do not have a satisfactory explanation of why the negative velocity was not observed in the other pitot tube experiments; perhaps, modeling of these flow cases can shed insight into the flow patterns.

The U_{max} increases approximately linearly with voltage in this range of operating conditions. Other studies such as Forte [27] have shown a similar relation nearly linearly in the voltage range of 2 kV – 26 kV. Frequency also increases U_{max}, however, works such as Forte [27] and Jolibois [70] have shown that U_{max} eventually reaches an asymptotic limit at increasing frequencies. Some reports suggest that the initial increase in U_{max} is due to ion generation per cycle remaining constant as the frequency increases leading to increasing total ion generation, and momentum [5]. The plateau is attributed to a short enough AC voltage cycle that the generated ions on the dielectric surface between two discharge cycles do not have enough time to relax and transfer their momentum into an ionic wind [5]. Due to the uncertainty in the y-position of the probe integration of the velocity profile over the probe diameter, further experiments are needed to quantify the U_{max} trends.

4.5 Energy transfer characteristics

Figure 9 illustrates the energy conversion efficiency calculated as the ratio of mechanical power (or kinetic energy flux in the flow) to the electrical power as shown in Eq. (11) for 1 kHz and 2 kHz. The plasma actuator's electrical power consumption is calculated using Eq. (2). At the lowest electrical power consumption configuration of 14 kV and 1 kHz, the 110 mm spanwise electrode's power consumption was 3.34 W, which translates to approximately 0.304 W/cm. At the highest power consumption configuration of 18 kV and 2 kHz, the power consumption was 12.8 W, which translates to approximately 1.17 W/cm. These electrical power consumption levels support previous data of ~ 1 W/cm [5]. Similar to the momentum calculations, the kinetic energy flux is calculated using Eq. (10) at x = 15 mm. At both frequencies, the mechanical power increased with voltage.

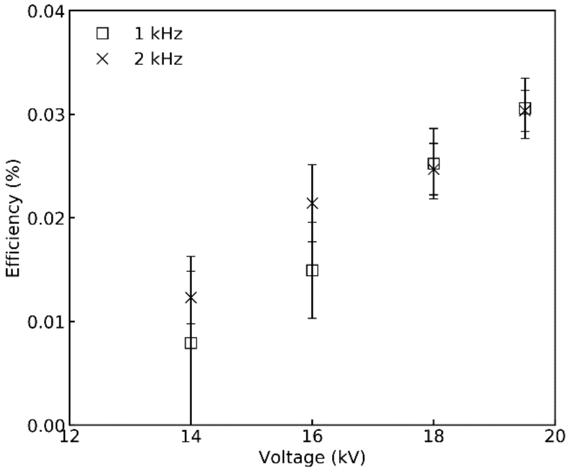

Figure 4.8. Electromechanical efficiency determined at different voltages for two different frequencies reaches a maximum value of 0.03%.

From equation Eq. (11), the maximum electromechanical efficiency is ~ 0.03% at 19.5 kV and 1 kHz. The DBD's lowest efficiency of ~0.008% is the mildest conditions (14 kV and 1 kHz). In this voltage and frequency range, the efficiency continued to increase approximately linearly with voltage. The calculated efficiency values agree with previous studies of traditional DBDs with thin dielectrics [70]. Other studies have shown that electromechanical efficiency reaches an asymptotic limit with higher electrical power input, and factors such as dielectric thickness and material properties affect the overall electromechanical efficiency [5]. For example, Laurentie *et al*. [60] studied the effect of electrode encapsulation and reached an efficiency value of 0.2%. Optimization of electrical input characteristics has shown promising results in increasing the electromechanical efficiency [73].

4.6 Relationship between discharge current and momentum

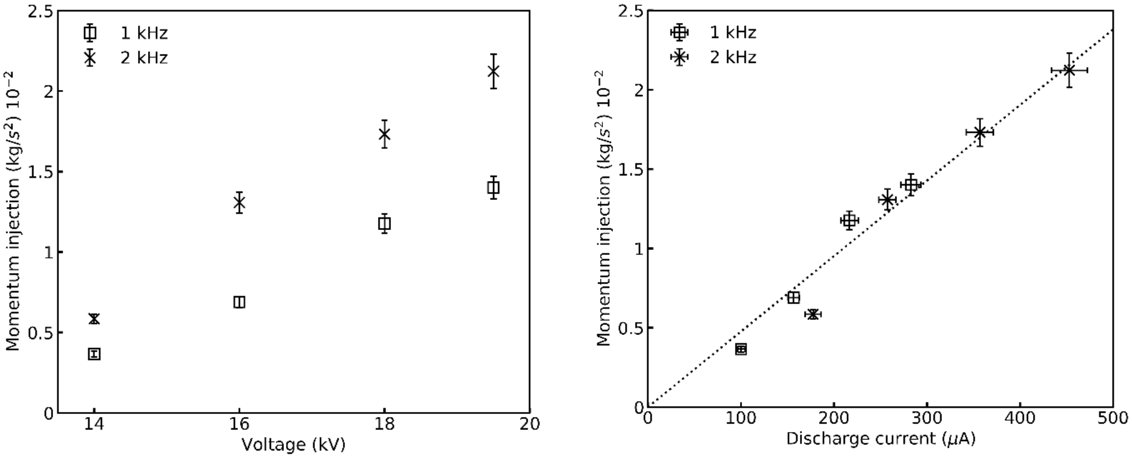

(a) (b)

Figure 4.9. Momentum of the wall jet vs. (a) voltage and (b) discharge current. The wall -jet momentum collapses onto a single line for both frequencies and is directly proportional to the discharge current.

Analysis of wall jet momentum arguably is more important for characterizing the wall jet. It is also less susceptible to probe positioning and geometry errors as multiple data points are taken at each x location. Figure 10(a) shows the DBD wall jet momentum calculated using equation (9) at x = 15 mm. The x = 10 mm location is not used; for 19.5 kV condition, the 10mm case had lower velocities than 15 mm. This is likely due to (i) probe interaction with plasma volume (plasma length ~ 7 mm), (ii) the flow was still accelerating (X >1). Excluding the 19.5 kV case, the momentum calculated at x = 10 mm is nearly identical to the momentum calculated at x = 15 mm. The momentum increases with the applied voltage and frequency for all studied conditions.

To understand the relationship between the fluid dynamic and plasma discharge, the induced wall jet momentum is plotted against the voltage and discharge current in Figure 10. As expected, the increase in voltage and frequency leads to higher momentum. We do not have sufficient data to quantify the trend. However, the comparison of momentum and total discharge current combines both frequency and voltage effects, reducing the data to a single line. In this analysis, only 8 data points are included over a relatively narrow range of frequencies. The least-square fit shows that the momentum increases linearly with the discharge current, as shown in Figure 10(a), and it can be approximated by Eq (16). From a mechanistic perspective, this is intuitive as the larger plasma volume, higher ion concentration, and stronger E-field lead to a greater number of ion-neutral molecule collisions accelerating the flow. The relationships linking frequency and voltage to discharge current are presented in Eq. (5). The obvious observation is that the planar DBD actuator can produce a higher momentum when the discharge current is maximized. The reduced-order model for DBD wall jet momentum is given by the following expression

$$M = \beta K {f_{AC}}^{\alpha}(\varphi - \varphi_0)^2. \tag{16}$$

The coefficients of this model are likely to depend on the electrode configuration and the properties of the dielectric media. It is also possible that the assumption of momentum being directly proportional to discharge current would break down at higher frequencies [64], and the exponents in the power-law relationship would change. At this time, we do not have sufficient data to extrapolate the model to these conditions. Table 1 summarizes the formulation of the reduced-order model for asymmetric DBD actuator developed from the experimental measurements for the range φ = 12 – 19.5 kV, f_{AC} = 0.5 – 2 kHz

Table 4.1: Summary of empirical expressions for different properties of DBD actuator

Property	Expression	Coefficients
Plasma length (L_P)	${K_1 f_{AC}}^{\alpha_1}(\varphi - \varphi_0)$	$K_1 = 2.46 \times 10^{-2}$ $\alpha_1 = 0.38$ $\varphi_0 = 4.75$ kV
Plasma volume (V_P)	$K_2 {f_{AC}}^{\alpha}(\varphi - \varphi_0)^{\gamma}$	$K_2 = 1.29 \times 10^{-4}$ $\alpha = 0.8$ $\gamma = 1.67$
Total discharge current (I_{dis})	$K {f_{AC}}^{\alpha}(\varphi - \varphi_0)^2$	$K = 4.71 \times 10^{-3}$
Positive discharge current (I_{dis_PD})	$K_3 {f_{AC}}^{\alpha}(\varphi - \varphi_0)^2$	$K_3 = 3.33 \times 10^{-3}$
Negative discharge current (I_{dis_ND})	$K_4 {f_{AC}}^{\alpha}(\varphi - \varphi_0)^2$	$K_4 = 1.38 \times 10^{-3}$
Momentum (M)	$\beta K {f_{AC}}^{\alpha}(\varphi - \varphi_0)^2$	$\beta = 4.76 \times 10^{-3}$

4.7 Chapter Summary

We developed a reduced-order model for discharge current, current density, and momentum injection utilizing the data from DBD actuator, i.e., plasma volume, electrical discharge current, and resulting velocity profiles over a range of voltage (12 kV – 19.5 kV) and frequency (0.5 kHz – 2 kHz). The plasma length increases linearly with voltage, matching previous studies, and the plasma volume varies quadratically with voltage. The plasma volume continues to grow with a frequency up to 2 kHz, whereas the plasma length approaches a limit at 2 kHz at these operating conditions. The increase in volume is due to continued growth in plasma height, suggesting that plasma volume can be a better input in CFD modeling.

The current associated with microdischarges was measured using a Rogowski coil with high temporal resolution. The charge transport in each microdischarge and the corresponding discharge current were calculated for both PD and ND semi-cycles. The discharge current analysis yielded a power law for the positive and negative discharge current associated with microdischarges in the form of $I_{dis} = Kf^{\alpha}(\varphi - \varphi_0)^2$. Comparing the expressions for the discharge currents, there is an asymmetry in the discharge currents between positive and negative cycles. The current density was calculated using discharge current and plasma volume. The discharge current density increases with voltage, independent of frequency.

The momentum and mechanical power of the DBD actuator were determined using vertical velocity profiles at different downstream positions over a range of operating conditions. DBD wall jet momentum increases with voltage and frequency, which are directly proportional to the discharge current. The electromechanical efficiency increases with voltage; a maximum efficiency of ~0.03% agrees with previous data from thin dielectric DBD actuators. The discharge current expressions and baseline velocity were used to develop a reduced-order model of DBD momentum injection. The analysis of the plasma volume can be used in the multiphysics modeling of the DBD.

Future research building upon this should extend the study to higher frequencies to develop a more robust relationship between the discharge current and plasma volume and determine the body force acting on the fluid. Future experimental efforts should also explore the effects of different dielectric materials and thicknesses to create a more robust and universal empirical model. Testing with different geometries may also prove insightful. However, the empirical trends will shift as the electrical capacitance depends on the electrode spacing and separation. Instead, numerical modeling based on the empirical relationships may prove more insightful to the underlying plasma dynamics.

Chapter 5. DBD Actuator in External Flow

Building upon the characterization and empirical model theory of the DBD actuator in quiescent conditions, the DBD actuator's performance in co- and counter-external flow is explored in this section. Characterizing and understanding DBD performance in external flow is necessary for numerical modeling. Nearly all numerical models were developed and validated in quiescent conditions and are yet to be tested in an external flow condition with inertial and viscous flow interactions. Experimental results of the DBD actuation effect on boundary layer flow, in both co-flow and counter-flow, are necessary to estimate the changes in surface pressure and flow dynamics around an airfoil and to provide guidance for numerical simulation for DBD-driven flow actuation. To date, the literature does not report any experimental characterization of velocity profiles in the counter-flow injection by DBD. Analytical and numerical efforts related to plasma-flow interactions are generally limited to studies in quiescent air. The general approach demonstrated for the flat plate can be further extended to flows over aerofoils.

This section explores the effect of EHD momentum injection by the DBD actuator at $U_\infty = 5$ m/s and $U_\infty = 11$ m/s in co-flow and counter-flow. AC voltage was varied in the range $V_{AC} = 12$ kV – 19.5 kV, and the frequency was constant at 2 kHz. This section first explores the fluid characteristics of DBD-driven flow in counter-flow and quantifies the onset separation due to an adverse pressure gradient. This work provides insight into the interaction between the DBD flow and a freestream flow over a flat plate, informing the potential placement of actuators on airfoils for maximum impact and providing validation for numerical studies.

The DBD actuator and power electronics are identical to the previous section's DBD actuator and power supply, with a thin Kapton dielectric barrier and a Trek 615-10 power supply. The results of the DBD momentum injection are published in the Journal of Electrostatics [13].

5.1 Experimental Setup

We characterize the electromechanical performance of a DBD actuator in an external flow with an open-circuit wind tunnel with a 100 mm × 100 mm cross-sectional test section. The wind tunnel includes an inlet section, a 1000 mm long flow development section, and a final test section. The DBD actuator plate surface rests in line with the bottom wall of the wind tunnel at the final test section, see Figure 5.1. The inlet section consists of an array of four 120 mm x 120 mm fans with inlet cowls, a large honeycomb screen, and a contraction cone. The fan array can be replaced with fans of different power to vary the freestream wind speed. For this study, two sets of fans were used to allow for freestream velocities of $U_\infty = 4 – 11$ m/s range. The data for two sets, $U_\infty =$ 5 m/s and $U_\infty = 11$ m/s, are plotted. The wind tunnel boundary layer can also be characterized through its shape factor, H, defined for an incompressible fluid as:

$$\mathrm{H} = \frac{\delta_1}{\delta_2} = \frac{\displaystyle\int_{y\,=\,0}^{y\,=\,\infty} \left(1 - \frac{U(y)}{U_{\infty}}\right) dy}{\displaystyle\int_{y=\,0}^{y\,=\,\infty} \frac{U(y)}{U_\infty}\left(1 - \frac{U(y)}{U_{\infty}}\right) dy} \tag{14}$$

where δ_1 and δ_1 are the boundary layer displacement thickness and momentum thickness, respectively. For the two different external flow condition, H = 1.3 and 1.1, respectively. The contraction cone with a 9:1 contraction ratio results in a 100mm x 100mm wind tunnel section constructed of plexiglass. An aluminum extrusion frame supports the wind tunnel section. Velocity measurements were obtained using custom glass pitot tubes with a 0.4mm ID and 0.5mm OD. The boundary layer height (δ_{99}) of the wind tunnel at $U_\infty = 5$ m/s external flow was measured at the location of the actuator ~8.0 mm. Using the height of the wind tunnel as the characteristic length, the Reynolds number (Re) is approximately 35,000 at $U_\infty = 5$ m/s and 75,000 at $U_\infty = 11$ m/s. All experiments were taken at the University of Washington Clean Energy Institute with a regulated temperature of ~ 20 C. The density and kinematic viscosity of air is assumed to be 1.225 kg/m^3 and 1.48E-5 m^2/s. The turbulence intensity of ~1% was measured using hot-wire anemometer. The hot-wire anemometer was not used for velocity measurements of the DBD actuator as the hot-wire wires and electronics would introduce a risk of arc discharge from the high-voltage electrode.

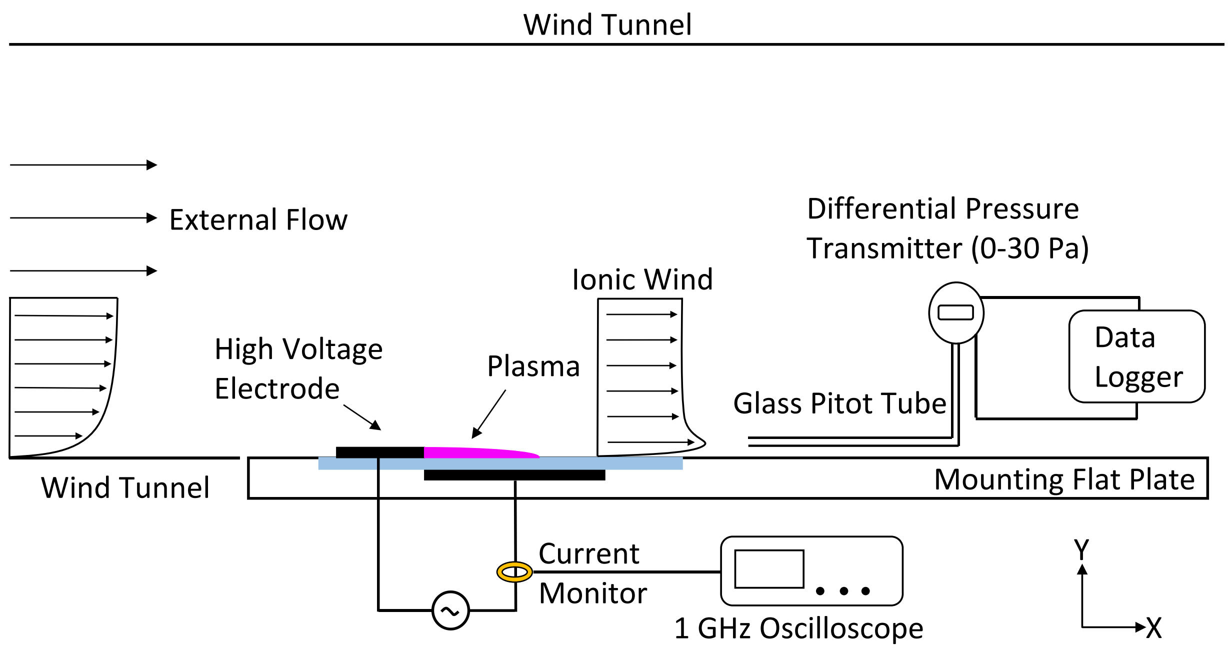

Figure 5.1. Schematic of the experimental setup: The DBD actuator is mounted on an acrylic glass plate flushed with the wind tunnel bottom. The blue region is the dielectric layer separating the electrodes.

In this study, the electrical power consumption is calculated in this work also with a Lissajous curve. A Lissajous curve is created by introducing a capacitor between the grounded electrode and the ground [57, 129]. Integrating the charge-voltage relationship multiplied by the frequency yields the total power usage of the DBD system. The time-averaged electrical power consumed by the actuator is computed as

$$W_{elec} = f_{AC} \int_{t^*=0}^{t^*=1} V dQ, \tag{15}$$

where f_{AC} is the frequency of the applied voltage in Hz, and V and Q are the voltage and charge at each point in the period. The normalized time (t^*) represents a single cycle. We compute the average resulting power from at least ten periods to reduce the noise impact. In the wind tunnel study by Pereira *et al.*, the DBD actuator in co-flow and counter-flow was found not to have significantly different electrical characteristics [97].

While the pitot tube set-up is mechanically identical to the previous work, the external flow slightly changes the control volume analysis. Considering a 2D control volume (with a spanwise unit length), integration of the streamwise velocity along a vertical profile in the wind tunnel with the DBD actuator provides the total mass flow rate per meter spanwise, Q, of the total system:

$$Q_{system} = \rho \int_{y=0}^{y=\mathrm{h}} U(y) dy, \tag{16}$$

where $U(y)$ is the velocity measured along the vertical profile at a constant x - location. Similarly, the system's total momentum can be found by integrating the square of the velocity along a vertical profile:

$$M_{system} = \rho \int_{y=0}^{y=\mathrm{h}} U^2(y) dy. \tag{17}$$

To identify the momentum produced by only the DBD actuator, we obtain the identical velocity profiles with the DBD actuator ON and OFF. The difference in momentum integrated from the wall to the point where the two velocity profiles intersect is the momentum injected by the DBD. Above the intersection of the two profiles, there is entrainment due to mass conservation, and this entrainment is confirmed by taking the velocity profile of the entire wind tunnel with and without actuation. The resulting momentum is expressed as

$$M_{DBD} = \rho \int_{y=0}^{y=\mathrm{h}} {U_{DBD\ ON}}^2(y) - {U_{DBD\ OFF}}^2(y) dy \tag{18}$$

and this approach similarly holds for mass flow rate and mechanical power. The mechanical power of the system (W_{mech}) can be computed by

$$W_{mech} = \frac{1}{2} \rho L \int_{y=0}^{y=\infty} U^3(y) dy. \tag{19}$$

The derived values of mass flow rate, momentum, and power of the DBD in external flow are compared to the results of similar measurements in quiescent flow.

5.2 Effect of External Flow on Electrical Power Consumption

Figure 5.2 illustrates the power usage of the DBD for a range of operating voltages, external flow speed, and DBD actuator orientation. Integration of Lissajous Q-V curves yielded an average power consumption of the actuator. The power usage is normalized to the spanwise length of the actuator (0.11 m). In general, the power consumption increases quadratically with applied voltage, which is consistent with previous reports for AC DBD [32, 54] and the EHD corona discharge flow [68, 69]. Power usage between the AC cycles for any configuration had a maximum variance of ~ 8%. Pereira *et al*. also found power usage to vary less than 10% between co-flow and counter-flow forcing [35]. The data were taken for the DBD actuator in quiescent, counter-flow, and co-flow conditions at the two external flow speeds. Our results support that the electrical power consumption is independent of external flow conditions in co-flow and counter-flow, supporting that the electrostatic performance of DBD is mainly independent of an external flow, possibly due to significant differences in time and length scales. In the quiescent experiments and the external flow conditions, DBD power was averaged over 10 AC cycles; the maximum difference between is ~ 4 % at VAC=12kV and ~3% at 19.5 kV. The standard deviation across the 10 cycles is ~ 1.3% at 12kV and ~ 6.5% at 19.5kV, which is similar to the changes in the average power consumption. Thus, in our experiments, the presence of external flow does not influence the DBD power requirements. The magnitude of normalized power usage measured for this study is slightly higher than Pereira *et al*., which used a thicker 3 mm dielectric; however, other studies, such as Forte *et al*., have found similar power usage for thinner thicknesses and noted that the increase in dielectric thickness decreases DBD capacitance, thus decreasing power [32, 51, 54].

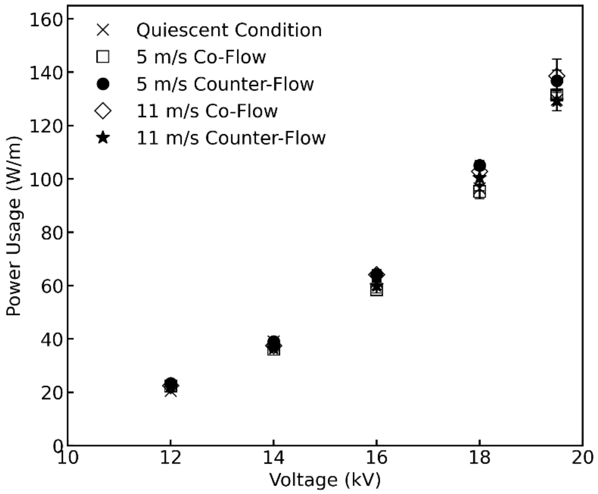

Figure 5.2. DBD power usage at U∞ = 5 m/s and U∞ = 11 m/s external flow in co-flow and counter-flow

5.3 Operation in Quiescent Condition

First, the momentum injection of the AC DBD actuator is considered in a quiescent environment. Figure 5.3 shows the velocity profile of the DBD jet at x = 10 mm and x = 25 mm downstream of the active electrode edge at 19.5 kV and 2 kHz [12]. The velocity profile of the DBD jet in quiescent condition was confirmed to be identical inside and outside of the wind tunnel using the same experimental setup. At this electrical condition, the maximum velocity Umax = 4.8 m/s is at y = 0.25 mm. Although the velocity decay and the spreading of the jet are apparent, as expected in wall jets, the Coulombic force and the fact that the fluid is being accelerated over the fluid volume rather than the point source make the parameterization of the flow challenging. The addition of co- and counter-flow further complicates the analytical interpretation.

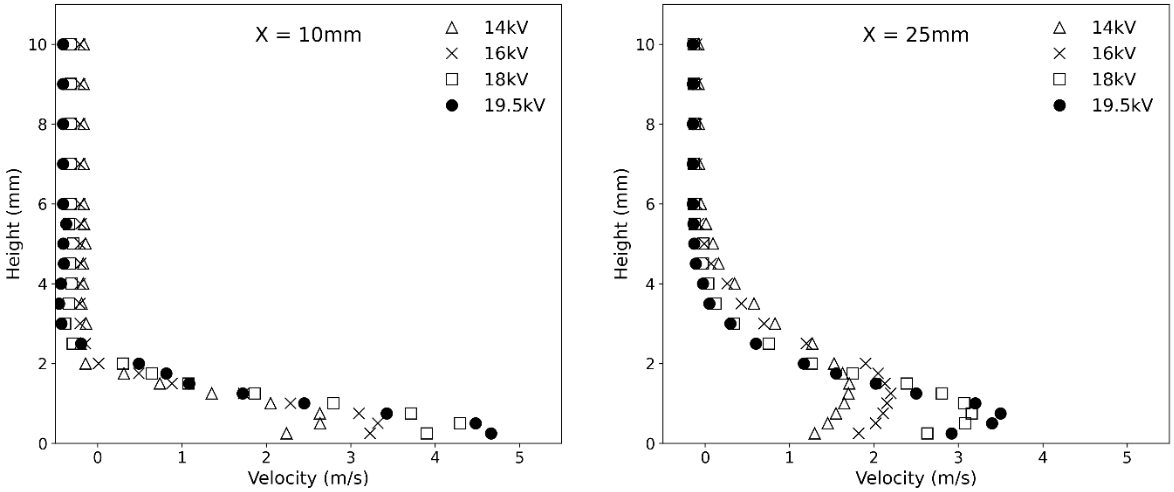

(a) (b)

Figure 5.3. DBD with no external flow at x = 10 mm (a) and x = 25 mm (b) downstream. The maximum velocity at 19.5 kV is ~ 4.7 m/s at y = 0.5 mm at x = 10 mm downstream.

5.4 Co-Flow EHD Momentum Injection

This section discusses the DBD actuator performance in co-flow over the range V_{AC} = 14 – 19.5 kV, a frequency of 2 kHz, U_∞ = 5 m/s (Re = 35,000) and U_∞ = 11 m/s (Re = 75,000). The virtual origin and coordinate system are defined in Figure 5.4. The velocity profiles of the EHD jet are measured at x = 10 mm and x = 25 mm downstream of the active electrode edge.

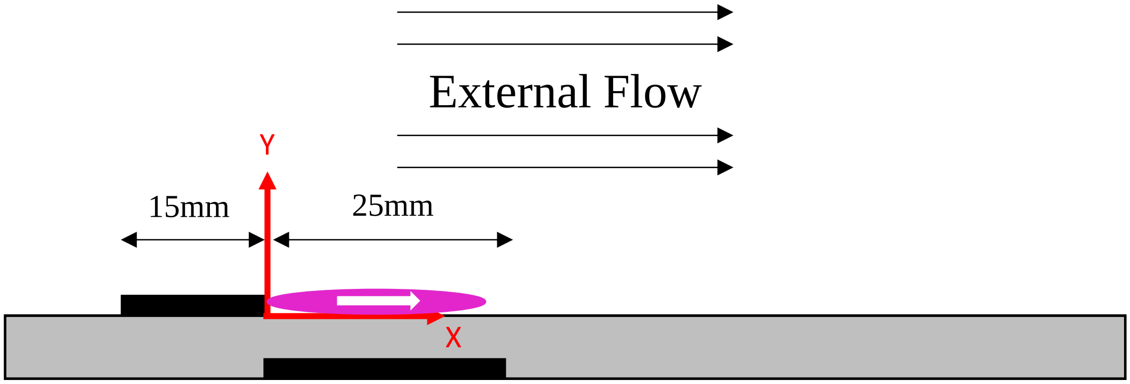

Figure 5.4. DBD actuator in co-flow configuration, the first measurement is taken at x=10 mm to avoid plasma region disruption with pitot probe. The plasma region is colored purple.

Due to EHD momentum injection, the velocity in the boundary layer increases; however, the freestream boundary layer affects the momentum displacement difference. Figure 5.5 shows the velocity data versus DBD voltage at two downstream locations. The dotted line is the wind tunnel velocity profile without DBD actuation. Note that in quiescent conditions (Figure 5.3), the DBD wall jet has a maximum velocity, U_{max} ~ 4.8 m/s at x = 10 mm, y = 0.25 mm when V_{AC} = 19.5 kV and f_{AC} = 2 kHz, and the peak velocity of the jet decays quickly away, downstream and wall-normal, from this maximum. At $U_\infty = 5$ m/s, EHD-induced velocities are comparable to the freestream, and the effects of DBD actuation are dominant. The increase in boundary layer velocity of ~ 2 m/s is nearly identical to that of Bernard *et al*. [61] for similar conditions. In the co-flow experiment, the U_{max} ~ 5.4 m/s, which is greater than that in quiescent condition (~ 4.8 m/s) but located at y = 0.75 mm for the same x-position, as viscous effects shift the location of U_{max} away from the wall. At y = 0.25 mm, the U velocity is 5.3 m/s and is greater than that of the quiescent jet at y = 0.25 mm; thus, the dominant effect between the DBD jet and freestream can be seen as mixing and entraining fluid from the external freestream into the boundary layer, and more specifically within the DBD forcing region. The DBD forcing region height and length have been previously reported at these same electrical conditions [12] and is also reflected in the ~ 2 mm tall DBD wall jet in quiescent condition, as seen in Figure 5.3. In co-flow, the DBD-induced momentum does not diffuse into the outer flow as quickly as in the quiescent environment, and this can be observed from the velocity profile at x = 25 mm. The interaction of the wall jet with the freestream depends on the shape, the nature of the boundary layer, and the DBD jet characteristic. When DBD operates at $U_\infty = 0$ m/s, the outer jet region entrains quiescent air [51, 52, 130]. With free velocities similar to or lower than the EHD jet, the injected momentum promotes the entrainment of freestream fluid into the boundary layer. In the case of high momentum injections (higher DBD voltages), both the maximum velocity and the jet thickness increase, resulting in greater changes in the velocity profile. This entrainment can be seen by a slight decrease in the external flow with the energized DBD actuator starting at approximately y = 3.75 mm. Conservation of mass in the wind tunnel means that as the boundary layer accelerates by the EHD-added momentum, the freestream velocity decreases slightly (the momentum thickness of the boundary layer is smaller). The complete velocity profile confirms that mass is conserved as the entrainment section eventually merges with the base wind tunnel profile.

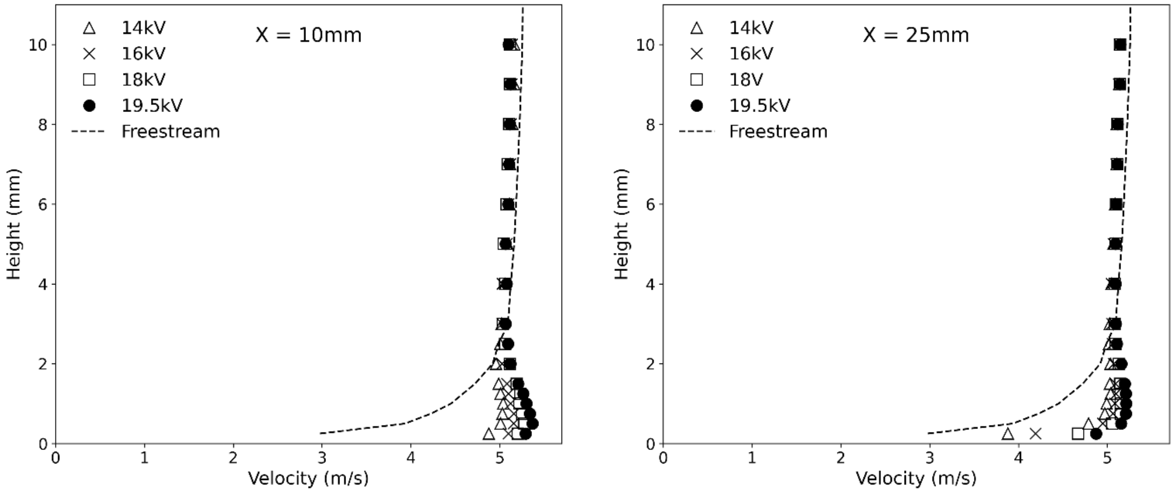

(a) (b)

Figure 5.5. DBD actuator in $U_\infty = 5$ m/s co-flow at (a) x = 10 mm and (b) x = 25 mm downstream. The dashed line shows the freestream profile without plasma injection. The DBD voltage varies in the 14 - 19.5 kV range; the AC frequency is set constant at 2 kHz.

Figure 5.6 shows the effect of the EHD wall jet in the boundary layer at $U_\infty = 11$ m/s. In this case, the EHD velocity is about half the freestream for the highest DBD settings. In addition, the momentum of the freestream within the height of the DBD forcing region ($y < 2$ mm) is significantly more than the DBD momentum injection. As a result, the effect of momentum injection is reduced, as the enhanced mixing in this higher Reynolds number case is more effective at spreading the effect of the EHD momentum injection throughout a thinner boundary layer. Even at maximum DBD power, the velocity increase is less than 1 m/s at x = 10 mm. At x = 25 mm, the effect of the EHD momentum injection is almost negligible. At higher external flows, the EHD momentum addition results in a lower overall impact on the boundary layer, as the enhanced mixing in the thin boundary layer rapidly restores the boundary layer profile to the unactuated case.

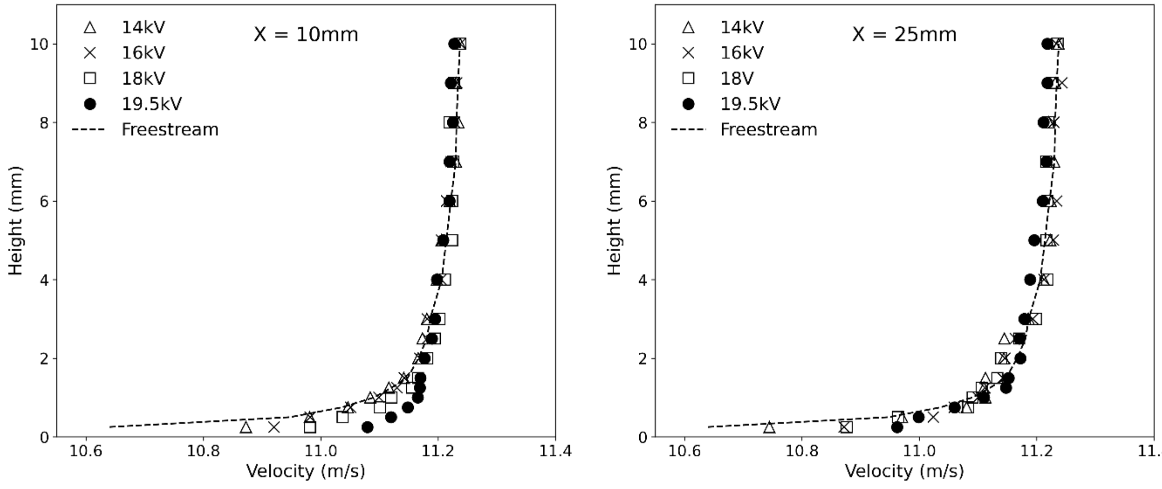

(a) (b)

Figure 5.6. DBD actuator in $U_\infty = 11$ m/s co-flow at x = 10 mm (a) and x = 25 mm (b) downstream. The DBD voltage varies in the 14kV-19.5kV range, and the AC frequency is set constant at 2kHz.

The EHD momentum addition cannot be treated as a linear superposition of the EHD jet in a quiescent environment, and the momentum is associated with the boundary layer of the free stream. For external flows compatible with EHD wall jet velocities, the momentum injection into the co-flow leads to effective boundary layer thinning; this effect diminishes at higher freestream velocities (higher Reynolds numbers and thinner boundary layers). The wall jet mixing is influenced by (i) interaction with the freestream and (ii) viscous wall shear increase in the viscous sublayer. This point is explored further in Figure 5.12.

5.5 Counter-Flow EHD Momentum Injection

This section describes the behavior of counter-flow EHD jet at DBD V_{AC} = 14 kV – 19.5 kV at f_{AC} = 2 kHz and wind speeds of $U_\infty = 5$ m/s and $U_\infty = 11$ m/s. The virtual origin and coordinate system of the DBD in counter-flow are defined above in Figure 5.7. The datum for analysis is set at the plasma generation edge of the active electrode; however, the EHD momentum injection is now in the negative x-direction.

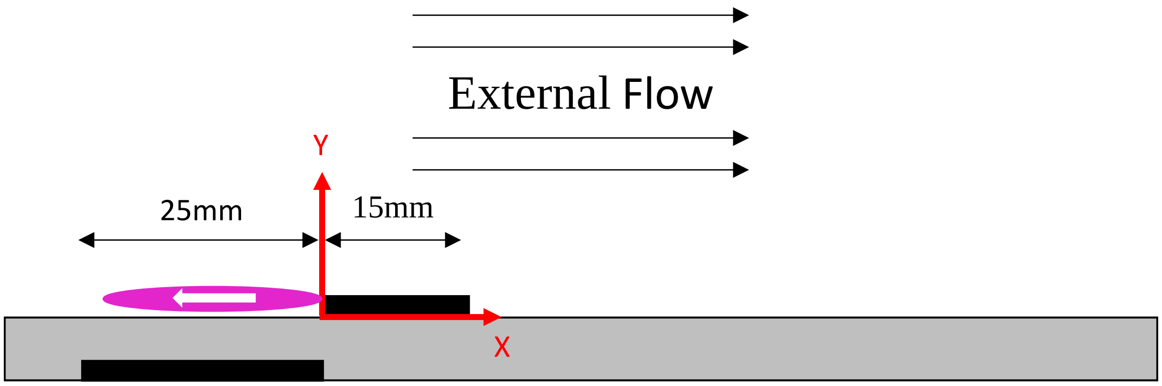

Figure 5.7. DBD actuator in counter-flow configuration. The plasma region is colored purple.

Figure 5.8 and Figure 5.9 show the velocity profiles for the EHD momentum injection into the counter-flow. The dotted line is the measured wind tunnel velocity profile without DBD actuation. At $U_\infty = 5$ m/s, the velocity of the EHD jet has a similar magnitude to the external flow, resulting in a significant adverse pressure gradient and the formation of a recirculation zone. The exact boundaries of the separation region are difficult to determine experimentally in the plasma region ($x < 0$ mm, $y < 2$ mm) as inserting the pitot probe directly into the plasma possibly interferes with the experiment, see Figure 5.7. However, to preserve continuity, the EHD jet entrains fluid from above and behind the jet; thus, transects downstream and along x for constant y can be used to determine the boundaries of the separation bubble.

First, we examine the y-scan at the fixed x-position. Figure 5.8 and Figure 5.9 show the profiles at x = 10 mm (above the active electrode) and x = 25 mm for $U\infty = 5$ m/s and $U\infty = 11$ m/s, respectively. As with the co-flow experiments, the EHD jet strength is varied by varying VAC = 14 kV - 19.5 kV, while the AC frequency is 2 kHz. For all voltages, the DBD in counter-flow creates a more significant deficit in the boundary layer than its co-flow counterpart, e.g., the counter-flow EHD jet creates a $\Delta U > 5$ m/s at $V_{AC} = 19.5$ kV compared to the $\Delta U \sim 2$ m/s in the co-flow case. Figure 5.8 (a) also shows that in counter-flow cases at 18kV and 19.5kV, the wall shear stress changes direction due to the increased strength of the EHD jet. In the co-flow scenario and lower voltage counter-flow configurations, the wall shear stress remains opposite of the freestream direction. The maximum negative velocity is likely in the EHD momentum injection region (x= - 10 mm – 0 mm). However, we cannot measure within the plasma region due to the plasma interactions with the pitot tube. Figure 5.8 shows that in the V_{AC} = 19.5 kV case, the separation bubble extends past x = 10mm downstream of the active electrode edge, while other conditions exhibit flow reattachment. The flow is fully attached at x = 25 mm; however, the pressure gradient in the flow boundary layer has not yet recovered.

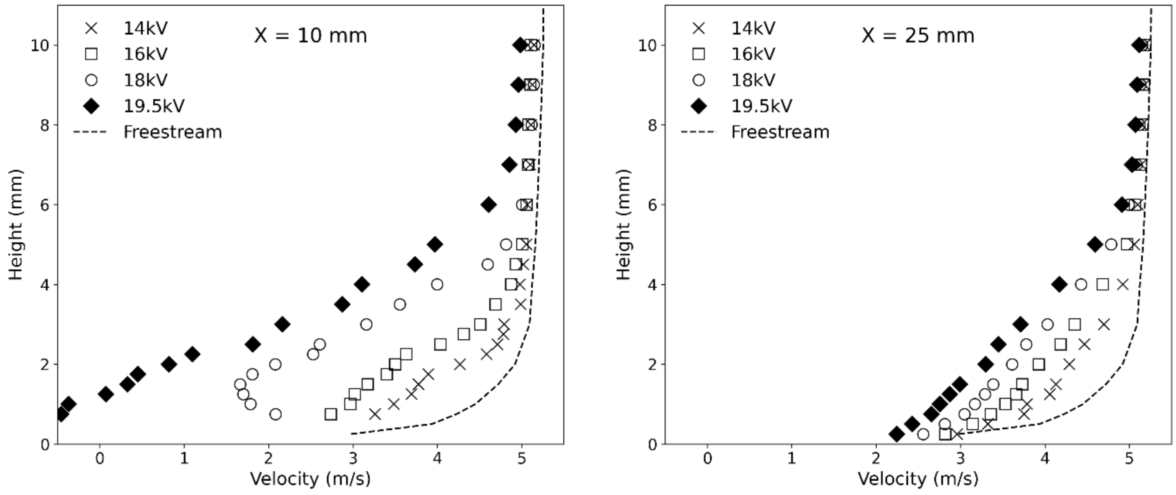

(a) (b)

Figure 5.8. DBD actuator in U_∞ = 5m/s counter-flow at x = 10 mm (a) and x = 25 mm (b) downstream. The DBD voltage varies in the 14 - 19.5 kV range, and the AC frequency is set constant at 2 kHz.

For higher external flow, the effects of the DBD jet are less dramatic. Within the boundary layer, the most significant decrease in velocity in counter-flow with U_∞ = 11 m/s is approximately 2.0 m/s at y = 0.5 mm and x = 10 mm. No separation was observed in the U_∞ = 11 m/s counter-flow cases, though we did not probe the plasma region. While the effects of the DBD in counter-flow at U_∞ = 11 m/s are less dominant than for slower freestream experiments, the effects of the EHD wall jet are still more significant than in co-flow at the same U_∞.

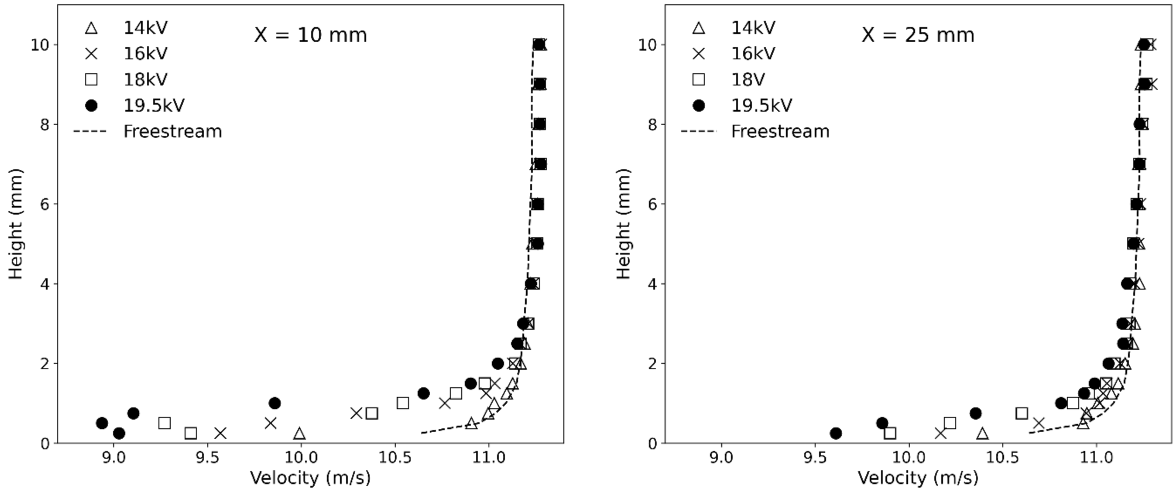

(a) (b)

Figure 5.9. DBD actuator in U_∞ = 11 m/s counter-flow at x = 10 mm (a) and x = 25 mm (b) downstream. The DBD voltage varies in the 14 - 19.5 kV range, and the AC frequency is set constant at 2 kHz.

We performed x-scans by holding the y position constant to determine the boundaries of the separation region. Figure 5.10 shows the velocity profiles for y = 0.5 mm and y = 1.0 mm, while the x position was varied from x = 0 mm (edge of the active electrode) to x = 15 mm. The DBD voltage was V_{AC} = 12, 14, 16, 18 kV at f = 2 kHz. The data for V_{AC} = 19.5 kV is not shown due to the limited range of the pressure gauge.

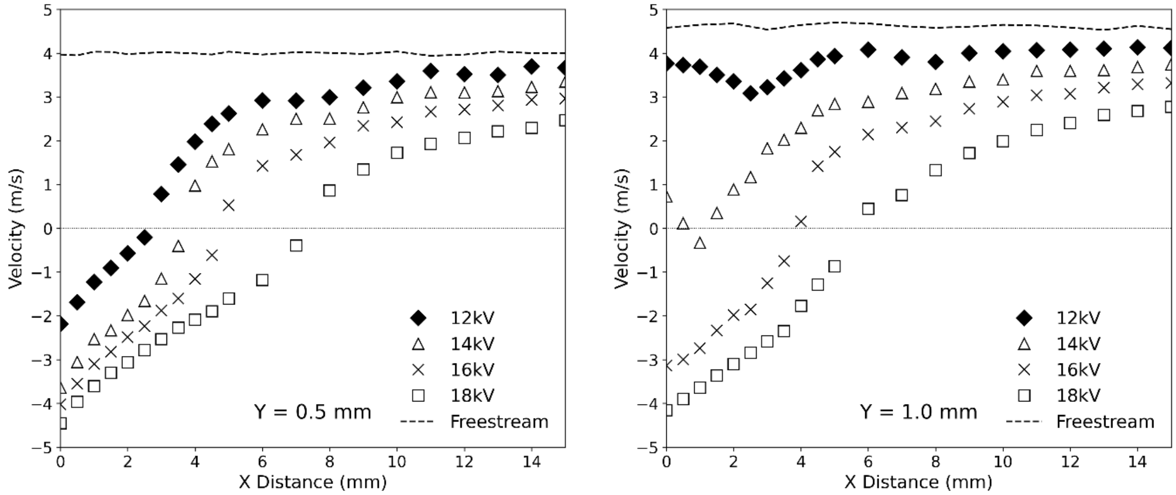

(a) (b)

Figure 5.10. DBD actuator in U_∞ = 5 m/s counter-flow at y = 0.5 mm (a) and y = 1.0 mm (b). The DBD voltage varies in the 14 - 19.5 kV range, and the AC frequency is set constant at 2 kHz.

We observe separation at all voltages at y = 0.5 mm, immediately above the dielectric layer. The x-location, where the velocity direction changes from backward to forward, determines the separation bubble's edge. At VAC = 18 kV, the separation length is approximately 7.5 mm downstream. At y = 1.0 mm, there is no signature of the separation bubble for VAC = 12 kV; however, it exists for the higher voltages.

To better visualize the flow pattern at 5 m/s, additional x-scans were performed, and the 2D velocity fields were reconstructed. Figure 5.11 shows the velocity contour plots for the counter-flow EHD jet obtained by merging x and y scans at U∞ = 5 m/s. Each grid point in the figure is associated with a velocity measurement; the spatial resolution was 0.5 mm in both x and y directions, totaling approximately 400 measurements for each condition.

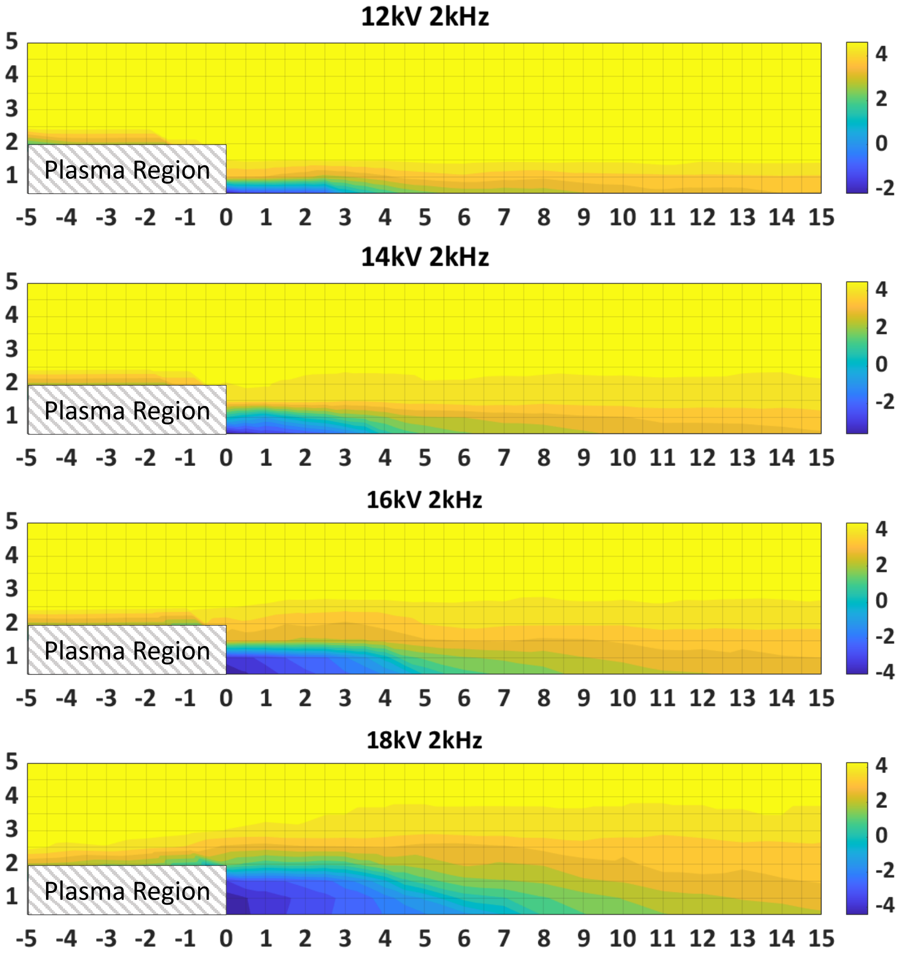
12kV 2kHz

14kV 2kHz

16kV 2kHz

18kV 2kHz

Figure 5.11. X-velocity contour plot for EHD jet in counter-flow for U∞ = 5 m/s for varying voltages. Gridlines correspond to recorded points spaced 0.5 mm apart in the x- and y-direction.

All DBD actuations cause a separated region (for U∞ = 5 m/s, R=35,000) with a negative x-velocity downstream of the plasma injection. With the increase in DBD voltage, the edge of the reversed flow region within the separation bubble extends from 3.0 mm (12 kV) to >10.0 mm (18 kV) in the x-direction from the edge of the active electrode and from 0.6 mm (12 kV) to > 1.75 mm (18 kV) in the y-direction. This growth in the length and height of the reversed flow region of the separated bubble is nonlinear with increasing voltage. The size and shape of the recirculation bubble are determined by the competition of the EHD jet strength vs. the forward momentum in the boundary layer. As the EHD injects negative momentum at high DBD voltages, it can overtake the momentum in the boundary layer at greater heights. Without sampling within the plasma region, it is challenging to characterize the entire length of the separation regions. It can be expected that the separation region extends into the forcing plasma region. Multiphysics CFD simulations can potentially address this issue; however, robust models must be developed and validated. Although robust multiphysics CFD analysis is beyond the scope of this paper, preliminary results with a simplified momentum model proposed in [12] also suggest that the momentum injection in the counter-flow scenario triggers flow separation, though additional validation is required.

5.6 Momentum Difference

Momentum difference is calculated at x = 10 mm downstream of the DBD wall jet by integrating the velocity profiles in the y-direction up to a height where mass and momentum are injected and not entrained. Note that the x = 10 mm location is in the direction of the external flow with the datum at the plasma generation edge of the DBD actuator. Thus, in the co-flow case, the x = 10 mm location is downstream or in front of the plasma region and above the dielectric and grounded electrode (Figure 5.4); however, in the counter-flow case, the x = 10 mm location is behind the plasma region and above the active electrode (Figure 5.7).

Figure 5.12 compares the DBD with external flow cases against an EHD jet in a quiescent environment. The absolute value of the momentum difference is shown, as the momentum difference is calculated by subtracting the counter-flow actuation profile from the unactuated boundary layer profile.

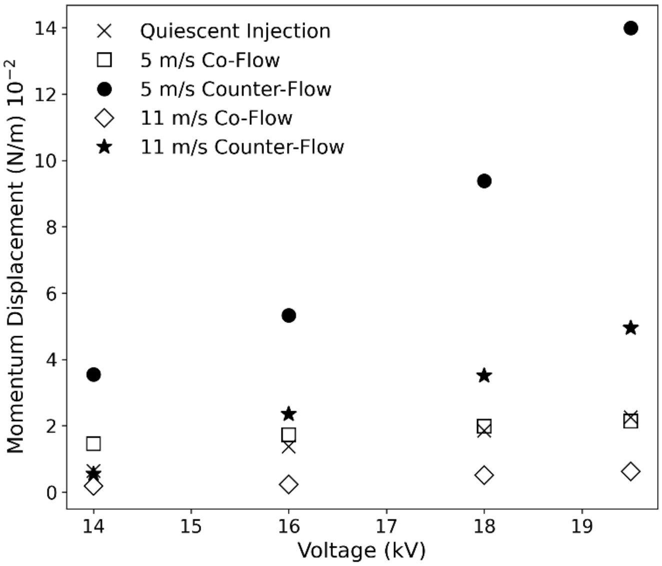

Figure 5.12. DBD momentum difference at $U_\infty = 5$ m/s and $U_\infty = 11$ m/s external flow

In the co-flow scenarios, the momentum addition into the boundary layer is equal to or lower than the momentum injected in the EHD jet. The momentum difference appears linear with V_{AC}; however, the change in total momentum is relatively flat, suggesting that momentum dissipation is driven primarily by the inner layer wall jet interaction with the wall. At 11 m/s co-flow, lower momentum differences are found for all voltages, and an increase in turbulent dissipation can explain this. The increase in dissipation is shown in the velocity profiles in Figure 5.5 and Figure 5.6 as the effect of the DBD momentum can still be seen at x = 25 mm downstream when $U_\infty = 5$ m/s (Re = 35,000). Still, the effect of the DBD momentum is almost unseen at x = 25 mm downstream when $U_\infty = 11$ m/s (Re = 75,000). Unlike the experiments in quiescent conditions [12], the fluid momentum of the EHD jet in the co-flow injection is not conserved as it travels downstream. In the counter-flow configuration, the momentum difference is more significant due to reversing flow near the wall and a change in shear stress direction. The most significant difference is observed in counter-flow, at $U_\infty = 5$ m/s. The momentum difference is ~ 6.5x greater than its co-flow counterpart.

The ratio of momentums within the DBD jet heights, M^*, is proposed as a nondimensional relation that could predict separation in the counter-flow injection. M^* represents the DBD momentum injection compared to the inertial force in the external flow. M^* is defined as:

$$M^* = \frac{M_{DBD}}{M_{External}} = \frac{\int_0^{h_{jet}} U_{quiescent\ DBD}{}^2(y)dy}{\int_0^{h_{jet}} U_{external\ flow}{}^2(y)dy} \tag{20}$$

The M_{DBD} value and the height of the jet (h_{jet}) in a quiescent environment can be directly measured or estimated from the empirical relationship as proposed by Tang *et al*. [12]. E.g., the height of the DBD jet in Figure 5.3 varies from 2 mm to 2.25 mm at the range of the voltages tested. The $M_{External}$ value can be estimated analytically, numerically, or experimentally for a given value of the h_{jet}. The ratio of the terms can be evaluated to determine flow separation criteria M^*; the higher values are likely to result in flow separation. A higher value in co-flow also likely results in the DBD momentum injection exerting enough inertial force to entrain fluid from the freestream. The values of M^* in the 5 m/s and 11 m/s cases are shown in Table 5.1. In this limited set of experiments, the separation was observed for cases with $M^* > 0.1$ (for $M^* < 0.1$, counter-flow DBD did not induce separation). Additional testing and numerical simulations at various DBD and external flow conditions could further define separation threshold criteria. Note that MDBD varies with DBD parameters and the x-position within the jet as it expands and loses momentum due to viscous dissipation. At the same time, the value $M_{External}$ depends on the external flow conditions and the x-position of the DBD jet as the jet thickness changes with the x-position.

Table 5.1. Conditions of separation due to a DBD Jet in counter-flow

Reynolds	BL Height (mm)	DBD Momentum (mN/m)	M*	Separation
35,000	8.0	6 – 22	0.14 – 0.52	Yes
75,000	2.5	6 – 22	0.02 – 0.07	No

5.7 Chapter Summary

We have experimentally investigated the performance of a DBD plasma actuator over a range of voltages (12 kV – 19.5 kV) at 2 kHz in co-flow and counter-flow with freestream velocities of 5 m/s and 11 m/s. The power consumption associated with DBD discharge is measured through capacitive measurements, with high temporal resolution throughout several cycles. For all voltages and freestream conditions in this experiment, there was no significant difference in power expenditure between the co-flow, counter-flow, and quiescent conditions, consistent with previous results. The DBD jet increased boundary layer velocity by > 2.0 m/s in co-flow and decreased the boundary layer velocity by > 5 m/s in counter-flow (leading to fully reversed flow near the wall). The momentum difference in counter-flow leads to flow separation; separation zone boundaries and velocity magnitudes were evaluated using x-velocity magnitude contour plots.

At low freestream velocities, the EHD jet significantly influences boundary layer flow, and the dissipation is driven by the interaction of the DBD wall jet and the inner boundary layer. However, at the higher freestream velocity with more momentum in the inner boundary layer, the external flow diminishes the momentum injection of the DBD due to the more effective turbulent mixing. The counter-flow momentum difference is 6.5 times higher than its co-flow counterpart at $U_\infty = 5$ m/s. The momentum difference in counter-flow offers promising results for active flow control applications, and they can be used in combination with traditional co-flow DBD actuators.

A non-dimensional flow separation criteria M* is proposed as the ratio of DBD jet momentum to integrated boundary layer momentum at the height of the DBD forcing region. Since the onset of separation depends on the boundary layer momentum, the nature of the boundary, and DBD jet momentum properties (strength, angle, height of injection), the exact determination of critical value for M* is challenging. Phenomenologically, we proposed that the separation occurs when momentum in the DBD jet and the boundary layer are similar. In our experiments, threshold values were M* ~ 0.07 at U_∞ = 11 m/s and M* ~ 0.14 at U_∞ = 5 m/s. Consequently, the critical value of M* ~ 0.1 proposed in this study represents the ratio necessary for separation for a specific range of boundary layer shape factors in this study (1.1 – 1.3). However, further experiments with different boundary layer shape factors are necessary to establish the evolution of the critical M*. The finding related to modifications of fluid boundary layer profiles due to EHD forcing can be generalized using non-dimensional analysis. This experimental data set can be used to develop models and validate multiphysics simulations for EHD flow. This work highlights the need for future research efforts that should focus on understanding the relationship between the unsteady forcing of the DBD and the turbulent characteristics of the external flow. The time-dependent interaction between the DBD cycle and the force acting on the fluid can be examined by a combination of flow vitalization and time-resolved optical plasma emissions and electrical measurements. Furthermore, the fundamental work in the DBD research should be considered in the context of EHD interaction with practical systems.

To expand on this research effort, future efforts should extend the understanding of the relationship between the unsteady forcing of the DBD and the turbulent characteristics of the external flow. To do so, future efforts should explore the unsteady fluid interactions of the DBD jet and a co- and counter-flow with classical turbulence tools such as hot wire anemometry or more novel techniques like time-resolved particle imaging velocimetry (PIV) or laser-doppler anemometry (LDA). These power techniques require tracer particles, which risk being influenced by the electric field. However, previous and recent works have identified appropriate tracer particles for EHD-driven flows, including TiO_2 and DEHS [131-133]. Similar work can also explore DBD behavior at more robust flow conditions, such as at higher speeds or with a more robust DBD actuator with thicker dielectrics and higher voltages.

Chapter 6. DC-Augmented DBD Plasma Actuator

This section explores a DC-Augmented DBD plasma actuator in quiescent condition. DC-augmentation, or DCA, is one of the promising approaches to significantly enhance or modify the EHD force produced by a traditional DBD actuator by introducing a DV DC third electrode downstream. Combined, the DBD system with an air-exposed DC-third electrode is called a DCA-DBD, and the DCA can be biased using either positive or negative polarity to preferentially positive- or negative-charged species, serving as a probe into the behavior of the forcing mechanism. Previous works, including that of Moreau *et al.* [110], have noted some of the behavior of DCA-DBD and the overall goal is to augment the EHD forcing. However, the thrust enhancement and reverse DBD forcing mechanisms remained unclear. Since the coupling of the AC E-field, space and surface charges, and fluid dynamics is highly non-linear, the DCA can affect several aspects of the system, and understanding these effects requires multiple lines of evidence.

Unlike the corona discharge, elucidating the time-dependent plasma–flow interaction in DBD is more challenging. Several works, such as Benard *et al [66]*, Debien *et al* [63, 64], Neumann *et al* [134], and Herner *et al* [135] have probed the underlying unsteady forcing mechanisms of DBD pointing to the differences between the streamer and glow discharge regime. The experimental observations by Benard and Moreau suggest a push-push forcing mechanism for two different regions, with the glow discharge producing greater forcing than the streamer discharge cycle [20]. The unsteady actuation has been correlated to the surface and space charges that fluctuate with the discharge cycles [85, 136, 137]. Sato *et al* [85] and Cristofolini *et al* [83] demonstrated with a two-electrode DBD that increased EHD force is associated with greater downstream surface potential as it reflects enhanced ion acceleration; however, surface charge neutralization after each discharge cycle is necessary for subsequential discharge cycles. Fan et al [39] recently found surface charge extension in a three-electrode DBD. However, the study used an atypical $Bi_{12}SiO_{20}$ crystal as the dielectric barrier and did not explore the plasma-fluid interactions, especially at higher forcing.

Here, we investigate the forcing mechanisms of a three-electrode DCA-DBD with an asymmetric AC electrode pair and a third HV DCA electrode, which is biased with either polarity to preferentially interact with the positive or negative half-cycle. This method improves the horizontal thrust by greater than two-fold and serves as a probe into the time-dependent plasma/ flow interactions. While previous works have characterized the mechanical properties of three-electrode DBD systems. As the underlying temporal mechanisms of the augmentation remain primarily speculative, this work provides multiple lines of evidence through electrical, time-resolved optical, and time-resolved surface charge interaction.

One of the unclear yet underlying mechanisms for DCA is electron interactions, including electron bombardment and secondary ionization, which are often not discussed in active flow control. While some numerical works have pointed out the importance of different charged species, most refer to all positive and negative species as two general groups. However, when charged particles are selectively accelerating, discussing the various pathways and interactions between electrons and neutral air molecules that can drive the momentum transfer in a DCA system is essential. DBD first creates ions through the ionization of neutral air consisting primarily of N_2, O_2, and other trace elements. Since N_2 is the most abundant in the air, many works, including Kozlov *et al.* [123], focus on the nitrogen species and the various nitrogen species pathways. Through primary and secondary ionization, Kozlov *et al.* [123] found that the resulting nitrogen species in atmospheric air DBD include N_2^+, NO, NO_2^-, HNO_3, NO^{-}_{3}, and H_2N_2. The oxygen and nitrogen species are also further explored in Kovacevic *et al.* [124], where H_2O_2, O_3, NO_3^-, and NO_2^- were found to depend on moisture content in the air. Kovacevic *et al.* [124] highlights that the resulting equilibrium of ions is heavily dependent on moisture content in air. In a DCA system, the positively biased DC third electrode is expected to selectively accelerate electrons and negative species such as the $NO2^{-}$, which may create more negative electrons. However, as the polarity of the DBD potential changes, other ions, such as positive N_2^+ may also be selectively accelerated or decelerated. While these complex time-dependent interactions will differ for each species and are difficult to resolve due to time scales, the presented DCA-DBD work aims to better our understanding of these interactions.

6.1 Experimental Setup

The experimental setup of the DCA-DBD is presented in Figure 6.1. The DBD electrode pair consists of the primary DBD electrode pair, separated by the dielectric layer, a 3.15 mm quartz plate with 99.995% SiO_2 purity. The downstream length of the air-exposed electrode is 15 mm, and the encapsulated electrode is 25 mm. The edges of the electrodes are aligned. The encapsulated electrode is grounded and covered by thick polyimide (Kapton) and silicone rubber tape (~6.3 mm) to prevent backside discharge. The third air-exposed electrode is located 50 mm downstream of the first electrode. The DCA-DBD experiments primarily use the horizontal and vertical force experimental setup, current monitors on the two air-exposed electrodes, the custom high-voltage power supply, the Trek 40/15 high-voltage amplifier, and the high-speed Phantom V12.1 camera coupled to the SIL3 UV intensifier, and a surface potential probe. Thrust, velocity, and current measurements are normalized by the actuator's spanwise width of 110 mm.

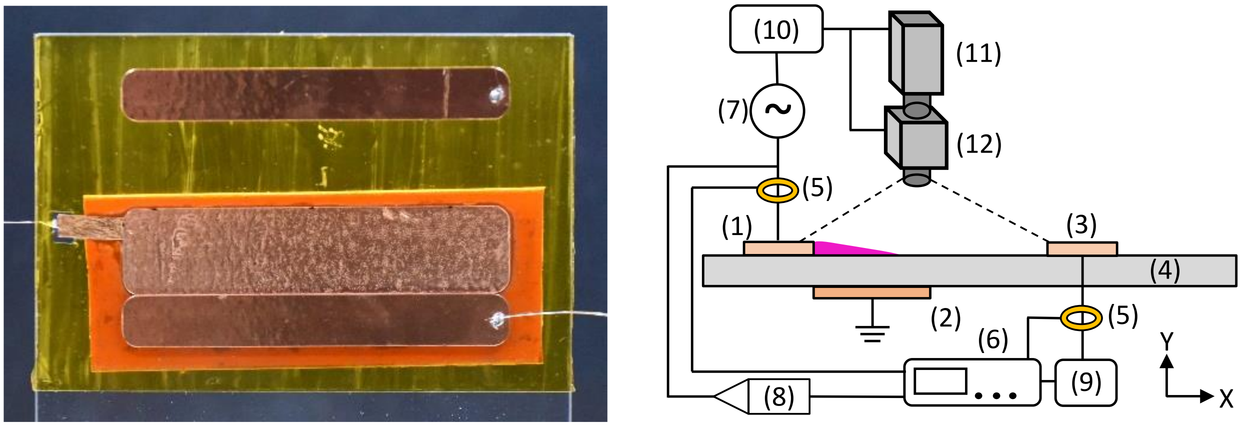

Figure 6.1.(a) The three-electrode DCA-DBD Plasma actuator has a 3.15 mm thick quartz dielectric barrier. The embedded electrode is covered with thick polyimide tape and silicone rubber. (b) The experimental schematic of the DCA-DBD actuator comprised of (1) an air-exposed electrode, (2) a grounded embedded electrode, (3) an air-exposed third electrode, and (4) a dielectric barrier. The current through the DBD electrode pair and the third electrode is measured with (5) a non-intrusive current monitor and (6) an oscilloscope. The DBD electrodes are powered by (7) a custom power supply with (8) a Trek P6015A HV probe. The third electrode is powered by (9) a Trek 40/15 HV amplifier with a function generator. The custom power supply is controlled with (10) a function generator. The function generator of the custom power supply also controls the trigger outputs to the CCD camera (11) and the UV intensifier (12).

The DBD electrodes are connected to the custom dual-hot HV power supply comprised of a function generator (Siglent SDG1032X), a power amplifier (Crown XLi3500), and two custom transformers (Corona Magnetics, Inc). The AC frequency is set constant, f = 2 kHz. For this study, the encapsulated electrode is grounded; thus only one of the two transformers is used. Note that our tests have not seen any difference in electromechanical results when the DBD is powered by a single transformer with ground versus two transformers for matching $V_{P\text{-}P}$. The AC frequency of the DBD is set at f = 2 kHz. The voltage output is monitored using a Tektronix 6015A HV probe. The DCA electrode is powered by a Trek 40/15 HV amplifier connected to a separate signal generator (Siglent SDG1032X); the V_{DCA} voltage was varied in the - 24 to + 24 kV range.

The mechanical and velocity measurements are completed with the previously outlined pitot tube system with a custom glass pitot tube with 0.6 mm OD and 0.4 mm ID connected to an Ashcroft CXLdp differential pressure transmitter (P = 0 to ±25 Pa, 0.25% accuracy). Velocity measurements were not taken inside the plasma region. The expressions to derive the mass flow, momentum, mechanical power, and total efficiency of the DBD in quiescent conditions are outlined in Chapter 4. The mathematical expressions are found in eq. ((4) through eq. (7). The typical velocity measurements had a standard deviation of < 0.02 ms-1 when averaged over 20 s. The thrust was measured directly using a battery-powered, electrically insulated analytical balance (Ohaus SPX223), similar to other works that measure EHD thrust. Velocity measurements were not taken inside the plasma region. The typical velocity measurements had a standard deviation of < 0.02 ms-1 when averaged over 20 s.

The DBD and DCA electrode currents are characterized using two non-intrusive high-bandwidth coil current monitors (Pearson 2877 with 2 ns rise time). The monitor is connected to a Tektronix DPO7254C oscilloscope (500 MHz bandwidth). At least 20 voltage cycles were recorded at 1 GS/s, and the total discharge current was obtained by filtering out the capacitive current using a fast-Fourier transform (FFT) analysis [12]. The standard deviation of discharge current measurements for 20 consecutive cycles was < 4% for all tested conditions. With the voltage of the electrodes measured by the Tektronix 6015A HV probe and the HV monitor of the Trek 40/15 HV amplifier, the total power used by the electrodes can be calculated using eq. (2) with the recorded voltage and current. All power measurements were averaged over ~ 20 consecutive voltage cycles with a standard deviation of <4%.

The surface potential is measured with a 3 mm x 10 mm wide copper electrode probe flush-mounted to the backside of the dielectric and connected to a Tektronix P6015A high voltage probe, similar to Leonov *et al.* [138]. A top view of the experimental schematic with the surface charge probe is provided in the supplemental information (Figure B.1). The probe is mounted at x = 27 mm immediately after the embedded electrode. The probe's 75 MHz bandwidth allows for temporal resolution on the AC voltage time scale (milliseconds) but not individual discharges that take place closer to the active electrode edge at the nanosecond scale [59]. The overall surface potential combines the HV AC electric field, the capacitive voltage between the air / dielectric, and the buildup of surface charges. Similar to previous works, the electric field and capacitive voltage contribution are determined by measuring the probe potential at lower applied voltages (< 10 kV) before plasma ignition [139, 140]. The thrust and electrical current measurements confirm that the surface charge probe did not affect the DBD actuator performance.

Phase-resolved optical plasma emissions are captured with a high-speed CCD camera (Phantom V12.1) equipped with a 200 – 550 nm UV intensifier lens (Specialized Imaging SIL3). The DBD emissions in atmospheric air include a positive streamer discharge and a negative glow discharge. The streamer discharge produces light emissions primarily from generating positively charged nitrogen and oxygen ions in the wavelength range of 300 – 450 nm [123, 124]. The negative ions from the glow discharge are generated through multiple processes, including secondary discharge and electron reattachment over the same wavelength range [123, 124]. The CCD shutter is synchronized with the voltage cycle and divided into four quadrants denoted as T1 – T4 (Figure 3.6). For f = 2 kHz, the CCD and intensifier trigger were set to 8 kHz with a CCD shutter of 124 μs and intensifier shutter of 110 μs. The CCD starts to capture images two seconds after the voltage is turned on to ensure a steady state; approximately 10,000 images are captured. Previous works such as Krigseis *et al.* [57] and Uchida *et al.* [58] analyzed steady-state plasma light emission strength for two-electrode DBD actuators. Time-resolved plasma images of a two-electrode DBD have been presented in works including Debien *et al.* [64] and Enloe *et al.* [141], however, no studies have investigated the time-resolved plasma morphology in a DCA three-electrode DBD system. Recently, Peng *et al.* [142] studied the changes in plasma morphology and surface charge in a three-electrode DBD; however, the study uses a nano-pulsed DBD that generates a thermal shockwave instead of the steady-forcing sinusoidal DBD and does not investigate the fluid interactions.

6.2 Vertical and Horizontal Thrust Characteristics of DCA-DBD

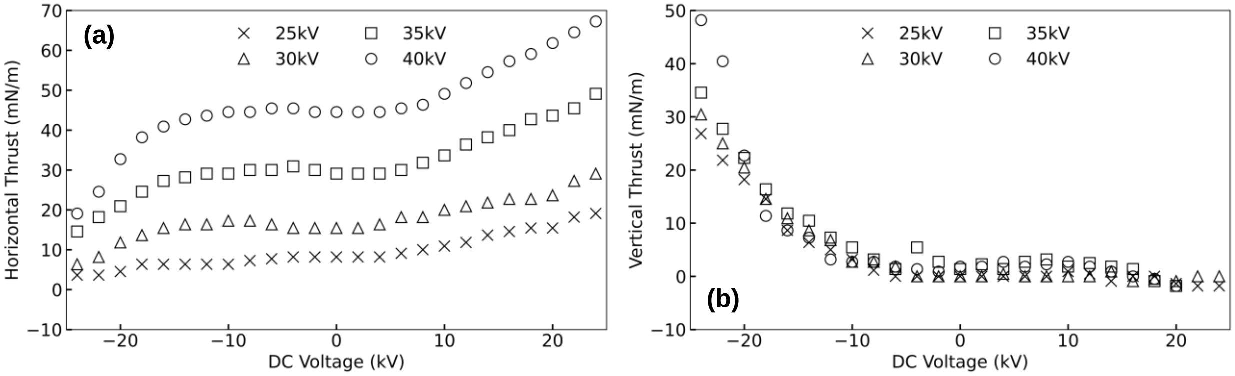

Figure 6.2(a) Horizontal and (b) vertical thrust of the DBD-DCA actuator, f=2kHz, AC voltage is varied 25 kV < VAC < 40kV; DCA voltage –24 kV < VDCA < +24 kV.

Figure 6.2 shows that the thrust increases with applied AC voltage, which generates more charged species and stronger electrical fields, leading to higher EHD forcing. These effects are well documented in corona-driven flows [27] and DBD systems [20, 24]. More interesting is the effect of the DCA potential, as it sheds insight into the thrust generation mechanism. Positive DCA bias leads to a monotonic increase in the strength of the EHD wall jet. At the highest tested AC potential condition (V_{AC} = 40 kV), the horizontal thrust increased from 45 mN/m to 67 mN/m at V_{DCA} = +24 kV (+51%). For less energetic ionization V_{AC} = 25 kV, the thrust increases from 8.2 mN/m to 19.1 mN/m (+133%). These gains could be potentially explained as follows: (i) thrust is enhanced by the net acceleration of negatively charged species during the negative going cycle; (ii) the wall jet defection from the viscous boundary layer due to accumulation of positive charges on the dielectric leading to lower viscosity losses.

A negative DCA potential had only a moderate trust increase at the low DCA voltages, followed by a significant drop at V_{DCA} ~ - 15 kV. The slight increase can be explained by an acceleration of positive species during the positive-going discharge; however, it is likely being countered by wall jet attraction into the viscous boundary layer due to negatively charged dielectric. The drop in the streamwise thrust corresponds to the increase in wall-normal force, suggesting that the EHD wall jet is deflected from the streamwise direction to the wall-normal direction. These trends are further investigated by taking velocity profiles and correlation with electrical and optical measurements.

6.3 Velocity Characteristics of DCA-DBD

The reconstructed 2D velocity contours in Figure 6.3 show the EHD jet at V_{AC} = 35 kV and varied V_{DCA} = 0 kV, –24 kV, and +24 kV. The velocity flow field was constructed by spanning the x-velocity measurements in the region between the air-exposed electrodes with a 1 mm x- and y-resolution.

Figure 6.3(b) shows that a reverse EHD jet is formed at the third electrode in the negative DCA case. Colliding the primary and reverse jets results in the wall-normal flow and the vertical reaction force (Figure 6.2.b). These wall-normal synthetic jets have been reported in the planar symmetric 3-electrode systems and axisymmetric DBD actuators [110, 143]. Integration of the velocity profiles at x = 15 mm, before deflection, shows a 28% increase in x-momentum over the unbiased case. This supports the observation of a slight rise in the horizontal thrust at the low values of negative DCA (Figure 6.2.a).

For the positive DCA scenario, at V_{DCA} = +24 kV, the maximum velocity, V_{max} = 5.3 m/s, is slightly higher than that of the unbiased case, V_{max} = 5.0 m/s. However, the direct thrust measurements show significantly higher thrust (+68%), consistent with a higher wall jet thickness (Figure B.2). The velocity-derived thrust from profile integration closely agrees with the direct thrust measurements (Table B.1). These results suggest that one of the factors responsible for stronger forcing is the repulsion of downstream ions and the EHD jet by the positive DCA, leading to lower wall shear stress. However, the gains in the thrust could not be attributed to only viscous effects, which typically account for <30% reduction in EHD wall jet momentum [67, 133]. The enhancement must also come from the additional momentum transfer mechanism between the negatively charged species and the bulk fluid.

One significant difference in the velocity profiles between an unbiased, negative, and positive DCA-DBD is the jet thickness and the location of the velocity peak. Interactions of positive ions with neutral molecules are primarily localized to the visible plasma region [123, 124]. Thus, as expected, the peak velocity in the unbiased case is located at the edge of the visible plasma region, e.g., x= 10 mm in Figure 6.3(a) and (b). In contrast, in positive DCA (Figure 6.3.c), the flow continues to accelerate with the maximum velocity location at x ~ 15 mm, indicating an additional pull on either the positive or negative ions. While typically positive DBD discharge is greater than negative discharge, Moreau *et al*. [110] suggested that there could be a significant contribution in forcing due to an acceleration of negative discharge during the negative half-cycle despite the repulsion of the positive discharge.

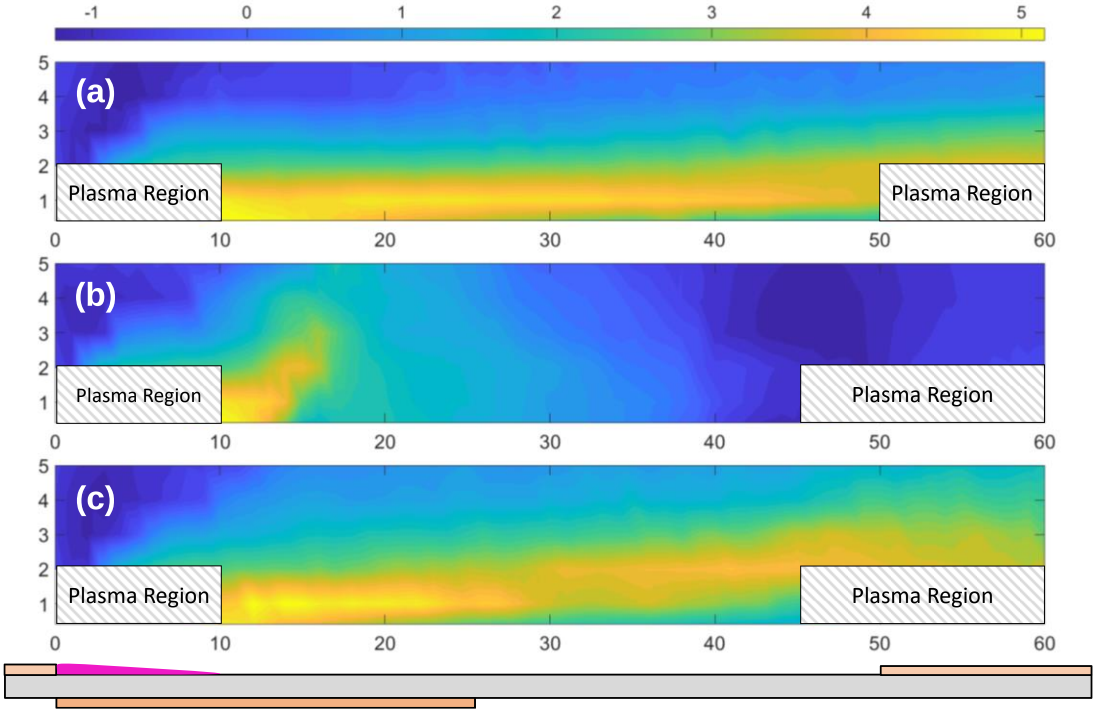

Figure 6.3. X-velocity contour plot at V_{AC} = 35 kV with (a) V_{DCA}= 0 kV, (b) V_{DCA}= – 24 kV, and (c) V_{DCA}= +24 kV. Grayed-out regions exhibit potential discharge; the data in these regions were not taken. The electrode positions are displayed.

6.4 Mechanisms of DCA-DBD

It is clear that the DCA affects the momentum transfer in the DBD system, and these interactions are different in the positive and negative DCA. The proposed mechanisms and the evidence for those are described below.

6.4.1 Negative DCA

The negative DCA shows only a moderate thrust increase, followed by a significant drop at V_{DCA}~ - 15 kV. The slight increase is likely due to a *field-augmented acceleration (FAA) of positive ions* produced in the positive going cycle enabled by the stronger E-field from negatively biased DCA. However, this action is limited due to the onset of streamer formation on the third electrode, leading to the sliding discharge and the onset counterflow. The drop in the streamwise thrust corresponds to the increase in wall-normal force, suggesting that the primary EHD wall jet is deflected from the streamwise to the wall-normal direction (Figure 6.2b).

6.4.2 Positive DCA

The effectiveness of the positive DCA is linked to two possible mechanisms: (i) field-augmented acceleration with electron (impact) ionization and (ii) oscillating residual charge interaction.

Field-Augmented Acceleration with Electron Ionization (FAA-EI): Negative ions and electrons are generated by dissociative reactions of neutral diatomic oxygen and nitrogen [144, 145]. Free electrons can provide momentum transfer to neutral molecules or can be utilized to negatively charge the neutral molecule via electron ionization (EI), also referred to as electron impact ionization or electron bombardment ionization [146]. The negative ion produced by EI and in the plasma region (having sufficient mass) can more effectively interact with bulk gas in the highly biased DCA-DBD system. The EI efficacy increases for faster-moving electrons and with an increase in electron density [20, 147]. Both are consistent with the increasing E-field in the positive DCA cases. The strong x-direction potential gradient focuses electrons trajectories in the streamwise direction, enhancing the ionization at higher positive V_{DCA}, in contrast to their diffusion-like motion (to infinite ground) without DCA. Thus, we propose that the FFA-EI mechanism increases momentum injection by accelerating negative ions through their attraction to the positive DCA electrode in the negative going DBD cycle.

Oscillating residual charge (ORC) is an extension of ions and surface charge in the streamwise direction that can accelerate opposite charge species in the subsequent half cycle. The shift in the max velocity location (Figure B.2.c) can result from the additional pull on either the positive or negative ions from a residual surface charge generated in the previous half-cycle. In this "bootstrapping" scenario, the positive DCA bias forces the negative species to travel closer to the third electrode during the negative-going half-cycle, providing an additional attraction for positive ions in the following half-cycle. Since this behavior repeats each AC cycle, it is referred to here as the *oscillating residual charge* mechanism.

Further examination of the discharge's electrical, optical, and surface potential provides additional insight into the *FAA-EI* and *ORC* mechanisms.

6.5 Electrical Characteristics of DCA-DBD

Electrical and optical characterization of the discharge provides additional insight into the multiphysics interactions between the space and surface charges and the oscillating electrical field. Figure 6.4 shows the time-resolved DBD and the DCA electrode currents measured using the non-intrusive high-bandwidth coil current monitor.

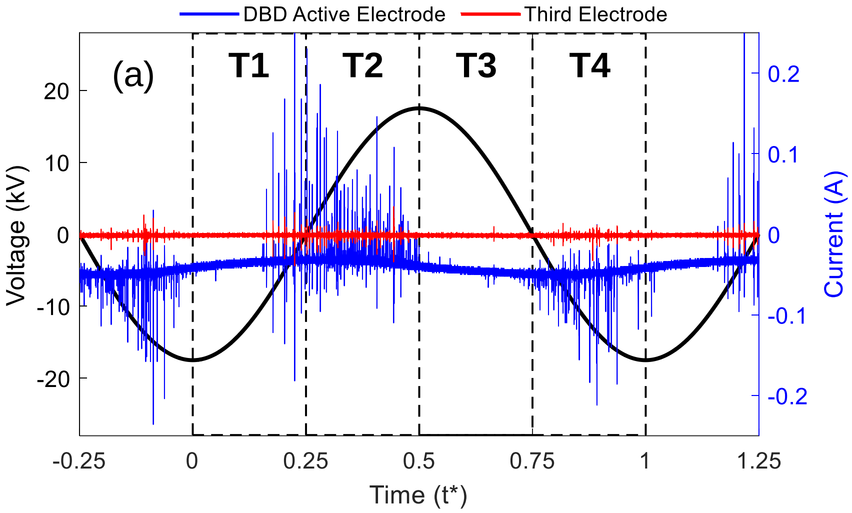

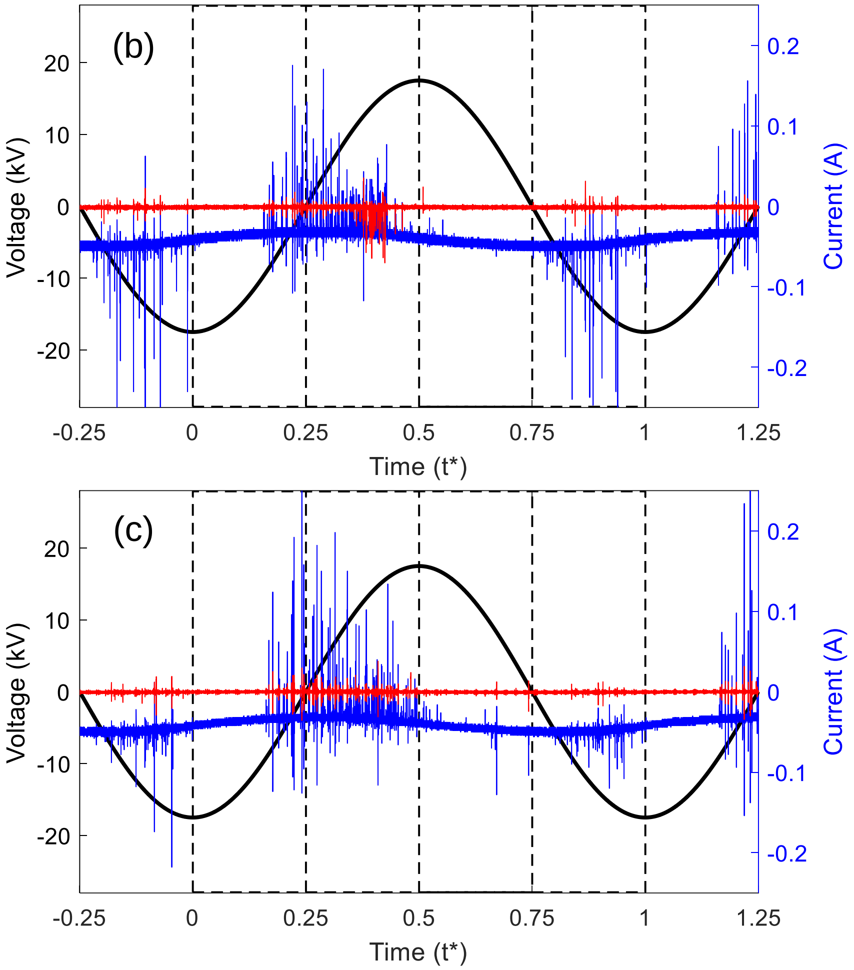

Figure 6.4. Trigger frames (dashed lines) superimposed with current on DBD active electrode (blue) and DCA electrode (red), VAC = 35 kV, f = 2kHz; (a) VDCA = 0 kV,(b) VDCA = –24 kV, and (c) VDCA = +24 kV. The t* is the period normalized time.

The discharge current characteristics on the DBD electrode match previous literature well and show a streamer discharge current during the voltage-rising half-cycle and a glow discharge current during the voltage-falling half-cycle [12, 20]. Unlike the AC-powered DBD electrodes, the DCA third electrode does not experience a significant capacitive current, and thus, the total power usage is significantly smaller. The DBD electrode's total power remained approximately constant at ~130 W regardless of the DCA polarity or potential. For the DCA electrode, the total power outside sliding discharge (V_{DCA} > - 15 kV) region increased linearly with voltage up to a maximum of 40 W. In the sliding discharge cases ($V_{DCA} < -15$ kV), the power increased significantly up to ~ 180 W at $V_{DCA} = -24$ kV due to the reverse discharge (Figure 6.4 .b).

6.6 Surface Potential

Figure 6.5 shows the surface potential over several cycles at $V_{AC} = 30$ kV cases. At the downstream stream location of x = 27 mm, the visible plasma discharge does not extend to the surface probe, allowing the measurement of the mean potential associated with the accumulated surface charges. The surface potential (red line vs blue dash line) oscillates nearly in phase with the applied V_{ACA}. For the $V_{DCA} = 0$ kV case, which is most analogous to a two-electrode DBD, the mean surface potential at x = 27 mm is ~500 V. These results match previous literature well, including Opaits *et al.* [139] and Enloe *et al*. [140]. Opaits *et al.* [139] reported a mean surface potential of ~500 V using a commercial non-contact electrostatic voltmeter probe at x = 25 mm downstream of a two-electrode DBD, while Enloe *et al*. [140] reported a mean surface potential of ~ 1,500 V at x = 9.75 mm using a similar custom surface potential probe. When a negative DCA is applied, the mean surface potential decreases to a minimum of -300 V at $V_{DCA} = -20$ kV (– 800 V from the non-biased case). With positive DCA, the surface potential increases by a similar margin at $V_{DCA} = +20$ kV; however, the maximum change occurs at $V_{DCA} = +24$ kV with an average surface charge of 1700 V. The mean surface potential over the range of V_{DCA} is presented in Figure 6.6. In all experiments, no significant change in phase shift was observed.

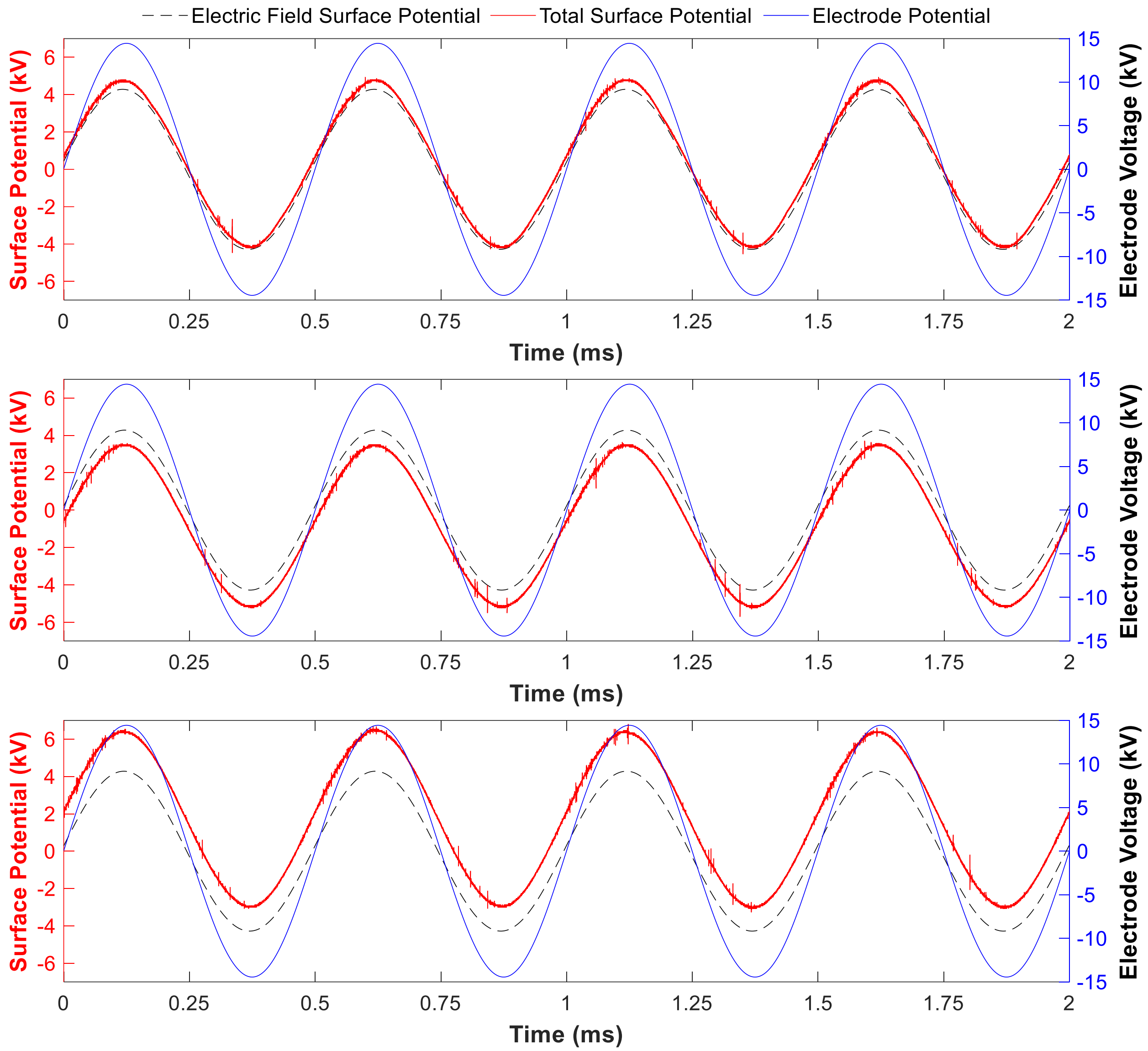

Figure 6.5. Surface potential measurements (red) at x = 27 mm superimposed with the surface potential due to the electric field and capacitive potential (dashed lines) and the potential applied to the DBD active electrode (blue). V_{AC} = 30 kV, f = 2 kHz at (a) V_{DCA} = 0 kV , (b) V_{DCA} = –20 kV, (c) V_{DCA} = + 24 kV.

While the oscillating surface potential is primarily due to the system's sinusoidal electric field and capacitive voltage, Figure 6.6(b) illustrates that a positive DCA increases the surface potential oscillation at a fixed downstream location, providing evidence for the oscillating residual charge interaction. With a positive DCA, the surface potential amplitude increased from ~ 4.30 kV at V_{DCA} = 0 kV to ~ 4.65 kV (~ 8% increase) at V_{DCA} = +24 kV. The downstream charge extension induces the additional surface potential, and the residual space and surface charge of opposite polarity promote the further acceleration of both the negative and positive species across the DBD voltage cycle. In return, the acceleration and generation of negative ions due to the positive downstream potential generates an electric field that promotes a net acceleration of positive ions. This effect is akin to ambipolar diffusion in quasi-neutral plasmas [148]. In this case, transport of one charged particle or ions may be expected to be greater than its oppositely charged counterparts; however, due to the change in charge density, the electric field is modified such that both charged species transport become nearly equal and the plasma remains quasi-neutral [149]. This work is the first to suggest ambipolar diffusion in atmospheric DBD, and future experiments with more extensive surface charge measurement are necessary to provide more insight into the modified surface potential in these complex DBD systems.

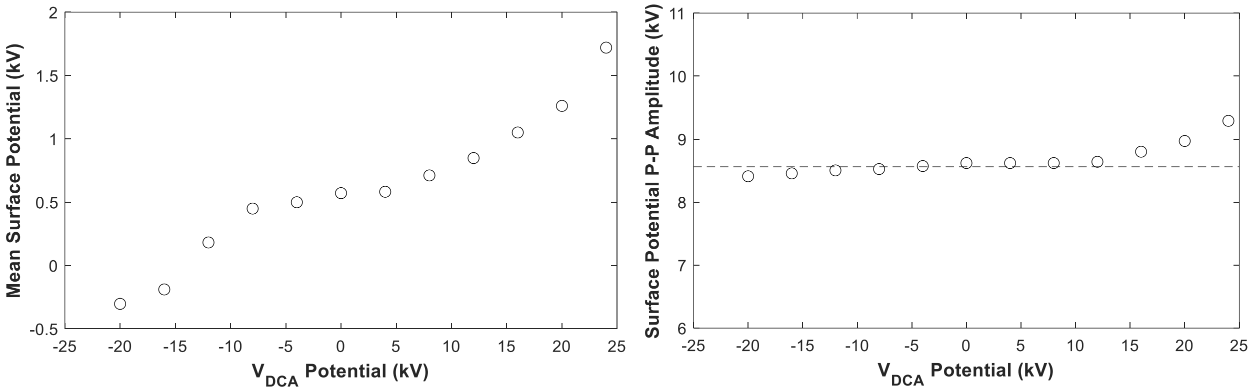

Figure 6.6(a) Mean surface potential at x = 27 mm downstream with varying VDCA potentials. The mean surface potential reflects the dielectric surface's steady accumulation of charged particles. (b) The peak-peak surface potential amplitude at x = 27 mm downstream with varying VDCA potentials. The surface potential increases with positive DCA relative to the peak-peak surface potential due to only the electrical field and capacitive potential (dashed lines).

6.7 Plasma Emission – Optical Characterization

Figure 6.7 shows phase-resolved optical plasma emissions from a high-speed CCD camera equipped with a 200 – 550 nm UV intensifier lens when the DBD at V_{AC} = 35 kV is powered with DCA = 0 kV, – 24 kV, and + 24 kV. The CCD shutter is synchronized with the voltage cycle, divided into four quadrants denoted as T1 – T4 (Figure 3.6).

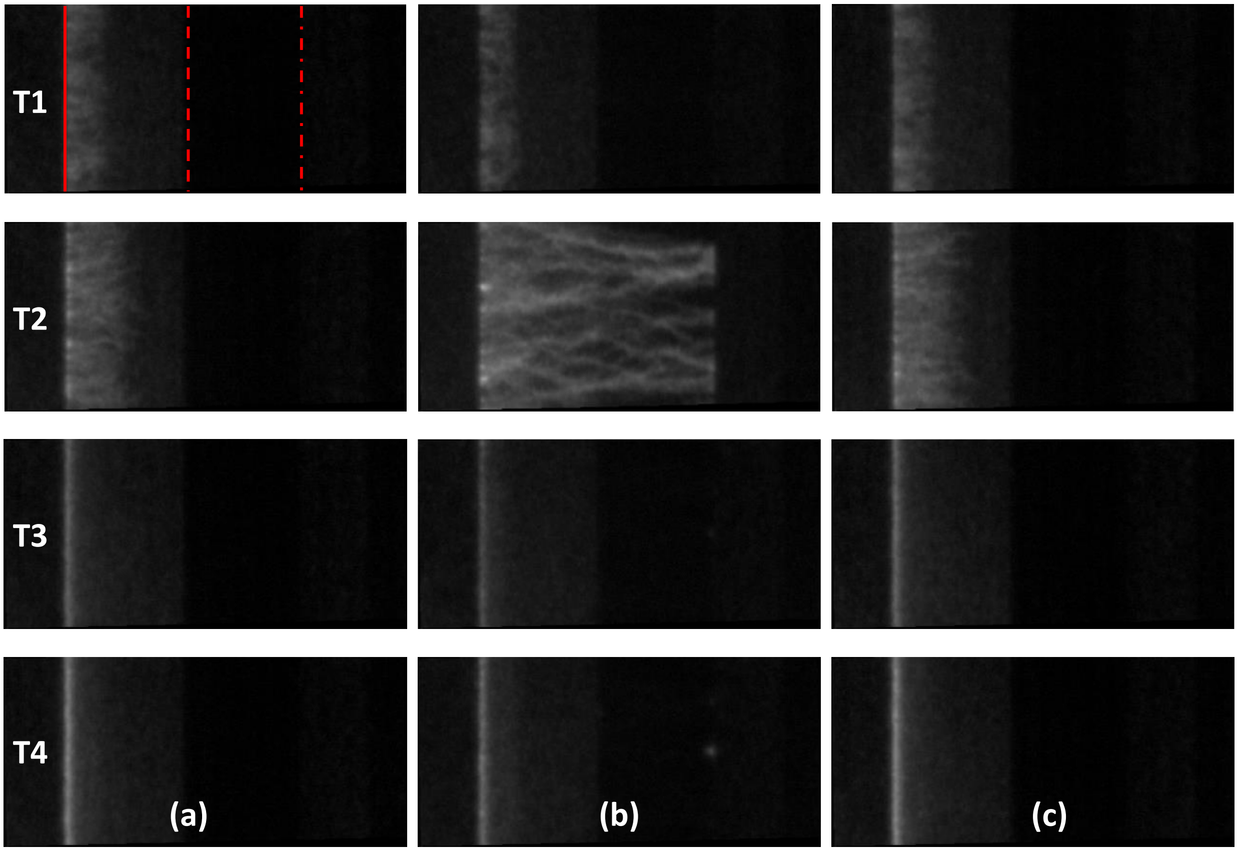

Figure 6.7. Phase-resolved plasma discharge images with DCA electrode; VAC = 35 kV, f = 2 kHz (a) VDCA = 0, (b) VDCA = –24 kV, (c) VDCA = +24 kV. T1 and T2 are positive-going cycles, showing a high concentration of positive ions; T3 and T4 are negative-going cycles, with low optical emission at the edge of the active electrode. The leading edge (–), embedded electrode edge (– –), and third electrode edge (–.–) are shown in the T1 phase of (a).

The positive discharge current, $I_{discharge}^{+}$, in the T1 and T2 regions, corresponds to electron emissions during the production of positive ions. This discharge mode is associated with the formation of streamers [65] (Figure 6.7). In the T3 and T4 regions, the negative discharge current ($I_{discharge^{-}}$) is associated with electrons leaving the air-exposed electrode, creating a glow discharge. For a flat plate DBD, the baseline DCA = 0 kV case matches previous high-speed CCD measurements from Debien *et al.* [64] well for the streamer discharge and glow discharge cycle. In line with the literature [20], the discharge current in the positive-half-cycle is typically higher, e.g., at V_{AC} = 40kV, the $I_{discharge^{+}}$ = 11.2 mA/m vs. $I_{discharge^{-}}$ = 3.65 mA/m, resulting in the overall abundance of positive charges in the system. A biased V_{DCA} electrode changes the electrical field strength, slightly influencing the discharge characteristics in the primary ionization zone. For example, for the V_{AC} = 40 kV, V_{DCA} = +24 kV case, the positive discharge current is suppressed by 9.4% and is 9.26% greater in the negative DCA case, V_{DCA} = –24 kV. This change is analogous to the positive corona discharge, where the higher field strength leads to higher plasma volume and charge density [26, 27]. Interestingly, the $I_{discharge^{-}}$ in the T3 and T4 quadrants is mainly unaffected by positive or negative V_{DCA} (0.02 mA/m change), which in turn suggests that the negative mode primary DBD discharge is not affected by DCA and interaction of electrons and negative ions with bulk fluid occur outside the primary ionization region by FAA-EI or OCRI mechanisms.

Under high negative DCA (V_{DCA} < –15 kV), the visible plasma discharge extends to the DCA electrode, resulting in the 'sliding' DBD (Figure 6.7b). A strong negative DCA repels negative species from the third electrode (Figure 6.3b) and accumulates on the dielectric, attracting positive species and allowing positive ions to easily ‘slide’ to the third electrode. The distribution of positive charges sliding over the negatively charged surface towards the negatively biased DCA electrode is shown in SI Figure 3 and is supported by negative surface charge measurements (Figure 6.6). The combination of positive sliding charges causes a negative discharge on the DCA electrode at a sufficiently high E-field, as shown in Figure 6.4b at t* ~ 0.4 in the T2 region. Time-resolved plasma emission images show that the sliding positive discharge streamers are present only in the T2 region of the cycle, i.e., during the strongest E-field.

Plasma emission analysis [150] across 10,000 consecutive images (2,500 discharge cycles) shows that all positive DCA cases and low negative DCA (VDCA > –15 kV) cases experienced an increase in the total plasma emissions across the T1 through T4 quadrants. Outside of sliding discharge, the DBD at a VDCA = +24 kV displayed an increase in total plasma emission by ~ 8% during the T2 phase (Figure 6.7.c) with a standard deviation of 2% across all images. During the start of the streamer discharge (T1) and glow discharge phases (T3 and T4), the positive DCA and low negative DCA show a 5% increase in plasma emissions with a similar 2% standard deviation across the 10,000 images captured per condition.

6.8 Discussion

The negative DCA shows a moderate thrust increase due to a *positive ion field-augmented acceleration mechanism*; however, it is limited by an onset of streamers on the DCA electrode. Integrating the discharge peaks on the DCA electrode (Figure 6.4) yields $I_{discharge,\ DCA^{-}}$=3.1 mA/m, indicating that negative species leave the DCA electrode to recombine with the positive streamers from primary DBD discharge. The negative species' motion creates a counter-flow EHD jet (Figure 6.3.b), which produces wall-normal thrust upon collision with the primary DBD jet, Figure 6.2(b). This negative DCA discharge to the positive space charge is analogous to a pulsed corona discharge or a DBD to the space charge. In weaker, negative potential DCA cases, the space charge is not sufficiently extended to trigger DCA discharge.

We observed a steady increase in horizontal thrust for all tested positive DCA conditions. Two complementary mechanisms are identified. (1) *Field-Augmented Acceleration with Electron Ionization* is enabled by the increased electron density and negative species vectorization in the streamwise direction. The negative ions driven by DCA experience greater downstream acceleration and, thus, higher momentum transfer to bulk fluid over non-biased DCA electrode cases. (2) *ORC* mechanism, in which an elongated positive surface potential enables further propagation of both negative and positive species towards the third electrode. Figure 6.7 (c, T2) and SI Figure 2 show that the visible discharge zone extends further downstream in positive DCA cases. Interestingly, this is despite the slight decrease in positive discharge current from the air-exposed active electrode, supporting that the acceleration of negative species can create a net acceleration of positive ions similar to ambipolar diffusion, where space charge interacts with the species of opposite polarity [151, 152]. This is supported by a ~8% increase in plasma emission during streamer discharge (T1 and T2 quadrants) and an up to 5% increase in emission during glow discharge (T3 and T4 quadrants) when a positive DCA is applied. Since visible photon and plasma emissions primarily occur during ion/electron recombination and dissociation [124], the increase in emissions reflects more frequent electron-ion collisions and their interaction or over a greater distance. The collision frequency increase correlates to a decrease in the electron mean free path. The enhancement in mechanical performance due to the increased collision frequency is similarly supported by Sohbatzadeh *et al.* [69]. Complex multi-species numerical modeling is likely necessary to characterize the changes in charged species velocities.

6.9 Chapter Summary

In conclusion, this is the first report on the mechanisms of a DC-augmented DBD actuator. A slight increase in the thrust values for the moderate negative DCA is due to the field-augmented (positive) ion acceleration. A sufficiently strong E-field leads to the onset of the reverse flow at the DCA electrode, producing a deflected jet with wall-normal forcing. A positive DCA monotonically improves horizontal thrust by greater than two-fold over unbiased cases. A field-augmented acceleration with electron impact and oscillating residual charge interaction mechanisms are proposed.

Future work should focus on understanding the spatiotemporal interaction of electrons interaction with neutral molecules in the context of momentum transport or explore the relative contribution of the two proposed mechanisms through time-resolved force and velocity measurements. Extra precautions are necessary to avoid EMI and adverse charging of particles if tracer particles are introduced into a DCA system. Spatio-temporal surface charge measurements can also be captured with high-speed CCD imaging and Pockel's effect; however, a $Bi_{12}SiO_{20}$ (BSO) crystal as the dielectric barrier is necessary. If future efforts do not want to use a BSO crystal to stay true to the traditional dielectrics, surface charge measurements at additional downstream positions may be able to elucidate the surface charge dynamics better. Time-resolved mass spectroscopy may also be able to help elucidate which ions specifically are accelerated or decelerated due to a DCA third electrode.

Chapter 7. AC-Augmented DBD Plasma Actuators

This section explores a three-electrode DBD with AC augmentation (ACA) and directly builds upon the previous section on DCA. In the DCA-DBD arrangement, the DBD electrode pair ionizes the gas, and the third electrode accelerates positive or negative species, promoting their interaction with neutral molecules. Negative DCA electrode bias led to modest improvements before the onset of sliding discharge and a counter jet at the DCA electrode, canceling the gains from positive ion acceleration. These opposing wall jets collide, creating a wall-normal thrust [109]. In contrast, in some cases, a positive DCA bias monotonically increased thrust by more than twofold. An oscillating residual charge interaction mechanism was identified to explain the increase in horizontal thrust, in which the acceleration of positive ions is augmented by the attraction from the residual (negative) charge. While the results of the DCA-DBD are promising, their practical implementation requires AC and DC power supplies and is challenging for large-scale DBD arrays. Additionally, a primary motivation for understanding the influence of an ACA-DBD is its similarity to DBD arrays, which use multiple HV AC electrodes for numerous stages of DBD.

The E-field augmentation by an AC electrode can be more robust as it can utilize both E-field magnitude and phase shift control. Previous research described DBD arrays implementing several AC electrodes in series [20]. DBD arrays increase the total thrust; however, the subsequential exposed electrode can produce a counter wall jet (sometimes called a cross-talk phenomenon), limiting the overall system's efficiency [115]. In one of the earliest attempts to minimize DBD cross-talk, Benard *et al.* [117] proposed an array of three-electrode DBD actuators with two embedded electrodes. Later works found that alternating AC and ground electrodes reduced the cross-talk and continuously accelerated EHD flow. Debien *et al.* [64] reported the EHD jet velocities up to ~ 10.5 m/s with a four-stage DBD array. Their wire-to-planar DBD had better results than the array reported by Benard *et al.* [117]. Sato *et al.* [118] studied multi-stage DBD-driven flow at low AC voltages. Their DBD configuration with alternative HV-ground electrodes was similar to Debien et al. [64]; however, the system used a nanosecond pulsed (NP) DC waveform.

This section investigates AC-augmented (ACA) DBD actuators and outlines the optimization strategy for maximizing horizontal trust. We utilize time-resolved electrical and optical measurements to optimize DBD performance as a function of electrical parameters, such as AC voltage, phase shift, and spacing. Time-resolved electrical and plasma discharge characteristics relate to time-averaged thrust and wall jet measurements, providing insights into the complex dynamics of ACA-DBD systems [15].

7.1 Experimental Setup

Overall, the ACA-DBD experimental study is similar to the DCA-DBD work outlined in Chapter 6. However, some experimental approaches differ from the DCA-DBD work because HV AC powers the third electrode. The experimental setup is shown in Figure 7.1.

The three electrodes are identified as the DBD active electrode, the DBD embedded electrode, and the third or AC-augmented electrode. The discharge is generated with a high-voltage AC signal between the active and embedded electrodes. A 3.175 mm quartz plate separates the active and embedded electrodes. The active electrode (0.07 mm thick, 15 mm long, and 110 mm wide) is flush-mounting copper tape to the top of the dielectric surface. The embedded electrode (0.07 mm thick, 25 mm long, and 110 mm wide) is a copper tape flush mounted to the backside of the dielectric surface. The embedded electrode is encapsulated with a thick 1 mm Kapton layer (~7700 VPM @ 25°C) and silicone rubber tape (3.175 mm) to ensure no backside discharge. There is no overlap between the active and embedded electrodes. The ACA electrode is made of copper tape (0.07 mm thick, 15 mm long, and 110 mm wide) and is mounted downstream of the active electrode on the air-exposed side. For this study, the gap (L) was set at 10 mm and 25 mm. All tests were conducted in quiescent atmospheric air, T ~ 18-23 ºC, with relative humidity (RH) of ~30-50%.

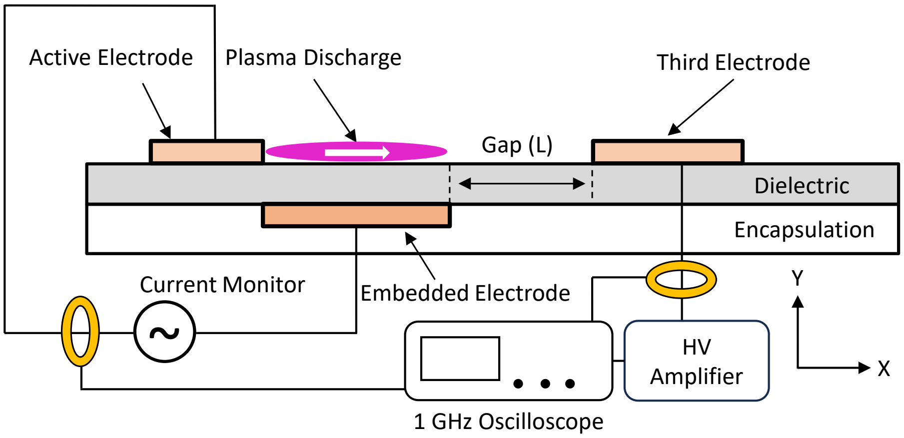

Figure 7.1 The ACA-DBD Experimental setup. The active and third electrodes are flush-mounted onto quartz dielectric. The embedded electrode is mounted on the back side of the dielectric layer and encapsulated with polyimide and silicone rubber layers. The active and embedded electrodes are connected to a custom power supply, while a Trek 40/15 HV amplifier powers the third electrode. The current is measured with a Pearson 2877 probe and a Tektronix DPO 7254C oscilloscope

The active and embedded electrodes are connected to the custom dual hot high-voltage power supply similar to that of Thomas *et al.* [99]. Briefly, the custom power supply comprises a Siglent SDG1032X signal generator, a Crown XLi 3500 power amplifier, and two custom high-voltage transformers (Corona Magnetics) rated up to 35 kV peak-to-peak voltage (V_{pp}) each. The secondary winding of each transformer are set out-of-phase from the other to reach up to V_{pp} = 70 kV between the electrodes. All tests in this study use a fixed 2 kHz sine wave with voltage across the active and embedded electrode between 25 to 40 kV peak-to-peak. The output voltage applied to the active electrode is monitored with a Tektronix P6015A high-voltage probe. The ACA electrode is connected to a Trek 40/15 high-voltage amplifier (0 to ± 40 kV peak voltage) and is excited with a 2 kHz AC sine wave with varying voltage and phase offset. The signal generator (Siglent SDG1032X) controls the input to the custom power supply and the Trek amplifier. The voltage to the ACA electrode is monitored directly from an output on the Trek amplifier. The voltage across the active and embedded electrodes will be referred to as $V_{DBD,}$ while the augmenting voltage applied to the third electrode will be referred to as V_{ACA}. The third electrode phase shift (Φ) is set relative to the active air-exposed DBD electrode, see Figure 7.2.

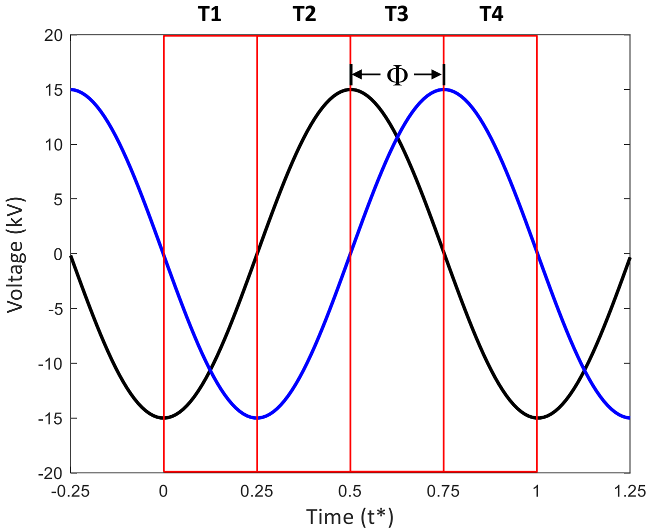

Figure 7.2. T1 - T4 quadrants of phase-resolved CCD imaging defined relative to VDBD. The VACA (blue) is phase-shifted by Φ from VDBD (black). The T1 and T2 quadrants capture discharges on the voltage-rising cycle associated with streamer discharge, while the T3 and T4 quadrants capture discharges on the voltage-falling cycle associated with glow discharge.

For this study, the ACA-DBD system is primarily characterized by its electrical discharge characteristics, power consumption, wall jet profiles, thrust characteristics, and time-integrated and time-resolved plasma characteristics. The total electrical power is computed identically to the DCA-DBD, using eq. (2), with the voltage and current measured with a Pearson 2877 probe on the DBD electrodes and third electrode and a Tektronix DPO 7254C oscilloscope with 500 MHz bandwidth on each channel. The capacitive current was similarly identified through FFT analysis to identify the frequencies up to ~ 5 times the voltage frequency and are close to that of the expected capacitive current.

The mechanical performance is characterized almost identically to the DCA-DBD study. However, only horizontal thrust is measured since a counter-jet is not produced. The direct thrust is measured by vertically holding the plasma actuator system onto an analytical balance. In this configuration, plasma-induced flow is directed away from the balance, and the balance measures the reactive downward thrust. An analytical balance (Ohaus SPX223) was used with a Faraday cage. To measure the time-averaged x-velocity profile, we used a custom-made glass pitot tube with a 0.6 mm ID and 0.8 mm OD, and the same equipment as the previous study. The expressions to derive the mass flow, momentum, mechanical power, and total efficiency of the DBD in quiescent conditions are outlined in Chapter 4. The mathematical expressions are found in Equation ((4) through Equation (7).

Time-integrated and phase-resolved optical images were taken to visualize the physical plasma discharge. Time-integrated images were taken using a 24 MP Nikon D750 DSLR camera with a 200 mm macro lens (f/4.5). Each image is captured with a 20 ms exposure time, such as at f_{AC} = 2kHz, corresponding to 40 voltage cycles. A high-speed monochromatic CCD camera (Vision Research Phantom V12.1) coupled to a 200 – 550 nm UV intensifier lens (Specialised Imaging SIL3) is used to resolve the plasma propagation for each voltage cycle. In atmospheric air DBD discharge, all (visible and UV) light emissions are in 300 - 450 nm range [123, 124]. For a 2 kHz frequency voltage cycle, the CCD and intensifier trigger is set to 8,000 Hz with a 120 μs CCD shutter and 105 μs intensifier shutter settings to divide the voltage cycle into four equal parts [64]. These quadrants denoted as T1 through T4, represent the two halves of the voltage-rising cycle and two halves of the voltage-falling cycle (Figure 3.6). The CCD camera and intensifier are triggered by a function generator (Siglent SDG1032X) synchronized with the waveform generator of the custom power supply that controls the DBD actuator. For each test, the DBD is powered first, then the CCD camera and intensifier are triggered to capture images 3 seconds after the maximum voltage amplitude point of the cycle.

7.2 Plasma Characteristics

7.2.1 Time-Integrated Plasma Visualization

This section presents the time-integrated plasma discharge visualization as a function of DBD voltage and phase shift in the ACA electrode $\Phi = 0$ - 180° with the smaller gap length, $L = 10$ mm, to understand the plasma regimes and interaction between the electrodes. Figure 7.3 shows the plasma images at varying third electrode phase shifts with a fixed $V_{ACA} = 30$ kV and 40 kV. The DBD active electrode is located on the bottom side of each image, and the third electrode is located on the top side. A steady glow discharge that increases with voltage can be seen from the DBD active electrode edge over the embedded electrode, with the possibility of the early formation of filamentary streamers.

For $\Phi = 0$ - 60°, a streaming plasma discharge between the third and embedded electrodes is seen at the tested voltages. This reverse discharge from the ACA electrode shows strong filamentary streamers that extend to the area above the embedded electrode, in contrast to a more uniform glow discharge at the DBD active electrode. Interestingly, when the AC voltage is applied between the ACA and embedded electrode with the active electrode not energized, a typical DBD glow is seen at the ACA electrode edge without strong filamentary streamers (not shown). One possible explanation is the primary DBD produces a dominating space charge, leading to ACA electrode/space charge interaction rather than ACA / embedded electrode due to the air gap (L =10mm) between the two. The gap allows for the formation of persistent streamers, which are stronger at the higher DBD voltage condition Figure 7.3(b), as more ions are generated.

Approaching $\Phi = 180°$, at higher V_{DBD} potentials ($V_{DBD} > 30$ kV) or at higher V_{ACA}, the primary plasma discharge is extended, Figure 7.3(c), which is similar to the “sliding” discharge when strong negative DC bias is applied to a third electrode [14, 153]. In sliding DBD, the third electrode introduces a counter-forcing discharge that results in a deflected DBD jet. To the authors’ knowledge, this is the first report of sliding DBD with a downstream AC bias. Mechanical behavior similar to other sliding DBD studies is observed in the thrust (Figure 7.9) and velocity measurements (Figure 7.12), which can be used to optimize the spacing of downstream electrodes before diminishing or interfering effects occur.

In the larger gap experiments (L = 25 mm), no sliding discharge was observed at the tested range of V_{ACA}, V_{DBD}, or Φ. At Φ = 0°, few reverse streamer discharges were observed at higher potentials, similar to Figure 7.3**;** however, the overall discharge was more homogenous. This is mainly due to a weaker electric field and reduced space charge density between the electrodes.

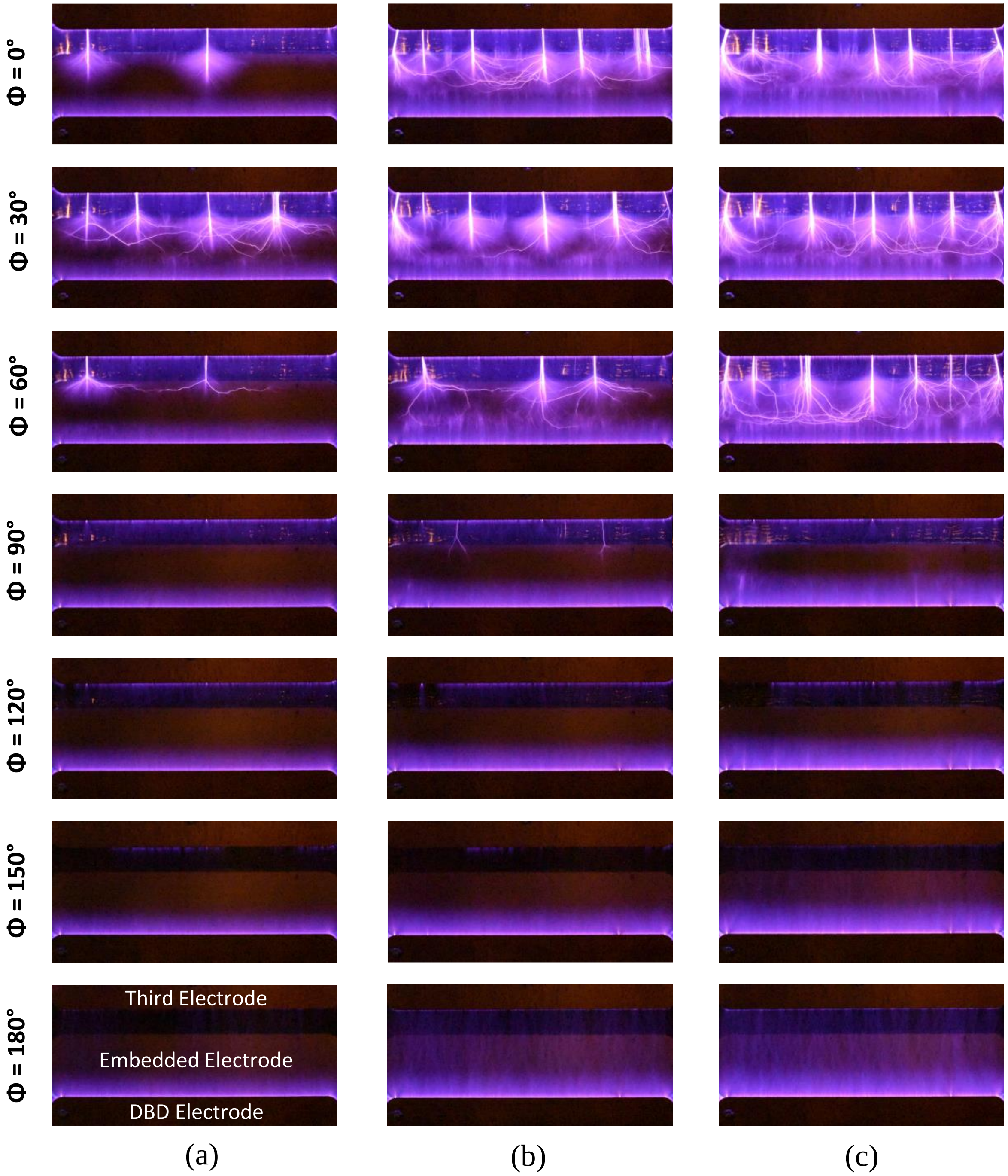

Figure 7.3. Time-integrated plasma emissions at varying ACA phase shift Φ, at VDBD = 30 kV (a), 35 kV (b), and 40 kV (c). The third electrode gap is 10 mm, and V_{ACA} = 28 kV. The active DBD electrode is located at the bottom of each image; the primary EHD flow is directed upwards. The third electrode is located on the top of each image; the third electrode discharge is directed downwards.

7.2.2 Phase-Resolved Plasma Characteristics

Building upon the time-integrated plasma visualizations, we capture phase-resolved plasma images to study the effect of the ACA on the plasma behavior. The baseline DBD case without ACA electrode at $V_{DBD} = 40$ kV, L = 10 mm is presented in Figure 7.4(a). The image orientation in Figure 7.4 is identical to Figure 7.3, with the DBD electrode pair located at the bottom of each image. In the baseline case, the third electrode has a floating potential, and the actuator acts as a standard two-electrode DBD, allowing for a side-by-side comparison with ACA cases.

Without an excited third electrode, the plasma luminosity and length for all phases of the cycle increase with voltage magnitude. In voltage-rising quadrants (T1 and T2), the generation and growth of streamers are observed, while the generation and development of a more homogenous glow discharge are seen during the voltage-falling quadrants (T3 and T4). The ends of each half cycle (T2 and T4) show higher luminosity and larger volume associated with the frequency and intensity of discharges, shown in Figure 7.5. Phase-resolved images of plate-to-plate DBD at 1 kHz in Debien et al. [64] agree well with the presented results and show that streamers in the positive-going half-cycle propagate further than the glow discharge of the negative-going half-cycle.

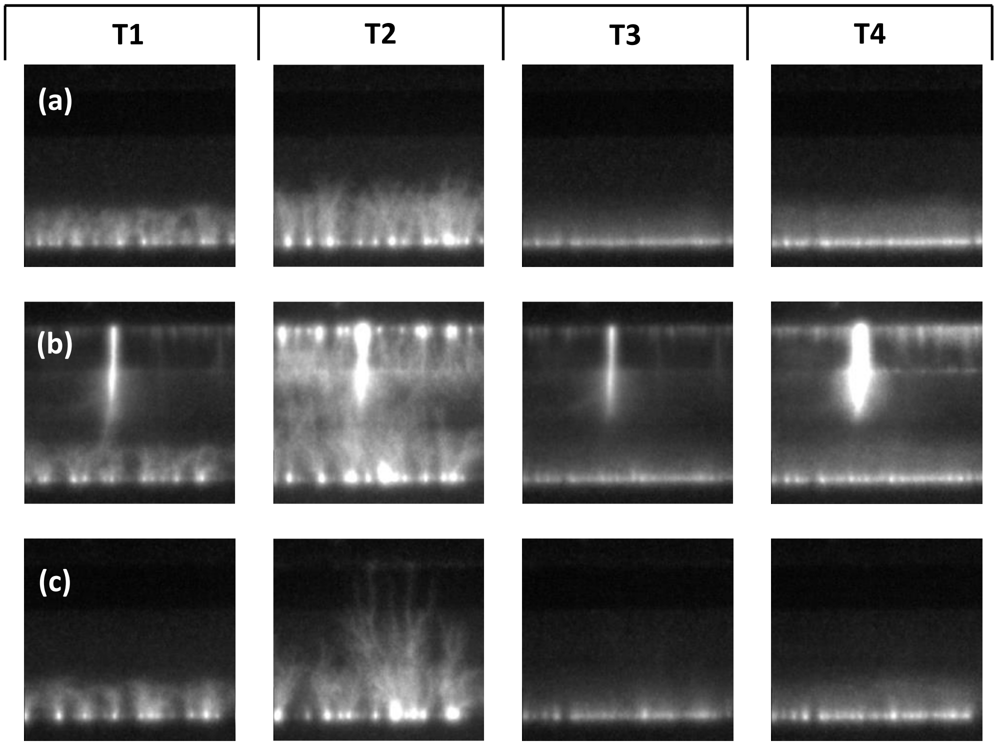

Figure 7.4. Phase-resolved plasma extension with a L = 10 mm gap at V_{DBD} = 40 kV without a V_{ACA} (a), with V_{ACA} = 28 kV / Φ = 0° (b), and V_{ACA} = 28 kV / Φ = 180° (c).

Adding ACA voltage leads to the strong interaction of the primary DBD plasma, dependent on the electric field strength and phase shift. The phase-resolved images for L = 10 mm gap, Φ = 0° and Φ = 180°, V_{DBD} = 40 kV with V_{ACA} = 28 kV are shown in Figure 7.4; these correspond to the time-averaged images in Figure 7.3. The reverse discharge on the ACA electrode for Φ = 0°, Figure 7.4(b), shows two opposing DBD discharges and the formation of persistent streamers present over several hundred cycles before moving along the electrode edge. Prior reports suggest that the residual surface charges can cause the onset of strong filamentary discharge [136]. Here, the discharge on the ACA electrode is similar to the primary electrode pair, e.g., in the T2 phase, several filamentary streamers extend to the embedded electrode, and a glow discharge is seen during the T3 and T4.

The out-of-phase ACA (Φ = 180°) case has the most noticeable difference during the T2 phase. Figure 7.4(c) shows that for V_{ACA} = 28 kV, the plasma extends to the third electrode, which is confirmed by negative discharge voltage on the ACA electrode, Figure 7.5. A drop in the momentum injection is observed during sliding discharge (see Figure 7.9). Note that the sliding occurs during the T2 part of the cycle with a near out-of-phase shift between the exposed electrodes (Φ ~ 180°). This condition corresponds to (i) a high primary discharge current, i.e., a high concentration of positive ions, and (ii) a high electric potential that drives the ions to the negatively charged ACA electrode. In the DBD-ACA system, the sliding discharge does not occur with negative species (T3 and T4) or when exposed electrodes are close to being in phase (Φ ~ 0°).

7.3 Electrical Characteristics

Here, we present time-resolved electrical and discharge characterization as a function of DBD voltage and the ACA phase shift Φ = 0° and 180°. Figure 7.5 shows a set of voltage and current graphs on the active DBD and ACA electrodes. The results for V_{DBD} = 40 kV and V_{ACA} = 32 kV are representative of the plasma emissions discussed above. Cases with L = 10 mm gap have a stronger electrical field than L = 25 mm. They examine the interaction between the charged species generated in the primary DBD plasma and E-filed modulated by the ACA electrode.

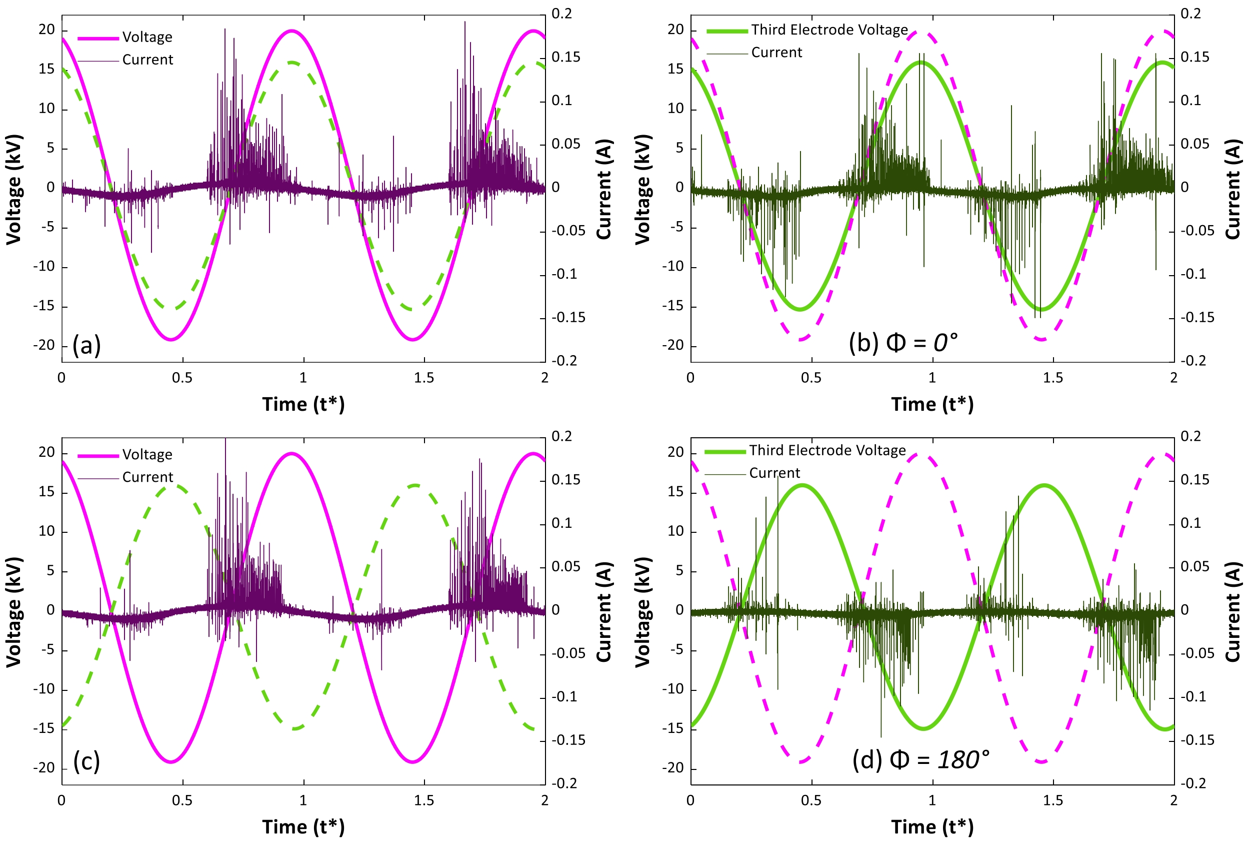

Figure 7.5. Instantaneous voltage and current of the primary DBD with gap distance L = 10 mm; smooth magenta line - primary DBD voltage, V_{DBD} = 40 kV; Smooth green line - ACA voltage, V_{ACA} = 32 kV. The thin purple line is the current on the primary, and the thin green line is the current through the ACA electrode. The dashed lines are provided for reference of the phase shift. (a, b) Φ = 0°; (c, d) Φ = 180°.

In the positive-going cycle, streamer discharges on the primary DBD are indicated by positive discharge current spikes that can reach ~ 200 mA, Figure 7.5(a, c). In the negative-going cycle, lower amplitude yet consistent, negative discharge current peaks reflect the glow discharge associated with the production of the negative species near the exposed electrode [20]. With the close position to the embedded electrode, the third electrode at Φ = 0° shows a significant positive discharge current at the same time as the primary DBD, Figure 5 (a, b), the opposing plasma discharges lead to saturation of the space between the exposed electrodes and persistent streamer formation (Figure 7.4, b). In contrast, Figure 7.5(c, d) shows the out-of-phase (Φ = 180°) case with a negative discharge current on the ACA electrode, which can be explained by emissions of electrons from the third electrode to the positive space charge. With sufficient E-field strength, the plasma extension to the ACA electrode leads to sliding discharge, see Figure 7.2, and the T2 phase in Figure 7.4(c). The negative discharge on a third electrode during the sliding discharge was previously observed with a downstream high-voltage DC electrode [14, 153].

The effect of Φ on the positive and negative discharge current from the third electrode at $L = 10$ mm with $V_{DBD} = 25$ kV and 40 kV is shown in Figure 7.7. The positive discharge current (I_{dis}^{+}) and negative discharge current (I_{dis}^{-}) are plotted as a function of Φ. This maximum I_{dis}^{+} reflects the reverse DBD associated with the saturated streamers observed in Figure 7.3. In the stronger $V_{DBD} = 40$ kV case (Figure 7.7,b), the ACA electrode experiences a reverse discharge at $\Phi = 0°$ with a maximum $I_{dis}^{+} = 10.5$ mA/m and $I_{dis}^{-} = 3.0$ mA/m. As Φ is increased, the reverse streamer discharge decreases. The onset of sliding discharge at $\Phi = 150°$ and $\Phi = 180°$ is reflected by an increase in I_{dis}^{-}. For low cases $V_{DBD} = 25$ kV (Figure 7.7, a), the ACA electrode does not induce sliding discharge; thus, the ACA electrode does not spike even at $\Phi = 180°$. For these conditions, the ACA electrode does not contribute significant discharges to the system or modify the primary discharge; its primary contribution is augmenting the space charge produced by the primary DBD. In the stronger E-field scenario ($L = 10$ mm, $V_{DBD} = 40$ kV), the third electrode produces significant discharge currents: positive in the opposing DBD discharge $\Phi = 0°$ (discharge power, $P_{DBD} = 193.9$ W/m) and negative during the sliding discharge $\Phi = 180°$ ($P_{ACA} = 48.7$ W/m). Note that the thrust values are lower in these conditions than during the optimal DBD-ACA operation, see Figure 7.9.

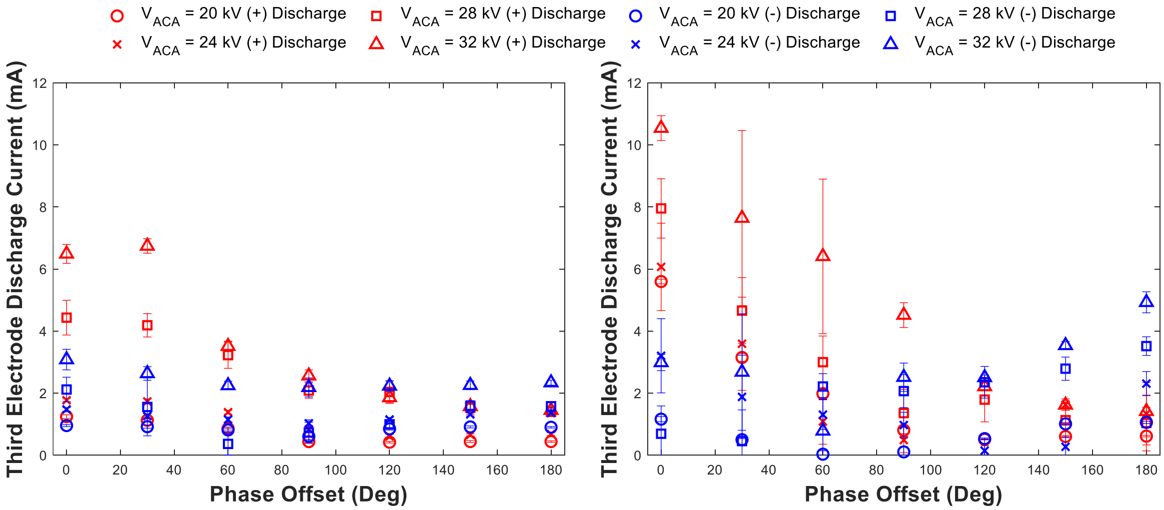

Figure 7.6. Third electrode positive and negative discharge current at varying phase shift and V_{ACA} with L = 10 mm spacing (a) V_{DBD} = 25 kV and (b) V_{DBD} = 40 kV. The positive and negative discharge current is determined similarly to previous works [12]. The standard deviation is determined across at least 10 voltage cycles. Two standard deviation error bars are plotted.

The optimization and generalization of the DBD-ACA actuator performance can be achieved through the adjustment of E-field, primary and ACA voltage amplitude and waveform, phase shift, or electrode spacing. In the experiments at larger gap spacing, the electrical characteristics of the primary DBD are mainly independent of the potential and phase shift of the ACA electrode. At V_{DBD} = 40 kV with a varying V_{ACA} potential and Φ, the total primary discharge current does not change significantly from its baseline of 11 mA/m. The electrical power usage of the DBD at V_{DBD} = 40 kV across the range of Φ approximately remained constant at approximately 129 W/m.

Figure 7.7 shows the voltage and current graphs of the active DBD and ACA electrodes with a spacing of 25 mm with V_{DBD} = 25 kV and 40 kV, similar to Figure 7.5. With the same V_{ACA} amplitudes, the E-field between the electrodes is weaker, leading to significantly lower discharge currents compared to L = 10 mm. For Φ = 0°, the electrical characteristics of a reverse DBD are not observed, and for Φ = 180° there is no significant sliding discharge current.

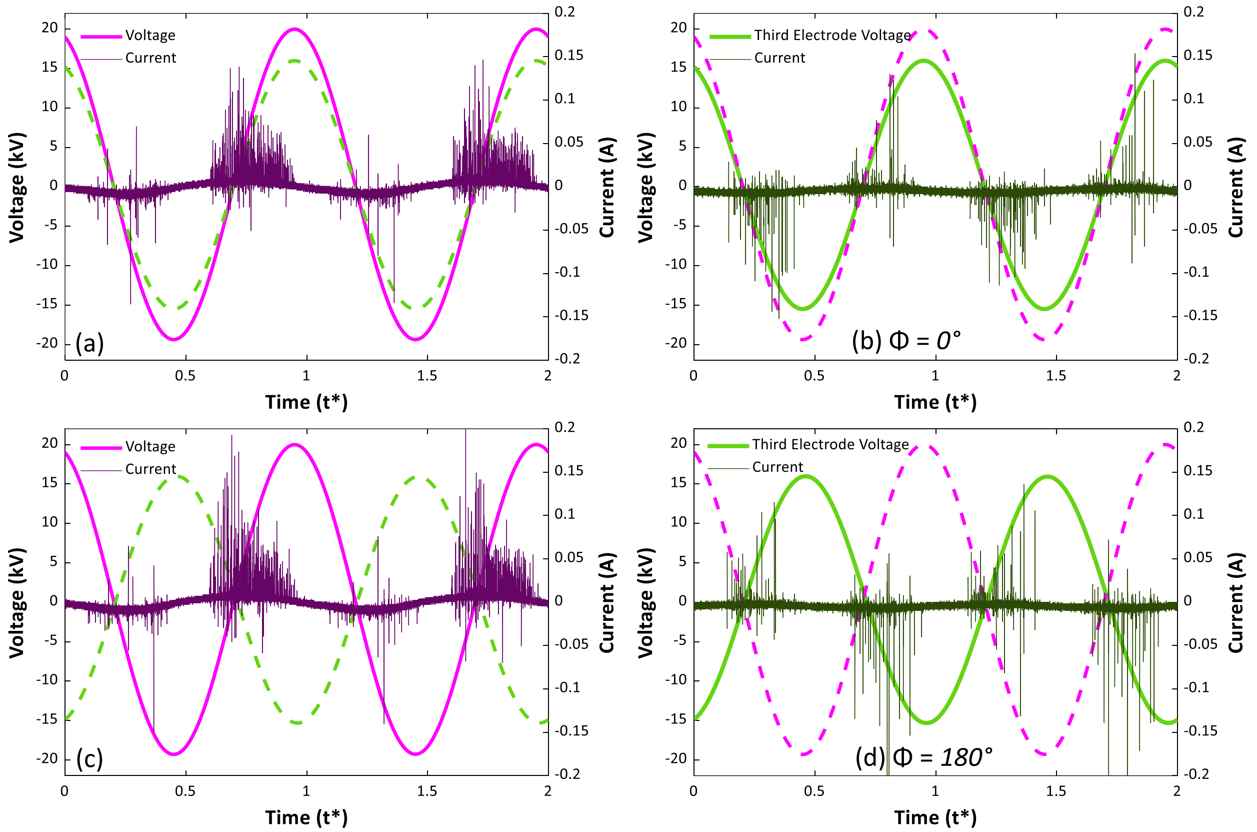

Figure 7.7. Instantaneous voltage and current of the primary DBD with gap distance L = 25 mm; magenta line = primary DBD voltage, V_{DBD} = 40 kV; green line = ACA voltage, V_{ACA} = 32 kV. The thin purple line is the current on the primary, and the thin green line is the current through the ACA electrode. The dashed line is provided for reference of the phase shift. (a, b) Φ = 0°; (c, d) Φ = 180°.

Integration of the discharge currents is shown in Figure 7.8. The effect of Φ on the positive and negative discharge current from the third electrode, V_{ACA}, at L = 25 mm with V_{DBD} = 25 kV and 40 kV. With no reverse nor sliding discharge at L = 25 mm, significantly lower positive and negative discharge current is seen on the ACA third electrode. At the extended spacing, the third electrode discharge characteristics become primarily independent of the phase difference from the DBD; however, the discharge current is still dependent on V_{ACA} potential. The third electrode mainly interacts with the unsteady plasma dynamics and the space charge, accelerating generated ions downstream from the DBD. The discharge current and total power usage for the primary DBD electrode for all Φ and V_{ACA} conditions for L = 25 mm is similar to the baseline DBD for the L = 10 mm and L = 25 mm cases.

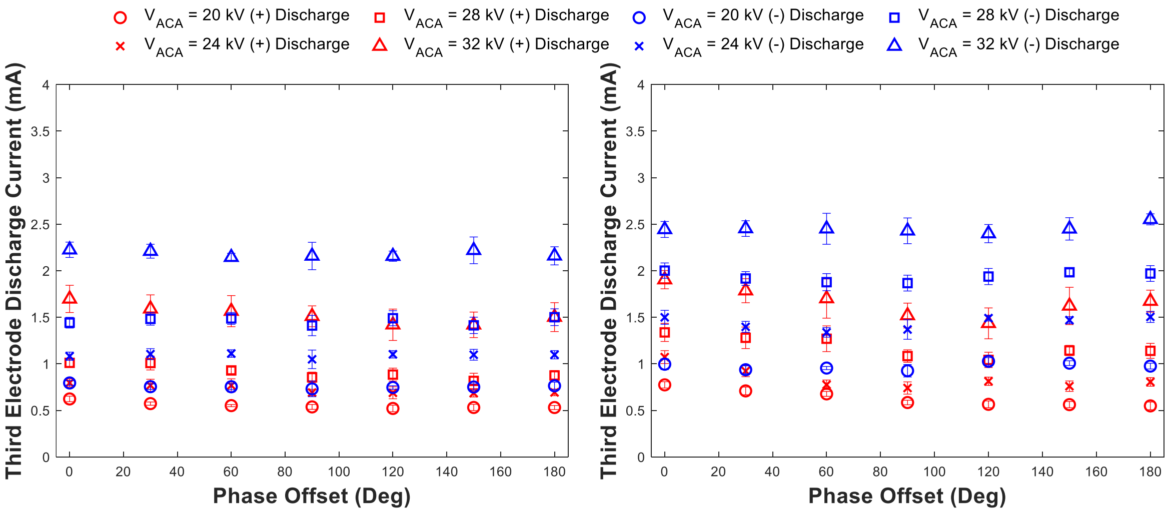

Figure 7.8. Third electrode positive and negative discharge current at varying phase shift and V_{ACA} with L = 25 mm spacing at V_{DBD} = 25 kV (a) and V_{DBD} = 40 kV (b). The standard deviation is determined across at least 10 voltage cycles. Two standard deviation error bars are plotted.

With the weaker E-field, the power through the third electrode is significantly lower compared to the L = 10 mm case. In this configuration (L = 25mm), the third electrode power use is at a maximum of 36.3 W/m when $\Phi = 60°$ and at a minimum of 21.9 W/m when $\Phi = 180°$ at V_{ACA} = 32 kV. A summary of the power usage of the DBD and ACA electrodes is presented below in Table 7.1. The power usage is computed identically to the previous and is averaged across at least 10 independent voltage cycles.

Table 7.1. DBD and ACA electrode power usage at L = 10 mm and L = 25 mm.

V_{DBD} (kV)	V_{ACA} (kV)	L (mm)	Φ (°)	P_{DBD} (W/m)	P_{ACA} (W/m)
40	32	10	0	128.9	193.9
40	32	10	180	122.8	48.7
40	20	10	0	121.8	63.6
40	20	10	180	115.7	15.3
40	32	25	0	121.3	28.7
40	32	25	180	129.7	21.9
40	20	25	0	131.4	4.0
40	20	25	180	128.5	3.4

7.4 Mechanical Characteristics

7.4.1 Thrust Characteristics

Figure 7.9 below shows the time-averaged thrust of the DBD-ACA actuator at L = 10 mm, f = 2 kHz, V_{DBD} = 25 kV - 40 kV range, and V_{ACA} = 20 kV - 32 kV with a varying phase shift. The typical standard deviation per point is <1 mN/m over the sampling period. The horizontal forcing is seen to generally increase from its baseline performance to a maximum at Φ = 180° and decrease to a minimum at Φ = 0°. In all cases, the two air-exposed electrodes operated in phase with produced lower horizontal thrust decreased due to a counter-forcing reverse DBD from the third electrode (Figure 7.3). The most significant increase from 31.8 mN/m (baseline) to 41.8 mN/m at Φ = 180° (31%) is observed at V_{DBD} = 35 kV, V_{ACA} = 24 kV (Figure 7.9.c). The highest total thrust of 54.5 mN/m was at V_{DBD} = 40 kV, V_{ACA} = 24 kV (Figure 7.9.d) at Φ = 150°. At lower V_{DBD}, such as V_{DBD} = 30 kV, an out-of-phase case (Φ = 180°), the thrust increased by ~ 38%. Since the primary DBD discharge was not significantly different between the baseline and the ACA cases, the results support that the third electrode acts to accelerate the ions generated at the primary DBD electrode, significantly increasing horizontal thrust.

The results suggest that ACA enhances the push-push DBD plasma/ flow interaction mechanism [66]. The out-of-phase third electrode enhances both the positive ion momentum transfer in the DBD positive-going cycle and the negative electron momentum transfer in the DBD negative-going cycle. This can be further supported by temporal surface charge measurements by Enloe *et al.*, which found that a negative surface potential in the negative-going cycle and positive surface potential in the positive-going cycle is dominated by physically charged ions on the dielectric surface [140]. This work does not evaluate the relative contribution of the positive or negative species to trust.

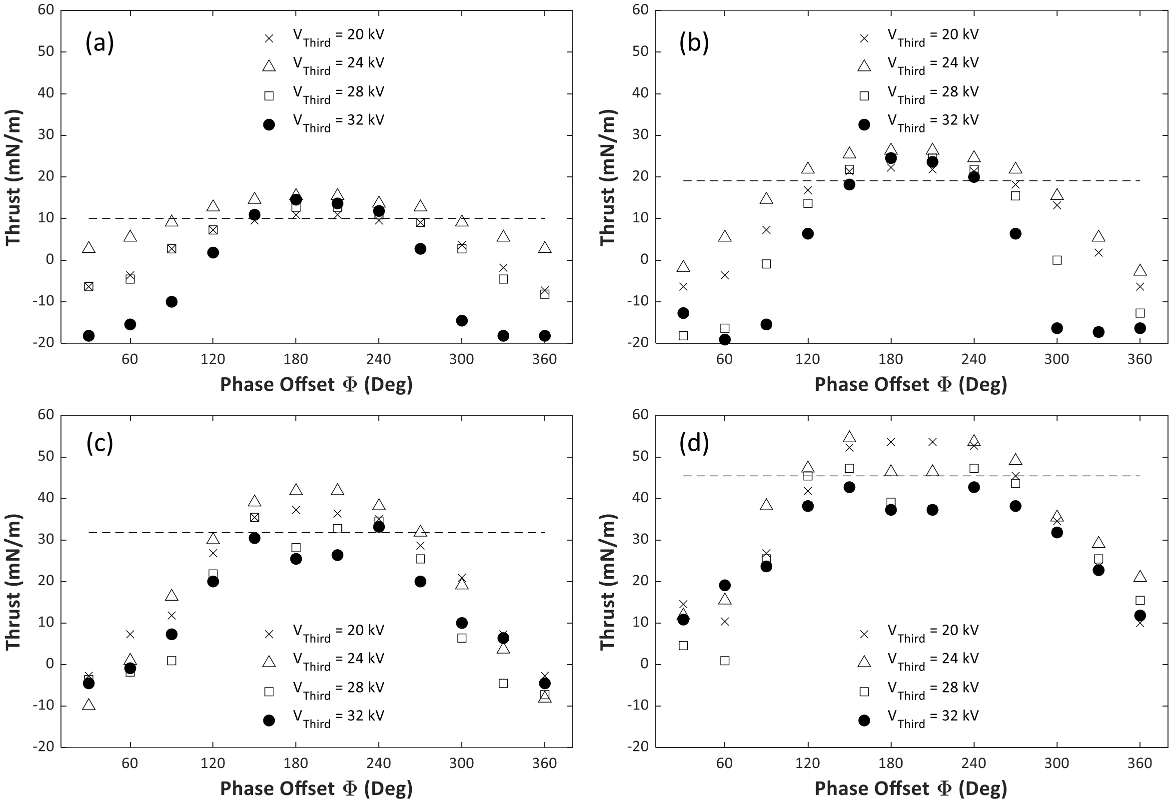

Figure 7.9. Horizontal Thrust at $V_{ACA} = 20 – 32$ kV at 2 kHz with varying Φ with $V_{DBD} = 25$ kV (a), 30 kV (b), 35 kV (c), and 40 kV (d) at 2 kHz. The distance from the embedded electrode to the third electrode is L = 10 mm. The DBD baseline thrust without a third electrode is a dashed line.

At the highest E-filed values, $V_{DBD} = 35$ kV and 40 kV, $V_{ACA} > 24$ kV, the trust values dip below baseline at $\Phi = 150 - 240°$. The decrease in horizontal forcing corresponds to sliding discharge cases exhibiting electrical characteristics similar to the DC-augmented sliding discharge [14]. In these cases, while the high electric field accelerates the positive ions generated at the DBD, negative electrical discharges from the third electrode to the space charge exert a backward force, diminishing the overall horizontal thrust. This observation is supported by discharge current measurements on the third electrode (Figure 7.6) and the time optical images of sliding discharge (Figure 7.3).

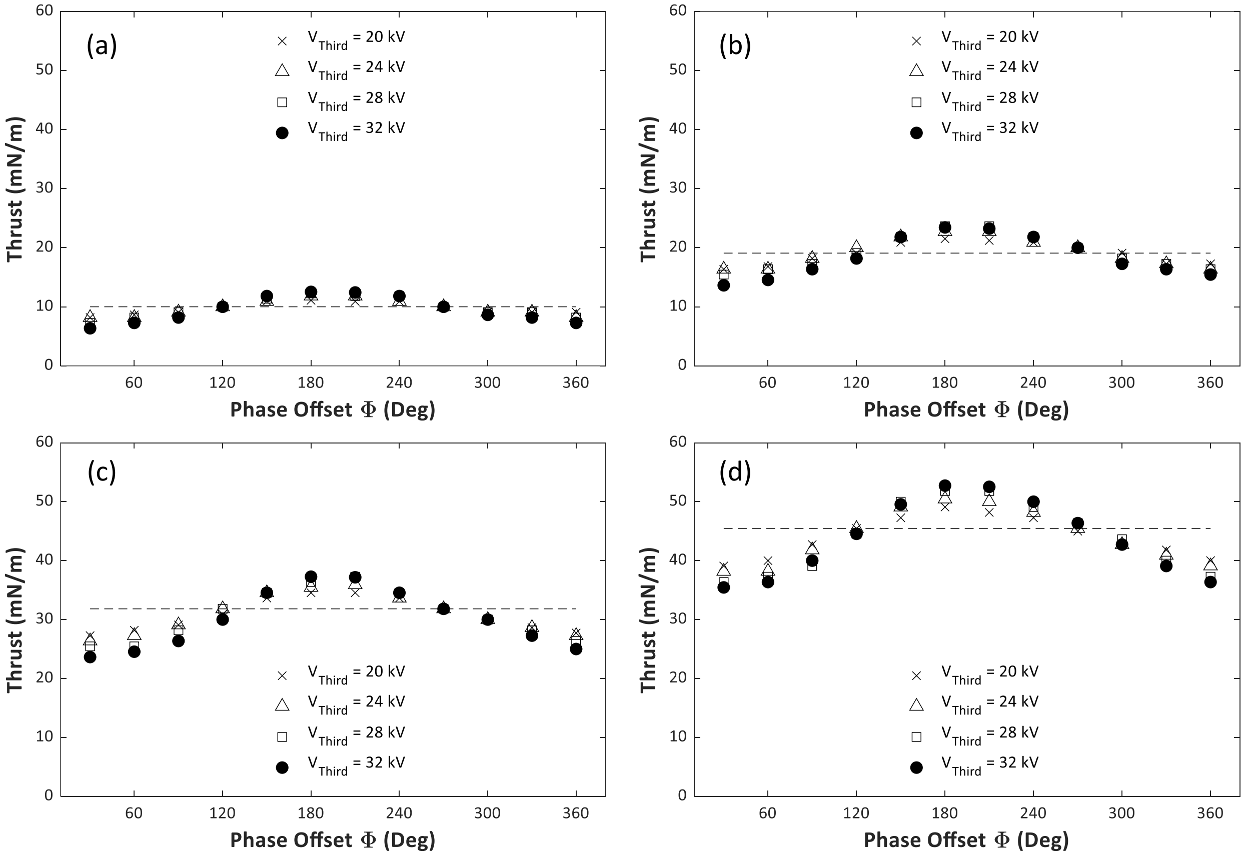

Figure 7.10. Thrust at V_{ACA} = 20 – 32 kV at 2 kHz with varying phase shift. V_{DBD} = 25 kV (a), 30 kV (b), 35 kV (c), and 40 kV (d). The third electrode gap L = 25 mm. The DBD baseline thrust without a third electrode is a dashed line.

Figure 7.10 shows the trust with the third electrode gap L = 25 mm. In all cases, the maximum thrust is Φ = 180 - 210°, and the lowest thrust is at Φ = 0°. The maximum forcing with a single third electrode was seen when the DBD was operated at its maximum tested potential, V_{DBD} =

40 kV. In this case, the total thrust increased from 46 mN/m to 54 mN/m, an 18% increase. When Φ = 0°, the DBD thrust decreased from 46 mN/m to 36 mN/m, a 20% decrease. With a spacing of 25 mm between the embedded electrode and the third electrode, no sliding discharge was seen in all cases, supporting that sliding discharges decrease in thrust at the highest potentials in the L = 10 mm case (Figure 7.9). Compared to the previous L = 10 mm case, the L = 25 mm condition experienced a slightly smaller thrust enhancement for the same V_{DBD} due to the weaker electric field; however, the weaker electric field allowed for a higher V_{DBD} before streamers or sliding discharge. When Φ = 180° with V_{DBD} = 40 kV with V_{ACA} = 32 kV, the L = 25 mm spacing allows for 53.6 mN/m compared to the 37.3 mN/m when L = 10 mm. A summary of the improvements in thrust along with the baseline thrust is displayed below in Table 7.2 for the V_{DBD} = 40 kV condition at L = 10 mm and L = 25 mm.

Table 7.2. Total thrust at V_{DBD} = 40 kV at L = 10 mm and L = 25 mm.

V_{DBD} (kV)	V_{ACA} (kV)	L (mm)	Φ (°)	Thrust (mN/m)
40	–	-	–	45.5
40	24	10	150	54.5
40	28	10	180	39.1
40	32	10	180	37.3
40	24	25	180	50.5
40	28	25	180	51.8
40	32	25	180	53.6

On the mechanism of plasma flow interaction in an AC-augmented system: As demonstrated by optical and electric measurements, primary DBD discharge characteristics do not significantly change between the baseline and the ACA cases; thus, change in horizontal thrust is the result of the temporal manipulation of the species generated in the primary DBD by the ACA modulated E-field. Mechanistically, while the ACA may enhance the push-push DBD plasma/ flow interaction in the primary DBD, *performance improvements are primarily enabled by the third electrode's* *charge pull action*. The out-of-phase third electrode enhances the positive ion momentum transfer in the DBD positive-going cycle and the electron momentum or charge transfer in the DBD negative-going cycle. Prior work on temporal surface charge measurements comments that a negative surface potential in the negative-going cycle and positive surface potential in the positive-going cycle is dominated by physically charged ions on the dielectric surface [140]. Our recent work on the DCA-DBD also suggests that (i) the complex interaction of negatively charged species with neutral molecules and (ii) the oscillating behavior of residual surface and space are likely to play a role in the AC-augmented plasmas [14]. This work did not directly evaluate the relative contribution of the positive or negative species to thrust.

7.4.2 Wall jet Characteristics

The EHD jet characterization allows us to confirm the thrust measurements and shed insight into momentum generation in the DBD-ACA system. The conditions with the most significant thrust measurement change are with the out-of-phase and in-phase ACA electrodes. Thus, we compare the X - velocity profiles for these two cases and the baseline. For L = 10 mm, the third electrode is 35 mm downstream of the active electrode; three positional measurements were taken at X = 15 mm, 25 mm, and 40 mm. These positions allow velocity characterization immediately after the DBD plasma region, X ~ 15 -20 mm, and in front of and after the third electrode. For L = 25 mm, the third electrode is 50 mm downstream of the active electrode; thus, the velocity profiles are taken at X = 15 mm, 25 mm, 40 mm, and 55 mm. The X-velocity profiles were also taken at Y = 1.0 mm, 2.0 mm, and 3.0 mm. Two standard deviation error bars are included with each data point.

Figure 7.11 shows the baseline DBD and the DBD-ACA with in-phase and out-of-phase spacing at an L = 25 mm. Figure 7.11(a) and Figure 7.11(b) show the baseline (2-electrode DBD) with a typical DBD wall jet: V_{max} = 5.68 m/s at X = 15 mm at the near-wall height of Y = 0.5 mm. Higher velocities can occur closer to or inside the plasma region; however, this region was not probed to prevent dielectric charging of the pitot tube. Viscous effects and surface /space charge interaction lead to momentum displacement downstream; this observation agrees with several previously published results in a quiescent environment [20]. The directly measured thrust (45.5 mN/m) closely agrees with the velocity-derived thrust of 48.6 mN/m using equation (17). The momentum at the furthest measured distance of 55 mm shows < 10% loss due to viscous dissipation. Figure 7.11(a) and Figure 7.11(b) show the velocities for cases with activated ACA electrodes; the DBD profiles show slightly diminished EHD forcing $\Phi = 0°$ or enhanced $\Phi = 180°$. Using the control, the velocity-derived thrust of the DBD with an in-phase third electrode is 39.8 mN/m, which agrees directly with the measured thrust of 36.4 mN/m (9%). Out-of-phase ACA velocity derived-trust of 52.3 mN/m agrees with the directly measured thrust of 53.1 mN/m.

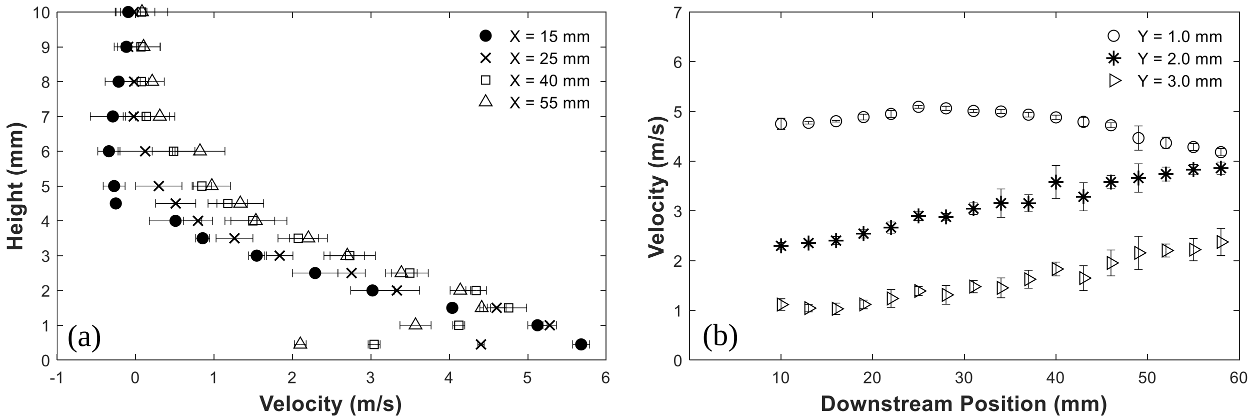

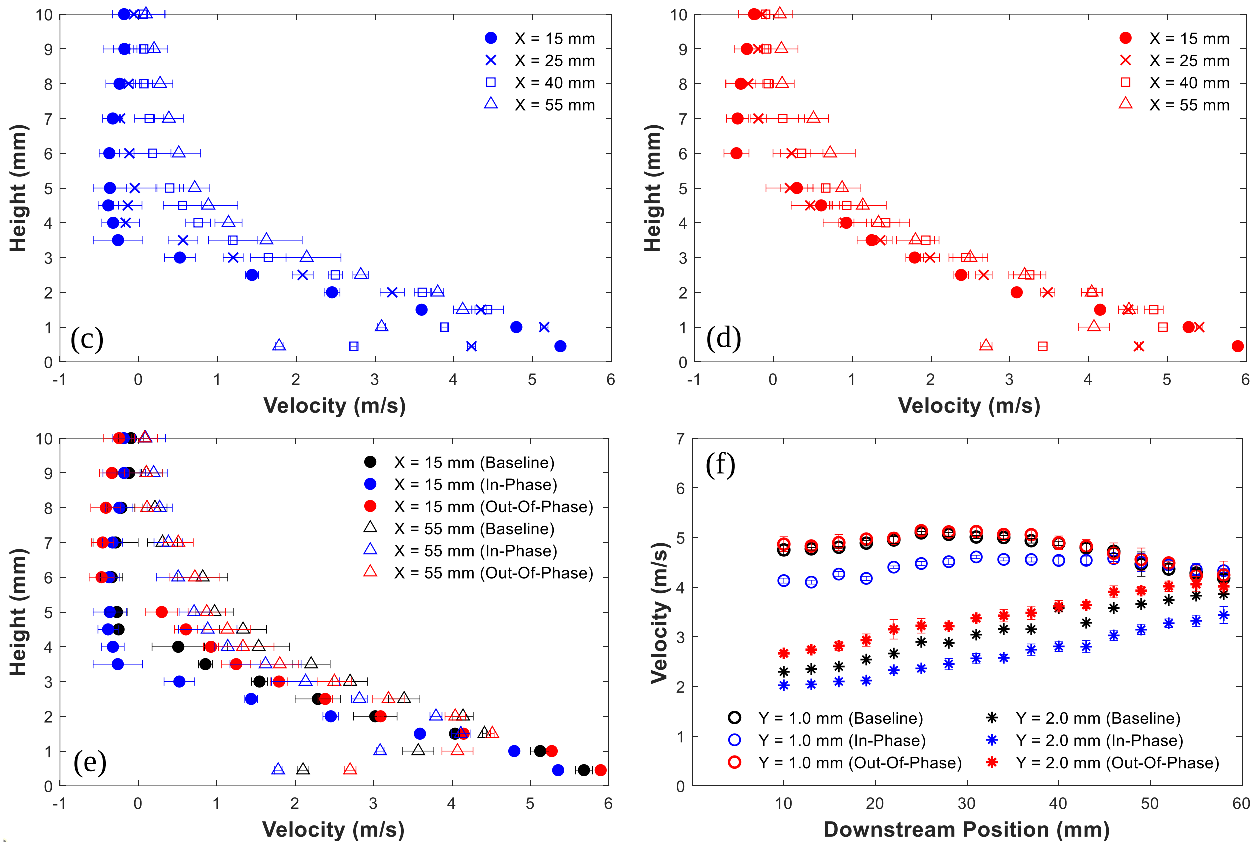

Figure 7.11. X-velocity profiles: V_{DBD} = 40 kV, L = 25 mm; V_{ACA} = 0 kV, (a) and (b). V_{ACA} = 32 kV Φ = 0° (c) and Φ = 180° (d). The profiles are compared at X = 15 mm and X = 55 mm (e), y = 1 mm and y = 2 mm (f).

Figure 7.11(e) and Figure 7.11(f) compare the baseline profiles with the activated ACA. The out-of-phase cases show a stronger jet near the wall. At Y = 2.0 mm, the DBD jet, in all cases, shows nearly identical velocities. Notably, the three conditions show no sign of any additional or reverse forcing at the third electrode since the three conditions show similar profile changes, especially immediately before and after the third electrode. Thus, the modified DBD forcing regions appear to be near the primary DBD electrode. For stronger E-filed L = 10 mm case, the effect of ACA shows the diminishing impact on the velocity profiles for Φ = 0° (opposing jet) and Φ = 180° (sliding discharge); see Figure 7.12.

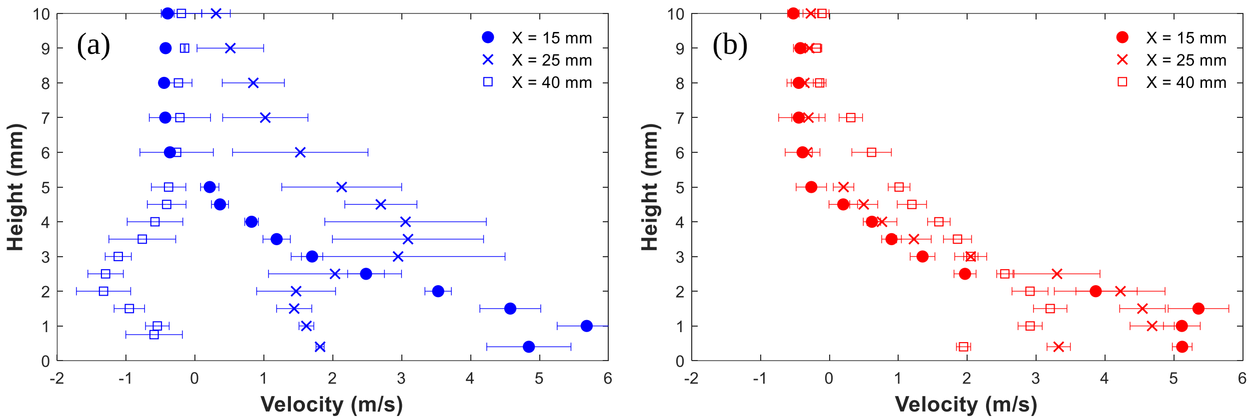

Figure 7.12. X-velocity profiles at VDBD = 40 kV in-phase with VThird = 20 kV (a) and VDBD = 40 kV out-of-phase with VThird = 28 kV (b) with a L = 10 mm third electrode gap.

When measuring profiles with Φ = 0° and a L = 10 mm gap, a V_{ACA} = 20 kV potential was used because higher potentials caused significantly more unsteadiness and nonuniformity, highlighting that the velocity field likely is no longer two-dimensional due to the strong reverse streamers, as shown in Figure 7.3. The directly measured thrusts of the two conditions are shown in Figure 7.12 and Figure 7.9. Figure 7.12 (a), Φ = 0°, shows the reverse flow at X = 40 mm; however, the profile at X = 15 is similar to the baseline profile. Momentum analysis of the Φ = 180° case (Figure 7.12.b) shows lower forcing due to sliding discharge likely originating at the third electrode. In this case, the integrated momentum at x = 15 mm and 25 mm is 58.1 mN/m and 53.4 mN/m, respectively. However, the momentum at X = 40 mm is 31.2 mN/m. Since X = 40 mm is located directly after the edge of the third electrode, the drop in momentum is likely from reverse forcing due to ACA discharge in the sliding DBD. This is supported by the measured negative discharge shown in Figure 7.5 and corresponds to the phase-resolved positive sliding discharge shown in Figure 7.4(c). Due to the higher momentum at the X = 15 mm position, the authors believe the out-of-phase ACA accelerates the positive ions from the primary DBD, as in the L = 25 mm case; however, this gain is lost by the reverse forcing from the sliding discharge. The L = 10 mm case highlights a possible spacing limit in multi-electrode systems for horizontal thrust as strong reverse discharge or sliding discharges may cause reverse forcing, leading to less efficient operation.

Based on equation (6), the mechanical power was calculated for V_{DBD} = 40 kV / V_{ACA} = 32 kV at Φ = 180° and L = 25 mm. The DBD actuator's power usage increased from the baseline of 0.133 W/m to 0.147 W/m with the out-of-phase third electrode. The efficiency of ACA-DBD is almost identical to that of the two-electrode DBD. The overall efficiency at the highest power condition is ~0.1 %, twice as high as reported in the literature (~ 0.05%) for dielectric of similar thickness [64]. Since the increase in momentum injection plateaus near V_{ACA} = 32 kV, weaker electrical cases may have greater efficiency. A summary of the electromechanical characteristics is shown inTable 7.3.

Table 7.3. Velocity-derived momentum, power, and efficiency of the three-electrode DBD system compared to the baseline two-electrode DBD. The momentum can be compared to the directly measured thrust.

V_{DBD} (kV)	V_{ACA} (kV)	L (mm)	Φ (°)	Thrust (mN/m)	Momentum (mN/m)	P_{mech} (W/m)	$P_{elec, total}$ (W/m)	η (%)
40	–	–	–	45.5	48.6	0.133	131.7	0.100
40	28	10	180	39.1	43.7	0.104	162.8	0.064
40	32	25	180	53.6	52.3	0.147	151.6	0.097

7.5 Chapter Summary

This section outlines the first research exploring the electromechanical characteristics of a DBD actuator enhanced with a third AC-powered electrode. The three-electrode DBD actuator is characterized using time-integrated and time-resolved plasma visualizations, time-resolved current analysis, thrust measurements, and velocity profiles. The experimental results and the analysis provide insights into the DBD-ACA operation and can be used to optimize high-power density non-thermal plasma devices. The key conclusions include:

- The performance of an AC-augmented DBD actuator depends on the phase shift in voltage waveform between the primary DBD and the third electrode, the voltage amplitude, and the spacing between the DBD and the third electrode.
- Directly measured thrust measurements, velocity profiles, and electrical current measurements support that an out-of-phase ACA enhances the primary DBD body forcing. The highest measured thrust with the out-of-phase ACA was 53.6 mN/m with a DBD jet V_{max} = 5.89 m/s. The electromechanical efficiency for this condition was ~0.10%.
- In-phase ACA ($\Phi = 0°$) sets up a strong E-field to the embedded electrode and can cause the formation of reverse flow. The out-of-phase ACA ($\Phi = 180°$) promotes the acceleration of both the positive and negative species generated by primary DBD, enhancing momentum transfer to the neutral molecules.
- For $\Phi = 180°$and with a sufficiently strong E-field, a sliding discharge occurs during the positive-going voltage cycle by inducing a negative discharge from the third electrode to the space charge. This previously was only seen in DC-augmented DBD systems. The onset of sliding discharge is likely to be a critical spacing limiting factor in DBD arrays, limiting horizontal thrust and efficiency.

Mechanistically, while the ACA may enhance the push-push DBD plasma/ flow interaction mechanism of the primary DBD, the improvements in thrust are primarily due to the additional charge pull by the third electrode. While this work does not directly evaluate the relative contribution of the positive or negative species, future research should probe (i) the complex interaction of charged species with neutral molecules and (ii) the oscillating behavior of residual surface and space in the AC-augmented plasmas. These investigations should include time-resolved velocity and surface charge measurements. The findings of this work can be used as validation data for numerical model developments and optimization of DBD arrays.

Future fundamental investigations into a mechanistic understanding of DBD discharge should include time-resolved velocity and surface charge measurements. Similar to the possible improvement of the DCA-DBD, time-resolved measurements of surface charge dynamics can be achieved with Pockel's effect or individual surface charge probes. The time-resolved momentum transfer dynamics or unsteady fluid analysis can be resolved through hot wire anemometry, PIV, or LDA. For a hot-wire to work in a DBD system, the hot-wire must float (non-grounded). Duong [34] constructed a custom floating Wheatstone bridge circuit to characterize a DBD with a hot-wire X-probe probe. The findings for this work can be used as validation data for numerical model developments and optimization of DBD arrays.

Chapter 8. DBD Plasma Actuator Arrays

This section explores a multi-electrode DBD actuator (or DBD array). There currently is little work on the capabilities or limits of multi-DBD actuators, and the effects of identified key parameters have not been well-studied. Based on the results of the ACA-DBD, sinusoidal DBDs can strongly accelerate a previous DBD when given an appropriate minimum spacing, and a multi-DBD with robust scalability is explored.

Early efforts tested DBD arrays constructed of DBD actuators in series to demonstrate an increase in the total thrust. However, a counter-wind (sometimes called a cross-talk phenomenon) is produced on the back side of a downstream active electrode when the electrodes are spaced closely, thus creating a small backward-facing discharge and limiting the overall system's efficiency [99, 115]. These works, including Forte *et al.* [115], Thomas *et al.* [99], and Berendt *et al.* [116] have tested DBD arrays with different electrode geometries, waveforms, and spacings.

Due to cross-talk at high voltages, it was previously stated that DBD array thrust does not increase linearly with the number of actuator stages [99]. Subsequential DBD array investigations have attempted to reduce the effect of cross-talk in DBD arrays by modifying the DBD actuator geometry. Benard *et al* [117] proposed a DBD array comprised of a three-electrode DBD actuator with two dielectric layers and two embedded electrodes per actuator stage. In this study, the modified geometry reduced backward flow due to cross-talk by up to 65%; however, some cross-talk persists and the additional embedded electrode significantly increases manufacturing complexity while requiring higher than typical voltages.

More recent optimizing work has expanded on DBD systems with multiple DBDs in series with varying geometric and electrical conditions. With the goal of a continuously accelerated EHD force, some works demonstrated that DBD arrays with alternating air-exposed HV electrodes and grounded electrodes experienced minimal cross-talk. This was first presented by Debien *et al.* when it was shown that the EHD jet was accelerated up to ~10.5 ms^{-1} with a four-actuator DBD system [64]. This approach used wire-to-planar electrodes and is simpler with better results than the multi-electrode system proposed by Benard *et al* [117]. Recent promising results of successively accelerated DBD actuation were presented in Sato *et al.* [118], demonstrating linearly scaling DBD array thrust for the first time using custom power electronics. This study uses a DBD configuration similar to Debien et al [26]. However, the electrodes were planar-to-planar, and the HV waveform was a nanosecond pulsed DC voltage. Sato *et al.* [118] also suggested introducing a resistor to the downstream air-exposed electrode to limit and prevent arc discharge from each downstream electrode. While these studies offer promising approaches to continuously accelerate an EHD jet and maximum thrust, most of the presented results are limited to low-power operations and include solely the velocity or thrust measurements in small parameters. There is a lack of understanding of the influence of various key DBD actuator parameters and their resulting electromechanical characteristics in these multi-electrode systems. It is of great interest to the active flow control community to understand the mechanisms of multi-DBD systems with more conventional electrical parameters (i.e. sinusoidal waveform) and their mechanical limits.

This presented study explores the electrical, mechanical, and plasma characteristics of a DBD array with alternating high-voltage electrodes to create a continuously accelerated DBD array. This work is the first to probe the mechanical limits and effects of key variables such as number of DBD stages, spacing, and resistors in DBD arrays with alternating electrodes. The characterization focuses on plasma emissions, direct thrust, wall jet characteristics, and electrical power usage. The thrust measurements provide a strong gauge of the mechanical performance of the DBD system while wall jet measurements allow for analysis of momentum transfer and mechanisms of the successively accelerated EHD jet. The total electric-to-kinetic energy transfer efficiency amongst the whole system is evaluated for the various electrical and

8.1 Experimental Setup

In this study, the DBD array is tested in two different geometric configurations: (1) a simple alternating electrode DBD array similar to that in Debien *et al.* [64] and (2) a “resistive” alternating DBD array with an additional electrode connected by a 1 MΩ resistor before each active electrode similar to that in Sato *et al.* [118]. Figure 8.1 illustrates the two different DBD array configurations. A resistive array (with segmented exposed electrodes) limits arcing and filamentary streamers. Since the DBD stages have staggered phases, embedded electrodes experience the same voltage as the following active electrode, preventing reverse discharge. For this manuscript, the alternating electrode DBD array and resistive alternating DBD array will be referred to as the DBD array and the RDBD array. The electromechanical characteristics of the

RDBD array were experimentally found to be nearly identical when the varying resistor from 500 kΩ and 10 MΩ. The DBD array is tested with a spacing between each stage L = 20 mm (DBD$_{L=20}$), and the RDBD is tested with spacing between each stage L = 20 mm (RDBD$_{L=20}$) and 10 mm (RDBD$_{L=10}$). The DBD array with L = 10 mm (DBD$_{L=10}$) was not characterized due to strong filamentary streamers. However, the plasma emission of the DBD$_{L=10}$ is discussed. Each configuration is tested with four DBD stages. Since there are several air-exposed and embedded electrodes, an active electrode will be referred to as any air-exposed electrode.

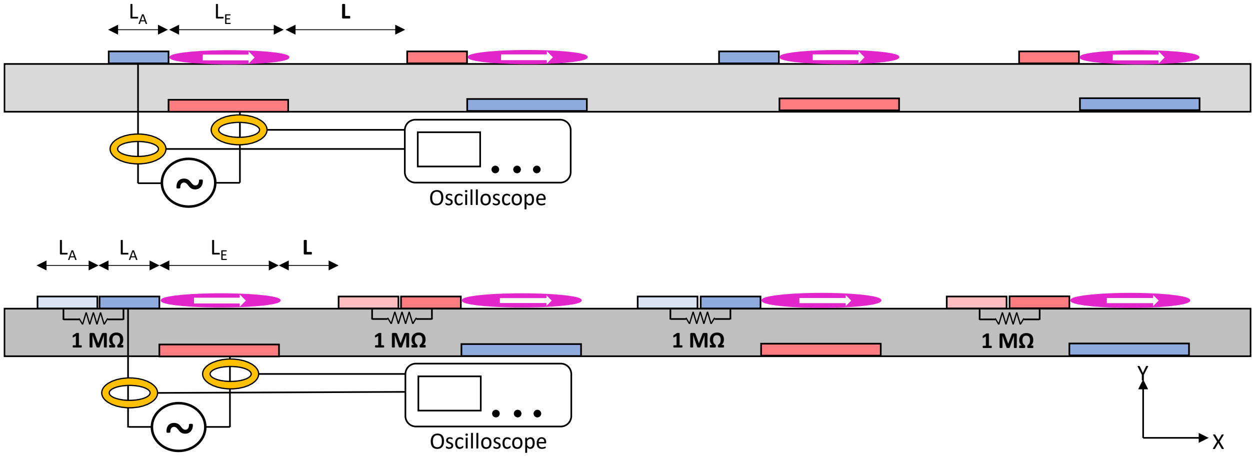

Figure 8.1. The experimental schematic of the alternating electrode DBD array (top) and “resistive” alternating electrode DBD array (bottom) with N = 4 stages. L_A represents the length of an air-exposed electrode, L_E represents the length of an embedded electrode, and L represents the spacing between each DBD actuator stage from the embedded electrode to the following air-exposed electrode. L_A and L_E are fixed at $L_A = 10$ mm and $L_E = 20$ mm. L varies from 10 mm to 20 mm depending on geometry. The electrodes are powered by a custom power supply with two out-of-phase high-voltage outputs similar to Thomas *et al.* [99]. The electrodes connected to the first air-exposed electrode (blue) are connected to one of the high-voltage outputs. In contrast, the alternating electrodes attached to the first embedded electrode (red) are connected to the second high-voltage output. In the resistive DBD array configuration, an additional electrode is placed before each air-exposed electrode and is connected by a 1MΩ resistor.

The dielectric barrier discharge is generated with a high-voltage AC between the active electrodes and the embedded electrodes. The active electrodes and the embedded electrodes are separated with a 3.175 mm quartz dielectric plate. The active electrodes (0.07 mm thick, 10 mm long, and 80 mm wide) are constructed of conductive copper tape and are flush-mounted directly to the top of the dielectric surface. The embedded electrodes (0.07 mm thick, 20 mm long, and 80 mm wide) are also constructed of conductive copper tape and are flush-mounted directly to the backside of the dielectric surface. The embedded electrode is encapsulated with a thick 2.5 mm layer of polyimide/Kapton layer (~7700 VPM @ 25°C) to ensure that there is no back-side discharge. There is no overlap between the active and embedded electrodes. All tests are conducted in quiescent atmospheric pressure air at ~20°C and between 40% and 60% relative humidity.

The active electrode and embedded electrode are connected to the custom dual-hot high-voltage power supply similar to that of Duong *et al.* [34] and Thomas *et al.* [99]. The custom power supply is comprised of a signal generator (Siglent 1032X), a power amplifier (Crown XLi 3500), and two custom high-voltage transformers (Corona Magnetics). All tests in this study use a fixed frequency *(f)* 2 kHz sine wave with voltage across the active and embedded electrode up to V_{pp} = 45 kV. Previous studies have shown that a sine waveform was the most efficient waveform for DBD actuation and the optimal frequency for DBD is approximately between 1.5 kHz and 4 kHz [12, 20, 154]. The output voltage applied to the active and embedded electrodes is monitored with a Tektronix P6015A high-voltage probe.

The DBD arrays are mechanically characterized by their direct horizontal thrust and time-averaged wall jets using the techniques outlined in Chapter 3. The thrust measurements are a standard gauge for the mechanical performance of DBD systems, while wall jet measurements allow for fluid analysis of the successively accelerated EHD jet. Similar to the previous sections, the direct thrust is measured by holding the actuator system vertically onto a sensitive and shielded force balance [99]. In this configuration, wall-parallel plasma-induced flow is directed away from the balance, and the reactive downward thrust is measured directly by the balance. For this study, the direct forces were measured with an Ohaus SPX622 analytical balance. To prevent electromagnetic interference (EMI) or electrostatic forcing to the scale, a metal shield / Faraday cage was placed around the scale, and the stand holding the plate rested on a non-conductive four-column stand that transferred the forcing from the plasma actuator assembly to the balance. Extremely thin conductive DBS (Drawn Brazed Strand) wire was used for all wire connections to the electrodes to ensure no tension or influence on the thrust measurements. All thrust data points were taken after the DBD thrust reached a steady state (typically < 2 seconds). Thrust readings were transferred from the scale to a computer through an electrically isolated USB cable and were averaged over three testing intervals of 10 seconds.

To measure and characterize the flow field, we employ a custom-made glass pitot tube with a 0.4 mm inner diameter and 0.8 mm outside diameter to measure the time-averaged x-velocity profile identical to previous sections. The expressions to derive the mass flow rate, momentum injection, and mechanical power are outlined in section 3.3.

The DBD array is electrically characterized by its current and power consumption. The current is measured using a 200 MHz bandwidth non-intrusive Pearson 2877 current monitor with a rise time of 2 ns on each HV output of the two transformers. The current monitor can be placed on either or both high-voltage wires, and it has been confirmed to produce the same current and power readings. The current monitor is connected to a Siglent SDS 2354X oscilloscope with a sampling rate of 1 GS/s to resolve up up 500 MHz based on the Nyquist sampling theorem. With the current monitor, we compute the total power and total efficiency. Several previous works including Debien *et al.* [64], Kreigseis *et al.* [150], Thomas *et al.* [99], and Hoskinson *et al.* [74] have presented force-power diagrams for single two-electrode DBD actuators across a range of frequencies and electrode geometries, and have found DBD actuator thrust to scale approximately linearly with power usage. These previous works have led to a dimensioned force efficiency commonly expressed as

$$\eta_{force} = \frac{F_{EHD}}{W_{elec}}. \qquad (21)$$

The DBD plasma emissions are captured to visualize the DBD actuator array. The DBD array plasma emissions are captured with a Nikon D750 DSLR camera with a Nikon AF-S NIKKOR 70-200 mm f/4G ED VR Zoom lens while the DBD array is mounted vertically. The camera is operated with an exposure time of 10 ms to capture the discharge emissions of 20 total discharge cycles.

8.2 Plasma Characteristics

This section presents and discusses the plasma emission characteristics of a four-stage DBD and RDBD array with and without alternating electrodes. A DBD array with non-alternating active electrodes and alternating-phase active electrodes is presented in Figure 8.2. When the active electrodes are in phase with each other (Figure 8.2.b), the downstream active electrodes create a reverse DBD towards the previously embedded electrodes, agreeing with previous literature [99]. The reverse DBD is generated because the air-exposed electrodes experience a potential difference from the previous embedded electrodes. When alternating the phase of each DBD stage (Figure 8.2.c), the cross-talk is effectively eliminated due to a potential difference between a previously embedded electrode and its following active electrode. Importantly, each active electrode still experiences a potential difference between its downstream embedded electrode to create a unidirectional plasma emission similar to that of Sato *et al.* [118]. While the $DBD_{L=10}$ with alternating-phase active electrodes demonstrates a reduction in cross-talk compared to the traditional in-phase DBD array, eventual sliding and then filamentary streamer discharge begins to occur at approximately $V_{p-p} > 40$ kV. Typically only seen in three-electrode DC-augmented

DBD cases [14], the sliding discharge has not been reported in any DBD array studies and the sliding discharge reflects an extension of the charges on the dielectric surface to the opposite-phased active electrode. In this special case, the horizontal thrust typically decreases with more sliding discharge as the ions more readily "slide" to the following active electrode without reacting with and transferring their momentum to surrounding neutral air molecules [14, 109]. The sliding discharge at the upper voltages suggests that alternating-electrode DBD arrays have an electrode geometric limit even when cross-talk is minimized. When the spacing is increased to L = 20 mm, the reverse discharge with in-phase active electrodes occurs at higher voltages and with less intensity due to the greater spacing. When the active electrodes are alternated, no sliding discharge is observed in the range of voltage up to 45 kV.

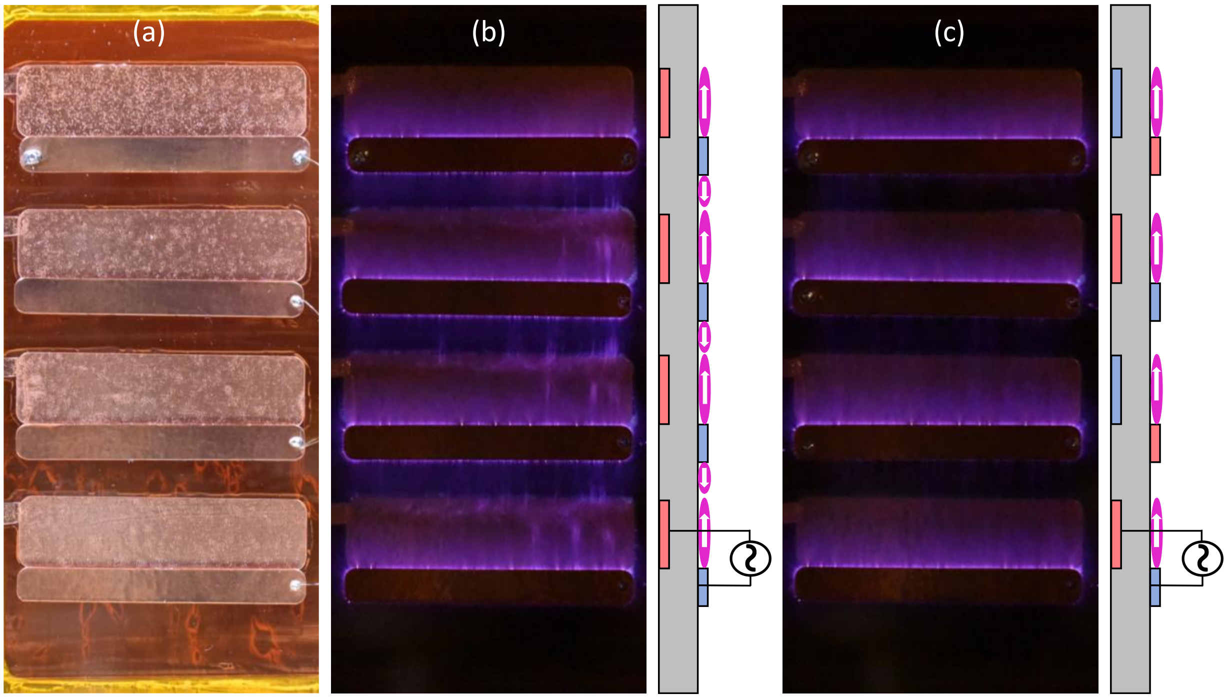

Figure 8.2. Plasma emissions of a four-stage DBDL=10 array (a) with in-phase active HV electrodes (b) and alternating-phase active HV electrodes (b). Both DBD arrays are powered at 40 kV / 2 kHz with a 10 ms exposure time to capture the plasma emission of 20 discharge cycles.

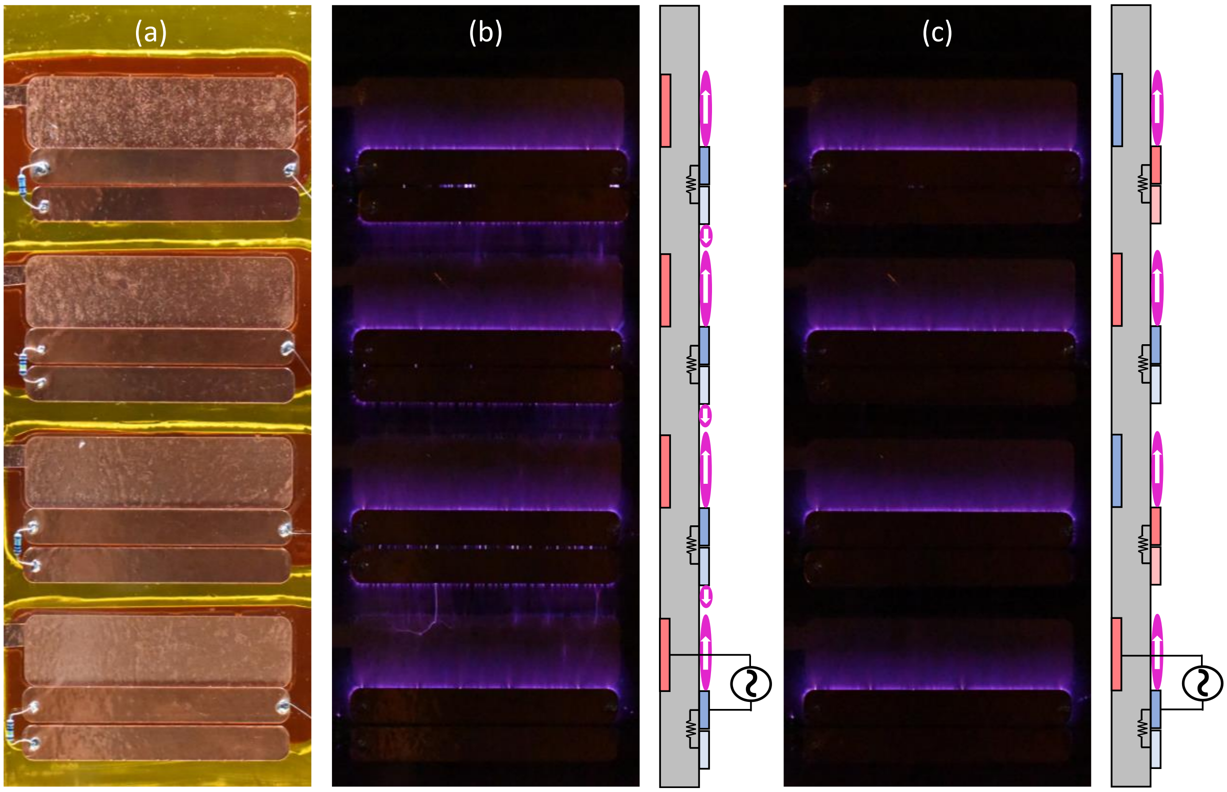

Figure 8.3. Plasma emissions of an RDBD$_{L=10}$ array (a) with air-exposed HV electrodes in series (b) and air-exposed HV electrodes alternating (b). Both DBD arrays are powered at 40 kV / 2 kHz with a 10 ms exposure time to capture the plasma emission of 20 discharge cycles.

Figure 8.3 shows an RDBD array with in-phase and alternating-phase active electrodes. When an additional electrode with a 1 MΩ resistor is added while maintaining the same L = 10 mm spacing, the RDBD$_{L=10}$ array experiences lower reverse discharge than the DBD$_{L=10}$ array for in-phase configuration (Figure 8.3.b). For alternating active electrodes (Figure 8.3.c), sliding and filamentary streamer discharge is delayed until higher voltages (> 45 kV), allowing for the DBD array to operate at higher voltages with greater thrust. The results of the AC RDBD array agree with the observations of the nanopulse DBD array reported by Sato *et al.* [118]. This work is the first to present plasma images of a unidirectional DBD array with a sinusoidal AC waveform. Like the DBD array without a resistor, the RDBD array does not show reverse or sliding discharge L = 20 mm spacing at operating voltages.

8.3 Thrust Characteristics

The thrust characteristics of the DBD array and RDBD array are discussed in this section. The DBD array configurations are found to scale linearly with the number of DBD stages before sliding and filamentary discharge onset. The thrust at varying voltages and number of DBD stages are plotted for the $DBD_{L=10}$, $RDBD_{L=20}$, and $RDBD_{L=10}$ in Figure 8.4

The linear thrust scaling with up to four DBD stages supports the plasma observations that each DBD stage behaves independently of each other when the active electrodes are phase-alternating and without any filamentary streamers or sliding discharge. The simple $DBD_{L=20}$ array experienced sliding and filamentary streamer discharge at $V_{p\text{-}p}$ = 45 kV, destabilizing the thrust, therefore, the $DBD_{L=20}$ array is tested only up to $V_{p\text{-}p}$ = 40 kV. In comparison, the $RDBD_{L=10}$ array began to exhibit an onset of sliding discharge at $V_{p\text{-}p}$ = 45 kV, however the thrust was stable. With a spacing of L = 20 mm, the $RDBD_{L=20}$ array reached a maximum thrust of 251 mN/m with N = 4 stages at 45 kV without the onset of sliding discharge or filamentary streamers. The $DBD_{L=20}$ array reached a maximum thrust of 181 mN/m with N = 4 stages at 40 kV and similar L = 20 mm spacing. The $RDBD_{L=20}$ array recorded a thrust of 183 mN/m at the same 40 kV, suggesting that the resistor likely does not significantly improve momentum transfer from each DBD stage and primarily prevents early transition to sliding and filamentary streamer discharge.

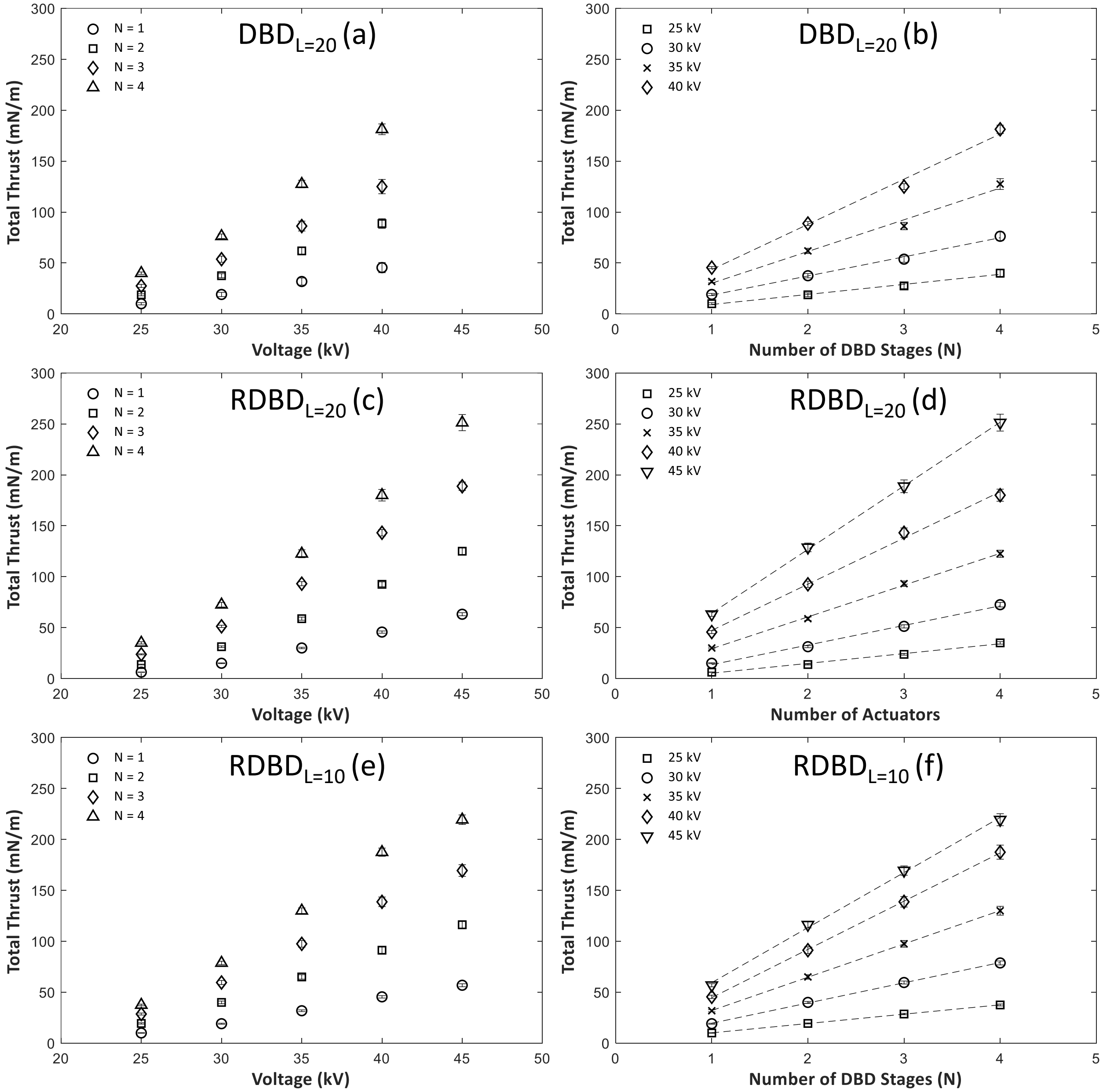

Figure 8.4. DBD$_{L=20}$ array thrust at varying voltages (a) and DBD stages (b), RDBD$_{L=20}$ array thrust at varying voltages (c) and DBD stages (d), and RDBD$_{L=10}$ thrust at varying voltages (e) and DBD stages (f). The DBD$_{L=20}$ array experienced filamentary streamers above 40 kV, while the RDBD$_{L=20}$ array and the RDBD$_{L=10}$ array withstood 45 kV before any filamentary streamers or arcing. The standard deviation of the time-averaged thrust across the three sampling periods for each data point is approximately 3%.

For the RDBD array, the maximum thrust at 45 kV decreased from 251 mN/m to 219 mN/m (a 12% decrease) when the spacing was reduced from L = 20 mm to L = 10 mm. While the RDBD$_{L=10}$ at 45 kV did not experience filamentary streamers, the decrease in mechanical performance at this maximum voltage is attributed to the onset of sliding discharges. In this case, the extended ions expelled from one stage reach the sequential air-exposed electrode, limiting momentum transfer to the surrounding air molecules. Before sliding discharges, the $\mathrm{RDBD}_{L=10}$ array shows 187 mN/m of total thrust at 40 kV, nearly equal to the thrust of the $\mathrm{RDBD}_{L=20}$ array. The similar force before the onset of sliding discharges highlights that the DBD stages produce an EHD force independent of each other at lower voltages with an alternating electrode configuration. However, the proximity of DBD stages to each other is a critical limiting factor due to the transition to sliding discharge.

Compared to previous and recent works, these results demonstrate linear thrust scaling for the first time in a DBD array with conventional electrical parameters at significantly higher voltages and thrust than previous literature. Using a custom pulsed-DC waveform, Sato *et al* [118] demonstrated the linear thrust scaling up to ~80 mN/m with a four-stage DBD array, significantly lower than the demonstrated maximum 251 mN/m thrust with the four-stage RDBD array. Thomas *et al.* [99] varied electrode widths and electrical waveforms, and found that a three-stage DBD array (N = 3) experienced at best ~2.4x the force of a single-stage DBD actuator.

At the highest tested voltage of 45 kV, the $\mathrm{RDBD}_{L=20}$ array has a maximum thrust per stage of 62.7 mN/m while the $\mathrm{RDBD}_{L=10}$ has a maximum thrust per stage of 56.5 mN/m. At 40 kV, the simple $\mathrm{DBD}_{L=20}$ array has a scaling of 43.8 mN/m, 5% lower than the 46.3 mN/m of the $\mathrm{RDBD}_{L=20}$. The improved thrust scaling of the RDBD array with L = 20 mm compared to the same array with L = 10 mm suggests that further spacing between each DBD stage can help with ion acceleration even in the presence of the resistor. Another possible explanation for a slight decrease in performance with the smaller spacing is slight repulsion from the next in-phase HV electrode. For example, ions accelerated from an air-exposed active electrode may experience a wall-normal repulsion from the embedded electrode of the next DBD stage as the two electrodes are in phase with one another. This adverse interaction may be minimized by introducing a gap between each air-exposed electrode and its embedded electrode, however, further testing is necessary.

8.4 Velocity Characteristics

X-velocity profiles of the DBD array across its multiple stages provide insight into the fluid dynamic behavior of the arrays' successive acceleration and linear scaling. Figure 8.5 shows the x-velocity across the $RDBD_{L=20}$ array at a fixed y-height and fixed x-position on the surface. Figure 8.6 shows the x-velocity across the $DBD_{L=20}$ array at a fixed y-height and the velocity-derived thrust compared to the directly measured thrust for the two geometries.

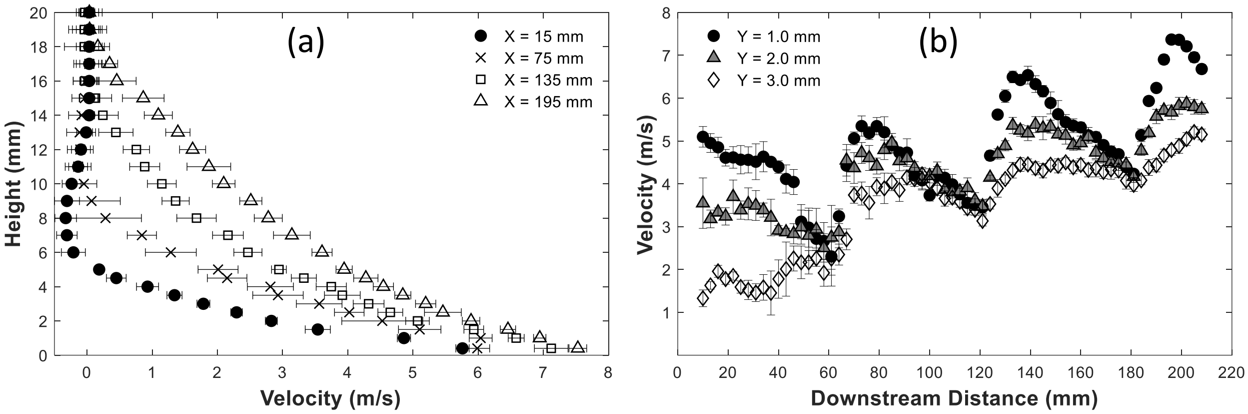

Figure 8.5. X-velocity profile of the $RDBD_{L=20}$ array at 40 kV at varying heights above the dielectric surface at a fixed x-position (a) and varying downstream distances at a fixed y-height (b). The starting x = 0 mm position corresponds to the edge of the first active electrode and the chosen x-positions for control volume analysis correspond to 15 mm after each active electrode. Two standard deviation error bars are plotted.

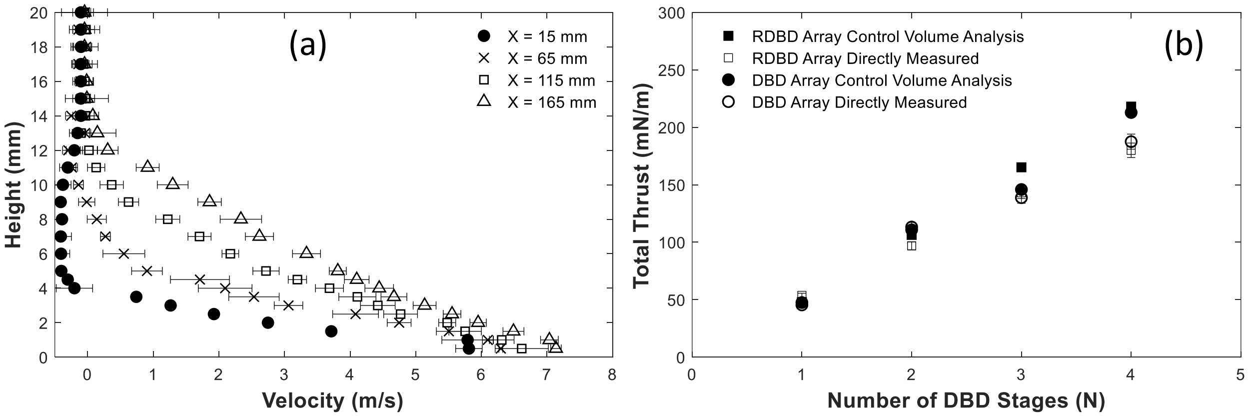

Figure 8.6. X-velocity profile of the $\mathrm{DBD}_{L=20}$ array at 40 kV at varying heights above the dielectric surface at a fixed x-position (a). The starting x = 0 mm position corresponds to the edge of the first active electrode and the chosen x-positions correspond to 15 mm after each active electrode. The velocity-derived thrust using eq.(17) is compared to the directly measured thrust after each DBD stage (b). Two standard deviation error bars across the >20 s sampling period are plotted.

In both the DBD and RDBD array configuration, the EHD jet after the first stage is greater than 5.5 m/s at the y = 0.4 mm, and the jet increases after each DBD stage up to a maximum velocity after its fourth stage. The $\mathrm{RDBD}_{L=20}$ array has a maximum velocity of V_{max}= 7.4 m/s while the simple $\mathrm{DBD}_{L=20}$ array recorded a similar V_{max} = 7.1 m/s. Interestingly, both configurations show a drop in x-velocity directly above the active electrode of each stage, before the next plasma discharge (Figure 8.5.b). This velocity reduction did not occur in AC-powered three-electrode systems with two exposed electrodes, such as the out-of-phase AC-augmented DBD actuator [15]. This drop in velocity is likely due to the additional mixing of the wall jet and the quiescent air during the momentum injection by the downstream stage (Figure 8.5 and Figure 8.6). This hypothesis is also supported by the thickening of the wall jet profile at each consecutive stage. Between the two configurations, the simpler $\mathrm{DBD}_{L=20}$ array has a thinner wall jet after the fourth stage due to less mixing over the shorter area.

The vertical velocity profiles are integrated at 15 mm past each active electrode stage to derive the total momentum after each stage (Figure 8.6.b). The velocity-derived thrust through control volume analysis around each stage is compared to the directly measured thrust. The two methods agree well and within 10%, similar to Dursher and Roy [119]. Additionally, wind tunnel studies on DBD actuators in external co-flow support the linear thrust scaling in a DBD array. Tang *et al.* [13] and Pereira *et al.* [97] demonstrated that a DBD actuator thrust and power consumption is independent of external flow. The scaling of the DBD array is similar to a DBD in external co-flow because each subsequential DBD stage injects momentum into a pre-existing fluid jet. Unlike a typical DBD actuator with a typical wall jet thickness <5 mm, the DBD array is found to produce a wall jet thickness of ~ 20 mm. With a velocity-derived momentum of 202 mN/m at 40 kV at 2 kHz, the wall jet of the multi-stage DBD array in this study's resistive and simple configuration is significantly thicker and with more momentum than currently published literature. While the authors are not aware of any literature demonstrating a wall jet with > 100 mN/m, the V_{max} is lower compared to similar DBD array works, including Debien *et al.* [64], which used a wire-to-plate configuration for a V_{max} = 10.5 m/s at y = 0.6 mm after 4-stage DBD array. The difference may be attributed to the geometric differences, such as a gap between the active wire and embedded electrodes or relatively long active electrodes used in this work. Additional time-resolved flow field measurements and modeling efforts can shed insights into the complex plasma flow interaction in the array.

8.5 Electrical Characteristics

The electrical power consumption of the DBD arrays is discussed in this section. Figure 8.7 displays the total power consumption results derived from the current monitor with a simple and resistive DBD array.

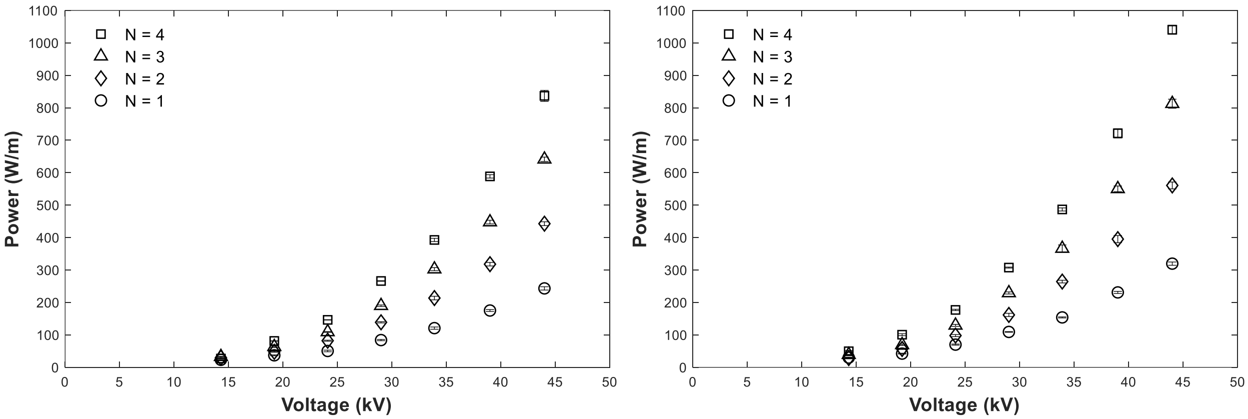

Figure 8.7. DBD Array power usage scaling with a simple $DBD_{L=20}$ array (left) and $RDBD_{L=20}$ array (right) with a fixed L = 20 mm gap. Two standard deviation error bars across a minimum of 10 voltage cycles are plotted. The simple DBD array was tested at 45 kV; however, filamentary streamers began to form at the highest voltage.

Like the mechanical thrust performance, the electrical power for both the $DBD_{L=20}$ array and the $RDBD_{L=20}$ array is found to scale linearly with the number of DBD actuator stages, supporting that each DBD stage acts independently from one another. Before the sliding discharge, the $RDBD_{L=10}$ also demonstrated linear power scaling with the number of DBD stages. For a single simple DBD, the power usage approaches 220 W/m at the maximum voltage of 45 kV and matches previous power usage results for single DBD actuators with a similar dielectric thickness and voltage [20]. The maximum power usage of the four-stage simple $DBD_{L=20}$ array and $RDBD_{L=20}$ array is approximately 840 W/m and 1080 W/m, respectively, at 45 kV. With the same spacing between each DBD stage, the increase in power for the resistive DBD array is attributed to the additional high-voltage electrode with a resistor that also increases the effective area and capacitance within the dielectric. Using Fast-Fourier Transform (FFT) analysis to identify the capacitive current similar to previous works [12, 14], the electrical measurements support that the RDBD array at 40 kV uses ~74% of its total power usage as capacitive power while the simpler DBD array uses ~64% of its total power as capacitive power.

8.6 Force Efficiency and Total Efficiency

With thrust, mechanical power, and electrical power measurements across varying voltages and the number of DBD stages, the force efficiency and total efficiency of the DBD and RDBD array are calculated and discussed in this section. The electrical power measurements of the simple and resistive DBD array are found to scale linearly with the total thrust across the range of DBD stages and at varying voltages as shown in Figure 8.8.

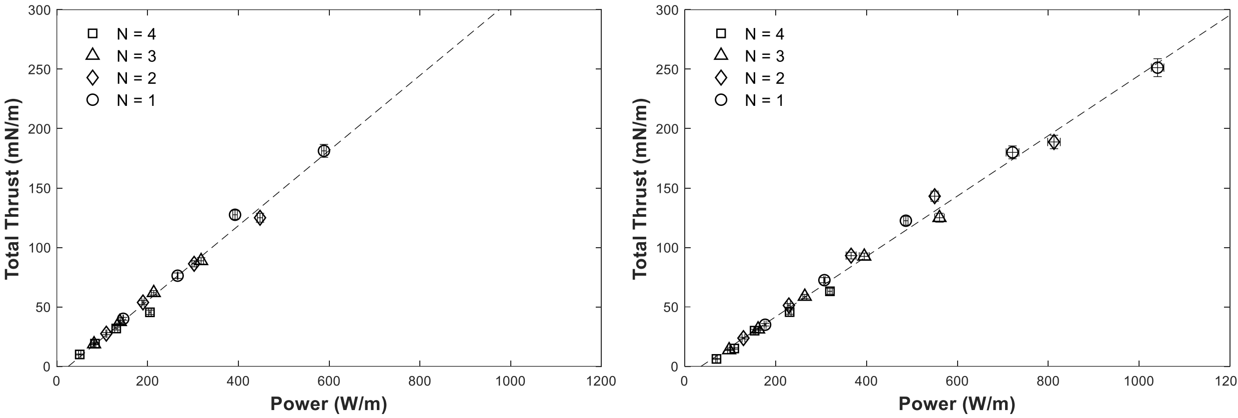

Figure 8.8. Total thrust scaling with power usage of $\mathrm{DBD}_{L=20}$ array and $\mathrm{RDBD}_{L=20}$. Two standard deviation error bars in power (horizontal) and thrust (vertical) are plotted.

The slope of the thrust-to-power graph represents the force efficiency, η_{force}, defined in eq. (21) and η_{force} is most commonly expressed in mN/W. The simple $\mathrm{DBD}_{L=20}$ array is found to have a force efficiency of $\eta_{force} = 0.316$ mN/W, while the $\mathrm{RDBD}_{L=20}$ demonstrated an efficiency of $\eta_{force} = 0.254$ mN/W. This work is the first to define a force efficiency for a simple DBD array and RDBD array with a conventional AC waveform. The DBD array force efficiencies strongly agree with previously published AC-powered two-electrode DBD results, including the $\eta_{force} = 0.25$ mN/W of Kreigseis *et al.* [150]. Sato *et al.* [118] reported a $\eta_{force} = 0.06$ mN/W using a custom pulsed-DC waveform and is the only currently published work with a DBD array force efficiency. Greater force efficiency is generally achieved with thicker dielectrics to decrease the system's capacitance as noted in Jolibois *et al.* [155]. A summary and comparison of recent force and total efficiencies is presented in Table 8.1.

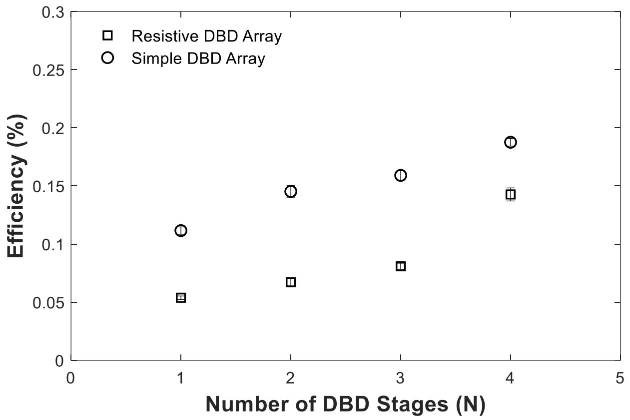

Figure 8.9. Total Efficiency of $DBD_{L=20}$ and $RDBD_{L=20}$ at 40 kV / 2 kHz.

Figure 8.9 shows the total efficiency of the two DBD arrays with varying DBD stages for 40 kV. Between the simple and resistive arrays, the RDBD array has a lower force efficiency and total efficiency across all numbers of DBD stages at 40 kV. The total efficiency of ~0.1% for a single-stage two-electrode DBD agrees with previous experiments [156, 157]. Interestingly, both DBD array configurations increase in total efficiency with the number of DBD actuator stages. This increase in efficiency with the number of DBD stages is likely due to the AC augmentation mechanism in the alternating (out-of-phase) exposed electrode configuration. For example, our recent work [15] demonstrates improvement in the performance of a planar DBD actuator by utilizing an AC-augmented electrical field in a three-electrode geometry. Time-resolved electrical and optical measurements, velocity profiles, and direct thrust measurements were used to characterize the EHD augmentation. The third electrode, the "pull" action, increased the EHD forcing by up to ~ 40%. The continuous plasma acceleration regions also reduce the viscous losses to the wall.

The RDBD array's lower efficiency than the simple DBD array suggests that the increased power usage due to the added electrode and resistor does not proportionally increase thrust for the same voltages. For example, the $RDBD_{L=20}$ generated approximately the same thrust as the simple $DBD_{L=20}$ at the same voltages before sliding or filamentary discharge. Therefore, since the RDBD array can be operated at a higher voltage, the primary advantage of the RDBD array is its greater maximum operating voltages and thrust. A disadvantage of the RDBD array is the added manufacturing complexity, space requirement, and efficiency. Given a need for efficiency or maximum thrust, each configuration can be uniquely considered for applications requiring a more robust DBD array. Future research efforts should further explore how resistors and other electrical components delay the formation of filamentary streamers and sliding regions, enhancing ion-momentum transfer.

Table 8.1. Summary of force and total efficiency. * Shows the range of efficiencies between 1 and 4 DBD stages.

	Configuration	Dielectric (thickness)	Waveform	P-P Voltage (kV)	Frequency (kHz)	η_{force}	η_{total}
Presented work	Planar – planar (DBD Array) (RDBD Array)	Quartz (3.175 mm)	Sine	25 – 45	2.0	0.25 0.32	(0.05 - 0.14)* (0.11 - 0.19)*
Sato *et al.* [118]	Planer – planer (RDBD Array)	Polyimide (0.32 mm)	Nanosecond Pulsed DC	8	0.5 – 2.0	0.05 – 0.07	N/A
Kriegseis *et al.* [150]	Planar – planar (Single DBD)	Polyimide (0.4 mm)	Sine	5 – 15	8.0 – 13.0	0.25	N/A
Hoskinson and Hershkowitz [158]	Wire – planar (Single DBD)	Polyester (0.25 mm)	Ramp	12 – 16	1.0	0.04 – 0.7	N/A
Benard and Moreau [154]	Planar – planar (Single DBD)	PMMA (3 mm)	Sine Square Ramp	40	1.5	0.64 0.37 0.22	N/A N/A N/A
Enloe *et al.* [159]	Planar – planar (Single DBD)	N/A	Sine	6 – 18	5.0	0.12	N/A
Debien *et al.* [64]	Planar – planar (Single DBD)	PMMA (3 mm)	Sine	24 – 44	1.5	0.65	0.06 – 0.18
Thomas *et al.* [99]	Planar – planar (Single DBD	Quartz (6.35 mm)	Sine	20 – 70	1.0 – 8.0	0.09 – 0.25	N/A
Ferry and Rovey [160]	Planar – planar (Single DBD)	Polyimide (0.2 mm)	Sine	6 – 9	1.0 – 18.0	0.02 – 0.1	N/A
Jolibois and Moreau [155]	Planer – planar (Single DBD)	PMMA (3 mm)	Sine Square Ramp Trapezoid	16 – 52	1.0	N/A	0.01 – 0.09

8.7 Discussions

Compared to previous works, these results demonstrate linear thrust scaling for high power density DBD arrays with voltages. Sato *et al.* [118] demonstrated the linear thrust scaling up to

~80 mN/m with a four-stage DBD array, significantly lower than the shown maximum 251 mN/m thrust with the four-stage RDBD presented here. Thomas *et al.* [99] varied electrode widths and electrical waveforms and found that a three-stage DBD array (N = 3) experienced, at best, ~2.4x the force of a single-stage DBD actuator, showing diminishing array efficiency.

The compounded effect of the DBD stages on momentum injection and overall trust is analogous to co-flow momentum injections into the existing flow profile. Our recent work shows that for the laminar boundary layer, the momentum injection by the DBD actuator in co-flow is nearly identical to the momentum injection into the quiescent environment [13]. For the DBD array (in laminar flow), each subsequent momentum injection is independent of the previous ones, which allows for building the overall wall jet momentum over the array's length. This work does not address the effect of turbulent mixing, typically present in the free stream flow, on array momentum injection.

The high efficiency of the array is linked to the AC augmentation of the primary DBD discharge in the alternating (out-of-phase) exposed electrode configuration. The mechanism described by Tang *et al*. [15] shows the benefits of the third electrode, similar to the alternating electrode configuration in this work. The third electrode, the "pull" action, increased the EHD forcing by up to ~ 40%. The continuous plasma acceleration regions also reduce the viscous losses, resulting in higher momentum injection.

8.8 Conclusion

In conclusion, this is the first report demonstrating a high-powered scalable DBD array actuator with minimal interference between each DBD stage and thrust greater than 250 mN/m. The DBD arrays are tested in two geometries with a conventional AC waveform with up to four alternating-phase DBD stages: (i) a simple DBD array with each DBD stage consisting of the traditional air-exposed electrode and an embedded electrode and (ii) a "resistive" DBD array with each DBD stage consisting of two air-exposed electrodes connected by a 1 MΩ resistor and an embedded electrode. Across multiple voltages and DBD stages, the results show a linear relationship between power consumption and thrust for both DBD array configurations before the onset of adverse sliding or filamentary streamer discharge. The added resistor in the RDBD array was found to delay the onset of sliding and filamentary discharge, allowing for higher voltage operation and greater thrust. However, the simple DBD array was more efficient because the added electrode and resistor increased electrical power consumption without improving momentum transfer from the plasma discharge. With an increase in total efficiency with each additional DBD stage, the presented results allow for more robust applications of DBD actuation with significantly greater forces and efficiencies than previously demonstrated. The limitation of this work includes average velocity measurements that do not allow for the study of the temporal effects of the EHD flow interaction. Future work should consider experiments in the turbulence boundary layer and realistic geometries relevant to active flow control applications.

Chapter 9. Effect of Active Electrode Shape in a DBD Array

This section explores and presents a multi-electrode DBD array with serrated edges. Since the geometry is different, this information does not build directly upon the previous section on straight-edged DBD arrays. Based on previous experiments [42], a serrated DBD produced more thrust than a straight edge, and it was hypothesized that a dual serrated DBD could produce significantly more thrust than its straight-edge counterpart.

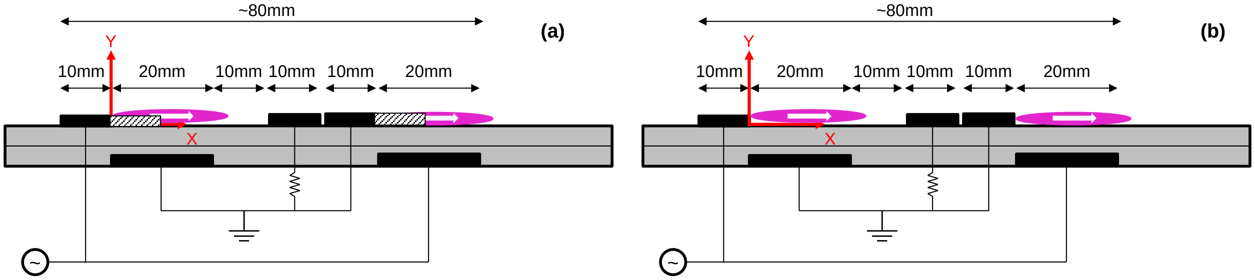

Figure 9.1. Schematic of dual serrated-edged DBD array (a) and the original dual straight-edge DBD array (b)

Figure 9.2. Serrated-Edged DBD Array

The dual-serrated DBD array is shown above in Figure 9.1 and Figure 9.2. Since the serrated edge is now extended over the embedded electrode, the distance from the tip to the next DBD array is shorter than its straight-edged counterpart. For these tests, a range of frequencies from 3 kHz – 5 kHz was tested. The results of the horizontal thrusts are presented below in Figure 9.3. In these tests, the straight-edged dual DBD array performed better than the serrated counterpart. This is believed to be due to the more vorticity and 3D flow profile generated by the serrated compared to the straight-edged DBD array, resulting in significantly more viscous losses in the serrated-edged DBD case. While the serrated-edge DBD array may not create as much linear momentum as the straight-edge, the added vorticity may be beneficial for some applications such as turbulent boundary layer control.

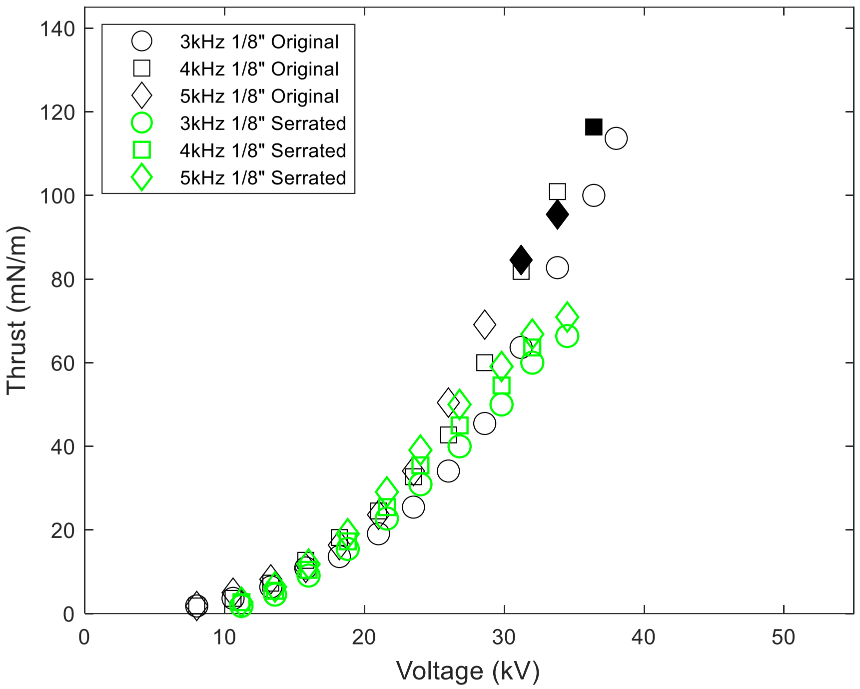

Figure 9.3. Serrated-Edged DBD Array

Chapter 10. Active Flow Control of a Clark Y Airfoil

This section applies an optimized DBD array plasma actuator to a Clark Y airfoil to demonstrate active flow control authority. Several studies have demonstrated DBD actuation on traditional airfoils [98-101], multi-element airfoils [102], flaps [103, 104], and in aircraft applications [38, 70, 161]. Some applied work [42, 103, 162] considered a single DBD actuator mounted in a co-flow orientation and demonstrated an ability to change aerodynamic performance, typically by increasing airfoil lift, decreasing drag, or changing pitching moment. The improved control authority can be achieved based on the recent advancements in DBD arrays, such as DBD augmentation [14, 15] and DBD array optimization [64, 72]. In the DBD arrays, each DBD electrode pair can be operated out-of-phase with the previous DBD pair, which minimizes adverse crosstalk between the stages.

While bench-scale experiments are relatively straightforward, very few researchers have reported on the performance of multi-stage DBD in wind tunnels. Moreau *et al.* [163]

demonstrated the use of a three-stage DBD array with alternating phase electrodes on a NACA 0015 airfoil showing separation delay but did not characterize the lift and drag performance. To our knowledge, no studies have experimentally explored enhancing an asymmetric airfoil with an improved alternating phase DBD array, nor have they presented force measurements on an airfoil with a multi-stage DBD actuator.

This section reports aerodynamic forces on an airfoil equipped with a two-stage DBD array with alternating phase DBD stages. The actuator is mounted in co-flow orientation on the Clark Y airfoil. Wind tunnel experiments were performed in 5 – 25 m/s windspeed range; lift and drag forces were analyzed to evaluate the effect of increasing momentum injection on the suction side of the airfoil. The results of this section are published in the 2025 AIAA SciTech conference proceedings.

10.1 Experimental Setup

10.1.1 Wind Tunnel

The experiments were conducted in an open return subsonic wind tunnel at the University of Washington, which has a 0.7 m × 0.383 m rectangular cross-section and a 1.2 m long test section (Figure 10.1). The tunnel consists of a modular inlet with 10 honeycomb screens to condition the flow. The inlet precedes a settling chamber and a 10:1 contraction cone that attaches to the test section. The sidewalls of the test section are plexiglass, allowing for optical access. Downstream of the test section is a diffuser section connected to a 40 hp, 3-phase 460 VAC blower controlled by a variable frequency drive (VFD) motor. The wind tunnel can operate at external flow up to $U\infty = 35$ m/s. The flow speed through the test section is monitored by a calibrated Ashcroft CXLdp (10 IWC) differential pressure gauge. Typical turbulence intensity is ~ 1%, measured by hot-wire anemometry. Hot-wire anemometry is not used during DBD operations to prevent electrical interference with the HV current. Experiments were performed at atmospheric pressure, room temperature of ~ 20°C and a typical relative humidity of ~ 40 - 50%.

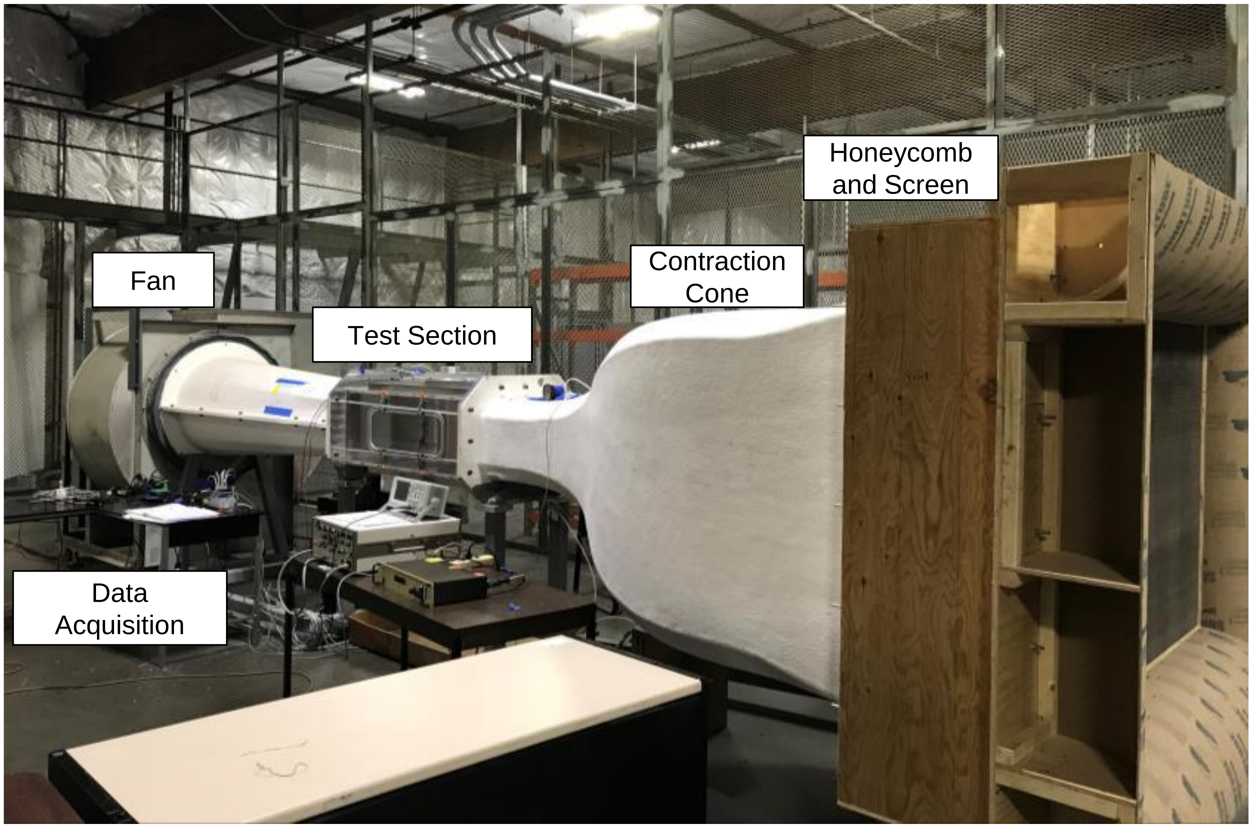

Figure 10.1. The University of Washington Sam Wilson 0.7 m x 0.383 m Wind Tunnel.

This wind tunnel is equipped with two sets of load cells designed to test 2D wings. While the wind tunnel does not currently allow for optical measurements, one main advantage of the 2D wind tunnel is that wires necessary for high-voltage operation can be routed through the center of airfoils and to the bottom of the wind tunnel.

The wind tunnel is designed for 2D airfoils such that the two ends of the airfoil are mated to a top and bottom plate that are flush mounted inside the test section to minimize three-dimensional flow effects and airfoil edge effects. The wing assembly with the load cell and stepper motor system is shown in Figure 10.2. The top and bottom plate is machined of rigid, nonconductive polyurethane foam (Obomodulan terracotta). The mounting plates are allowed to rotate. The rigid assembly of the airfoil and mounting plates is connected to a cylindrical bearing on the top plate and rests on an air bearing (New Way Air Bearings) on the bottom. The top and bottom plates that hold the airfoil are each connected to a system of two lift load cells (SMD Sensors S230 rated to 40 lbs each) and one drag load cell (SMD Sensors S215 rated 4 lbs each). The total lift capacity of the wind tunnel is 160 lbs, and the total drag capacity is 8 lbs. A National Instruments (NI) 9237 strain gauge amplifier connects to the strain gauges, and a data acquisition (DAQ) PC with a NI DAQ 9174 reads the force measurements. The DAQ PC is also connected to a stepper motor to rotate the airfoil assembly and an optical encoder positioning system (Avago AS 38). The optical encoder monitors the angle of attack, α, with an accuracy of ± 0.02 degrees, creating a closed-loop control system. For these experiments, the angle of attack was varied from α = -2 – 15 degrees. To compare the forces on the airfoil with or without DBD actuation, we measured the forces for all load cells in three intervals of 10s and then averaged the measurements. The coefficient of lift (C_L) and coefficient of drag (C_D) is then calculated using the averaged total lift and drag across the respective cells. C_L is defined as

$$C_L = \frac{2L}{\rho \mathrm{U}_\infty{}^2 A} \tag{22}$$

where L is the total lift force on the airfoil, ρ is the air densityU_∞ is the freestream velocity, and A; is the airforce chord length per unit length. The C_D is similarly defined as

$$C_D = \frac{2D}{\rho \mathrm{U}_\infty{}^2 A} \tag{23}$$

where D is the total drag force on the airfoil.

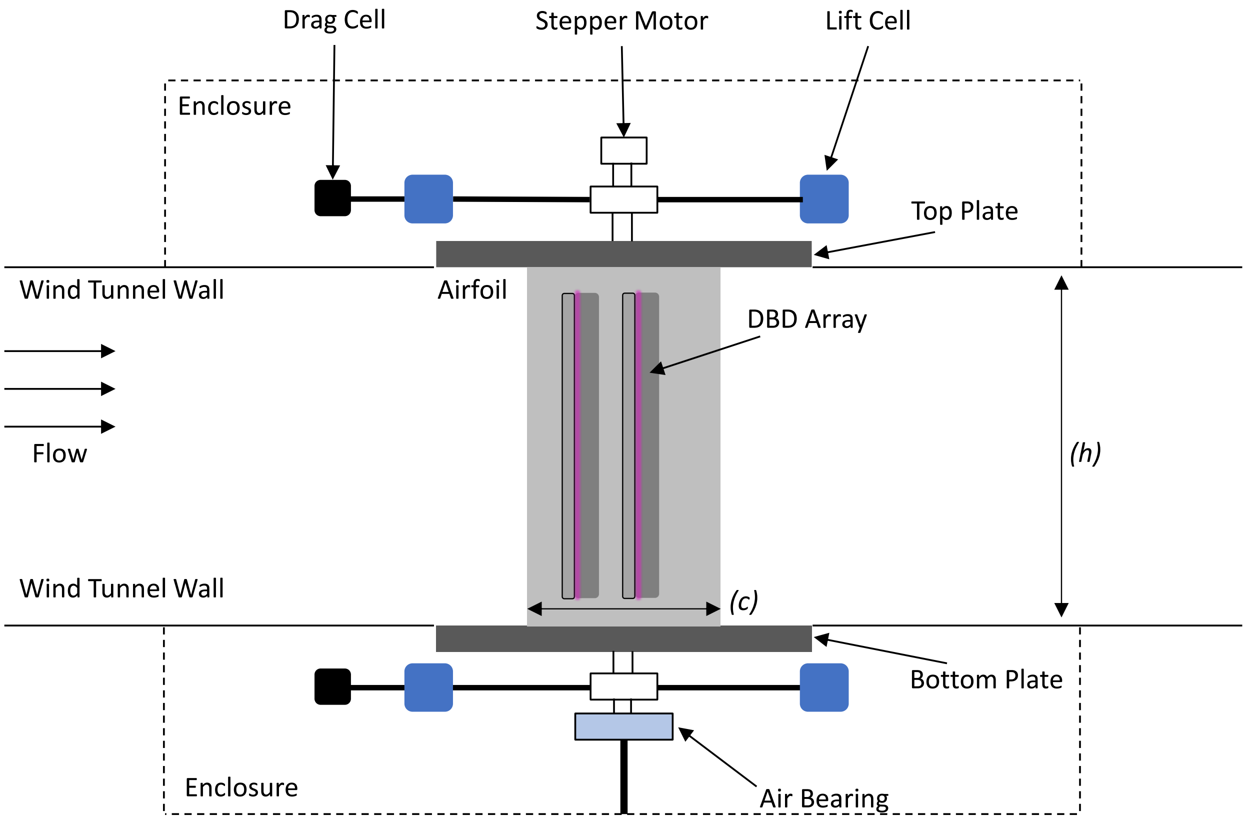

Figure 10.2. Experimental schematic for lift, drag, and pitching moment measurements with angle attack control. The bottom and top plates sit flush with the wind tunnel wall, and the airfoil assembly rests on an air bearing. Electrically grounded metal walls surround the load cells to prevent electrical interference.

10.1.2 DBD Actuator and Airfoil

In this study, a two-stage DBD array actuator is flush-mounted to the Clark Y airfoil's top surface (suction side). The dual DBD actuator configuration consists of two sets of two-electrode DBDs separated by a dielectric barrier, similar to previous work [12]. In each DBD stage, the active electrode is exposed to air, while the ground is encapsulated beneath the dielectric layer, which separates them. The two DBD stages are electrically out-of-phase from one another to minimize crosstalk, as proposed by Sato *et al.* [118]. The dielectric is a 1.65 mm (0.065") layer of Kapton polyimide film. The air-exposed electrodes are 10 mm long and 304.5 mm wide. The embedded electrodes are 20 mm long and 304.5 mm wide, with no overlap between the active and ground electrodes. The thickness of both electrodes is 0.25 mm. The overall electrode geometry on the airfoil is shown in Figure 10.3. Benchtop thrust tests determined the length of the electrodes and the gap between the two DBD stages to confirm minimal crosstalk. Kapton is widely used in DBD research and has a dielectric constant of 3.4 with a breakdown strength of ~3000 V/mil [20]. The embedded electrode is encapsulated with a thick 3.175 mm silicone rubber layer. The electrodes are excited with a fixed potential alternating current (AC), with the applied DBD voltage, V_{DBD} = 25, 30, 35, and 40 kV (peak-to-peak) at f = 2 kHz. The high-voltage is provided by a custom power supply similar to Duong *et al*. [34]. Briefly, the custom power supply comprises a Siglent SDG1032X signal generator, a Crown XLi 3500 power amplifier, and a custom high-voltage transformer (Corona Magnetics) rated up to 70 kV peak-to-peak voltage (V_{pp}) each. The voltage from the power supply is monitored with a Trek P6015a high-voltage probe connected directly to the high-voltage output.

We first constructed the dual DBD actuator array outside the airfoil with the dielectric layer between the electrodes and back encapsulation. This assembly was then mounted in co-flow in a divot on a Clark Y airfoil's suction side, allowing the actuator to sit flush with the wing's surface. Before tests with DBD actuation, this study first characterizes the Clark Y airfoil with a DBD array installed but without any HV power to determine any changes in the baseline aerodynamic properties of the modified airfoil. This asymmetric airfoil is chosen for its high lift properties at low Reynold's numbers and well-established aerodynamic effects. The airfoil has a 190.5 mm chord (c) and 381 mm span (h), shown in Figure 10.3, with the electrodes, dielectric, and encapsulation. The chord length of the airfoil was determined to minimize the blockage effects at high angles of attack while maintaining the Reynolds number. The airfoil was 3D printed using polylactic acid (PLA). The Reynolds number for a 2D airfoil is defined as

$$Re = \frac{\rho \mathrm{U}_\infty L_c}{\mu} \tag{24}$$

where L_c is the airfoil's chord length, and μ is the fluid's dynamic viscosity. With a chord length of 190.5 mm and $5\ \mathrm{m/s} < \mathrm{U}_\infty < 25\ \mathrm{m/s}$, the Reynolds number for this study ranges from approximately *Re* = 60,000 – 315,000.

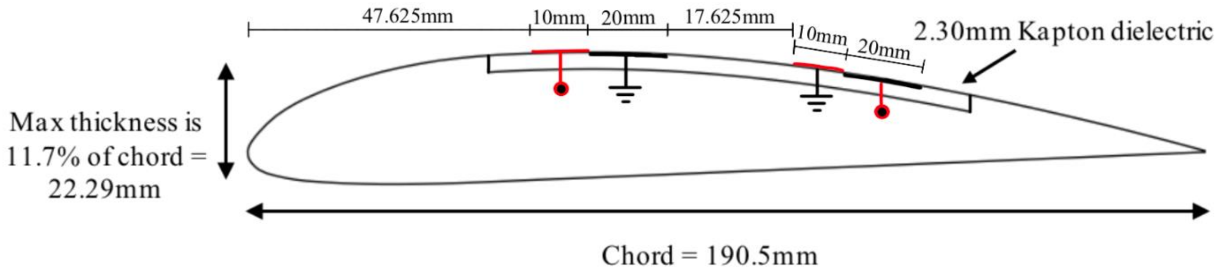

Figure 10.3. Diagram for Clark Y airfoil with dual DBD configuration.

The Clark Y airfoil's high lift and low drag characteristics at low Reynolds numbers allow for a more significant impact from the EHD forcing of plasma actuators. The gap between the two electrodes was determined through benchtop optimization. Previous studies have demonstrated that the most significant impact of a single DBD actuator stage is when the actuator is positioned near the airfoil's quarter chord or its leading edge [163]. Here, we position the first DBD stage at quarter-chord and the second DBD stage at approximately half-chord. The actuator is oriented for co-flow EHD momentum injection, i.e., in the same direction as the external flow.

10.2 Results

10.2.1 Effect of Embedded DBD Actuator

The Clark Y airfoil is designed to flush-mount the DBD actuator. However, slight protrusion of the electrodes and imperfect contouring of the dielectric lightly alters the baseline aerodynamic performance of the Clark Y airfoil. Thus, the aerodynamic effect of the plasma actuator as a geometric addition without the presence of high voltage is explored first. These tests validate force measurements for the Clark Y airfoil, which can be compared to previously published experimental Clark Y results [164-166]. With a bare Clark Y airfoil, the lift and drag results at Re = 180k agree well with the previous literature. For the airfoil with actuators (and not powered), the aerodynamic characteristics of the airfoil change slightly. Most notably, the lift increases by ~ C_L = 0.1 at low angles of attack, but the lift and drag characteristics are similar during and after separation. This increase in lift is mainly due to a slight increase in airfoil thickness and an increase in curvature with the mounted actuator. After establishing the baseline aerodynamic characteristics with the DBD actuator as the new appropriate baseline, the impact of plasma actuation on aerodynamic lift and drag is analyzed.

10.2.2 Effect of Dual DBD Actuator Array in Co-Flow

This section presents the results of the Clark Y airfoil with dual DBD array powered at V_{DBD} = 25 – 40 kV in increments of 5 kV at 2 kHz. Figure 10.4 through Figure 10.8 show the aerodynamic performance of the Clark Y airfoil with a dual DBD activation compared to its baseline results at varied wind speeds U_∞ = 5 – 25 m/s in free stream increments of 5 m/s.

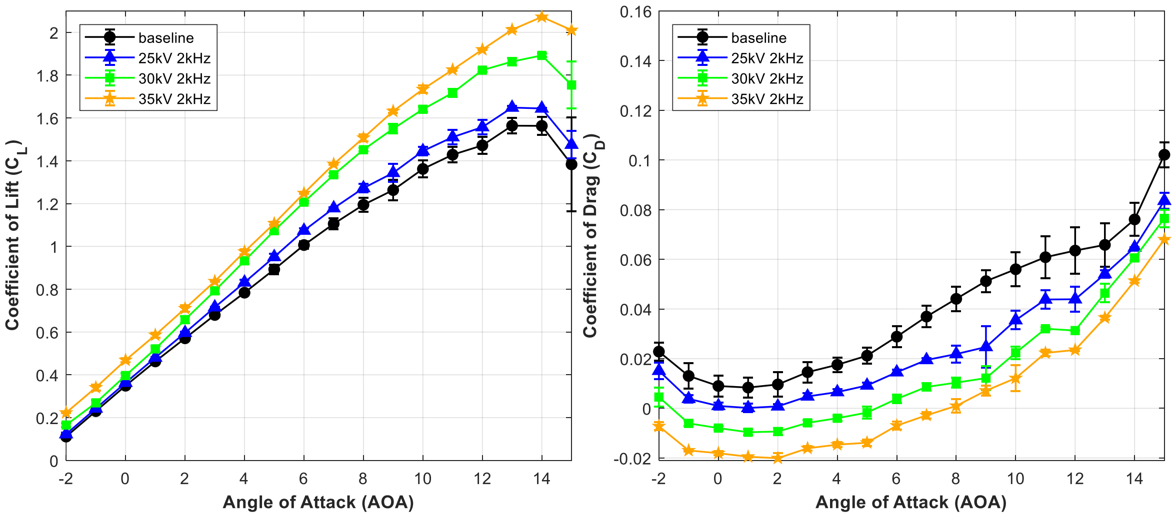

Figure 10.4. C_L and C_D versus angle of attack for a Clark Y airfoil at 5 m/s.

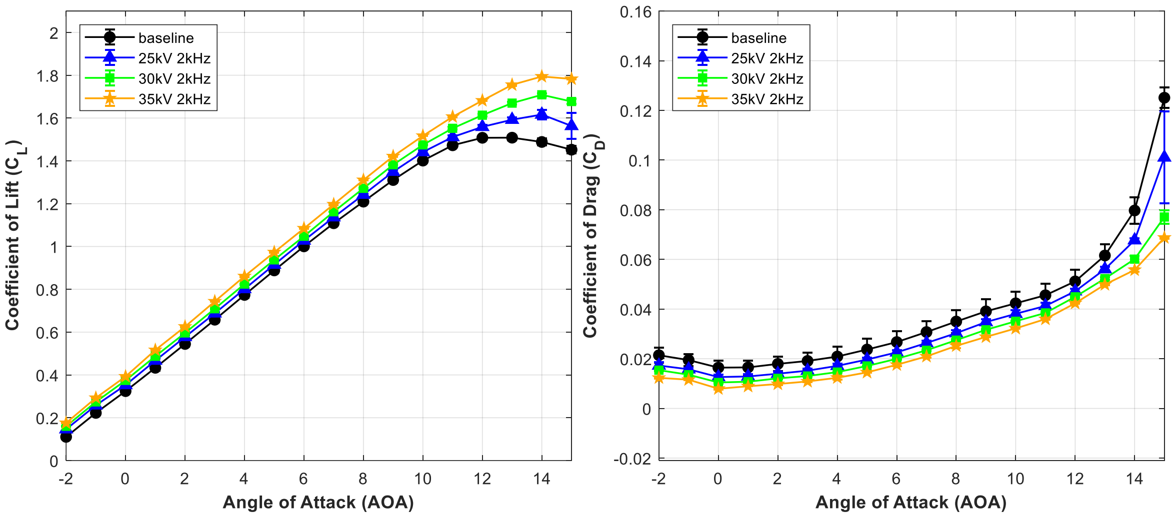

Figure 10.5. C_L and C_D versus angle of attack for a Clark Y airfoil at 10 m/s.

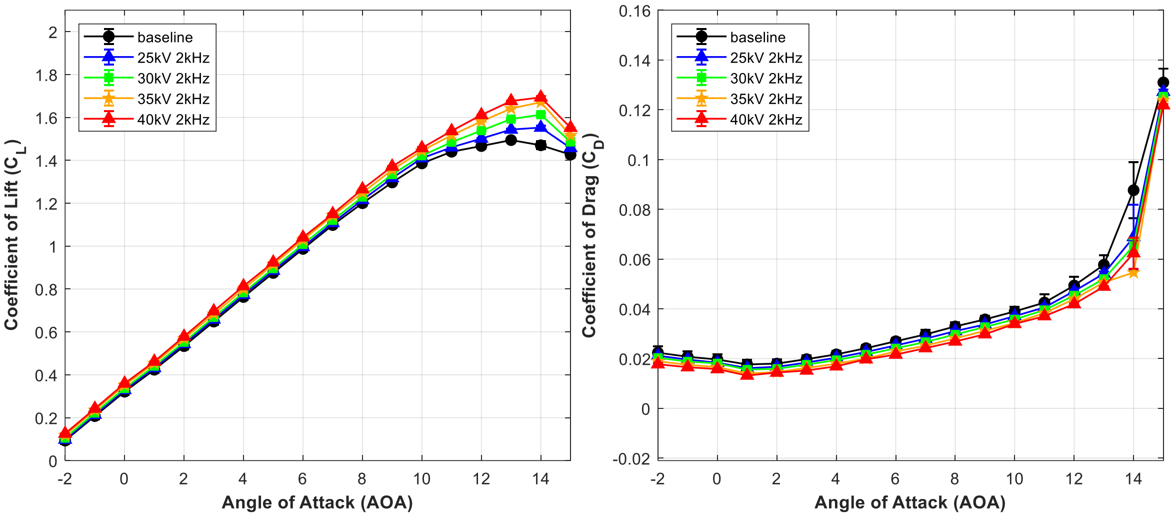

Figure 10.6. C_L and C_D versus angle of attack for a Clark Y airfoil at 15 m/s.

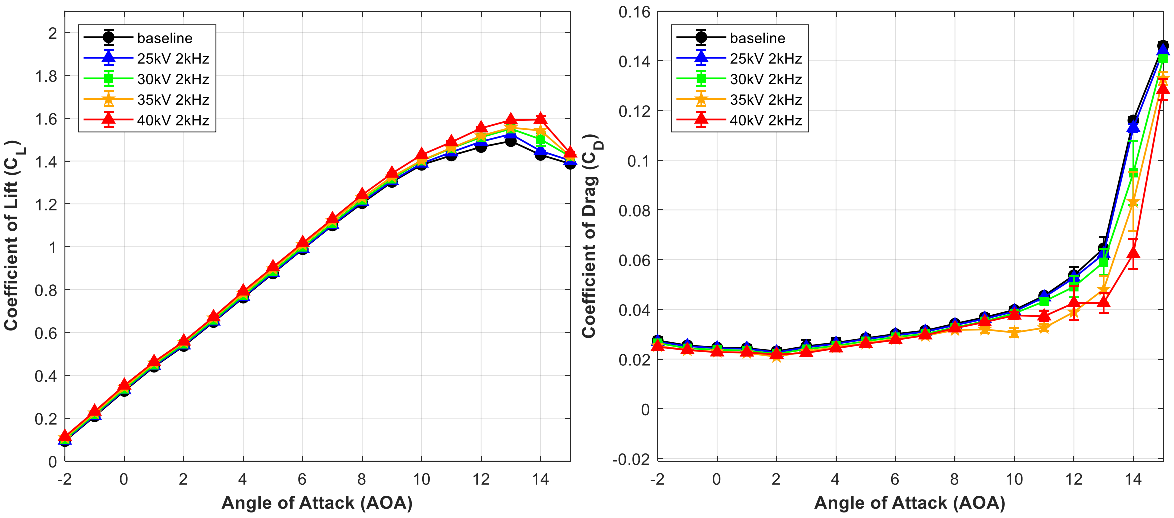

Figure 10.7. C_L and C_D versus angle of attack for a Clark Y airfoil at 20 m/s.

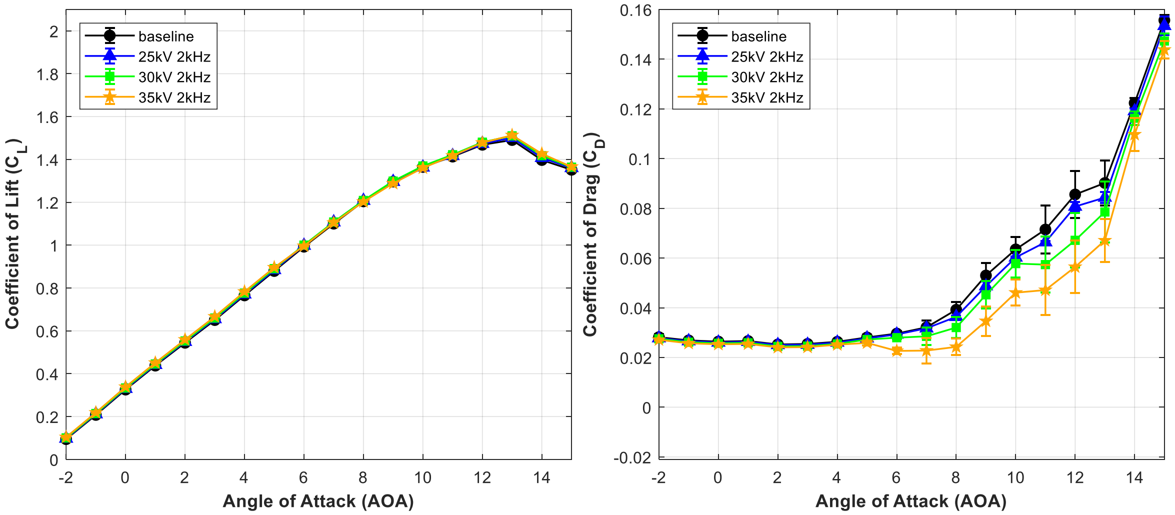

Figure 10.8. C_L and C_D versus angle of attack for a Clark Y airfoil at 25 m/s.

The DBD array significantly enhances the Clark Y airfoil's aerodynamic lift and drag performance. At high angles of attack and velocities up to 20 m/s, a substantial decrease in drag and an increase in lift is observed, which correlates with an increase in actuator voltage V_{DBD}. Previous studies have demonstrated that DBD momentum injection increases at a second-order polynomial rate with V_{DBD} [12]. At the lowest external speed of $U_\infty = 5$ m/s, the maximum lift coefficient increased from $C_{L,max} = 1.58$ to $C_{L,max} = 2.09$, with a decrease in drag coefficient down to ~ $C_D = -0.02$. The negative drag suggests that the DBD array provides greater EHD propulsive force than the aerodynamic drag.than of large fluid viscous structures [34], and the negative values suggest the EHD forcing was greater than the aerodynamic drag. The previous work for a similar actuator geometry shows that the DBD wall jet velocities regularly exceed 5m/s [15].The increase in lift can also be attributed to the blowing effect on the airfoil's top surface, which increases the local velocity and creates lower pressure on the suction side. At higher external flow, the impact of the actuation diminishes, which is consistent with previous literature [167]. At the highest external speed of $U_\infty = 25$ m/s, the DBD actuation did not noticeably impact the lift; however, a reduction in drag was observed.

The EHD momentum injection results in delayed separation and lift augmentation at high angles of attack. At external speeds up to $U_\infty = 20$ m/s, the DBD actuation increased C_L and decreased C_D across all angles of attack. As separation occurred around $\alpha = 12°$, the DBD actuation increased the C_L and decreased the C_D. At $U_\infty = 15$ m/s, the DBD actuation delayed separation by ~ 1 - 2°. For $U_\infty > 15$ m/s, the DBD actuation delays the increase in drag and most significantly increases the lift, which is likely associated with the separation delay. However, the DBD actuation effects lift only at higher angles of attack.

Compared to previous works, our results show that for chambered airfoil, the aerodynamic lift and drag improvement before separation can be significant. The earlier works with symmetric airfoils, such as a NACA 0015 airfoil and a single DBD actuator, did not significantly improve aerodynamic performance before separation [168]. In these studies, separation occurred suddenly, and the DBD actuation delayed the sudden drop in lift and increased drag associated with separation. In this study with the Clark Y airfoil, separation occurs more gradually, and the DBD array demonstrated significant improvements in aerodynamic lift over the entire range of angles of attack. Note that based on benchtop DBD thrust tests, the two-stage DBD array driven by custom power supplies has significantly higher momentum injection than previously reported DBD actuator studies. The actuator used in this work operates at a higher voltage than previous works (typically < 20 kV). Mechanistically, the high-power density two-stage actuation has an extended plasma region, operating over a longer cord length, suppressing the growth of fluid structures on the airfoil's suction side. Another factor that allows for more effective flow control is the chambered Clark Y airfoil shape, which experiences greater lift and drag at all angles of attack. With the chambered body, the Clark Y likely experiences some degree of separation at all angles of attack, and the DBD actuation can control smaller-scale fluid structures before complete separation could occur.

10.2.3 Lift/Drag Ratio Enhancement with Dual DBD

The C_L / C_D results of the Clark Y airfoil with dual DBD array powered at a varied from V_{DBD} = 25 kV – 40 kV in wind speed increments of 5 kV at 2 kHz at U_∞ up to 25 m/s are presented in Figure 10.9 through Figure 10.12. In the U_∞ = 5m/s case, the actuator produces thrust greater than the aerodynamic drag force (Figure 10.4), which results in the singularities with the lift-to-drag coefficient calculation; thus, these results are not plotted.

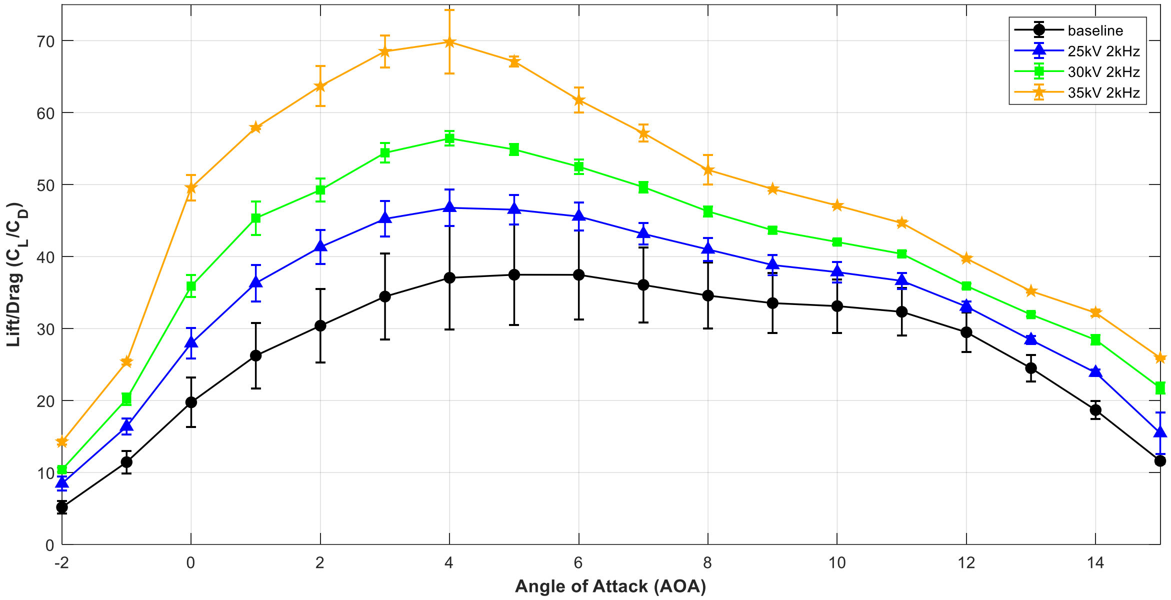

Figure 10.9: CL / CD versus angle of attack for a Clark Y airfoil at U∞ = 10 m/s. DBD actuator voltage is varied, VDBD = 25 - 35 kV.

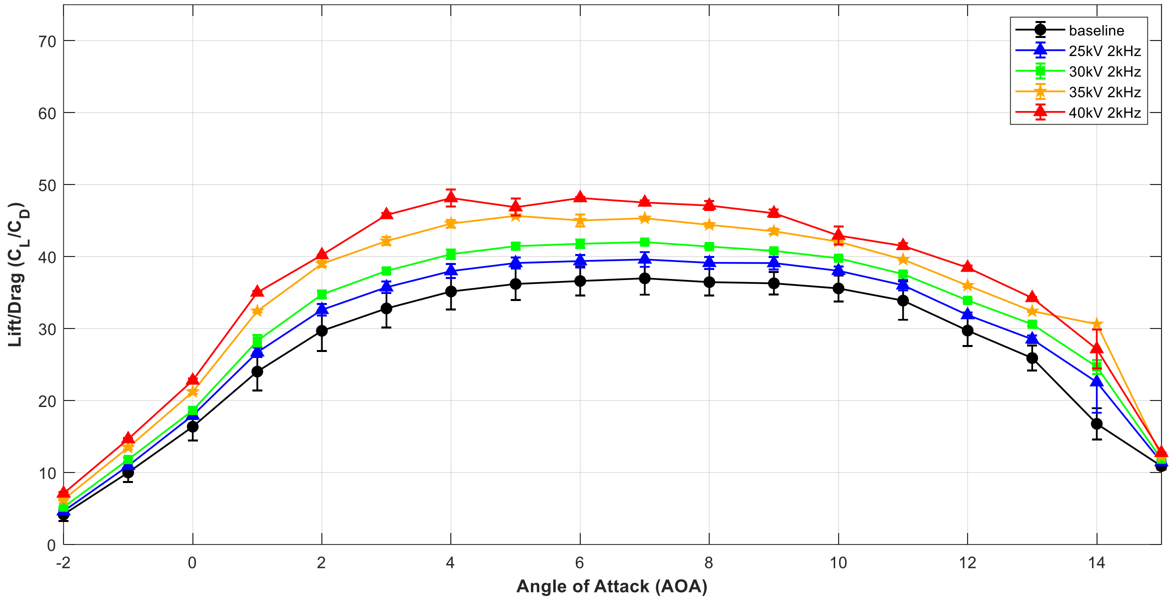

Figure 10.10: CL / CD versus angle of attack for a Clark Y airfoil at U∞ = 15 m/s. DBD actuator voltage is varied, VDBD = 25 - 40 kV.

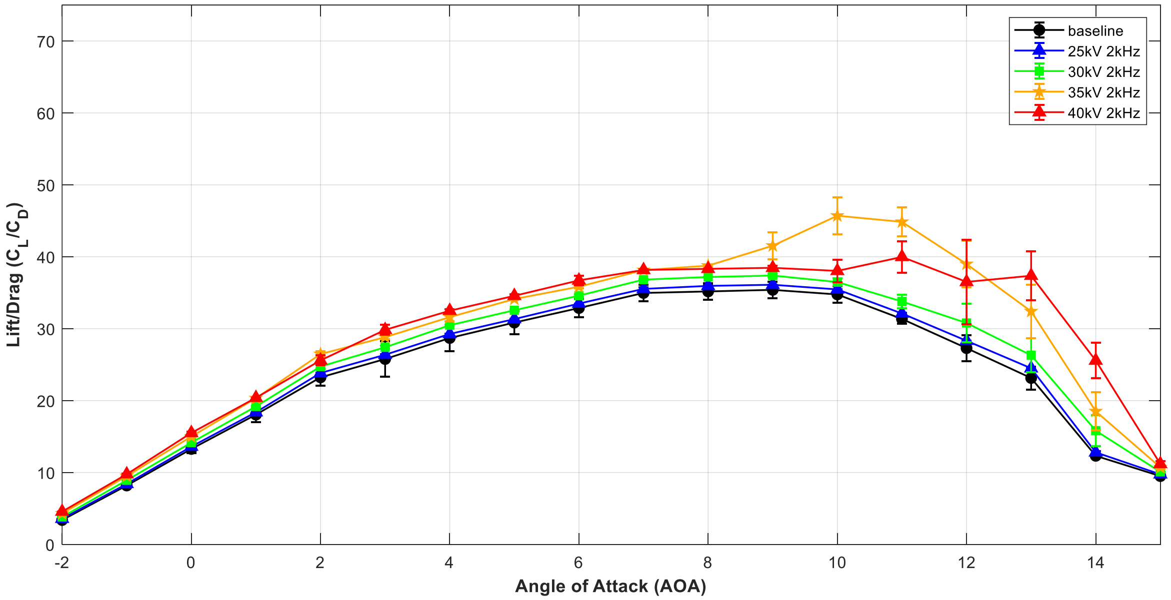

Figure 10.11: CL / CD versus angle of attack for a Clark Y airfoil at U∞ = 20 m/s. DBD actuator voltage is varied, VDBD = 25 - 40 kV.

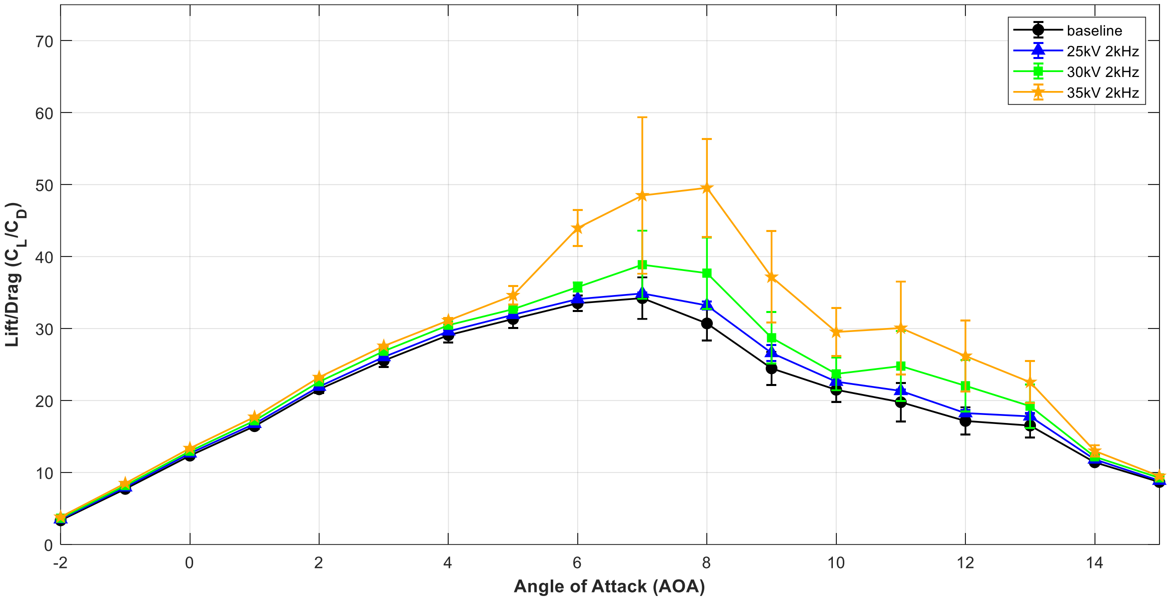

Figure 10.12. CL / CD versus angle of attack for a Clark Y airfoil at U∞ = 25 m/s. DBD actuator voltage is varied, VDBD = 25 - 35 kV.

A substantial increase in the lift-to-drag ratio is observed across all angles of attack up to 20 m/s, demonstrating a more significant impact across different angles. At the highest speed with noticeable aerodynamic improvement at $U_\infty = 25$ m/s, the lift/drag ratio increased by ~60% with a $\delta(C_L/C_D) \sim 20$. The $\delta(C_L/C_D)$ with and without plasma actuation decreases with free stream velocity, similar to the trends in C_L and C_D. The effect of the DBD actuators can further be improved by using a higher voltage or a thicker dielectric with a higher voltage, and tests with higher voltages are currently being investigated.

10.3 Chapter Summary

This study experimentally investigated the active flow control strategies for a Clark Y airfoil using a high power density DBD array. Experimental analyses assess the effectiveness of dual co-flow DBD actuators across a windspeed range of 5 – 25 m/s, corresponding to Reynolds numbers of 60k – 315k and varying angles up to $\alpha = -2°$ to 15°. The results demonstrated substantial improvements in the aerodynamic performance of high-power DBD actuators and lower wind speeds. With a 5 m/s external flow, the DBD array increased C_L by up to 50% and achieved EHD propulsion, as shown by negative drag forces. Notably, the two-stage DBD array significantly improved lift and drag at speeds of up to 20 m/s. While the influence of the actuators diminished at higher Reynolds numbers, our findings highlight that further advances in DBD technology can enhance the active flow control application at higher windspeed and angles of attack than previously demonstrated.

The DBD array should be adapted for counter-flow actuation to demonstrate greater control authority for future work. Additionally, the combination of counter-flow and co-flow can significantly alter the moment of the airfoil. While the current wind tunnel is unsuited for flow measurements, a hot-wire probe may be introduced through the front removable panel to capture velocity statistical data and characterize the wake region. Numerical modeling will significantly enhance and complement the experimental effort by extracting/predicting the velocity field around the airfoil. The airfoil can be numerically modeled with an ion injection or momentum injection model. Both approaches may serve as valuable numerical case studies.

Chapter 11. Conclusions

This dissertation has developed and explored several critical aspects of dielectric barrier discharge plasma actuators for active flow control. Starting with fundamental scientific inquiry, this work explores underlying fluid-plasma interactions to optimize DBD actuator systems and presents high-fidelity aerodynamic behavior of a realistic Clark Y airfoil to demonstrate active flow control at more robust flow conditions than previously published.

This dissertation first presents a reduced-order empirical model of DBD actuators to derive their discharge current, current density, plasma volume, and momentum injection using fundamental input parameters. The discharge current analysis found positive and negative discharge current to follow an $I_{dis} = K{f_{AC}}^{\alpha}(\varphi - \varphi_0)^2$ relationship. Furthermore, the discharge current was linearly proportional to the momentum injection derived through velocity profiles. This empirical model brought new key DBD parameters to light and created more accurate boundary conditions for the numerical modeling of DBD.

With a new model of a DBD actuator in quiescent condition, the DBD model is then tested and validated in an external flow. After constructing an in-house small wind tunnel, we present extensive fluid boundary layer flow profiles when the DBD actuator is in co-flow and counter-flow. Fluid analysis supports that a DBD actuator displaces significantly more momentum (up to ~ 6.5x more) within a boundary layer in counter-flow configuration than in co-flow configuration. The DBD actuator power usage is independent of orientation and external flow speed. This work proposes a new non-dimensional flow separation criteria, M^*, as a ratio of DBD jet momentum to boundary layer momentum.

With empirical models of the DBD in quiescent and external flows, this dissertation then explores the underlying mechanisms of augmented DBD systems to optimize electromechanical performance. This dissertation first explores a three-electrode DC-augmented DBD (DCA-DBD) where an additional HV DC electrode augments the DBD thrust when positively biased but creates a deflected jet when negatively biased. Through high-speed imaging and surface charge measurements, we found that a positive DCA augments horizontal thrust by greater than twofold due to electric field acceleration with electron impacts and oscillating residual charge interactions. The negatively biased DCA experiences a deflected jet because sliding positive discharge towards the third electrode causes a reverse discharge to the extended plasma. This work is the first to explore the underlying causes of these forcing behaviors.

Building upon the DCA-DBD research, we present a new AC-augmented (ACA) DBD with increased performance over its baseline. This work is motivated by floating battery-powered DBDs and DBD arrays. We find that an out-of-phase (relative to the air-exposed DBD electrode) HV AC third electrode promotes the acceleration of both positive and negative species generated by the primary DBD, enhancing momentum transfer to neutral molecules. However, with a sufficiently strong electric field, sliding discharge can occur with the out-of-phase third electrode, inducing negative discharges from the third electrode to the space charge. This phenomenon was previously only seen in DCA-DBD systems and represents a critical space limiting factor in DBD arrays.

This work then extends the ACA-DBD by optimizing a DBD array with out-of-phase electrodes to demonstrate linearly scaling thrust with the number of DBD stages at high forces, a feat never before seen. Highlighting that DBD arrays have a strong spacing dependency, the DBD array power usage also scales linearly with the number of DBD stages. The DBD array is also tested with a resistor module to demonstrate the delay of arcing and filamentary streamers. With a compact four-stage DBD array, we report a thrust greater than 250 mN/m with a significantly thicker wall jet than previously published.

Finally, a robust Clark Y airfoil is tested with an optimized two-stage DBD array in a 2D wind tunnel to demonstrate flow control. Measuring aerodynamic forces (lift, drag, and moments), we demonstrate significant lift and drag control with the DBD array at speeds up to 20 m/s, greater than previous literature. This work is the first to test a Clark Y airfoil with DBD actuators and the first to test an optimized DBD array.

Although several complex engineering and scientific hurdles prevent large-scale DBD implementation today, this dissertation contributes greatly to the augmentation of DBD capabilities and points towards many new research avenues. With the newfound mechanisms and demonstration of DBD augmentation in this body of work, future applied research work can focus on implementing these systems for robust flow control at higher external flow speeds. Future fundamental research work can more deeply explore the unsteady plasma-fluid coupling of the proposed augmentation mechanisms through time-resolved measurements such as Laser Doppler anemometry (LDA) or particle imaging velocimetry (PIV) with high-speed imaging and surface charge measurements. Future engineering work can focus on auxiliary systems, such as miniature power electronics, to allow a plug-and-play DBD actuator to have a higher overall thrust-to-weight ratio. While these research efforts span several fields of study, these developments are imperative for the future of DBD actuators for active flow control.

Chapter 12. Highlights

- Developed a reduced-order empirical model of a two-electrode DBD actuator's plasma and electromechanical characteristics, including discharge current, current density, and momentum injection from key input variables (i.e, voltage and frequency)
- Validated the reduced-order empirical model and performance of a two-electrode DBD actuator in co- and counter-flow conditions at external flow speeds up to $U_\infty = 11$ m/s
- Proposed new non-dimensional separation criteria for DBD actuators in counter-flow
- Demonstrated a > 100% increase in thrust with a three-electrode positive DC-augmented (DCA) DBD actuator and explored the underlying DCA augmentation mechanisms
- Presented time-resolved high-speed images and space charge measurements of positive and negative DCA for the first time, revealing the cause of the wall-normal jet in negative DCA
- Explored and tested a three-electrode AC-augmented (ACA) DBD actuator for the first time to demonstrate up to ~40% increase in thrust by varying phase differences
- Developed a scalable high-power DBD array with no adverse cross-talk between DBD stages to achieve the highest thrust in the current DBD literature
- Demonstrated active flow control at external speeds up to ~ 20 m/s with a chambered Clark Y airfoil using an optimized dual-DBD array and an in-house wind tunnel.

Appendix A. Numerical Modeling of DBD in Co- and Counter-Flow

Numerical modeling of DBD has generally been categorized into three categories with increasing complexity: momentum injection models, simplified ion injection models, and species transport models. Momentum injection models such as that of Yoon *et al* [95] and Kriegseis *et al.* [128] have been shown to accurately predict steady state resulting fluid flow field of DBD actuators in a few configurations using empirically estimated forcing fields while remaining extremely computationally inexpensive. Simplified ion injection models such as the Orlov [125], Shyy [169], and the Suzen and Huang model [88] employ analytically or semi-empirically estimated charge density boundary conditions or charged density regions to model the transport of electrons and generalized ions. The electric potential and the charge density is then used to calculate the electrostatic Lorentz force with no magnetic field and this EHD force is then coupled to the Navier-Stokes. In species transport models such of that of Bie *et al*. [170] and Soloviev *et al*. [171], the dominant chemical species, the resulting ions, and the radicals are modeled as a transport phenomenon, and the distribution of ions are used to compute the electrostatic force similarly to the simple ion models. Simplified ion injection models and momentum injection models have often been the most popular as they can readily be used for different applications while remaining relatively computationally lean.

An early implementation of a momentum injection model based on previously published empirical measurements is tested in co-flow and counter-flow. No published DBD model is tested in an external co-flow or counter-flow. This supplemental information further supports the previously proposed momentum injection model in an external flow while shedding insight into the fluid interactions of this manuscript. The two-dimensional schematic is identical to Figure 5.1 and Figure 5.4. The domain height is set to match the experimental wind tunnel of 10cm. The velocity profile of the wind tunnel is defined as a custom user-defined velocity profile. A mesh of

332,000 cells is employed with refinement near the forcing region, and courser meshes are tested to ensure mesh independence. Since the DBD actuator does not have a fluid mass flux, the resulting fluid governing equations is expressed as the incompressible Navier-Stokes continuity and momentum equation with an added momentum source term as defined as

$$\nabla \cdot \mathbf{u} = 0 \tag{25}$$

$$\rho \frac{D\boldsymbol{u}}{Dt} = -\nabla P + \mu \nabla^2 \boldsymbol{u} + \vec{f}_{EHD} \tag{26}$$

The area of the momentum injection is within a right triangle region similar to the approach of Shyy [169] which assumes a linear approximation between plasma length and height. The author's previous work outlines that plasma length approaches ~8mm for these electrical parameters and the length-to-height ratio is approximately constant at L/H = 4. For all simulations, the steady-state K-W turbulence model is used. A steady-state assumption for the DBD forcing is often assumed as the electrostatic and unsteady forcing timescales and variances are considered sufficiently small. High-temporal resolution PIV data has shown that the time fluctuations of the DBD jet is often approximately 10% within a single voltage period, however, this variance depends on the applied voltage waveform [61, 154]. Yoon *et al* used the one-equation Spalart-Allmaras turbulence model to model the DBD jet in quiescent flow, however, this was found to underpredict the separation region in the counter-flow significantly.

The resulting velocity profiles and momentum displacement calculations are presented below in Figure A.1. In the co-flow configuration, the momentum injection model matches the maximum velocity within 10%. However, the location of the maximum velocity in the model is higher than the experimentally measured location and the velocity displacement appears more focused. This is believed to be due to the inability for a two-dimensional CFD simulation to capture vorticity and turbulence effects well. In addition, the higher location of the maximum velocity supports that the forcing distribution shape likely should be more focused in the near-wall region, possibly similar to the modified Gaussian used in Yoon *et al [95]*. Using the integration of the X = 10mm velocity profile, the total momentum displacement matches the experimental momentum displacement.

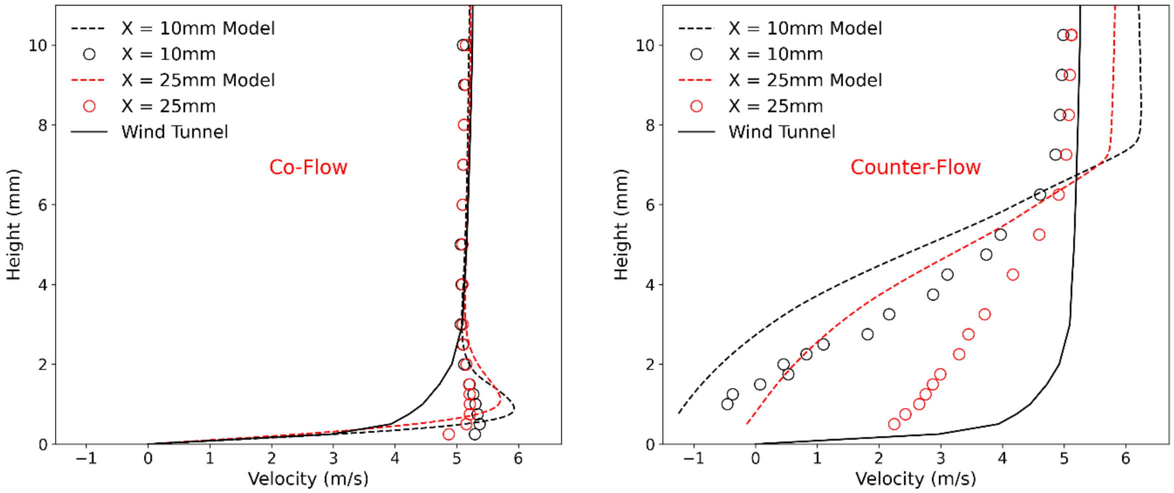

Figure A.1. Numerical and Experimental DBD Velocity Profiles with 19.5kV 2kHz Forcing (~22 mN/m) in 5 m/s External Co- and Counter-Flow

In the counter-flow configurations, the strength of the separation region is over-predicted. The over-prediction is believed to be due to the K-W turbulence model incorrectly predicting the separation region, and this is generally in line with many other adverse-pressure gradient studies, including backward-facing step problems that over-predict shear stress and reattachment locations [172]. The momentum deficit measured at the X = 10mm position after the momentum injection region has an error of about 30%. In addition, experimental results show the mass entrainment at higher locations in the wind tunnel compared to the numerical results that show entrainment as low as ~7mm above the plate. The downstream dissipation does not match well as the X = 25 profile experimentally dissipates more than the numerical solution.

Overall, the presence of a separation region in the counter-flow case proved to be the most complex cases to match well, and it is unlikely that a basic RANS turbulence model will accurately predict an adverse pressure gradient. Thus, more advanced numerical efforts are needed to predict the separation region accurately. The main strength yet main limitation of this model is its simplicity. With further fine-tuning to the given physical parameters, this model can predict and accurately model specific DBD applications. However, that strength can only be reached with further investigations into its dependencies on turbulent models, unsteady forcing, and plasma forcing volume. More robust turbulent models such as Large Eddy Simulation (LES), Detached Eddy Simulation (DES), or a Direct Numerical Simulation (DNS) approach may be needed to properly resolve the viscous effects, especially in the counter-flow case. Time-averaged forcing with a triangular plasma force shape may be appropriate for simple cases such as in co-flow, but in cases such as the counter-flow or crossflow, shear stress and turbulent effects over the momentum volume are magnified, and proper time-resolution may be required. With these aspects tackled, this model can serve as an inviable DBD design tool while providing accurate results and shedding important insight into the DBD forcing.

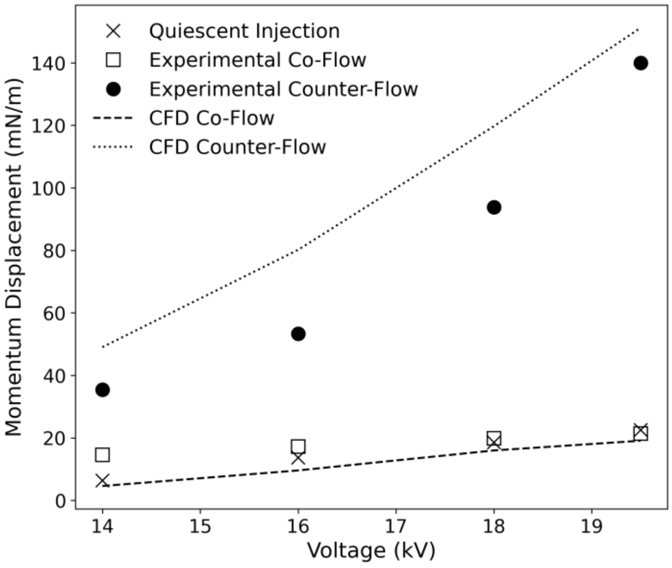

Figure A.2. Numerical and Experimental DBD Momentum Displacement with 19.5kV 2kHz Forcing (~22 mN/m) in 5 m/s External Co- and Counter-Flow

Appendix B. DC-Augmented DBD Supplemental Information

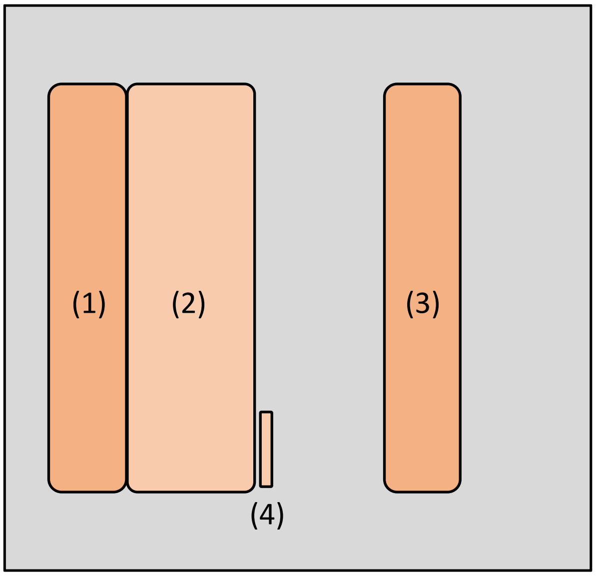

Figure B.1 Top view experimental schematic of the DBD actuator comprised an air-exposed electrode (1), embedded electrode (2), air-exposed third electrode (3), and 3 mm long x 10 mm wide surface charge probe (4) located on the backside of the dielectric at x = 27 mm downstream from the active electrode.

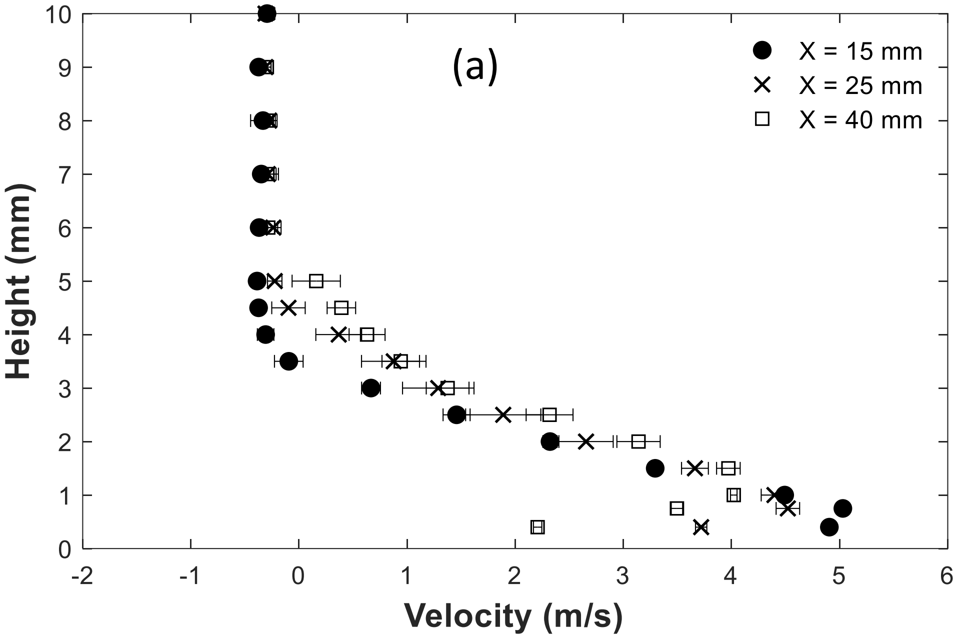

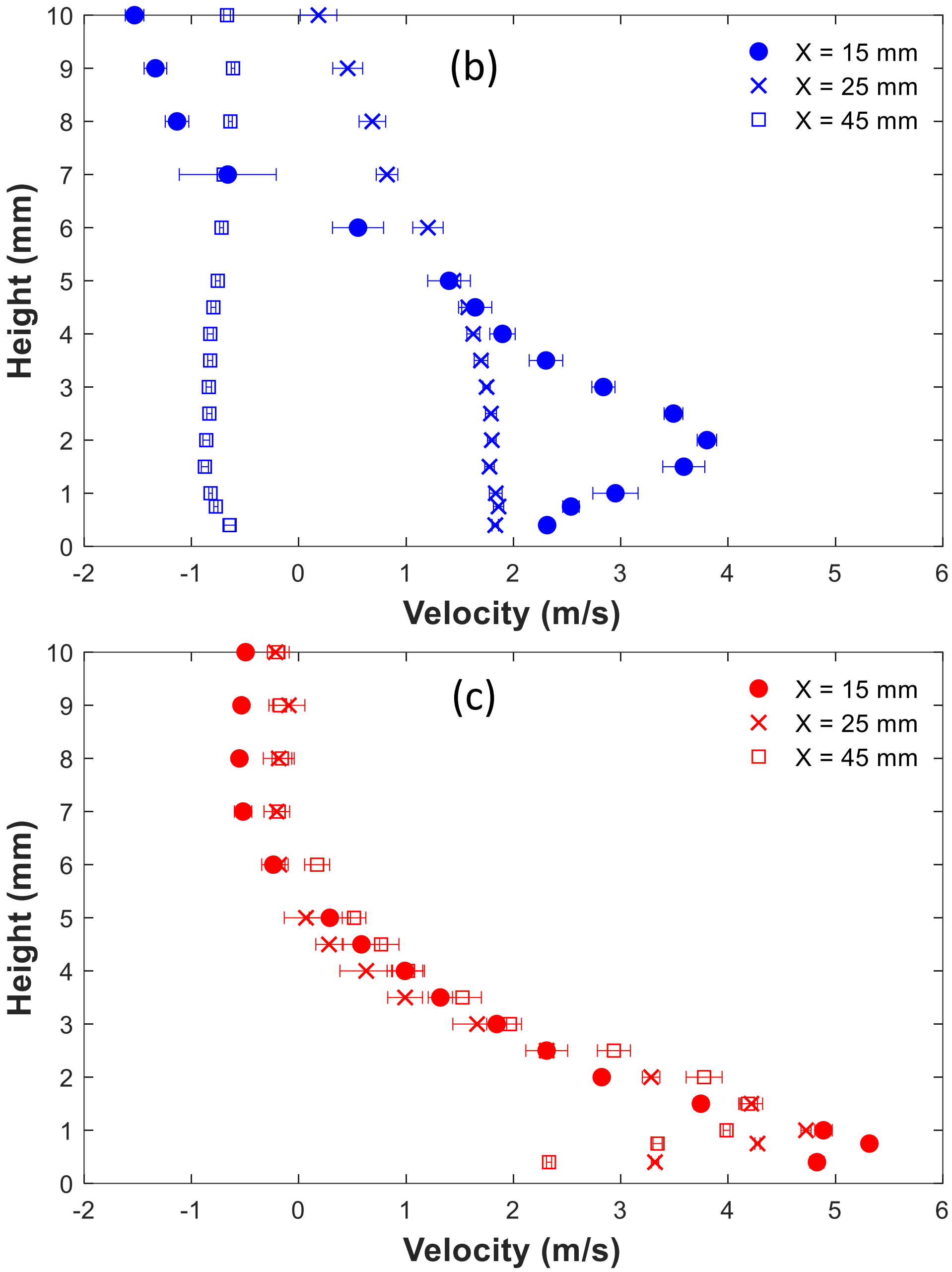

Figure B.2 Vertical velocity profiles at X = 15 mm, 25 mm, and 45 mm downstream at identical conditions of Figure 3. Control volume analysis up until X = 15 mm yields the momentum produced from the DBD. Conditions: *f* = 2kHz, V_{AC}= 35 kV with (a) V_{DCA}= 0 kV, (b) V_{DCA}= – 24 kV, and (c) V_{DCA}= +24 kV.

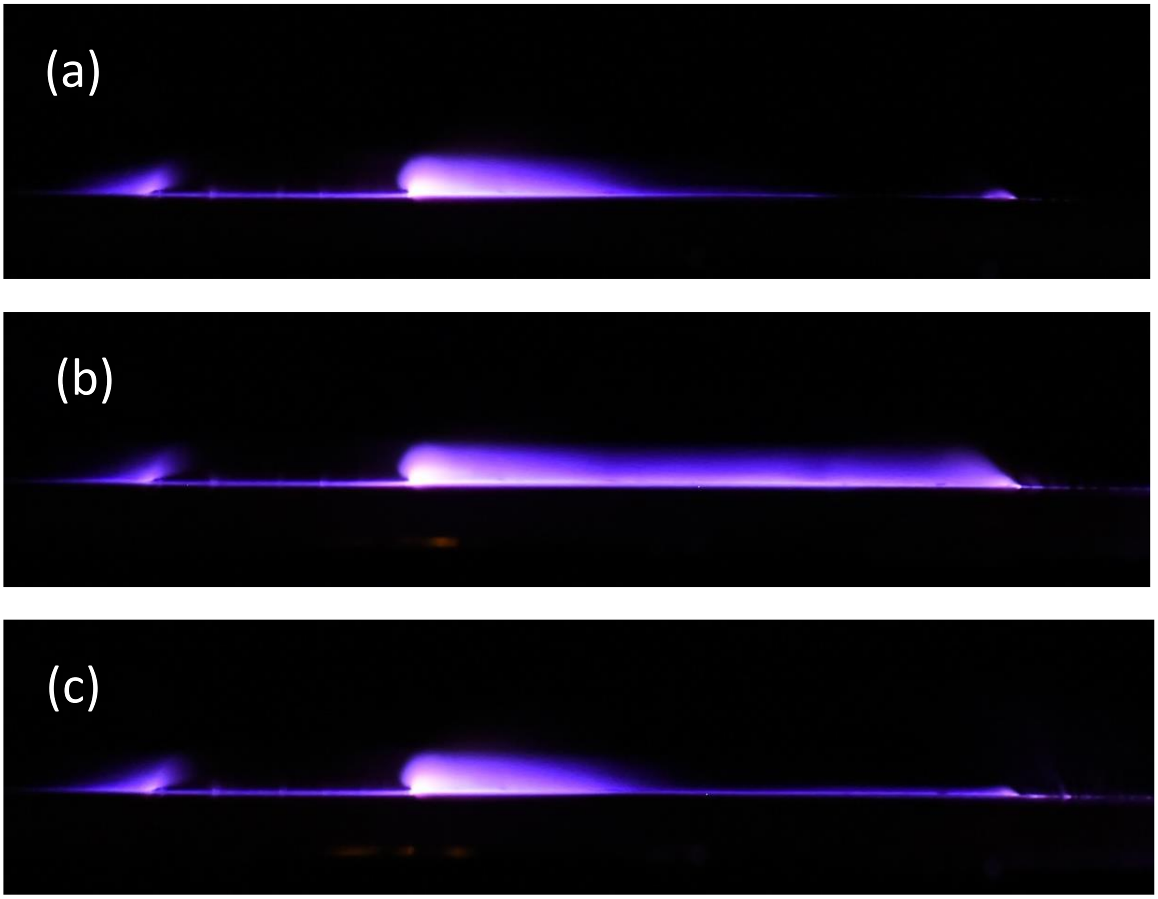

Figure B.3 Side view image of DBD with V_{DCA} = 0 kV (a), V_{DCA} = –24 kV (b), and V_{DCA} = +24 kV (c). The exposure time of 25 ms is equivalent to 50 DBD cycles.

Table B.1 Comparison of directly measured thrust and velocity profile integration

Experimental Configuration	Directly Measured Thrust (mN/m)	Velocity-Derived Thrust (mN/m)
V_{DCA} = 0 kV	29.1	32.0
V_{DCA} = + 24 kV	49.1	45.5

Appendix C. Surface Virus Inactivation by Impinging Flow Non-Thermal Plasma Reactor

This section presents work on virus inactivation by an impinging flow non-thermal plasma (NTP) reactor generated by DBD. This work is motivated by the need for a non-contact virus inactivation highlighted by the recent COVID-19 pandemic (SARS-CoV-2). This work is published in IEEE Transactions on Plasma Science [1].

The COVID-19 pandemic raised awareness about the spread of infectious diseases via fomite and respiratory routes. The persistence of potentially infectious agents in public spaces and the spread of nosocomial infections in medical settings needs investigation. Aerosol transition routes have been evaluated by multiple researchers. Exposure to these aerosols presents a risk to patients and medical staff [173]. Modeling and aerosol plume tracking studies in medical facilities and other public spaces have been published in recent years. The typical strategies for aerosol management include increased air exchange rates and the introduction of portable particle filters. [174-178]. Fomite-mediated transmission is an important pathway for many viral pathogens, such as adenovirus, norovirus, rhinovirus, coronavirus (e.g., SARS-CoV-2), etc. [179-182]. The strategies for surface disinfection can be designed to prevent disease transmission; they depend on the surface types and operational scenarios [183]. Broadly, the application can be divided into contact and non-contact surface treatments. Contact treatments are effective for smooth, non-porous surfaces; they are inexpensive and easy to implement. However, using corrosive chemicals, such as bleach or hydrogen peroxide, can present problems in some scenarios. Liquid-based and aerosol-based disinfectants may damage surfaces chemically, gradually erode surface finish, and penetrate through small openings inside the equipment, affecting the electronics. The CDC's Guidelines for Disinfection and Sterilization in Healthcare Facilities lists the shortcomings of various disinfection agents, including damages from their application [184]. Recent studies evaluated a variety of chemical disinfectants containing hydrogen peroxide, quaternary ammonia, and chlorine. Disinfection procedures were found to change surface properties [185, 186]. Non-contact methods can eliminate some concerns. Germicidal ultraviolet light (UVC, typically 222 or 254 nm) is used to inactivate pathogens on surfaces and in the aerosol phase. However, UV inactivation requires long exposure times, and direct exposure to high-intensity UVC can cause damage to the eyes and skin or degrade materials like plastics, polymers, and dyed textiles. Plasma-based surface treatments have been shown to inactivate various viruses and biological agents at short exposure times [187, 188]. The pioneering plasma-based treatments for bacteria and viruses have been published by Laroussi et al. [189-191], Fridman et al. [192], Xiong et al. [193], and Lu et al. [194]. Non-thermal plasma was demonstrated to inactivate various bacteria and viruses through inactivation routes such as oxidation and disruption of the cell membrane.

Ozone is used as an oxidizing agent for various industrial and domestic treatment/disinfection applications. The main benefits are that the treatment leaves no harmful residue after oxidation, it can be used on electronic components, and, unlike UV, does not require line-of-sight access. For both approaches, pathogens encapsulated in bodily fluids will be harder to inactivate to a specified level than pathogens not in a fluid. The common ozone generation methods are the electrochemical method, UV, and non-thermal plasma (NTP). The two NTP generation approaches are corona discharge and dielectric barrier discharge (DBD). In corona discharge, high voltage (HV) direct current (DC) between two electrodes ionizes a working fluid [26, 27, 67]. In an enclosed configuration, the charged species can be expelled by an external flow, such as a pump or fan, to avoid ion loss on the ground electrode [195, 196]. Corona discharge is more commonly used in commercial devices due to its simpler physical design and required power electronics. In DBD, a high-voltage alternating current (AC) is applied to two electrodes separated by a dielectric barrier.

At low power levels, corona generators are found to produce similar ozone levels to DBD ozone generators [28]. Due to the separation of the electrodes in DBD with a dielectric barrier, the charged species cannot readily recombine compared to corona discharge, and DBD may produce ion concentrations of an order magnitude greater than in the corona discharge. Unlike the corona discharge, the DBD is resistant to streamer propagation, making it a robust approach with respect to operating pressure, relative humidity (RH), and environmental contamination. For example, Ono and Oda showed that adding 2.4% water vapor to dry air decreased corona ozone production by a factor of ~6 [29]. In comparison, the effect of RH on DBD is significantly smaller; only a ~50% decrease in ozone concentration was reported with the increase of RH [30, 31]. The decrease in ozone was attributed to a lower electron density and ozone interaction with water. Commercial generators typically produce ozone levels in the 0.2-20 PPM range; it is suitable for aerosol and surface non-targeted surface treatment [32]. DBD has been demonstrated to produce ozone concentrations up to ~1000 ppm [30]. Because of its flexibility and environmental robustness, DBD plasmas have been used as an ionization source in mass spectrometry applications [33] and boundary layer modification for active flow control [34, 35].

Recent works demonstrated virus inactivation after plasma treatment of porous and smooth surfaces. Lee *et al.* used a DBD ionization source to disinfect face masks contaminated with the SARS-CoV-2 virus; the authors showed a 4-log reduction when the surfaces were treated for 10 seconds with 120 ppm of ozone [187]. The DBD treatment did not lead to structural damage or functional deterioration on the face masks as there was no statistical difference in particle filtration efficiency (PFE) between an ozone-treated and untreated mask. Baek *et al.* treated coronavirus trapped in a polypropylene melt-blown filter; the viable counts were reduced by 99.8% when exposed to ~52 ppm of ozone for 30 minutes [197]. Chen *et al.* investigated the disinfection of several different surfaces, including plastic, metal, and leather [2]. Thomas *et al*. used a DC-powered plasma torch with atmospheric air showing 2 log (99%) after 120s [3]. Wu *et al.* showed that viruses exposed to reactive oxygen species exhibited surface protein and RNA damage [198].

The literature reports the ability of RONS generated by NTP to inactivate viruses; however, the effectiveness of individual species is not well understood. In air, NTP generates O_3, O, H_2N_2, NO, NO_2, HNO_3, NO_3, and several other reactive oxygen and nitrogen species [60]. These species have been measured through spectroscopy [123, 124]. Ozone (O_3) has often been suggested as a key reactive species responsible for virus inactivation in air and water, and since the measurement instruments for ozone are well-developed, it has been used as an indicator of RONS levels in biological studies [60, 199-201]. Note that several studies indicated that hydroxyl and nitrogen groups are equally or more capable of virus inactivation [202-204]. This study recognizes the previously reported claims that both ozone and RNS contribute to virus inactivation [205]. Measured ozone levels are used as a relative indicator for flow reactor performance with respect to RONS production. In the DBD, the RONS generation rate can be controlled using multiple inputs, such as frequency, waveform, voltage amplitude, etc. The high production rate allows for developing small-scale generators with a low power input that can be used for localized surface disinfection applications. A controllable ionization source with the addition of external flow allows the delivery of an oxidizing agent to the surface of interest, minimizing overall ozone emissions and the health and environmental impact of the treatment. These flow reactors can be used in decontaminating electronic devices and complex surfaces where using UV and liquid chemicals is problematic.

In this study, we present and characterize a novel atmospheric air DBD-NTP flow reactor for surface virus inactivation. Compared to existing literature, atmospheric air DBD reactors have not been demonstrated for aerosol or surface virus inactivation, and little work has been reported on the inactivation of surface viruses through NTP. Most studies correlate pathogen inactivation to ozone concentration and exposure time; thus, consistent methods of free radical production and reactor optimization as a function of operating conditions are important. This study first characterizes the ozone production of a novel DBD-NTP flow reactor as a function of geometrical parameters and flow rate. The reactor is then used for the MS2 virus inactivation on surfaces.

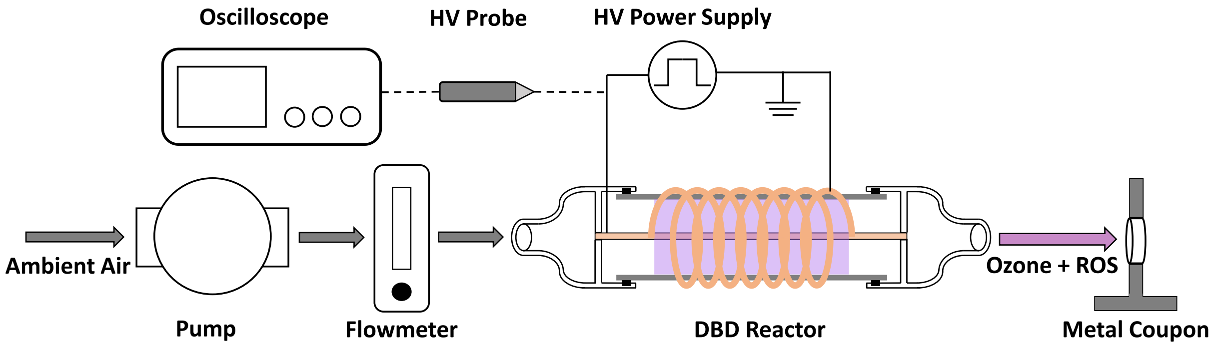

Figure C.1 Schematic of the experimental setup including metered air source, DBD reactor with power electronics, and instrumentation to measure DBD current and voltage. The ionized air exiting the reactor impinges onto a coupon spike with virus culture. An ozone meter (not shown) can also be placed at the location of the coupon.

Figure C.2. 19.05 mm DBD reactor with 6.35 mm electrode spacing and a 6.35 mm ID exit nozzle (left); 19.05 mm DBD reactor with 12.7 mm electrode spacing and 12.7 mm ID exit nozzle (right)

C.1 Experimental Setup

C.1.1 DBD Flow Reactor

DBD ionization was previously used for pathogen inactivation; however, in previous studies, the pathogens were typically placed on the electrode surface or between the active and ground electrodes [49]. Several DBD flow reactor designs were reported [36, 37]; their optimization could improve pathogen inactivation efficacy. The experimental setup used in this work is shown in Figure . The concentric DBD reactor consists of a high-temperature quartz glass tube, an inner high-voltage electrode, a coiled grounded outer copper electrode, and two end caps. The concentric DBD reactor was designed to generate volumetric plasma discharge and transport RONS toward the treated surface operating with low air resistance, such that the high flow rates can be achieved with modest pumping requirements. The DBD reactor ozone production was tested for different quartz tube dimensions, electrode coverage, and exit nozzle size. The two different quartz tubes are 19.05 mm (0.75") outer diameter (OD) with 16 mm (0.630") inner diameter (ID) and OD = 12.7 mm (0.50") and ID = 10.49 mm (0.413"). All experiments use the copper inner (active) electrode with a 3.175 mm (1/8") diameter. Electric field strengths change for the same applied voltage as the spacing between the electrodes and tube size are varied. The lengths of the quartz tubes and the inner electrode are 304.8 mm. The coiled grounded electrode is constructed of 6.35 mm wide copper tape with 6.35 mm or 12.7 mm spacing between each coil. The coiled electrode spanned the reactor's middle section; this coiled section length was ~ 152 mm to minimize dielectric heating and arcing around the tube ends.

Figure shows the 19.05 mm OD DBD reactor with two different electrode coverages and two different exit nozzle sizes. The quartz tube acts as the dielectric barrier between the HV and ground electrodes due to its high dielectric constant and excellent resistance to corrosion and temperature degradation [50, 51]. The inlet and outlet ends are 3D-printed with high-temperature resin

(Formlabs High Temp Resin 1L) with a heat deflection temperature of 238°C @ 0.45 MPa. The caps are sealed against the tube with O-rings to create an air-tight fit. The inlet cap end has a barbed fitting connected to flexible tubing. The outlet nozzle dimensions were 6.35 mm ID and 12.7 mm ID. Upstream and downstream of the ionization region, 3D-printed spacers ensure that the inner electrode is centered while not inhibiting the flow.

C.1.2 Reactor Operation: Electrical and Flow Parameters

The plasma discharge was driven by a high-voltage (HV) square wave generated by a high-voltage AC power supply (model PVM500-2500, Information Unlimited, NH) with a 25kV (peak-to-peak) voltage amplitude and 20 kHz frequency. Ozone production tests were performed for several reactor geometries. The power supply input power (P_{in}) was varied between 30 W and 210 W. The output power was set at 150 W for the virus inactivation test, and only one geometry was used. In all tests, the voltage amplitude and frequency were confirmed by a high-voltage probe (Tektronix, model P6015A). The electrical parameters are monitored and stored on a Tektronix DPO 7254C oscilloscope. A variable control pump (Medo ML-120) controlled the airflow through the reactor, monitored by an in-line flowmeter (Dwyer, model RMC-102). The DBD ozone production was characterized at 10-40 LPM.

To measure the DBD reactor ozone generation, the flow rate through the DBD reactor was first set to the target operational level. When the high voltage is applied between the electrodes, the ambient air entering the reactor becomes ionized. The ionized gas is then expelled directly onto the coupon spiked with viral culture. The outlet of the DBD reactor was positioned 10 mm away and normal to the surface of the spiked coupon. The ozone concentration was measured using an ozone sensor (Forensics Detectors, model FD-90, 0-100 ozone ppm) at the same location as the spiked coupons in the inactivation tests**.** Figure shows the DBD reactor operating at P_{in} = 150W.

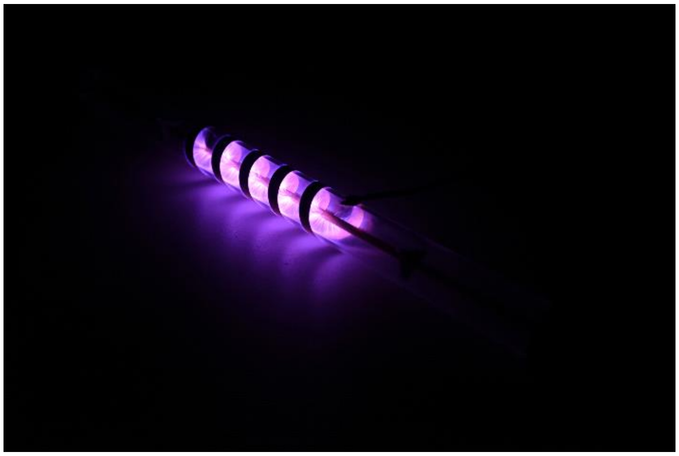

Figure C.3. A photograph of the DBD reactor operating at 150W power input. Reactor configuration: 12.7 mm coil spacing and ID = 12.7 mm.

C.1.3 Surface Treatment

A single-stranded, positive-sense RNA virus, MS2 bacteriophage, was used to determine virus inactivation levels. With a similar structure to noroviruses, MS2 is commonly used in virus transmission and inactivation studies [206-208]. Depending on the surface type and environmental conditions, MS2 and other viral RNA can survive several days on surfaces [209]. A 100 µl droplet with ~10^7 MS2 copies/1mL PBS (phosphate buffer saline) titer was deposited onto a 12.7 mm diameter circular stainless-steel coupon and allowed to dry for approximately 90 min, forming a thin film. The pH = 7.4 PBS titer (Corning 21-040) did not contain calcium or magnesium and comprises 0.144 g/L KH_2PO_4, 9.00 g/L NaCl, and 0.795 g/L Na_2HPO_4. Once the droplet has dried, the MS2 remains stable on the metal coupon. The dried PBS components may potentially create a coating or buffer around the MS2, hindering inactivation. In this case, the measured inactivation results are conservative.

The coupon was placed 10 mm from the exit of the DBD reactor. The ambient temperature during the tests was controlled to ~ 65°F. The ion temperature was not measured however, previous literature has reported the ion temperature of the atmospheric air plasma at ~ 10^3 K [210]. The exposure time of the DBD reactor onto a spiked coupon was varied between 0 (control), 30, 60, 90, and 120s. Each exposure time was tested on two coupon samples on at least three independent days for a minimum of six total tested samples per exposure time. Control samples were prepared but not treated using the NTP to account for the potential virus viability loss during drying and treatment time.

A double-agar layer plaque assay was used to assess MS2 (MS2 ATCC #15597-B1) viability in a bacterial host (*Escherichia coli*). [211-213]. Tryptic soy agar (TSA) (BD Difco #236950) was prepared following the manufacturer's directions and added to Petri dishes (Fisherbrand 100 × 15 mm #FB0875712). The plates were cooled at room temperature. 100 μL of diluted sample and 100 μL of *E. coli* Famp (ATCC #700891) suspension were added to 7 mL of top agar (0.5% [/v] NaCl [Fisher Scientific #S271-500] and 0.7% [w/v] Bacto Agar [BD #214010]) in a borosilicate glass tube (Fisherbrand #14-961-27). The solution was mixed by rolling the tube between hands and poured on the prepared TSA plates. The top agar was cooled before the plates were inverted and incubated overnight at 37 °C. The plaques were counted the following day. The assay was performed in duplicates for all sample dilutions. A negative control (only *E. coli*) and PBS control (only PBS) were included in the analysis.The results are averaged over at least 6 samples and three independent tests. Inactivation was calculated as

$$Inactivation = -Log_{10}\frac{N_t}{N_0} \tag{27}$$

where N_t is the number of viruses on the test coupon after the DBD ozone treatment and N_0 is the number of viruses on a control test coupon without the DBD ozone treatment. The comparison with a control spiked test coupon ensures that the virus inactivation results were not influenced by the transportation or exposure to the ambient environment.

C.2 Results and Discussion

C.2.1 Reactor Operation and Ozone Production

A typical voltage input and current measured in the DBD reactor are shown in Figure ; the x-axis shows a normalized time scale (based on 20 kHz input frequency). A square wave input with a peak-to-peak voltage amplitude of 25 kV and frequency of 20 kHz shows a series of discharge current peaks following voltage polarity change. In the flat regions in the cycle, the system equilibrates (acts as a capacitor), and the discharge spikes are not present.

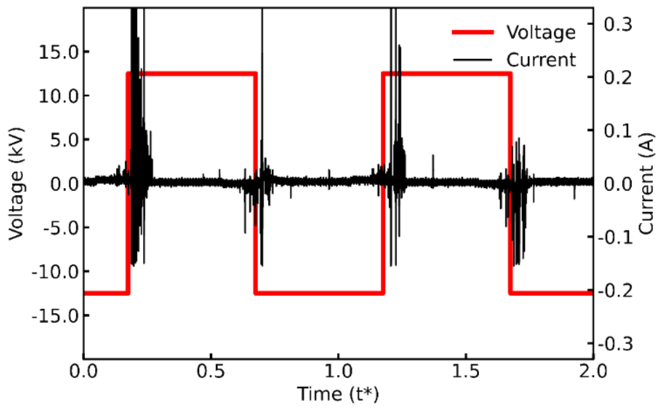

Figure C.4. DBD reactor voltage and current as a function of time at the P_{in} = 150 W input power, $V_{P\text{-}P}$ = 25 kV, *f* = 20 kHz.

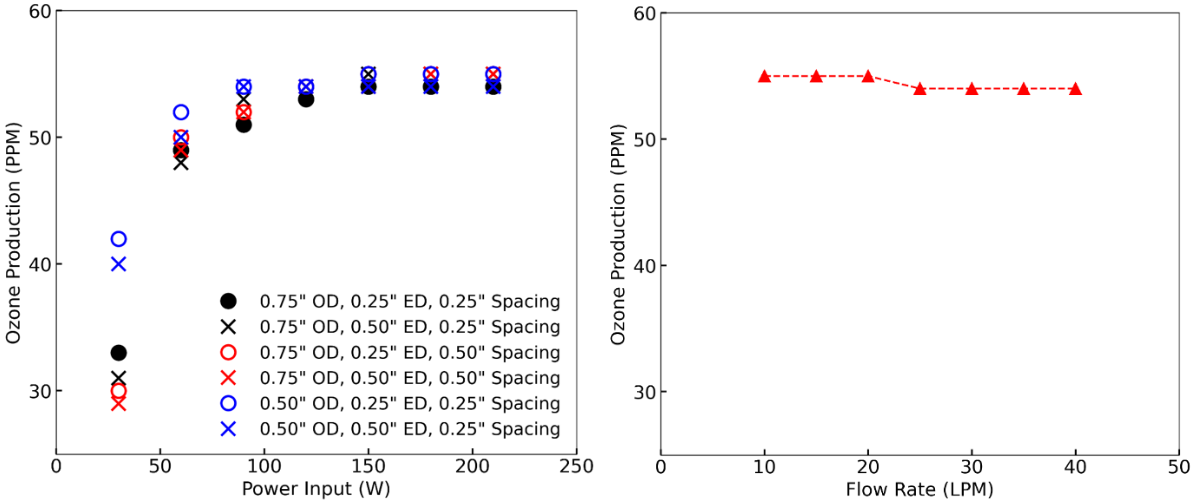

Figure C.5. Left – DBD ozone generation vs. power input for fixed flow rate (10 LPM) and varying outer diameter (OD), nozzle exit diameter (ED), and electrode spacing. Right – DBD ozone generation with varying flow rates, Pin = 150 W, reactor OD = 19.05 mm, coil spacing - 6.35 mm.

Dissociation and recombination of multiple free radicals occur during the ionization process. The RONS yields depend on the strength and polarity of the E-field, stability (reactivity) of the specific free radicals, and ability to remove the species before recombination occurs or when electrode polarity switches to the other half-cycle. Stable species in the NTP environment include ozone and nitrogen oxides, and with increasing relative humidity, NH_3 and HNO_3 are also present [214, 215]. Ozone is formed when monoatomic oxygen atoms are combined with diatomic oxygen [4]. Ozone is easy to monitor; thus, it has been used as an indicator for RONS levels in pathogen inactivation studies, e.g., refs [187] [197]. Figure (left) shows the ozone production as a function of operating parameters and the geometrical configuration of the reactor. Generally, at the lowest tested condition (30 W), the ozone level at the exit was in the 30-40 ppm range and at the highest (210 W) ~55 ppm. At lower power settings (P_{in} < 75 W), ozone production increases rapidly with power input. Ozone production reaches the saturation limit at higher power settings (P_{in} > 150 W). This limit can be explained by the balance of ion production, species recombination, and positive species scavenging in the negative half-cycle. Ion production in DBD reactors depends on the electrical parameters and the flow rate. E.g., frequency affects ozone output limits due to varying reaction rates [99]. The dependency on flow rates has been noted in the literature [206]. For a constant ozone generation rate, ozone concentration decreases as the fluid flow rate increases. Although the test facility is not humidity controlled, the relative humidity was measured to be between ~ 30 – 50 % throughout the testing period. The ozone concentration from the DBD reactor was measured in each test. The variation across the different test days for the same electrical input was within the rated accuracy of the ozone meter (±1 ppm).

The smaller reactor OD = 12.7 mm achieves the highest ozone yields at lower power input due to more efficient ionization in a stronger E-field (closer proximity between active and ground electrodes) and more effective ozone removal from the reactor tube (high velocities for the same flow rate). All geometries displayed a similar maximum ozone concentration for $P_{in} > 100$ W. In the lower input power cases, the DBD reactor with a grounded electrode with 12.7 mm coil spacing exhibited a slightly lower ozone concentration; however, the smaller plasma region did not cause a different ozone concentration production post-saturation. The ozone concentration does not increase for $P_{in} > 100$ W input, which would be the optimal electrical operating condition for this DBD reactor. Note that a higher flow rate results in more total reactive species over time; however, the ozone concentration at the reactor exit remains the same as the 10 LPM.

Figure (right) shows the ozone level at the reactor exit for $P_{in} = 150$W, reactor tube OD = 19.05 mm / ID = 16 mm, exit nozzle inner diameter - 6.35 mm, and coil spacing - 6.35 mm as a function of flow rates. These reactor conditions were used in the virus inactivation tests. In this range of flow rates, ozone production appears largely independent of the flow rate. The average exit velocity at these flow rates ranges from 5.26 m/s at 10 LPM to 26.3 m/s at 50 LPM. Few surface virus inactivation studies characterize the effect of flow rates on ROS production, e.g., Xia *et al.* reported a drop in ozone concentration from ~ 0.20 ppm to ~ 0.10 ppm in a porous packed-bed geometry when the flow rate increased from 170 LPM to 455 LPM [206]. In our work, the ozone concentration did not change at a higher flow rate; thus, the total number of reactive species ejected from the reactor increased linearly with the flow rate. These results demonstrate the potential for scalability of the system; however, the flow rates above 50 LPM were not tested in this work. The DBD flow reactor outputs significantly higher ozone concentration than Xia *et al*. The low surface-to-volume form factor and chemically inert quartz walls of the axisymmetric DBD reactor allow for maintaining a high concentration of free radicals, allowing to efficiently expel the RONS from the reactor by the airflow.

C.2.2 Virus Inactivation

Virus inactivation tests were performed at varied exposure times using a DBD reactor with OD = 19.05 mm, exit nozzle diameter – 6.35 mm, coil spacing – 6.35 mm. The flow reactor was operated at a fixed power P_{in} = 150 W, flow rate – 10 LPM, and standoff distance – 10mm. Figure shows typical colony count results on double agar plates. Figure illustrates the inactivation rates as a function of time and shows that at the lowest exposure time of the 30s, the DBD reactor yielded a 1.34 log reduction (~95.4%), and at the longest exposure time of 120s, the process yielded a 5.28 log reduction (~99.999%). The two standard deviation error bars for a minimum of 6 samples are shown. The inactivation is approximately linear, with exposure time in this range with a ~2.54 log reduction per minute. The highest exposure experiment yielded samples with very few viable colony counts approaching the detection limit for this titer concentration.

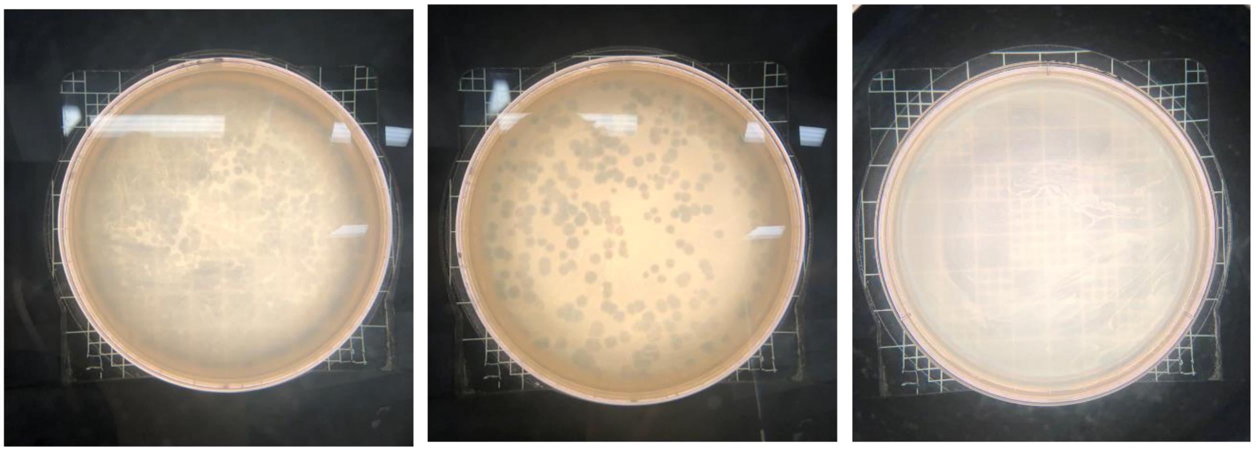

Figure C.6. Example agar plates with untreated control at ~106 colonies (left), 30s inactivation at with 1.3 Log10 reduction (middle), and 120s inactivation with 5.29 Log10 reduction (right).

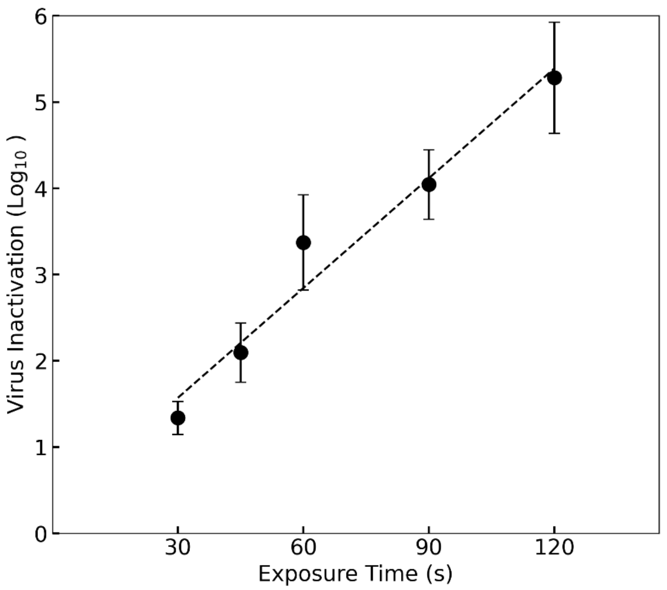

Figure C.7. MS2 inactivation on metal coupons for the 30 s –120 s exposure to impinging jet from the DBD reactor with two standard deviation error bars.

DBD flow reactors were not previously used in MS2 surface inactivation studies. Still, the results can be comparable to Thomas et al. [3] and Chen et al. [2], who used an ionized impinging jet. Thomas *et al.* used the air-fed DC-powered plasma torch on virus sample wells (round-bottom cell culture plates) instead of a flat coupon surface. The plasma torch yielded a 1.15 log reduction (93%), compared to the 1.34 log reduction of our DBD reactor with a 30 s exposure time. Thomas *et al*. show ~2 log reduction after 120 s exposure while operating their reactor at 320 W. This difference can be attributed to the plasma generation methods DC vs. AC-DBD, lower RONS concentration at the surface due to space charge shielding (well vs. flat coupon and conductive vs. non-conductive surfaces). Chen *et al*. used the DBD flow reactor with Ar and He gases. The Ar experiments yielded the best inactivation results at ~ 3 log reduction (99.9%) after ~ 60s exposure. The deposition on metal surface inactivation showed better inactivation; the authors suggested this is due to a higher discharge intensity and reactive species concentration. The inactivation rates agree with the results of the current study, although a different gas was used, and in this study, the DBD discharge does not occur on the interrogated surface as in Chen et al. Furthermore, the virus samples of Chen et al. are presented in a wet well, unlike the dried coupon virus samples of the presented work. Compared to DBD reactors used for aerosol inactivation (Xia et al. reported up to 2.3 log viable virus reduction), the surface inactivation rate in the current study is higher and the maximum inactivation is greater than 2 log greater; however, longer exposure times were used [206]. The largest challenge in comparing the aerosol-based studies is that aerosol passed through the high-intensity ionization zone becomes highly charged and may be collected on the reactor walls and electrodes due to electrostatic forces [216, 217]. To determine whether the aerosolized virus is inactivated or electrostatically collected inside the DBD reactor, Xia et al. collected aerosols in liquid impingers and analyzed the fluid by Tissue Culture Infectious Dose ($TCID_{50}$) assay and quantitative polymerase chain reaction (qPCR) analysis [218].

C.3 Chapter Summary

This work describes a novel concentric DBD flow reactor for MS2 surface virus inactivation. The airflow is passed through the DBD reactor, and the ionized air impinges onto the surface, deactivating the virus. The effect of varying DBD reactor sizes, exit nozzle diameters, and electrode coverages on ozone generation was explored. DBD reactor outputs a maximum ozone concentration of ~ 55 ppm for input power > 100 W. The concentration decreases slightly when airflow increases from 10 to 40 LPM. Before the saturation limit, the smaller DBD reactor generates more ozone due to the stronger electric field for the same given power input. The impinging jet exiting the DBD reactor at a fixed flow rate was used to test MS2 virus inactivation on the metal coupon at varying exposure times. At 30-second exposure, a 1.34 log reduction was shown, and after 90 seconds, a 5.28 log reduction was observed. The inactivation rate follows an approximately linear relationship with exposure time. The maximum inactivation of 5.28 log is significantly higher than previous non-thermal plasma reactors operated with ionized atmospheric air. While the different reactive species' exact mechanisms and relative contributions are not fully elucidated, the DBD flow reactor approach provides a promising method for non-contact surface disinfection. Future studies should investigate the scalability of the approach and consider a variety of pathogens.Figure C.1

REFERENCES

[1] A. Tang, A. Ong, N. Beck, J. S. Meschke, and I. V. Novosselov, "Surface Virus Inactivation by Non-Thermal Plasma Flow Reactor," 2023.

[2] Z. Chen, G. Garcia Jr, V. Arumugaswami, and R. E. Wirz, "Cold atmospheric plasma for SARS-CoV-2 inactivation," *Physics of Fluids,* vol. 32, no. 11, p. 111702, 2020.

[3] S. V. Thomas *et al.*, "Inactivation of SARS-CoV-2 on Surfaces by Cold-Plasma-Generated Reactive Species," *Bioengineering,* vol. 10, no. 3, p. 280, 2023.

[4] S. Pekárek, "Non-thermal plasma ozone generation," *Acta Polytechnica,* vol. 43, no. 6, 2003.

[5] X. Zhang, B. J. Lee, H. G. Im, and M. S. Cha, "Ozone production with dielectric barrier discharge: effects of power source and humidity," *IEEE transactions on plasma science,* vol. 44, no. 10, pp. 2288-2296, 2016.

[6] I. Levchenko *et al.*, "Space micropropulsion systems for Cubesats and small satellites: From proximate targets to furthermost frontiers," *Applied Physics Reviews,* vol. 5, no. 1, 2018, doi: 10.1063/1.5007734.

[7] T. Morris and M. Jugroot, "Study of an electrostatic micropropulsion system for nanosatellites," *Canadian Aeronautics and Space Journal,* vol. 57, no. 1, pp. 99-105, 2011, doi: 10.5589/q11-017.

[8] E. Moreau, "Airflow control by non-thermal plasma actuators," *Journal of Physics D: Applied Physics,* vol. 40, no. 3, pp. 605-636, 2007, doi: 10.1088/0022-3727/40/3/S01.

[9] I. Adamovich *et al.*, "The 2017 Plasma Roadmap: Low temperature plasma science and technology," *Journal of Physics D: Applied Physics,* vol. 50, no. 32, p. 323001, 2017.

[10] M. E. Ellion, "A study of electrical discharge in low-pressure air," 1965.

[11] K. Iranshahi, T. Defraeye, R. M. Rossi, and U. C. Müller, "Electrohydrodynamics and its applications: Recent advances and future perspectives," *International Journal of Heat and Mass Transfer,* vol. 232, p. 125895, 2024.

[12] A. Tang, R. S. Vaddi, A. Mamishev, and I. V. Novosselov, "Empirical relations for discharge current and momentum injection in dielectric barrier discharge plasma actuators," *Journal of Physics D: Applied Physics,* vol. 54, no. 24, p. 245204, 2021/03/31 2021, doi: 10.1088/1361-6463/abec0b.

[13] A. Tang, N. Li, B. Price, A. Mamishev, A. Aliseda, and I. Novosselov, "Dielectric barrier discharge actuators: Momentum injection into co-flow and counter-flow freestream," *Journal of Electrostatics,* vol. 129, p. 103918, 2024.

[14] A. Tang, A. Aliseda, A. Mamishev, and I. Novosselov, "DC-Augmented Dielectric Barrier Discharge (DCA-DBD)," *arXiv preprint arXiv:2403.18064,* 2024.

[15] A. Tang, A. Mamishev, and I. Novosselov, "AC-Augmented Dielectric Barrier Discharge," *arXiv preprint arXiv:2411.17677,* 2024.

[16] A. Tang, A. Mamishev, and I. Novosselov, "Multi-Electrode Dielectric Barrier Discharge Actuators: Geometrical Optimization of High Power Density Array," *arXiv preprint arXiv:2412.01237,* 2024.

[17] E. Moreau, "Airflow control by non-thermal plasma actuators," *Journal of physics D: applied physics,* vol. 40, no. 3, p. 605, 2007.

[18] J. W. Zimmerman, A. Palla, D. L. Carroll, G. Hristov, and P. J. Ansell, "Plasma Actuator with Arc Breakdown in a Magnetic Field for Active Flow Control Applications," in *48th AIAA Plasmadynamics and Lasers Conference*, 2017, p. 3477.

[19] T. Orrière, É. Moreau, and D. Z. Pai, "Electric wind generation by nanosecond repetitively pulsed microplasmas," *Journal of physics. D, Applied physics,* vol. 52, no. 46, p. 464002, 2019, doi: 10.1088/1361-6463/ab372f.

[20] N. Benard and E. Moreau, "Electrical and mechanical characteristics of surface AC dielectric barrier discharge plasma actuators applied to airflow control," *Experiments in Fluids,* vol. 55, no. 11, p. 1846, 2014.

[21] A. Ebrahimi and M. Hajipour, "Flow separation control over an airfoil using dual excitation of DBD plasma actuators," *Aerospace Science and Technology,* vol. 79, pp. 658-668, 2018, doi: 10.1016/j.ast.2018.06.019.

[22] Y. Guan, R. S. Vaddi, A. Aliseda, and I. Novosselov, "Experimental and numerical investigation of electrohydrodynamic flow in a point-to-ring corona discharge," *Physical Review Fluids,* vol. 3, no. 4, 2018, doi: 10.1103/PhysRevFluids.3.043701.

[23] T. C. Corke, M. L. Post, and D. M. Orlov, "SDBD plasma enhanced aerodynamics: concepts, optimization and applications," *Progress in Aerospace Sciences,* vol. 43, no. 7, pp. 193-217, 2007, doi: 10.1016/j.paerosci.2007.06.001.

[24] T. C. Corke, C. L. Enloe, and S. P. Wilkinson, "Dielectric Barrier Discharge Plasma Actuators for Flow Control *," *Annu. Rev. Fluid Mech.,* vol. 42, no. 1, pp. 505-529, 2010, doi: 10.1146/annurev-fluid-121108-145550.

[25] M. Han, J. Li, Z. Niu, H. Liang, G. Zhao, and W. Hua, "Aerodynamic performance enhancement of a flying wing using nanosecond pulsed DBD plasma actuator," *Chinese Journal of Aeronautics,* vol. 28, no. 2, pp. 377-384, 2015, doi: 10.1016/j.cja.2015.02.006.

[26] Y. Guan, R. S. Vaddi, A. Aliseda, and I. Novosselov, "Analytical model of electro-hydrodynamic flow in corona discharge," *Physics of Plasmas,* vol. 25, no. 8, p. 083507, 2018.

[27] Y. Guan, R. S. Vaddi, A. Aliseda, and I. Novosselov, "Experimental and numerical investigation of electrohydrodynamic flow in a point-to-ring corona discharge," *Physical Review Fluids,* vol. 3, no. 4, p. 043701, 2018.

[28] G. Touchard, "Plasma actuators for aeronautics applications-State of art review," *International Journal of Plasma Environmental Science and Technology,* vol. 2, no. 1, pp. 1-25, 2008.

[29] J. Yao, J. Miao, J. Li, X. Lian, and J. Ouyang, "Asymmetric discharges of dielectric barrier discharge in atmospheric air," *Applied Physics Letters,* vol. 122, no. 8, 2023.

[30] M. M. Wojewodka, C. White, S. Shahpar, and K. Kontis, "A review of flow control techniques and optimisation in s-shaped ducts," *International Journal of Heat and Fluid Flow,* vol. 74, pp. 223-235, 2018.

[31] V. Ioannou and S. Laizet, "Numerical investigation of plasma-controlled turbulent jets for mixing enhancement," *International Journal of Heat and Fluid Flow,* vol. 70, pp. 193-205, 2018.

[32] J.-L. Chen and Y.-H. Liao, "The influence of a plasma actuator embedded in a bluff-body on the stabilization of nonpremixed jet flames," *International Journal of Heat and Fluid Flow,* vol. 100, p. 109111, 2023.

[33] M. T. Hehner, D. Gatti, and J. Kriegseis, "Stokes-layer formation under absence of moving parts—A novel oscillatory plasma actuator design for turbulent drag reduction," *Physics of Fluids,* vol. 31, no. 5, p. 051701, 2019.

[34] A. Duong, T. Corke, F. Thomas, and K. Yates, "Turbulent boundary layer drag reduction using pulsed-dc plasma actuation," *Journal of Fluid Mechanics,* 2019.

[35] N. Benard, J. Jolibois, and E. Moreau, "Lift and drag performances of an axisymmetric airfoil controlled by plasma actuator," *Journal of Electrostatics,* vol. 67, no. 2 3, p. 133, 2009, doi: 10.1016/j.elstat.2009.01.008.

[36] S. G. Pouryoussefi, M. Mirzaei, F. Alinejad, and S. M. Pouryoussefi, "Experimental investigation of separation bubble control on an iced airfoil using plasma actuator," *Applied Thermal Engineering,* vol. 100, pp. 1334-1341, 2016.

[37] L. Francioso, C. De Pascali, E. Pescini, M. De Giorgi, and P. Siciliano, "Modeling, fabrication and plasma actuator coupling of flexible pressure sensors for flow separation detection and control in aeronautical applications," *Journal of Physics D: Applied Physics,* vol. 49, no. 23, p. 235201, 2016.

[38] H. Xu *et al.*, "Flight of an aeroplane with solid-state propulsion," *Nature,* vol. 563, no. 7732, pp. 532-535, 2018.

[39] D. S. Drew and K. S. Pister, "First takeoff of a flying microrobot with no moving parts," in *Manipulation, Automation and Robotics at Small Scales (MARSS), 2017 International Conference on*, 2017: IEEE, pp. 1-5.

[40] H. K. Hari Prasad, R. S. Vaddi, Y. M. Chukewad, E. Dedic, I. Novosselov, and S. B. Fuller, "A laser-microfabricated electrohydrodynamic thruster for centimeter-scale aerial robots," *PloS one,* vol. 15, no. 4, p. e0231362, 2020.

[41] R. S. Vaddi, Y. Guan, A. Mamishev, and I. Novosselov, "Analytical model for electrohydrodynamic thrust," *Proceedings A: Mathematical, Physical and Engineering Sciences,* vol. 476, no. 2241, 2020.

[42] R. S. Vaddi, "Electrohydrodynamic Actuators for Propulsion and Flow Control," 2021.

[43] R. S. Vaddi, Y. Guan, and I. Novosselov, "Particle Dynamics in Corona Induced Electro-hydrodynamic Flow," 2019.

[44] R. S. Vaddi, C. Sota, A. Mamishev, and I. Novosselov, "Active Flow Control of NACA 0012 airfoil using Sawtooth Direct Current Augmented Dielectric Barrier Discharge Plasma Actuator," *arXiv preprint arXiv:2106.11453,* 2021.

[45] Y. Guan, R. S. Vaddi, A. Aliseda, and I. Novosselov, "Comparison of Analytical and Numerical Models for Point to Ring Electro-Hydrodynamic Flow," 2019.

[46] Y. Guan, J. Riley, and I. Novosselov, "Three-dimensional Electro-convective Vortices in Cross-flow," 2019.

[47] Y. Guan and I. Novosselov, "Two relaxation time lattice Boltzmann method coupled to fast Fourier transform Poisson solver: Application to electroconvective flow," *Journal of Computational Physics,* vol. 397, 2019, doi: 10.1016/j.jcp.2019.07.029.

[48] I. Novosselov, A. Aliseda, J. Riley, and Y. Guan, "Study of Laminar Electrohydrodynamic Flows," I. Novosselov, A. Aliseda, and J. Riley, Eds., ed: ProQuest Dissertations Publishing, 2019.

[49] Y. Guan, J. Riley, and I. Novosselov, "Numerical analysis of 2D and 3D electrohydrodynamic convection instability with crossflow," *Bulletin of the American Physical Society,* 2019.

[50] P. Fillingham, Y. Guan, R. Sankar Vadi, and I. Novosselov, "Numerical, Experimental and Analytical Investigation of the Planar Electrohydrodynamic Wall Jet," *Bulletin of the American Physical Society,* vol. 64, 2019.

[51] P. Fillingham and I. V. Novosselov, "Wall jet similarity of impinging planar underexpanded jets," *International Journal of Heat and Fluid Flow,* vol. 81, p. 108516, 2020.

[52] P. Fillingham, A. Viswanathan, and I. V. Novosselov, "Model for Wall Shear Stress from Obliquely Impinging Planar Underexpanded Jets," *Applied Sciences,* vol. 12, no. 14, p. 7311, 2022.

[53] L. Tonks and I. Langmuir, "A general theory of the plasma of an arc," *Physical review,* vol. 34, no. 6, p. 876, 1929.

[54] H. R. Velkoff and J. Ketcham, "Effect of an electrostatic field on boundary-layer transition," *Aiaa Journal,* vol. 6, no. 7, pp. 1381-1383, 1968.

[55] J. Roth, D. Sherman, and S. Wilkinson, "Boundary layer flow control with a one atmosphere uniform glow discharge surface plasma," in *36th AIAA Aerospace Sciences Meeting and Exhibit,* 1998, p. 328.

[56] C. L. Enloe, T. E. McLaughlin, R. D. VanDyken, K. D. Kachner, E. J. Jumper, and T. C. Corke, "Mechanisms and responses of a single dielectric barrier plasma actuator: plasma morphology," *AIAA Journal,* vol. 42, no. 3, p. 589, 2004, doi: 10.2514/1.2305.

[57] J. Pons, E. Moreau, and G. Touchard, "Asymmetric surface dielectric barrier discharge in air at atmospheric pressure: electrical properties and induced airflow characteristics," *Journal of physics D: applied physics,* vol. 38, no. 19, p. 3635, 2005.

[58] J. Pons, E. Moreau, and G. Touchard, "Electrical and aerodynamic characteristics of atmospheric pressure barrier discharges in ambient air," 2004.

[59] J.-C. Laurentie, J. Jolibois, and E. Moreau, "Surface dielectric barrier discharge: Effect of encapsulation of the grounded electrode on the electromechanical characteristics of the plasma actuator," *Journal of Electrostatics,* vol. 67, no. 2-3, pp. 93-98, 2009.

[60] D. B. Graves, "The emerging role of reactive oxygen and nitrogen species in redox biology and some implications for plasma applications to medicine and biology," *Journal of Physics D: Applied Physics,* vol. 45, no. 26, p. 263001, 2012.

[61] N. Benard, P. Noté, M. Caron, and E. Moreau, "Highly time-resolved investigation of the electric wind caused by surface DBD at various ac frequencies," *Journal of electrostatics,* vol. 88, pp. 41-48, 2017, doi: 10.1016/j.elstat.2017.01.018.

[62] E. Moreau *et al.*, "Surface dielectric barrier discharge plasma actuators," *ERCOFTAC Bulletin,* vol. 94, pp. 5-10, 2013.

[63] A. Debien, N. Benard, L. David, and E. Moreau, "Unsteady aspect of the electrohydrodynamic force produced by surface dielectric barrier discharge actuators," *Applied Physics Letters,* vol. 100, no. 1, 2012.

[64] A. Debien, N. Benard, and E. Moreau, "Streamer inhibition for improving force and electric wind produced by DBD actuators," *Journal of Physics D: Applied Physics,* vol. 45, no. 21, p. 215201, 2012.

[65] A. Hoskinson, L. Oksuz, and N. Hershkowitz, "Microdischarge propagation and expansion in a surface dielectric barrier discharge," *Applied Physics Letters,* vol. 93, no. 22, p. 221501, 2008.

[66] N. Benard, A. Debien, and E. Moreau, "Time-dependent volume force produced by a non-thermal plasma actuator from experimental velocity field," *Journal of Physics D: Applied Physics,* vol. 46, no. 24, p. 245201, 2013.

[67] R. S. Vaddi, Y. Guan, A. Mamishev, and I. Novosselov, "Analytical model for electrohydrodynamic thrust," *Proceedings of the Royal Society A,* vol. 476, no. 2241, p. 20200220, 2020.

[68] E. Moreau, P. Audier, and N. Benard, "Ionic wind produced by positive and negative corona discharges in air," *Journal of Electrostatics,* vol. 93, pp. 85-96, 2018.

[69] F. Sohbatzadeh, H. S. Ahmadi, and H. Mirzanejhad, "Enhancement of thrust force of an atmospheric pressure positive corona discharge by DC superimposed AC high voltage," *Journal of Physics D: Applied Physics,* vol. 55, no. 44, p. 445201, 2022.

[70] D. Keisar, D. Hasin, and D. Greenblatt, "Plasma actuator application on a full-scale aircraft tail," *AIAA Journal,* vol. 57, no. 2, pp. 616-627, 2019.

[71] H. Akbıyık, H. Yavuz, and Y. E. Akansu, "Comparison of the linear and spanwise-segmented DBD plasma actuators on flow control around a NACA0015 airfoil," *IEEE Transactions on Plasma Science,* vol. 45, no. 11, pp. 2913-2921, 2017.

[72] K. Suzuki *et al.*, "Development of small high-voltage AC power supply for a dielectric barrier discharge plasma actuator," *Review of Scientific Instruments,* vol. 92, no. 2, 2021, doi: 10.1063/5.0015377.

[73] H. T. Truong, M. Hayashi, Y. Uesugi, Y. Tanaka, and T. Ishijima, "Novel design of high voltage pulse source for efficient dielectric barrier discharge generation by using silicon diodes for alternating current," *Review of scientific instruments,* vol. 88, no. 6, pp. 065105-065105, 2017, doi: 10.1063/1.4984947.

[74] A. R. Hoskinson and N. Hershkowitz, "Differences between dielectric barrier discharge plasma actuators with cylindrical and rectangular exposed electrodes," *Journal of Physics D: Applied Physics,* vol. 43, no. 6, p. 065205, 2010, doi: 10.1088/0022-3727/43/6/065205.

[75] E. Moreau, J. Cazour, and N. Benard, "Influence of the air-exposed active electrode shape on the electrical, optical and mechanical characteristics of a surface dielectric barrier discharge plasma actuator," *Journal of Electrostatics,* vol. 93, pp. 146-153, 2018.

[76] F. Rodrigues, J. Pascoa, and M. Trancossi, "Analysis of innovative plasma actuator geometries for boundary layer control," in *ASME International Mechanical Engineering Congress and Exposition*, 2016, vol. 50510: American Society of Mechanical Engineers, p. V001T03A007.

[77] J. Omidi and K. Mazaheri, "Micro-plasma actuator mechanisms in interaction with fluid flow for wind energy applications: Physical parameters," *Physics of Fluids,* vol. 32, no. 7, p. 077107, 2020.

[78] E. Moreau, K. Bayoda, and N. Benard, "Streamer propagation and pressure waves produced by a nanosecond pulsed surface sliding discharge: effect of the high voltage electrode shape," *Journal of Physics D: Applied Physics,* 2020.

[79] R. J. Durscher and S. Roy, "Three-dimensional flow measurements induced from serpentine plasma actuators in quiescent air," *Journal of physics. D, Applied physics,* vol. 45, no. 3, p. 035202, 2012, doi: 10.1088/0022-3727/45/3/035202.

[80] R. Joussot, A. Leroy, R. Weber, H. Rabat, S. Loyer, and D. Hong, "Plasma morphology and induced airflow characterization of a DBD actuator with serrated electrode," *Journal of physics. D, Applied physics,* vol. 46, no. 12, p. 125204, 2013, doi: 10.1088/0022-3727/46/12/125204.

[81] F. Rodrigues, A. Mushyam, J. Pascoa, and M. Trancossi, "A new plasma actuator configuration for improved efficiency: The stair-shaped dielectric barrier discharge actuator," *Journal of Physics D: Applied Physics,* vol. 52, no. 38, p. 385201, 2019.

[82] M. Kuhnhenn, B. Simon, I. Maden, and J. Kriegseis, "Interrelation of phase-averaged volume force and capacitance of dielectric barrier discharge plasma actuators," *Journal of Fluid Mechanics,* vol. 809, 2016.

[83] A. Cristofolini, G. Neretti, and C. A. Borghi, "Effect of the charge surface distribution on the flow field induced by a dielectric barrier discharge actuator," *Journal of Applied Physics,* vol. 114, no. 7, 2013.

[84] D. F. Opaits *et al.*, "Experimental investigation of dielectric barrier discharge plasma actuators driven by repetitive high-voltage nanosecond pulses with dc or low frequency sinusoidal bias," *Journal of Applied Physics,* vol. 104, no. 4, 2008, doi: 10.1063/1.2968251.

[85] S. Sato, K. Mitsuhashi, T. Enokido, A. Komuro, A. Ando, and N. Ohnishi, "Surface-charge control strategy for enhanced electrohydrodynamic force in dielectric barrier discharge plasma actuators," *Journal of Physics D: Applied Physics,* vol. 54, no. 45, p. 455203, 2021.

[86] B. Ibrahimoglu, M. Z. Yilmazoglu, and A. Cücen, "Numerical Analysis of Active Control of Flow on a DBD Plasma Actuator Integrated Airfoil," in *Sustainable Aviation*: Springer, 2016, pp. 363-374.

[87] C. Shi, K. Adamiak, and G. Castle, "Numerical study of the characteristics of a dielectric barrier discharge plasma actuator," *Journal of Physics D: Applied Physics,* vol. 51, no. 9, p. 095201, 2018.

[88] Y. Suzen, G. Huang, J. Jacob, and D. Ashpis, "Numerical simulations of plasma based flow control applications," in *35th AIAA Fluid Dynamics Conference and Exhibit*, 2005, p. 4633.

[89] Y. Guan and I. Novosselov, "Numerical analysis of electroconvection in cross-flow with unipolar charge injection," *Physical Review Fluids,* vol. 4, no. 10, 2019, doi: 10.1103/PhysRevFluids.4.103701.

[90] Y. Guan, R. S. Vaddi, A. Aliseda, and I. Novosselov, "Analytical model of electro-hydrodynamic flow in corona discharge," *Physics of Plasmas,* vol. 25, no. 8, 2018, doi: 10.1063/1.5029403.

[91] Y. B. Suzen, P. G. Huang, J. D. Jacob, and D. E. Ashpis, "Numerical simulations of plasma based flow control applications," ed, 2005, p. <xocs:firstpage xmlns:xocs=""/>.

[92] D. M. Orlov, *Modelling and simulation of single dielectric barrier discharge plasma actuators*. 2006.

[93] B. Jayaraman and W. Shyy, "Modeling of dielectric barrier discharge-induced fluid dynamics and heat transfer," *Progress in Aerospace Sciences,* vol. 44, no. 3, pp. 139-191, 2008.

[94] H. Zhang, Y. Wu, and Y. Li, "Mechanism of compressor airfoil boundary layer flow control using nanosecond plasma actuation," *International Journal of Heat and Fluid Flow,* vol. 80, p. 108502, 2019.

[95] J.-S. Yoon and J.-H. Han, "One-equation modeling and validation of dielectric barrier discharge plasma actuator thrust," *Journal of Physics D: Applied Physics,* vol. 47, no. 40, p. 405202, 2014.

[96] Z. Li, B. Hu, S. Lan, J. Zhang, and J. Huang, "Control of turbulent channel flow using a plasma-based body force," *Computers & fluids,* vol. 119, pp. 26-36, 2015, doi: 10.1016/j.compfluid.2015.07.001.

[97] R. Pereira, D. Ragni, and M. Kotsonis, "Effect of external flow velocity on momentum transfer of dielectric barrier discharge plasma actuators," *Journal of applied physics,* vol. 116, no. 10, p. 103301, 2014, doi: 10.1063/1.4894518.

[98] N. Benard, L. N. Cattafesta, E. Moreau, J. Griffin, and J. P. Bonnet, "On the benefits of hysteresis effects for closed-loop separation control using plasma actuation," *Physics of Fluids,* vol. 23, no. 8, 2011, doi: 10.1063/1.3614482.

[99] F. O. Thomas, T. C. Corke, M. Iqbal, A. Kozlov, and D. Schatzman, "Optimization of Dielectric Barrier Discharge Plasma Actuators for Active Aerodynamic Flow Control," *AIAA Journal,* vol. 47, no. 9, pp. 2169-2178, 2009, doi: 10.2514/1.41588.

[100] G. Correale and M. Kotsonis, "Effect of nanosecond-pulsed plasma actuation on a separated laminar flow," *Experimental Thermal and Fluid Science,* vol. 81, pp. 406-419, 2017.

[101] J. Kissing, S. Wegt, S. Jakirlic, J. Kriegseis, J. Hussong, and C. Tropea, "Leading edge vortex formation and detachment on a flat plate undergoing simultaneous pitching and plunging motion: Experimental and computational study," *International Journal of Heat and Fluid Flow,* vol. 86, p. 108726, 2020.

[102] L. Yang, J. Li, J. Cai, G. Wang, and Z. Zhang, "Lift augmentation based on flap deflection with dielectric barrier discharge plasma flow control over multi-element airfoils," *Journal of Fluids Engineering,* vol. 138, no. 3, 2016.

[103] J. Little, M. Nishihara, I. Adamovich, and M. Samimy, "High-lift airfoil trailing edge separation control using a single dielectric barrier discharge plasma actuator," *Experiments in fluids,* vol. 48, no. 3, pp. 521-537, 2010.

[104] L.-H. Feng, T. N. Jukes, K.-S. Choi, and J.-J. Wang, "Flow control over a NACA 0012 airfoil using dielectric-barrier-discharge plasma actuator with a Gurney flap," *Experiments in fluids,* vol. 52, no. 6, pp. 1533-1546, 2012.

[105] C. Anzalotta, K. Joshi, E. Fernandez, and S. Bhattacharya, "Effect of forcing the tip-gap of a NACA0065 airfoil using plasma actuators: A proof-of-concept study," *Aerospace Science and Technology,* p. 106268, 2020.

[106] L. H. Feng, T. Y. Shi, and Y. G. Liu, "Lift enhancement of an airfoil and an unmanned aerial vehicle by plasma Gurney flaps," *AIAA Journal,* vol. 55, no. 5, pp. 1622-1632, 2017, doi: 10.2514/1.J055426.

[107] X. Gu, H. Duc Vo, N. W. Mureithi, and E. Laurendeau, "Plasma Gurney Flap Flight Control at Low Angle of Attack," *Journal of Aircraft,* pp. 1-18, 2022.

[108] T. Brauner, S. Laizet, N. Benard, and E. Moreau, "Modelling of dielectric barrier discharge plasma actuators for direct numerical simulations," in *8th AIAA Flow Control Conference*, 2016, p. 3774.

[109] A. Debien, N. Benard, and E. Moreau, "Electric wind produced by sliding discharges," *Proceeding of 2nd ISNPEDADM new electrical technologies for environment, Nouméa*, 2011.

[110] E. Moreau, R. Sosa, and G. Artana, "Electric wind produced by surface plasma actuators: a new dielectric barrier discharge based on a three-electrode geometry," *Journal of Physics D: Applied Physics,* vol. 41, no. 11, p. 115204, 2008.

[111] C. Louste, G. Artana, E. Moreau, and G. Touchard, "Sliding discharge in air at atmospheric pressure: electrical properties," *Journal of Electrostatics,* vol. 63, no. 6-10, pp. 615-620, 2005.

[112] M. Xue, Z. Ni, C. Gao, B. Wu, and B. Zheng, "Deflected Synthetic Jet due to Vortices Induced by a Tri-Electrode Plasma Actuator," *AIAA Journal,* vol. 60, no. 6, pp. 3695-3706, 2022.

[113] H. Nishida, K. Nakai, and T. Matsuno, "Physical mechanism of tri-electrode plasma actuator with direct-current high voltage," *AIAA journal,* vol. 55, no. 6, pp. 1852-1861, 2017.

[114] B. Peng *et al.*, "Evolution of three-electrode pulsed surface dielectric barrier discharge: primary streamer, transitional streamer and secondary reverse streamer," *Plasma Sources Science and Technology,* vol. 29, no. 3, p. 035018, 2020.

[115] M. Forte, J. Jolibois, J. Pons, E. Moreau, G. Touchard, and M. Cazalens, "Optimization of a dielectric barrier discharge actuator by stationary and non-stationary measurements of the induced flow velocity:

application to airflow control," *Experiments in Fluids,* vol. 43, no. 6, pp. 917-928, 2007, doi: 10.1007/s00348-007-0362-7.

[116] A. Berendt, J. Podliński, and J. Mizeraczyk, "Elongated DBD with floating interelectrodes for actuators," *The European Physical Journal-Applied Physics,* vol. 55, no. 1, p. 13804, 2011.

[117] N. Benard, A. Mizuno, and E. Moreau, "A large-scale multiple dielectric barrier discharge actuator based on an innovative three-electrode design," *Journal of physics. D, Applied physics,* vol. 42, no. 23, p. 235204, 2009, doi: 10.1088/0022-3727/42/23/235204.

[118] S. Sato, H. Furukawa, A. Komuro, M. Takahashi, and N. Ohnishi, "Successively accelerated ionic wind with integrated dielectric-barrier-discharge plasma actuator for low-voltage operation," *Scientific reports,* vol. 9, no. 1, pp. 1-11, 2019.

[119] R. Durscher and S. Roy, "Evaluation of thrust measurement techniques for dielectric barrier discharge actuators," *Experiments in fluids,* vol. 53, pp. 1165-1176, 2012.

[120] T. C. Corke, M. L. Post, and D. M. Orlov, "Single dielectric barrier discharge plasma enhanced aerodynamics: physics, modeling and applications," *Experiments in Fluids,* vol. 46, no. 1, pp. 1-26, 2009.

[121] I. Biganzoli, R. Barni, and C. Riccardi, "Temporal evolution of a surface dielectric barrier discharge for different groups of plasma microdischarges," *Journal of physics. D, Applied physics,* vol. 46, no. 2, p. 025201, 2013, doi: 10.1088/0022-3727/46/2/025201.

[122] J. Kriegseis, B. Möller, S. Grundmann, and C. Tropea, "Capacitance and power consumption quantification of dielectric barrier discharge (DBD) plasma actuators," *Journal of Electrostatics,* vol. 69, no. 4, pp. 302-312, 2011.

[123] K. Kozlov, H. Wagner, R. Brandenburg, and P. Michel, "Spatio-temporally resolved spectroscopic diagnostics of the barrier discharge in air at atmospheric pressure," *Journal of Physics D: Applied Physics,* vol. 34, no. 21, p. 3164, 2001.

[124] V. V. Kovačević, B. P. Dojčinović, M. Jović, G. M. Roglić, B. M. Obradović, and M. M. Kuraica, "Measurement of reactive species generated by dielectric barrier discharge in direct contact with water in different atmospheres," *Journal of Physics D: Applied Physics,* vol. 50, no. 15, p. 155205, 2017.

[125] T. C. Corke and D. Orlov, "Modelling and simulation of single dielectric barrier discharge plasma actuators," T. C. Corke, Ed., ed: ProQuest Dissertations Publishing, 2006.

[126] T. Brauner, S. Laizet, N. Benard, and E. Moreau, "Modelling of dielectric barrier discharge plasma actuators for direct numerical simulations," ed: AAAI, 2016.

[127] C. Enloe, T. McLaughlin, R. Van Dyken, and J. Fischer, "Plasma structure in the aerodynamic plasma actuator," in *42nd AIAA Aerospace Sciences Meeting and Exhibit*, 2004, p. 844.

[128] J. Kriegseis, C. Schwarz, A. Duchmann, S. Grundmann, and C. Tropea, "PIV-based estimation of DBD plasma-actuator force terms," in *50th AIAA aerospace sciences meeting including the new horizons forum and aerospace exposition*, 2012, p. 411.

[129] D. E. Ashpis, E. L. Griebeler, and M. C. Laun, "Progress Toward Accurate Measurements of Power Consumptions of DBD Plasma Actuators," ed, 2012.

[130] M. Glauert, "The wall jet," *Journal of Fluid Mechanics,* vol. 1, no. 6, pp. 625-643, 1956.

[131] A. Melling, "Tracer particles and seeding for particle image velocimetry," *Measurement science and technology,* vol. 8, no. 12, p. 1406, 1997.

[132] M. Hamdi, M. Havet, O. Rouaud, and D. Tarlet, "Comparison of different tracers for PIV measurements in EHD airflow," *Experiments in fluids,* vol. 55, pp. 1-12, 2014.

[133] J. Kriegseis, C. Schwarz, C. a. Tropea, and S. Grundmann, "Velocity-information-based force-term estimation of dielectric-barrier discharge plasma actuators," *Journal of Physics D: Applied Physics,* vol. 46, no. 5, p. 055202, 2013.

[134] M. Neumann, C. Friedrich, J. Czarske, J. Kriegseis, and S. Grundmann, "Determination of the phase-resolved body force produced by a dielectric barrier discharge plasma actuator," *Journal of Physics D: Applied Physics,* vol. 46, no. 4, p. 042001, 2012.

[135] M. T. Hehner, G. Coutinho, R. B. S. Pereira, N. Benard, and J. Kriegseis, "On the interplay of body-force distributions and flow speed for dielectric-barrier discharge plasma actuators," *Journal of Physics D: Applied Physics,* vol. 56, no. 37, p. 375205, 2023.

[136] J. Deng, S. Matsuoka, A. Kumada, and K. Hidaka, "The influence of residual charge on surface discharge propagation," *Journal of Physics D: Applied Physics,* vol. 43, no. 49, p. 495203, 2010.

[137] T. Li *et al.*, "The role of surface charge and its decay in surface dielectric barrier discharges," *Plasma Sources Science and Technology,* vol. 31, no. 5, p. 055016, 2022.

[138] S. B. Leonov, V. Petrishchev, and I. V. Adamovich, "Dynamics of energy coupling and thermalization in barrier discharges over dielectric and weakly conducting surfaces on μs to ms time scales," *Journal of Physics D: Applied Physics,* vol. 47, no. 46, p. 465201, 2014.

[139] D. Opaits, M. Shneider, R. B. Miles, A. Likhanskii, and S. Macheret, "Surface charge in dielectric barrier discharge plasma actuators," *Physics of Plasmas,* vol. 15, no. 7, 2008.

[140] C. L. Enloe, G. I. Font, T. E. McLaughlin, and D. M. Orlov, "Surface Potential and Longitudinal Electric Field Measurements in the Aerodynamic Plasma Actuator," *AIAA Journal,* vol. 46, no. 11, pp. 2730-2740, 2008, doi: 10.2514/1.33973.

[141] C. Enloe, M. McHarg, and T. E. McLaughlin, "Time-correlated force production measurements of the dielectric barrier discharge plasma aerodynamic actuator," *Journal of applied physics,* vol. 103, no. 7, 2008.

[142] B. Peng, N. Jiang, K. Shang, N. Lu, J. Li, and Y. Wu, "Characteristics of three-electrode pulsed surface dielectric barrier discharge: streamer-to-spark transition and hydrodynamic expansion," *Journal of Physics D: Applied Physics,* vol. 55, no. 26, p. 265202, 2022.

[143] A. Hatamoto, K. Nakai, and H. Nishida, "Experimental Study on the Working Characteristics of Tri-Electrode Plasma Actuator Utilizing a Combination of Corona and Barrier Discharges," in *Actuators,* 2022, vol. 11, no. 11: MDPI, p. 322.

[144] A. V. Likhanskii, M. N. Shneider, S. O. Macheret, and R. B. Miles, "Modeling of dielectric barrier discharge plasma actuator in air," *Journal of Applied Physics,* vol. 103, no. 5, p. 053305, 2008.

[145] K. Singh, S. Roy, and D. Gaitonde, "Modeling of dielectric barrier discharge plasma actuator with atmospheric air chemistry," in *37th AIAA Plasmadynamics and Lasers Conference,* 2006, p. 3381.

[146] K. Nagato, Y. Matsui, T. Miyata, and T. Yamauchi, "An analysis of the evolution of negative ions produced by a corona ionizer in air," *International journal of mass spectrometry,* vol. 248, no. 3, pp. 142-147, 2006.

[147] J. D. Skalny, T. Mikoviny, S. Matejcik, and N. J. Mason, "An analysis of mass spectrometric study of negative ions extracted from negative corona discharge in air," *International Journal of Mass Spectrometry,* vol. 233, no. 1-3, pp. 317-324, 2004.

[148] A. Phelps, "The diffusion of charged particles in collisional plasmas: free and ambipolar diffusion at low and moderate pressures," *Journal of research of the National Institute of Standards and Technology,* vol. 95, no. 4, p. 407, 1990.

[149] R. Hill, "Nonneutral and quasi-neutral diffusion of weakly ionized multiconstituent plasma," *Journal of Geophysical Research: Space Physics,* vol. 83, no. A3, pp. 989-998, 1978.

[150] J. Kriegseis, S. Grundmann, and C. Tropea, "Power consumption, discharge capacitance and light emission as measures for thrust production of dielectric barrier discharge plasma actuators," *Journal of Applied Physics,* vol. 110, no. 1, 2011, doi: 10.1063/1.3603030.

[151] J. Boeuf and L. Pitchford, "Electrohydrodynamic force and aerodynamic flow acceleration in surface dielectric barrier discharge," *Journal of Applied Physics,* vol. 97, no. 10, 2005.

[152] Y. Akishev *et al.*, "DBD surface streamer expansion described using nonlinear diffusion of the electric potential over the barrier," *Journal of Physics D: Applied Physics,* vol. 46, no. 46, p. 464014, 2013.

[153] E. Moreau, C. Louste, and G. Touchard, "Electric wind induced by sliding discharge in air at atmospheric pressure," *Journal of Electrostatics,* vol. 66, no. 1-2, pp. 107-114, 2008.

[154] N. Benard and E. Moreau, "Role of the electric waveform supplying a dielectric barrier discharge plasma actuator," *Applied Physics Letters,* vol. 100, no. 19, p. 193503, 2012.

[155] J. Jolibois and E. Moreau, "Enhancement of the electromechanical performances of a single dielectric barrier discharge actuator," *IEEE Transactions on Dielectrics and Electrical Insulation,* vol. 16, no. 3, pp. 758-767, 2009.

[156] M. Kotsonis and S. Ghaemi, "Performance improvement of plasma actuators using asymmetric high voltage waveforms," *Journal of Physics D: Applied Physics,* vol. 45, no. 4, p. 045204, 2012.

[157] R. Giepman and M. Kotsonis, "On the mechanical efficiency of dielectric barrier discharge plasma actuators," *Applied Physics Letters,* vol. 98, no. 22, 2011.

[158] A. Hoskinson, N. Hershkowitz, and D. Ashpis, "Comparisons of force measurement methods for DBD plasma actuators in quiescent air," in *47th AIAA Aerospace Sciences Meeting including The New Horizons Forum and Aerospace Exposition*, 2009, p. 485.

[159] C. L. Enloe, T. E. McLaughlin, G. I. Font, and J. W. Baughn, "Parameterization of Temporal Structure in the Single-Dielectric-Barrier Aerodynamic Plasma Actuator," *AIAA Journal,* vol. 44, no. 6, pp. 1127-1136, 2006, doi: 10.2514/1.16297.

[160] J. Ferry and J. Rovey, "Thrust measurement of dielectric barrier discharge plasma actuators and power requirements for aerodynamic control," in *5th Flow Control Conference*, 2010, p. 4982.

[161] N. Gaug and A. Tang, "Lightweight Surveillance and Target Acquisition Radar Characterization for High Density Vertiplex Beyond Visual Line of Sight Operations," in *2022 IEEE/AIAA 41st Digital Avionics Systems Conference (DASC)*, 2022: IEEE, pp. 1-6.

[162] J. H. Mabe, F. T. Calkins, B. Wesley, R. Woszidlo, L. Taubert, and I. Wygnanski, "Single dielectric barrier discharge plasma actuators for improved airfoil performance," *Journal of Aircraft*, vol. 46, no. 3, pp. 847-855, 2009.

[163] E. Moreau, A. Debien, J.-M. Breux, and N. Benard, "Control of a turbulent flow separated at mid-chord along an airfoil with DBD plasma actuators," *Journal of electrostatics*, vol. 83, pp. 78-87, 2016.

[164] A. Silverstein, "Scale effect on Clark Y airfoil characteristics from NACA full-scale wind-tunnel tests," 1935.

[165] I. MARCHMAN, J, "Clark-Y airfoil performance at low Reynolds numbers," in *22nd Aerospace Sciences Meeting*, 1984, p. 52.

[166] K. Eto, Y. Kondo, K. Fukagata, and N. Tokugawa, "Assessment of friction drag reduction on a Clark-Y airfoil by uniform blowing," *AIAA journal*, vol. 57, no. 7, pp. 2774-2782, 2019.

[167] A. Tang, N. Li, B. Price, A. Mamishev, A. Aliseda, and I. Novosselov, "Dielectric Barrier Discharge Actuators: Experimental and Numerical Study of Momentum Injection into Co-flow and Counter-flow Freestream," *arXiv preprint arXiv:2304.00079*, 2023.

[168] L. Wang, C. W. Wong, Z. Lu, Z. Wu, and Y. Zhou, "Novel sawtooth dielectric barrier discharge plasma actuator for flow separation control," *AIAA journal*, vol. 55, no. 4, pp. 1405-1416, 2017.

[169] B. Jayaraman, Y.-C. Cho, and W. Shyy, "Modeling of dielectric barrier discharge plasma actuator," *Journal of Applied physics*, vol. 103, no. 5, p. 053304, 2008.

[170] C. De Bie *et al.*, "Dielectric barrier discharges used for the conversion of greenhouse gases: modeling the plasma chemistry by fluid simulations," *Plasma Sources Science and Technology*, vol. 20, no. 2, p. 024008, 2011.

[171] V. R. Soloviev and V. M. Krivtsov, "Numerical modelling of nanosecond surface dielectric barrier discharge evolution in atmospheric air," *Plasma Sources Science and Technology*, vol. 27, no. 11, p. 114001, 2018.

[172] F. Menter, "Zonal two equation kw turbulence models for aerodynamic flows," in *23rd fluid dynamics, plasmadynamics, and lasers conference*, 1993, p. 2906.

[173] W. H. Organization, "The burden of health care-associated infection worldwide," *World Health Organization*, 2010.

[174] J. G. Hecker *et al.*, "Measuring aerosols in the operating theatre and beyond using a real-time sensor network," *Anaesthesia*, vol. 77, no. 10, pp. 1097-1105, 2022, doi: https://doi.org/10.1111/anae.15842.

[175] K. Glenn, J. He, R. Rochlin, S. Teng, J. G. Hecker, and I. Novosselov, "Assessment of aerosol persistence in ICUs via low-cost sensor network and zonal models," *Scientific Reports*, vol. 13, no. 1, p. 3992, 2023/03/10 2023, doi: 10.1038/s41598-023-30778-7.

[176] S. Makhsous *et al.*, "Methodology for Addressing Infectious Aerosol Persistence in Real-Time Using Sensor Network," *Sensors*, vol. 21, no. 11, p. 3928, 2021.

[177] H. Ching-Hsuan *et al.*, "Assessing the effectiveness of portable HEPA air cleaners for reducing particulate matter exposure in King County, Washington homeless shelters: Implications for community congregate settings," *Science of The Total Environment*, p. 164402, 2023, doi: https://doi.org/10.1016/j.scitotenv.2023.164402.

[178] J. He, C.-H. Huang, N. Yuan, E. Austin, E. Seto, and I. Novosselov, "Network of low-cost air quality sensors for monitoring indoor, outdoor, and personal PM2.5 exposure in Seattle during the 2020 wildfire season," *Atmospheric Environment*, vol. 285, p. 119244, 2022/09/15/ 2022, doi: https://doi.org/10.1016/j.atmosenv.2022.119244.

[179] J. Wang and G. Du, "COVID-19 may transmit through aerosol," *Irish Journal of Medical Science (1971-)*, pp. 1-2, 2020.

[180] E. L. Anderson, P. Turnham, J. R. Griffin, and C. C. Clarke, "Consideration of the aerosol transmission for COVID-19 and public health," *Risk Analysis*, vol. 40, no. 5, pp. 902-907, 2020.

[181] W. H. Organization, "Water, sanitation, hygiene, and waste management for the COVID-19 virus: interim guidance, 23 April 2020," World Health Organization, 2020.

[182] A. Bivins *et al.*, "Wastewater-based epidemiology: global collaborative to maximize contributions in the fight against COVID-19," ed: ACS Publications, 2020.

[183] A. N. Kraay *et al.*, "Fomite-mediated transmission as a sufficient pathway: a comparative analysis across three viral pathogens," *BMC infectious diseases,* vol. 18, no. 1, pp. 1-13, 2018.

[184] W. A. Rutala and D. J. Weber, "Guideline for disinfection and sterilization in healthcare facilities, 2008. Update: May 2019," 2019.

[185] H. Jo, A. M. West, P. J. Teska, H. F. Oliver, and J. A. Howarter, "Assessment of early onset surface damage from accelerated disinfection protocol," *Antimicrobial Resistance & Infection Control,* vol. 8, no. 1, pp. 1-10, 2019.

[186] P. Strader, Y. Lee, P. Teska, X. Li, and J. L. Jones, "Approaches for characterizing surfaces damaged by disinfection in healthcare," *Nano Life,* vol. 9, no. 04, p. 1950002, 2019.

[187] J. Lee *et al.*, "Fast and easy disinfection of coronavirus-contaminated face masks using ozone gas produced by a dielectric barrier discharge plasma generator," *Environmental Science & Technology Letters,* vol. 8, no. 4, pp. 339-344, 2021.

[188] M. J. Pavlovich, D. S. Clark, and D. B. Graves, "Quantification of air plasma chemistry for surface disinfection," *Plasma Sources Science and Technology,* vol. 23, no. 6, p. 065036, 2014.

[189] M. Laroussi, "Low Temperature Plasma-Based Sterilization: Overview and State-of-the-Art," *Plasma Processes and Polymers,* vol. 2, no. 5, pp. 391-400, 2005, doi: https://doi.org/10.1002/ppap.200400078.

[190] M. Laroussi, "Nonthermal decontamination of biological media by atmospheric-pressure plasmas: review, analysis, and prospects," *IEEE Transactions on plasma science,* vol. 30, no. 4, pp. 1409-1415, 2002.

[191] M. Laroussi, J. P. Richardson, and F. C. Dobbs, "Effects of nonequilibrium atmospheric pressure plasmas on the heterotrophic pathways of bacteria and on their cell morphology," *Applied Physics Letters,* vol. 81, no. 4, pp. 772-774, 2002, doi: 10.1063/1.1494863.

[192] G. Fridman *et al.*, "Comparison of direct and indirect effects of non-thermal atmospheric-pressure plasma on bacteria," *Plasma Processes and Polymers,* vol. 4, no. 4, pp. 370-375, 2007.

[193] Z. Xiong *et al.*, "Room-temperature, atmospheric plasma needle reduces adenovirus gene expression in HEK 293A host cells," *Applied Physics Letters,* vol. 99, no. 25, 2011, doi: 10.1063/1.3669534.

[194] X. Lu *et al.*, "The roles of the various plasma agents in the inactivation of bacteria," *Journal of Applied Physics,* vol. 104, no. 5, 2008, doi: 10.1063/1.2977674.

[195] R. S. Vaddi, Y. Guan, and I. Novosselov, "Behavior of ultrafine particles in electro-hyfrodynamic flow induced by corona discharge," *Journal of Aerosol Science,* vol. 105587, 2020.

[196] K. Whitby, "Generator for producing high concentrations of small ions," *Review of Scientific Instruments,* vol. 32, no. 12, pp. 1351-1355, 1961.

[197] K. H. Baek *et al.*, "Polyimide Surface Dielectric Barrier Discharge for Inactivation of SARS-CoV-2 Trapped in a Polypropylene Melt-Blown Filter," *ACS Applied Polymer Materials,* vol. 4, no. 11, pp. 8127-8135, 2022.

[198] Y. Wu *et al.*, "MS2 virus inactivation by atmospheric-pressure cold plasma using different gas carriers and power levels," *Applied and environmental microbiology,* vol. 81, no. 3, pp. 996-1002, 2015.

[199] C.-C. Tseng and C.-S. Li, "Ozone for inactivation of aerosolized bacteriophages," *Aerosol science and technology,* vol. 40, no. 9, pp. 683-689, 2006.

[200] M. Moreau, N. Orange, and M. Feuilloley, "Non-thermal plasma technologies: new tools for bio-decontamination," *Biotechnology advances,* vol. 26, no. 6, pp. 610-617, 2008.

[201] B. K. Murray *et al.*, "Virion disruption by ozone-mediated reactive oxygen species," *Journal of virological methods,* vol. 153, no. 1, pp. 74-77, 2008.

[202] G. Nayak *et al.*, "Rapid inactivation of airborne porcine reproductive and respiratory syndrome virus using an atmospheric pressure air plasma," *Plasma Processes and Polymers,* vol. 17, no. 10, p. 1900269, 2020.

[203] J. L. Zimmermann *et al.*, "Effects of cold atmospheric plasmas on adenoviruses in solution," *Journal of Physics D: Applied Physics,* vol. 44, no. 50, p. 505201, 2011.

[204] H. A. Aboubakr, U. Gangal, M. M. Youssef, S. M. Goyal, and P. J. Bruggeman, "Inactivation of virus in solution by cold atmospheric pressure plasma: identification of chemical inactivation pathways," *Journal of Physics D: Applied Physics,* vol. 49, no. 20, p. 204001, 2016.

[205] G. Nayak, H. A. Aboubakr, S. M. Goyal, and P. J. Bruggeman, "Reactive species responsible for the inactivation of feline calicivirus by a two-dimensional array of integrated coaxial microhollow dielectric barrier discharges in air," *Plasma Processes and Polymers,* vol. 15, no. 1, p. 1700119, 2018.

[206] T. Xia, A. Kleinheksel, E. M. Lee, Z. Qiao, K. R. Wigginton, and H. L. Clack, "Inactivation of airborne viruses using a packed bed non-thermal plasma reactor," *Journal of physics D: Applied physics,* vol. 52, no. 25, p. 255201, 2019.

[207] I. Assadi *et al.*, "Review on inactivation of airborne viruses using non-thermal plasma technologies: from MS2 to coronavirus," *Environmental Science and Pollution Research,* vol. 29, no. 4, pp. 4880-4892, 2022.

[208] W. L. Dietrich, J. S. Bennett, B. W. Jones, and M. H. Hosni, "Laboratory modeling of SARS-CoV-2 exposure reduction through physically distanced seating in aircraft cabins using bacteriophage aerosol—November 2020," *Morbidity and Mortality Weekly Report,* vol. 70, no. 16, p. 595, 2021.

[209] L. M. Casanova, S. Jeon, W. A. Rutala, D. J. Weber, and M. D. Sobsey, "Effects of air temperature and relative humidity on coronavirus survival on surfaces," *Applied and environmental microbiology,* vol. 76, no. 9, pp. 2712-2717, 2010.

[210] J.-S. Chang, P. A. Lawless, and T. Yamamoto, "Corona discharge processes," *IEEE Transactions on plasma science,* vol. 19, no. 6, pp. 1152-1166, 1991.

[211] M. H. Adams, "Bacteriophages," *Bacteriophages.*, 1959.

[212] C. S. Fagnant *et al.*, "Development of an elution device for ViroCap virus filters," *Environmental monitoring and assessment,* vol. 189, pp. 1-10, 2017.

[213] U. N. Lee *et al.*, "Miniaturizing wet scrubbers for aerosolized droplet capture," *Analytical chemistry,* vol. 93, no. 33, pp. 11433-11441, 2021.

[214] A. Dascalu, V. Pohoata, K. Shimizu, and L. Sirghi, "Molecular species generated by surface dielectric barrier discharge micro-plasma in small chambers enclosing atmospheric air and water samples," *Plasma Chem. Plasma Process.,* vol. 41, pp. 389-408, 2021.

[215] A. Al-Abduly and P. Christensen, "An in situ and downstream study of non-thermal plasma chemistry in an air fed dielectric barrier discharge (DBD)," *Plasma Sources Science and Technology,* vol. 24, no. 6, p. 065006, 2015.

[216] G. Mahamuni, B. Ockerman, and I. Novosselov, "Electrostatic Capillary Collector for In-Situ Spectroscopic Analysis of Aerosols," *Aerosol Science and Technology,* pp. 1-40, 2019, doi: 10.1080/02786826.2019.1600653.

[217] R. S. Vaddi, Y. Guan, and I. Novosselov, "Behavior of ultrafine particles in electro-hydrodynamic flow induced by corona discharge," *Journal of Aerosol Science*, p. 105587, 2020.

[218] T. Xia *et al.*, "Inactivation of airborne porcine reproductive and respiratory syndrome virus (PRRSv) by a packed bed dielectric barrier discharge non-thermal plasma," *Journal of hazardous materials,* vol. 393, p. 122266, 2020.